

**OPTIMIZING THE USE OF THE THERMAL INTEGRITY SYSTEM  
FOR EVALUATING AUGER-CAST PILES**

**BDV25-977-09**

**FINAL REPORT**

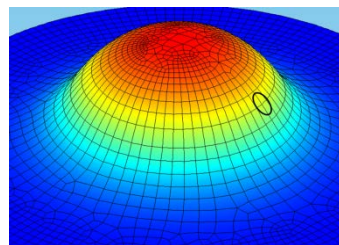
*Gray Mullins, Ph.D., P.E.*

*Principal Investigator*

*And*

*Kevin Johnson, MCE, E.I.*

*Doctoral Candidate*



July 2016

## **Disclaimer**

The opinions, findings, and conclusions expressed in this publication are those of the authors and not necessarily those of the State of Florida Department of Transportation.

### APPROXIMATE CONVERSIONS TO SI UNITS

SYMBOL	WHEN YOU KNOW	MULTIPLY BY	TO FIND	SYMBOL
<b>LENGTH</b>				
<b>in</b>	inches	25.4	millimeters	mm
<b>ft</b>	feet	0.305	meters	m
<b>yd</b>	yards	0.914	meters	m
<b>mi</b>	miles	1.61	kilometers	km

SYMBOL	WHEN YOU KNOW	MULTIPLY BY	TO FIND	SYMBOL
<b>AREA</b>				
<b>in<sup>2</sup></b>	square inches	645.2	square millimeters	mm <sup>2</sup>
<b>ft<sup>2</sup></b>	square feet	0.093	square meters	m <sup>2</sup>
<b>yd<sup>2</sup></b>	square yard	0.836	square meters	m <sup>2</sup>
<b>ac</b>	acres	0.405	hectares	ha
<b>mi<sup>2</sup></b>	square miles	2.59	square kilometers	km <sup>2</sup>

SYMBOL	WHEN YOU KNOW	MULTIPLY BY	TO FIND	SYMBOL
<b>VOLUME</b>				
<b>fl oz</b>	fluid ounces	29.57	milliliters	mL
<b>gal</b>	gallons	3.785	liters	L
<b>ft<sup>3</sup></b>	cubic feet	0.028	cubic meters	m <sup>3</sup>
<b>yd<sup>3</sup></b>	cubic yards	0.765	cubic meters	m <sup>3</sup>
NOTE: volumes greater than 1000 L shall be shown in m <sup>3</sup>				

SYMBOL	WHEN YOU KNOW	MULTIPLY BY	TO FIND	SYMBOL
<b>MASS</b>				
<b>oz</b>	ounces	28.35	grams	g
<b>lb</b>	pounds	0.454	kilograms	kg
<b>T</b>	short tons (2000 lb)	0.907	megagrams (or "metric ton")	Mg (or "t")

SYMBOL	WHEN YOU KNOW	MULTIPLY BY	TO FIND	SYMBOL
<b>TEMPERATURE (exact degrees)</b>				
°F	Fahrenheit	5 (F-32)/9 or (F-32)/1.8	Celsius	°C

SYMBOL	WHEN YOU KNOW	MULTIPLY BY	TO FIND	SYMBOL
<b>ILLUMINATION</b>				
fc	foot-candles	10.76	lux	lx
fL	foot-Lamberts	3.426	candela/m <sup>2</sup>	cd/m <sup>2</sup>

SYMBOL	WHEN YOU KNOW	MULTIPLY BY	TO FIND	SYMBOL
<b>FORCE and PRESSURE or STRESS</b>				
lbf	poundforce	4.45	newtons	N
lbf/in <sup>2</sup>	poundforce per square inch	6.89	kilopascals	kPa
kip	kilopound	4.45	kilonewtons	kN

### APPROXIMATE CONVERSIONS TO SI UNITS

SYMBOL	WHEN YOU KNOW	MULTIPLY BY	TO FIND	SYMBOL
<b>LENGTH</b>				
mm	millimeters	0.039	inches	in
m	meters	3.28	feet	ft
m	meters	1.09	yards	yd
km	kilometers	0.621	miles	mi

SYMBOL	WHEN YOU KNOW	MULTIPLY BY	TO FIND	SYMBOL
<b>AREA</b>				
mm <sup>2</sup>	square millimeters	0.0016	square inches	in <sup>2</sup>
m <sup>2</sup>	square meters	10.764	square feet	ft <sup>2</sup>
m <sup>2</sup>	square meters	1.195	square yards	yd <sup>2</sup>
ha	hectares	2.47	acres	ac
km <sup>2</sup>	square kilometers	0.386	square miles	mi <sup>2</sup>

SYMBOL	WHEN YOU KNOW	MULTIPLY BY	TO FIND	SYMBOL
<b>VOLUME</b>				
<b>mL</b>	milliliters	0.034	fluid ounces	fl oz
<b>L</b>	liters	0.264	gallons	gal
<b>m<sup>3</sup></b>	cubic meters	35.314	cubic feet	ft <sup>3</sup>
<b>m<sup>3</sup></b>	cubic meters	1.307	cubic yards	yd <sup>3</sup>

SYMBOL	WHEN YOU KNOW	MULTIPLY BY	TO FIND	SYMBOL
<b>MASS</b>				
<b>g</b>	grams	0.035	ounces	oz
<b>kg</b>	kilograms	2.202	pounds	lb
<b>Mg (or "t")</b>	megagrams (or "metric ton")	1.103	short tons (2000 lb)	T

SYMBOL	WHEN YOU KNOW	MULTIPLY BY	TO FIND	SYMBOL
<b>TEMPERATURE (exact degrees)</b>				
<b>°C</b>	Celsius	1.8C+32	Fahrenheit	°F

SYMBOL	WHEN YOU KNOW	MULTIPLY BY	TO FIND	SYMBOL
<b>ILLUMINATION</b>				
<b>lx</b>	lux	0.0929	foot-candles	fc
<b>cd/m<sup>2</sup></b>	candela/m <sup>2</sup>	0.2919	foot-Lamberts	fl

SYMBOL	WHEN YOU KNOW	MULTIPLY BY	TO FIND	SYMBOL
<b>FORCE and PRESSURE or STRESS</b>				
<b>N</b>	newtons	0.225	poundforce	lbf
<b>kPa</b>	kilopascals	0.145	poundforce per square inch	lbf/in <sup>2</sup>
<b>kN</b>	kilonewtons	0.225	kilopound	kip

\*SI is the symbol for the International System of Units. Appropriate rounding should be made to comply with Section 4 of ASTM E380.

### Technical Report Documentation Page

1. Report No.	2. Government Accession No.	3. Recipient's Catalog No.	
4. Title and Subtitle OPTIMIZING THE USE OF THE THERMAL INTEGRITY SYSTEM FOR EVALUATING AUGER-CAST PILES		5. Report Date July 2016	
		6. Performing Organization Code	
7. Author(s) G. Mullins and K. Johnson		8. Performing Organization Report No.	
9. Performing Organization Name and Address University of South Florida Department of Civil and Environmental Engineering 4202 E. Fowler Avenue, ENB 118s Tampa, FL 33620		10. Work Unit No. (TRAIS)	
		11. Contract or Grant No. BDV25-977-09	
12. Sponsoring Agency Name and Address Florida Department of Transportation 605 Suwannee Street, MS 30 Tallahassee, FL 32399		13. Type of Report and Period Covered Final Report 06/12-9/15	
		14. Sponsoring Agency Code	
15. Supplementary Notes FDOT Project Manager: David Horhota			
16. Abstract Auger-cast piles (sometimes called auger-cast-in-place, or ACIP, piles) are a subset of the larger category of deep foundation elements known as bored piles. Although similar to drilled shafts at first glance, ACIP piles differ in the construction processes and design capacity. Therein, ACIP piles require no slurry or casing to hold open the excavation; rather, a continuous flight auger is used which maintains the stability and volume of the excavation via the soil that fills the auger flights. In this regard, no means of inspecting the dimensions of the borehole is provided and the as-built pile dimensions can only be inferred from grout pumping logs. The resultant shape of the foundation element is further dependent on the rate of auger extraction relative to the grout pumping rate. With this in mind, there is concern of the as-built shape and integrity. As such, use of ACIP by the Florida Department of Transportation (FDOT) has been limited to foundations for sound walls.  The thermal integrity test has proven to be an effective method to evaluate the integrity of newly constructed drilled shafts (i.e. identifying anomalies, rebar cage alignment, concrete cover, etc.). However, very few auger-cast piles have been tested with this method as standard integrity access tubes are not typically installed. If an improved quality assessment tool is developed to ascertain the final, as-built configuration (size, depth, diameter, concrete cover, etc.) of auger-cast piles, their use in other applications can be reevaluated. The results of this study showed the limitations of various instrumentation schemes and introduced alternate analysis methods specific to ACIP piles.			
17. Key Word Augercast pile, thermal integrity test, quality assurance		18. Distribution Statement No restrictions.	
19. Security Classif. (of this report) Unclassified.	20. Security Classif. (of this page) Unclassified.	21. No. of Pages 180	22. Price

**Form DOT F 1700.7** (8-72) Reproduction of completed page authorized

## **Acknowledgments**

The authors would like to acknowledge the Florida Department of Transportation for funding this project, with specific thanks to Dr. David Horhota, Juan Castellano, Larry Jones, Rodrigo Herrera and the entire review team for their insightful contributions.

## Executive Summary

Auger-cast piles (sometimes called auger-cast-in-place, or ACIP, piles) are a subset of the larger category of deep foundation elements known as bored piles. Although similar to drilled shafts at first glance, ACIP piles differ in the construction processes and design capacity. Therein, ACIP piles require no slurry or casing to hold open the excavation; rather, a continuous flight auger is used which maintains the stability and volume of the excavation via the soil that fills the auger flights. In this regard, no means of inspecting the dimensions of the borehole is provided and the as-built pile dimensions can only be inferred from grout pumping logs. The resultant shape of the foundation element is further dependent on the rate of auger extraction relative to the grout pumping rate. With this in mind, there is concern of the as-built shape and integrity. As such, use of ACIP by the Florida Department of Transportation (FDOT) has been limited to foundations for sound walls.

The thermal integrity test has proven to be an effective method to evaluate the integrity of newly constructed drilled shafts (i.e., identifying anomalies, rebar cage alignment, concrete cover, etc.). However, very few auger-cast piles have been tested with this method as standard integrity access tubes are not typically installed. If an improved quality assessment tool is developed to ascertain the final, as-built configuration (size, depth, diameter, concrete cover, etc.) of auger-cast piles, their use in other applications can be reevaluated. This project included numerical modeling, field data collection and analysis methods specific to ACIP pile sizes to assess the applicability of thermal integrity methods.

While single bar systems are not likely to be used for highway bridge foundations, information from such a configuration is sometimes sufficient for integrity evaluation. Using single bar (center) measurement locations the pile integrity and shape can be analyzed and the radius computed using alternate methods not common to shaft analyses. These methods include numerical modeling, gradient assessment or a simplified T-soil approach. However, when the bar is not centered, the simplified method cannot be used; gradient information is needed.

Piles instrumented with various schemes were monitored and the data analyzed using a wide range of techniques. Results concluded that larger piles (e.g. 24in diameter or larger) instrumented with 4 measurement locations (in plan) provided the best integrity assessment. This was based on the assumption that a cage type reinforcing detail would be used that provided 4.5in of cover. Larger diameter piles provide even better evaluation.

## Table of Contents

Disclaimer .....	ii
Conversion Factors .....	iii
Technical Report Documentation .....	vi
Acknowledgments.....	vii
Executive Summary .....	viii
List of Tables .....	xi
List of Figures .....	xii
Chapter One: Introduction .....	1
1.1 Background.....	1
1.2 Organization of the Report.....	2
Chapter Two: Literature Review .....	3
2.1 Auger-Cast Piles .....	3
2.1.1 ACIP Quality Control .....	4
2.1.2 ACIP Post-Construction Quality Assurance.....	6
2.2 Thermal Integrity Profiling.....	10
2.2.1 TIP Methods & Equipment.....	11
2.2.2 TIP Theory .....	12
2.2.3 TIP Analysis.....	16
2.2.4 TIP Modeling.....	23
2.3 Use of TIP for ACIP .....	39
Chapter Three: Numerical Modeling.....	41
3.1 Modeling Hyperbolic Temperature Corrections.....	41
3.2 Analysis of field data for hyperbolic parameter selection .....	49
3.3 Modeling for time and spatial sensitivity of measurements .....	55
3.4 Chapter Summary .....	65
Chapter Four: Feasibility of Probe-Based Inclination Measurements.....	68
4.1 Past Case Studies .....	68
4.2 Thermal Probe-Based Inclination Systems.....	74
4.2.1 Basic System.....	74
4.2.2 Probe-Based System .....	75
4.3 Thermal Gradient Method.....	76
4.4 Lab Testing of Inclination Systems .....	78
4.4.1 Wire Spin / Gradient Monitoring.....	83
4.4.2 3-D Position Tracking.....	85
4.5 Chapter Summary .....	93

Chapter Five: Field Testing .....	94
5.1 Overview .....	94
5.2 Case Studies .....	94
5.2.1 Case Study 1: 22in drilled shafts with single center access tube, tested with probe . .....	94
5.2.2 Case Study 2: 22in drilled shafts with four thermal wires fastened around a single center bar.....	102
5.2.3 Case Study 3: 14in auger-cast piles instrumented with a single wire on single center reinforcing bar.....	116
5.2.4 Case Study 4: 30in auger-cast piles with full reinforcing cage – comparison between 2- and 4-wire instrumentation.....	129
 Chapter Six: Conclusions.....	 134
6.1 Numerical Modeling .....	134
6.2 Probe-based Inclination Measurements .....	135
6.3 Field Testing and Evaluation .....	135
6.4 Summary .....	137
6.5 Recommendations for Analyzing TIP Data .....	139
 References.....	 141
 Appendix A.....	 145
 Appendix B.....	 153

## List of Tables

Table 2.1. Thermal conductivity of mature concrete based on aggregate type (Schindler & Folliard, 2002).....	29
Table 2.2. Specific heat of concrete materials (Schindler & Folliard, 2002) .....	29
Table 2.3. Conductive thermal properties of subsurface materials.....	30
Table 3.1. Hyperbolic equation parameters for model data at 18hr.....	43
Table 3.2. Hyperbolic equation parameters for field data at 18 hr .....	47
Table 4.1. DE-ACCM3D Tri-axis Accelerometer Specifications .....	72
Table 4.2. Top of settlement rod movement .....	73
Table 4.3. LORD MicroStrain® 3DM-GX4® Specifications .....	75
Table 4.4. InvenSense MPU-6000™ Specifications .....	76

## List of Figures

Figure 2.1. ACIP drill rig (left) and pile reinforcement (right) .....	3
Figure 2.2. Near-surface necks in ACIP piles found upon excavation for footing.....	5
Figure 2.3. Sonic Echo Testing (Silwinski & Fleming, 1983).....	6
Figure 2.4. Crosshole Sonic Logging, CSL (Hollema and Olson, 2003) .....	7
Figure 2.5. Single Hole Sonic Logging, SSL (USDOT, 2015) .....	8
Figure 2.6. Gamma-Gamma Logging, GGL (COLOG, 2010) .....	9
Figure 2.7. Testing coverage provided by CSL and GGL for varying shaft sizes (Mullins, 2010) .....	10
Figure 2.8. TIP setup – probe method.....	12
Figure 2.9. TIP setup – wire method.....	12
Figure 2.10. Temperature distributions in an idealized shaft.....	13
Figure 2.11. Radial temperature distribution for various shaft sizes (Mullins, 2012) .....	14
Figure 2.12. Relationship between cage position, shaft size, and temperature (Mullins, 2012) .....	15
Figure 2.13. Relationship between shaft size and temperature for a given cage position (Johnson, 2014).....	15
Figure 2.14. Example thermal profiles with anomalies (Johnson, 2014) .....	16
Figure 2.15. Yield plot data converted to effective diameter compared with thermal data (Mullins, 2010) .....	17
Figure 2.16. Temperature-radius relationship deduced from yield plot data (Mullins and Winters, 2012).....	18
Figure 2.17. Effective radius of shaft as interpreted from TIP analysis (Mullins and Winters, 2012).....	19
Figure 2.18. Single-point solution for determining T-R relationship based on average temperature and average radius of entire shaft, compared with theoretical true T-R relationship.....	20
Figure 2.19. Measured, theoretical, and corrected temperatures for top and bottom of a shaft (Johnson, 2014) .....	22
Figure 2.20. Ground temperatures in the United States (Pauly, 2010) .....	23
Figure 2.21. Hydration behavior of concrete (Schindler & Folliard, 2002) .....	24
Figure 2.22. Effect of shape parameters $\alpha$ on hydration curve (Folliard et. al., 2008).....	25
Figure 2.23. Effect of shape parameter $\beta$ on hydration curve (Folliard et. al., 2008).....	26
Figure 2.24. Effect of shape parameter $\tau$ on hydration curve (Folliard et. al., 2008).....	26
Figure 2.25. Soil density as a function of uncorrected SPT blow count (N) (Pauly, 2010) .....	31
Figure 2.26. Kersten’s conductivity vs. density at varied moisture contents for sandy soils (Pauly, 2010).....	31
Figure 2.27. Kersten’s conductivity vs. density at varied moisture contents for clayey soils (Pauly, 2010) .....	32
Figure 2.28. Mickley’s conductivity vs. density at varied moisture contents for sandy soils (Pauly, 2010) .....	32
Figure 2.29. Mickley’s conductivity vs. density at varied moisture contents for clayey soils (Pauly, 2010) .....	33

Figure 2.30. Gemant’s conductivity vs. density at varied moisture contents for sandy soils (Pauly, 2010).....	33
Figure 2.31. Gemant’s conductivity vs. density at varied moisture contents for clayey soils (Pauly, 2010) .....	34
Figure 2.32. De Vrie’s conductivity vs. density at varied moisture contents for sandy soils (Pauly, 2010).....	34
Figure 2.33. De Vrie’s conductivity vs. density at varied moisture contents for clayey soils (Pauly, 2010) .....	35
Figure 2.34. VanRooyen’s conductivity vs. density at varied moisture contents for sandy soils (Pauly, 2010) .....	35
Figure 2.35. VanRooyen’s conductivity vs. density at varied moisture contents for clayey soils (Pauly, 2010) .....	36
Figure 2.36. McGaw’s conductivity vs. density at varied moisture contents for sandy soils (Pauly, 2010).....	36
Figure 2.37. McGaw’s conductivity vs. density at varied moisture contents for clayey soils (Pauly, 2010) .....	37
Figure 2.38. Johansen’s conductivity vs. density at varied moisture contents for sandy soils (Pauly, 2010) .....	37
Figure 2.39. Johansen’s conductivity vs. density at varied moisture contents for clayey soils (Pauly, 2010) .....	38
Figure 2.40. Modeled and measured temperature profiles for a tested shaft. (Mullins, 2008) .....	39
Figure 3.1. Field data (left), computer-generated model (right).....	42
Figure 3.2. Results of model analysis at 18 hr.....	44
Figure 3.3. Variation of top roll-off inflection temperatures compared with air temperatures .....	45
Figure 3.4. Variation of alpha with time resulting from analysis of model data .....	45
Figure 3.5. Range of results from model analysis up to 60 hr.....	46
Figure 3.6. Results of analysis field data analysis at 18 hr .....	47
Figure 3.7. Top inflection point temperatures compared with measured air temperatures.....	48
Figure 3.8. Correlation between $\alpha$ and time.....	48
Figure 3.9. T-R results for analysis at 18hr (left) and range of results for all times (right) ..	49
Figure 3.10. Best fit $\alpha$ values for both the top and bottom of shaft .....	51
Figure 3.11. Probability density distribution for the coefficient c in the equation $\alpha=ct$ ....	52
Figure 3.12. Statistically derived boundaries for $\alpha$ selection.....	53
Figure 3.13. Top of shaft inflection temperature along with max. and min. daily air temperature .....	54
Figure 3.14. Hyperbolic inflection point offsets for top and bottom of shaft fits.....	55
Figure 3.15. Optimum testing/analysis time for different size shafts with drilled shaft concrete .....	56
Figure 3.16. Optimum testing/analysis time for different size shafts with ACIP grout ....	56
Figure 3.17. Acceptable measurement locations based on shaft size .....	57
Figure 3.18. Temperature-radius relationship zone for ACIP piles.....	58
Figure 3.19. T-R curve for center of shaft measurements .....	58
Figure 3.20. Computer-generated models for anomaly sensitivity.....	59

Figure 3.21. Model results for single centerline of shaft measurements .....	60
Figure 3.22. Model results for four perimeter measurements taken 6 in from edge of shaft .....	61
Figure 3.23. Center vs. perimeter measurements for 8 ft shaft with 2-, 6-, 10-, & 24-inch anomalies .....	62
Figure 3.24. Effect of a misaligned single center measurement location .....	63
Figure 3.25. Effect of two measurement locations misaligned in the x-direction (per drawing) .....	64
Figure 3.26. Effect of two measurement locations misaligned in the y-direction (per drawing) .....	65
Figure 4.1. Groove-less casing with wheel-less inclinometer .....	68
Figure 4.2. Defected shape of access tubes and cage distorted by casing removal (Crosstown Connector Project, Tampa, FL) .....	69
Figure 4.3. Inclined cage from inclinometer measurements (left) and thermal alignment measurements (right) (Jolley Bridge Project, Marco Island, FL) .....	70
Figure 4.4. Two of four settlement rods that exhibited excessive tilting.....	71
Figure 4.5. Circuit board installed in PVC delivery rod.....	72
Figure 4.6. Inclination measurements taken from four settlement rods at various degrees of inclination severity .....	72
Figure 4.7. Data collection from 3-axis accelerometer.....	73
Figure 4.8. LORD MicroStrain® 3DM-GX4® .....	74
Figure 4.9. InvenSense MPU-6000™ (left), probe system (middle and right) .....	75
Figure 4.10. Probe rotation based on direction of thermal gradient with respect to probe infrared sensors .....	76
Figure 4.11. Computed probe rotation based on thermal gradient calculations during testing.....	77
Figure 4.12. Stepper motor system components (Anaheim Automation, Anaheim, CA) .....	78
Figure 4.13. Gyro probe (left) and IMU (right) attached to stepper shaft assembly .....	79
Figure 4.14. Rotational trials with probe-based gyro sensor .....	79
Figure 4.15. Rotational trials with IMU sensor – 180° oscillations at 17 deg/sec.....	81
Figure 4.16. Rotational trials with IMU sensor – 180° oscillations at 450deg/sec.....	81
Figure 4.17. Rotational trials with IMU sensor – 5 revolutions CW then CCW at 20deg/sec.....	82
Figure 4.18. Inclination trials with IMU sensor – +/-45° oscillations at 17deg/sec .....	82
Figure 4.19. Inclination trials with IMU sensor – +/-45° oscillations at 450deg/sec .....	83
Figure 4.20. Temperature measurements from each IR sensor (left) and computed probe rotation based on thermal gradient from each three-sensor combination (right)...	84
Figure 4.21. 30ft PVC pipe with prescribed lateral deflections.....	86
Figure 4.22. Aluminum probe body with housed IMU sensor .....	87
Figure 4.23. Measured vs. actual pipe deflection in the X-Z (left) and Y-Z (right) planes.....	88
Figure 4.24. Measured vs. actual pipe deflection in the X-Y plane.....	89
Figure 4.25. Inclination error due diameter tolerance between probe and tube .....	90
Figure 4.26. Measured inclination error between fabricated probe body and PVC pipe... ..	90
Figure 4.27. Design of probe to aid in alignment and reduce inclination error .....	92
Figure 4.28. Reduced error and increased navigable radius with increasing probe length	93

Figure 5.1. Shaft with single center access tube for TIP probe testing.....	95
Figure 5.2. Shaft B4 raw temperature profile (left); interpreted results (right) .....	96
Figure 5.3. Shaft B5 raw temperature profile (left); interpreted results (right) .....	97
Figure 5.4. Shaft B6 raw temperature profile (left); interpreted results (right) .....	98
Figure 5.5. Shaft P6 raw temperature profile (left); interpreted results (right).....	99
Figure 5.6. Shaft P5 raw temperature profile (left); interpreted results (right).....	100
Figure 5.7. Top, middle, and bottom (left to right) of exhumed shaft P5.....	101
Figure 5.8. 1.5in PVC instrumented with four orthogonal thermal wires placed in center of shaft .....	102
Figure 5.9. Temperature history for each shaft.....	103
Figure 5.10. Shaft P1 raw temperature profile (left); interpreted results (right).....	104
Figure 5.11. Shaft P3 raw temperature profile (left); interpreted results (right).....	105
Figure 5.12. Shaft B3 raw temperature profile (left); interpreted results (right) .....	106
Figure 5.13. Shaft P2 raw temperature profile (left); interpreted results (right).....	107
Figure 5.14. Shaft B1 raw temperature profile (left); interpreted results (right) .....	108
Figure 5.15. Discrepancy between true T-R relationship and pole-point solution when center measurements are used on a small radius shaft.....	109
Figure 5.16. Shaft B1 interpreted results using hyperbolic T-R relationship .....	111
Figure 5.17. Shaft B1 interpreted results using hyperbolic T-R relationship with parameters adjusted for optimum fit .....	112
Figure 5.18. Model generated bell curves used to match measured temperature gradient between opposing wires from shaft B1 at 10ft .....	113
Figure 5.19. Thermal gradients at each depth matched to corresponding bell curves.....	114
Figure 5.20. Shaft B1 interpreted results using thermal gradient method .....	115
Figure 5.21. 14in ACIP pile instrumented with single center thermal wire .....	116
Figure 5.22. Reinforcing cage with internal hooks (left) and instrumented center bar with centralizing device and temporary protective PVC sleeve (right) .....	117
Figure 5.23. Shaft EP1 raw temperature profile (left); interpreted results (right) .....	118
Figure 5.24. Shaft EP2 raw temperature profile (left); interpreted results (right) .....	119
Figure 5.25. Shaft EP4 raw temperature profile (left); interpreted results (right) .....	120
Figure 5.26. Shaft EP6 raw temperature profile (left); interpreted results (right) .....	121
Figure 5.27. Shaft EP7 raw temperature profile (left); interpreted results (right) .....	122
Figure 5.28. Shaft EP8 raw temperature profile (left); interpreted results (right) .....	123
Figure 5.29. Shaft EP9 raw temperature profile (left); interpreted results (right) .....	124
Figure 5.30. Shaft EP10 raw temperature profile (left); interpreted results (right) .....	125
Figure 5.31. Shaft EP11 raw temperature profile (left); interpreted results (right) .....	126
Figure 5.32. Shaft EP12 raw temperature profile (left); interpreted results (right) .....	127
Figure 5.33. Shaft EP13 raw temperature profile (left); interpreted results (right) .....	128
Figure 5.34. ACIP reinforcing cage instrumented with four thermal wires .....	129
Figure 5.35. Cage instrumented with two wires being placed into grout .....	130
Figure 5.36. ACIP with full reinforcing cage instrumented with four thermal wires.....	131
Figure 5.37. ACIP with full reinforcing cage instrumented with two thermal wires .....	132
Figure 5.38. Isotherms for 30in diameter auger-cast overlain by a centered square cage and the only two possible positions that produce the two opposite side temperature measurements from the bottom of the pile .....	133
Figure 6.1. Rationale for determining smallest 4 tube (or wire) pile with full cage.....	138

Figure 6.2. Alternate T-soil method for determining the T to R correlation. ....	139
Figure A.1. Lord Microstrain 3DM-GX4-25 datasheet .....	146
Figure A.2. Invensense MPU-6000 datasheet.....	147
Figure A.3. Invensense MPU-6000 datasheet (cont'd).....	148
Figure A.4. Invensense MPU-6000 datasheet (cont'd).....	149
Figure A.5. Invensense MPU-6000 datasheet (cont'd).....	150
Figure A.6. Invensense MPU-6000 datasheet (cont'd).....	151
Figure A.7. Invensense MPU-6000 datasheet (cont'd).....	152
Figure B.1. Shaft B-1 (from top to bottom): shaft top (left) and toe (right); side views of shaft top section; side views of shaft middle section; side views of bottom section. ....	154
Figure B.2. Shaft P-1 (from top to bottom): shaft top (left) and toe (right); side views of shaft top section; side views of shaft middle section; side views of bottom section. ....	155
Figure B.3. Shaft P-3 (from top to bottom): shaft top (left) and toe (right); side views of shaft top section; side views of shaft middle section; side views of bottom section ....	156
Figure B.4. Shaft B-3 (from top to bottom): shaft top (left) and toe (right); side views of shaft top section; side views of shaft middle section; side views of bottom section ....	157
Figure B.5. Shaft P-2 (from top to bottom): shaft top (left) and toe (right); side views of shaft top section; side views of shaft middle section; side views of bottom section. ....	158
Figure B.6. Shaft B-4 (from top to bottom): shaft top (left) and toe (right); side views of shaft top section; side views of shaft middle section; side views of bottom section ....	159
Figure B.7. Shaft B-5 (from top to bottom): shaft top (left) and toe (right); side views of shaft top section; side views of shaft middle section; side views of bottom section. ....	160
Figure B.8. Shaft B-6 (from top to bottom): shaft top (left) and toe (right); side views of shaft top section; side views of shaft middle section; side views of bottom section ....	161
Figure B.9. Shaft P-5 (from top to bottom): shaft top (left) and toe (right); side views of shaft top section; side views of shaft middle section; side views of bottom section. ....	162
Figure B.10. Shaft P-6 (from top to bottom): shaft top (left) and toe (right); side views of shaft top section; side views of shaft middle section; side views of bottom section ....	163

Intentionally Left Blank

## *Chapter One: Introduction*

### **1.1 Background**

Auger-cast piles (sometimes called auger-cast-in-place, or ACIP piles) are a subset of the larger category of deep foundation elements known as bored piles. In the U.S., bored piles also include drilled shafts. As the name implies, bored pile construction involves drilling a deep cylindrical hole in the ground and installing a fluid concrete or grout within the walls of the excavation wherein the walls are the “formwork.” The dimensions of the as-built element are essentially defined by the shape taken-on after drilling and the application of hydrostatic pressure from the fluid concrete or grout onto the excavation walls.

Although similar at first glance, ACIP piles differ from drilled shafts both in construction processes and design capacity. Drilled shaft construction provides lateral stability to an open excavation via hydrostatic slurry pressure or mechanical bracing from a casing. Therein, the soil is methodically removed using repeated grabs, bites or scoops with a relatively short drill tool (usually only 2 or 3 flights). ACIP piles differ in that no slurry or casing is required to hold open the excavation; rather, a continuous flight auger is used which maintains the stability and volume of the excavation via the soil that fills the auger flights. The sidewalls therefore push against the soil-filled auger and are not free to collapse inward. The length of auger must extend to the deepest required tip elevation.

The net result of the significantly different auger configuration is that grout is pumped directly to the base of the excavation through the stem of the ACIP auger whereas drilled shafts place concrete through a separate and dedicated tremie pipe. Note that grout differs from concrete as it has no coarse aggregate and is easily pumped through smaller lines (e.g., drill stem). During grouting, the ACIP auger is extracted slowly enough such that the grout pumping rate can fill the entire theoretical volume plus a small over-pour percentage which can develop increased passive pressure. However, if the volume of the soil-laden auger is extracted faster than the inflowing grout, it will result in a net negative pressure that will pull the soil walls in below the tip of the auger. As the auger tip reaches the surface it becomes more difficult to sustain grout pressure and often the contractor stops pumping to reduce waste and cleanup. This can cause severe necks in the cross-section and is a primary concern about using ACIP piles. Further, the most common configurations use a single central bar to minimal reinforcing cages, which have traditionally been too small to equip with integrity access tubes. This has made post-construction integrity evaluation limited.

The thermal integrity test has proven to be an effective method to evaluate the integrity of newly constructed drilled shafts (i.e. identifying anomalies, rebar cage alignment, concrete cover, etc.). However, very few auger-cast piles have been tested with this method as standard integrity access tubes are not typically installed. The disadvantage of auger-cast piles relative to piles or drilled shafts is that the final, as-built configuration of these foundation units is largely unknown. As such, FDOT use has been limited to foundations for sound walls. If an improved quality

assessment tool is developed to ascertain the final, as-built configuration (size, depth, diameter, concrete cover, etc.) of auger-cast piles, their use in other applications can be reevaluated. It is the goal of this research to explore the use of the thermal integrity technology for auger-cast piles.

## **1.2 Organization of the Report**

This study entailed five tasks in the process of assessing the applicability of thermal integrity technologies to augercast piles. The Tasks included a literature review (Chapter 2), numerical modeling (Chapter 3), feasibility study of probe-based inclination measurements (Chapter 4), and field testing with various evaluation approaches (Chapter 5). Cfconclusions are presented in Chapter 6.

## Chapter Two: Literature Review

### 2.1 Auger-Cast Piles

Auger-cast piles, also referred to as auger-cast-in-place (ACIP) or continuous flight auger (CFA) piles, are a subset of the broader category of deep foundations which is bored piles. They are cousin to the more popular drilled shaft foundation, but are distinguished in their method of construction.

In drilled shaft construction, excavation is performed with multiple penetrations of a single or multi-flight auger, the hole is stabilized by slurry or casing, a rebar cage is placed, then concrete is tremied placed. In ACIP pile construction, excavation is performed by single penetration of a continuous flight auger to full depth, the auger is then extracted while grout is simultaneously pumped down through the hollow stem of the auger to fill the void left by the evacuating tool and soil. The sidewalls of the excavation are constantly supported throughout the process by either the soil filled auger or pressurized grout, eliminating the need for intermediate stabilization and resulting in a faster and less expensive installation than that of drilled shafts. Any reinforcing steel used is placed by pushing it down into the still fluid grout, immediately after withdrawal of the auger. Reinforcement in auger-cast piles may consist of a full rebar cage, similar to that for a drilled shaft, or, on smaller diameter piles, just a single center bar and/or a partial depth rebar cage. Note that grout is more commonly used, rather than concrete, for ease of pumping and rebar placement. Figure 2.1 shows an ACIP drill rig with continuous flight auger (left), and pile reinforcement consisting of partial depth rebar cages and full-length single center bars (right).



Figure 2.1. ACIP drill rig (left) and pile reinforcement (right)

Due to the high torque demands of continuous flight drilling, ACIP piles are generally limited to diameters of 12 – 36 inches and depths up to 100 feet. Used as single pile foundations, they are adequate for low demand structures, but used in group foundations, they can provide capacities that rival those of drilled shaft or driven pile foundations, and can offer an economical option for many larger structures. While auger-cast piles have experienced widespread success in private and commercial work, qualms over quality control and quality assurance issues have left them vastly under-utilized in U.S. transportation projects. Many of the control measures and evaluation techniques that are afforded by drilled shaft construction are simply not possible or have not been readily adapted for use with ACIP piles. Uncertainties over quality control and a lack of effective post-construction quality assurance methods has limited their use in transportation to mostly lighting/signage structures and sound walls. However, commercial success, potential for economy, and advancements in the power and technology of ACIP drill rigs, are leading toward a trend to address these perceived difficulties and to offer wider acceptance of auger-cast piles on transportation projects. (Brown et. al., 2007)

### **2.1.1 ACIP Quality Control**

Although reputed for their ease of installation, the speed and continuity of ACIP construction leaves little room for the stop-and-check type of control measures that many are accustomed with drilled shafts. Luxuries such as visual inspection of soil cuttings, verification of open excavation dimensions, and direct measurement of concrete level are not possible with auger-cast construction. However, quality control is instead achieved through the continuous monitoring and adjustment of various equipment performances during drilling and grouting.

During drilling, performance measures such as depth, rotation speed, and penetration rate of the auger are monitored and adjusted as needed to maintain stability of the hole. A common problem that can lead to defects in ACIP piles is excessive flighting/mining of the soil, wherein continued rotation without downward advancement literally pumps the soil from the ground like an Archimedes screw. This reduces lateral soil pressure or leaves the sidewalls of the excavation unsupported. To maintain hole stability, the balance between rotation speed and penetration rate must be constantly monitored and adjusted so that only the amount soil needed to offset the volume of the auger is displaced from the hole. The optimal ratio of rotation to penetration varies with soil type and can be particularly difficult to manage in subsurfaces of varying soil strata. Additional measurements that may be taken during drilling are the torque and crowd (downforce) of the auger, which can help to characterize the soil being drilled. (Brown et. al., 2007)

Upon reaching the final depth of drilling, grouting should begin immediately. Allowing the auger to sit stagnant can cause it to become stuck, and rotation of the auger without penetration can lead to excessive flighting of soil. To this end, grout should be ready prior to drilling and in sufficient amount so that placement can proceed without pause. To begin grouting, the auger should be raised a minimal distance from the bottom (about 6-12 in) to allow room for the initial influx of grout to blow out the plug from the bottom of the auger stem, then lowered back down

until back pressure on the grout system is established. The auger is then slowly extracted while grout is pumped, filling the void behind it. Critical measurements during this phase include auger depth, grout pressure, and volumetric flow rate. The extraction rate of the auger should match the flow rate of grout entering the hole, and sufficient pressure should be maintained (typically 150-250 psi) to ensure grout is fully filling all voids and providing hole stability in the absence of the auger. If the auger is withdrawn too quickly, a negative net pressure will form below the tip causing the soil walls to pull inward. Likewise, if the auger is extracted too slowly, grout will flow up the flights of the auger, making it increasingly difficult to track the as-placed volume vs depth of the pile. As the auger tip nears the surface, this becomes even more problematic as grout that has traveled up the flights is free to vent pressure to open air, often resulting in near surface necking defects like that shown in Figure 2.2.



Figure 2.2. Near-surface necks in ACIP piles found upon excavation for footing

Immediately upon completion of grouting and extraction of the auger, reinforcing steel should be placed. If a cage is being installed, it should be fully tied with centralizers attached prior to drilling to ensure there is no unnecessary delay. As the grout loses its workability, cage placement can be difficult. Cages should be lowered primarily by gravity, with only minimal downward pushing if necessary. Cage distortion and misalignment are difficult to control, even in fluid grout, and become severe if forced through un-workable grout or concrete.

### 2.1.2 ACIP Post-Construction Quality Assurance

Just as with drilled shafts, the blind nature of ACIP construction, and lack of visual inspection thereafter, requires the use of post-construction quality assurance techniques to ensure the as-built integrity of a pile. Load testing is the most reliable method for verifying pile capacity, but is also the most expensive and labor intensive. Static, dynamic, and rapid load testing can all be employed with ACIP piles using similar equipment and procedures as with drilled shafts, however non-destructive forms of testing can often provide enough information to assess pile integrity, and with greater economy.

Currently, the most popular form of evaluation for ACIP piles is surface testing, specifically sonic echo testing (Figure 2.3). This non-destructive test uses a hammer at the top of the pile to generate a low-strain compressive wave, and an accelerometer to record reflections as the wave travels down the pile and back up. Knowing the length of the pile,  $L$ , and the wave propagation speed in concrete,  $C$ , a reflection is expected to occur at a time equal to  $2L/C$  after the initial strike of the hammer. This is indicative of the wave traveling unobstructed to the toe of the pile, being reflected, and traveling back up. Any reflections occurring sooner than this suggest an anomaly in the pile. This test is popular due to its inexpensiveness and ease of use with ACIP piles, however it suffers from limitations in depth, size, and number of anomalies that can be detected. (Rausche et. al., 1994)

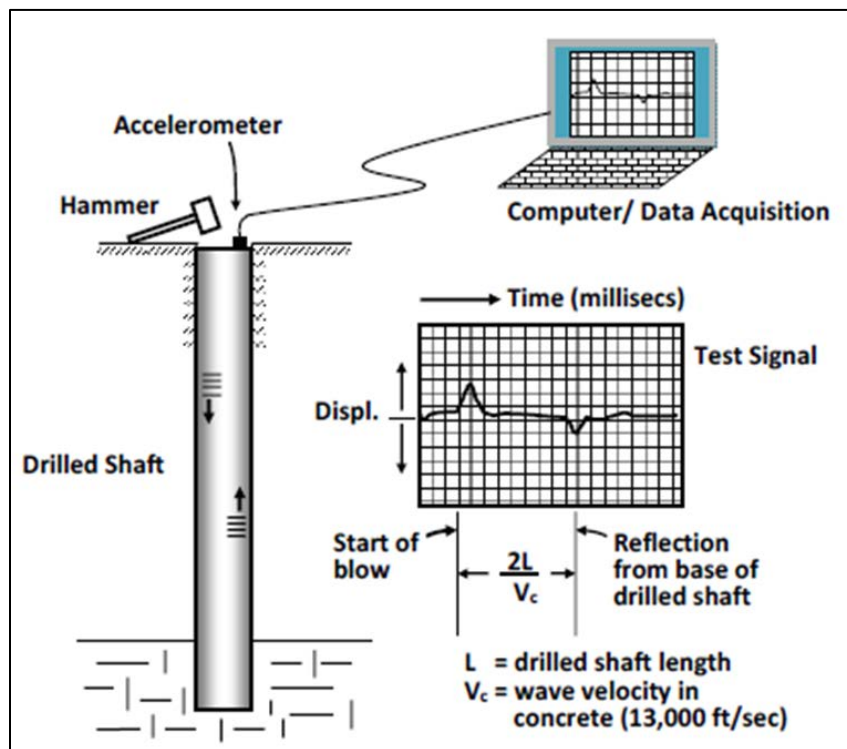


Figure 2.3. Sonic Echo Testing (Silwinski & Fleming, 1983)

More reliable forms of non-destructive testing for concrete deep foundations consist of down-hole methods. These methods typically require that access tubes be installed to accommodate sensor based probes. In drilled shaft construction, it is common practice (mandatory in many states) to install one access tube per foot of shaft diameter (e.g., six tubes in a 6ft diameter shaft), equally spaced around the rebar cage (with a minimum of three or four tubes). This practice is seldom used, however, in ACIP piles due to fact that rebar cages are smaller, often limited to only a single center bar, and must be pushed down into the fluid concrete. The additional time and effort associated with these methods over surface methods is often deemed uneconomical for ACIP piles on low capacity projects, but they are employed in some cases, and acceptance on larger structures and transportation projects certainly warrants their use.

Cross-hole Sonic Logging, CSL, is currently the most commonly used down-hole method (Figure 2.4). CSL utilizes a source probe and a receiver probe which are simultaneously lowered down two separate tubes. The source emits an acoustic wave which travels through the concrete and is detected by the receiver. The arrival time of the wave is used to assess the presence of sound concrete between the tubes. (Piscsalko, 2014)

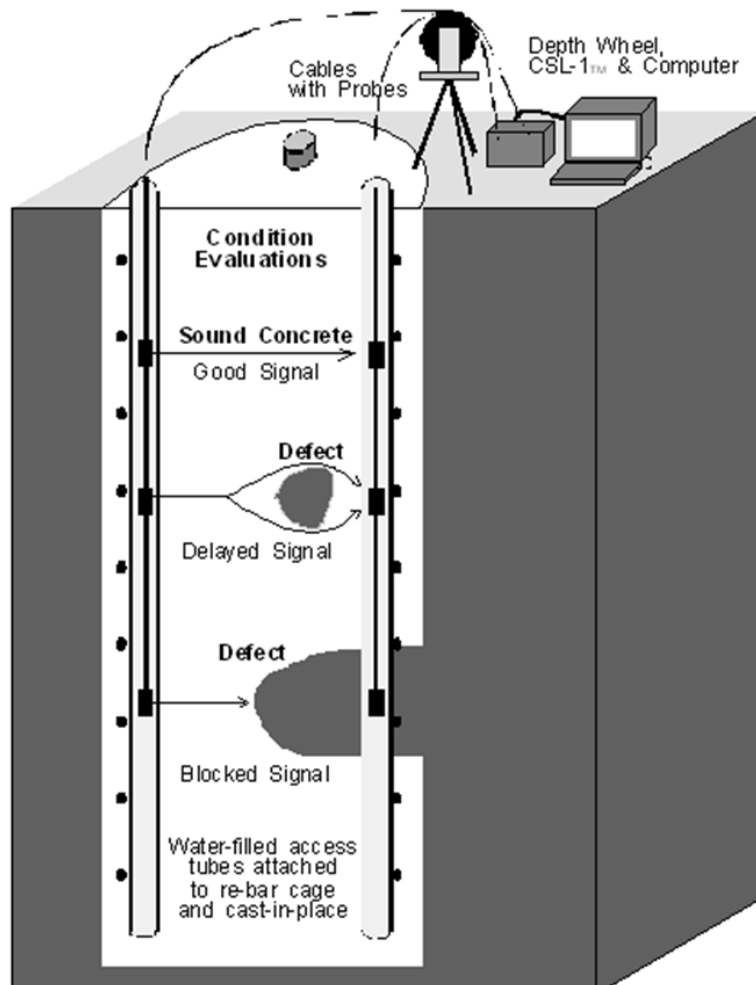


Figure 2.4. Crosshole Sonic Logging, CSL (Hollema and Olson, 2003)

A variation of CSL popular with auger-cast piles is SSL, or Single-hole Sonic Logging. Like CSL, this test was originally developed for boreholes in rock formations. The test is performed by lowering both the ultrasonic emitter and receiver down the access tube at a fixed spacing (Figure 2.5). Results are best if plastic access tubes are used to minimize energy/waves transmitted through steel tube walls. (USDOT, 2015)

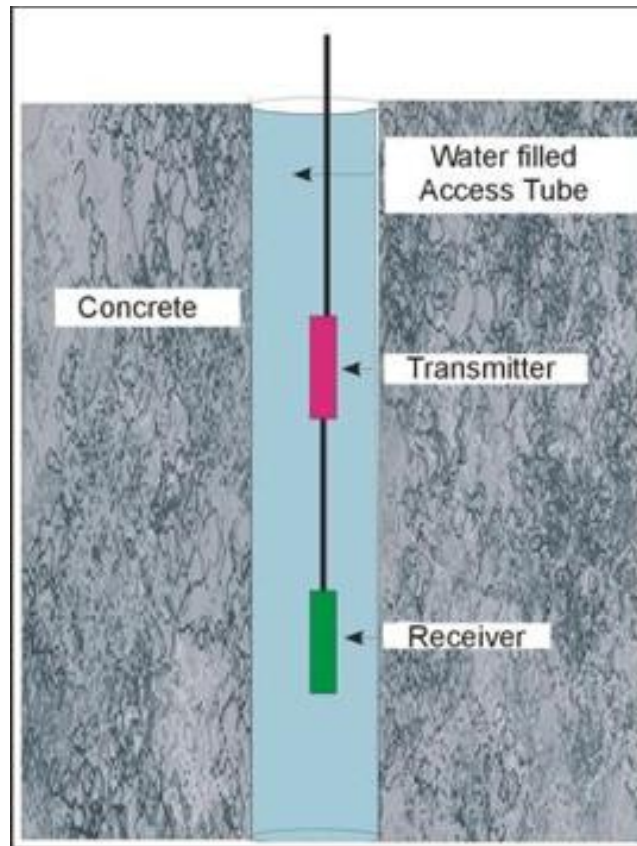


Figure 2.5. Single Hole Sonic Logging, SSL (USDOT, 2015)

Another, yet less common, down-hole method is Gamma-Gamma Density Logging, GGL, sometimes called Gamma Density Logging, GDL (Figure 2.6). In this test, a single probe with a cesium-137 radioactive source and detector is lowered down one access tube at a time. At the bottom of the probe, the source emits a constant plume of radioactive gamma particles which extends out into the concrete while, at the top of the probe, the receiver detects their arrival. The more radioactivity detected, the lower the density and vice versa (low counts = good concrete). The detection zone of the probe is dependent on the spacing between the emitter and detector. While the manufacturer data suggests the radius of detection is half the spacing (spherical plume), the true effective radius of detection is closer to 0.3 times the spacing (football shaped). The spacing is often set at 15 in making the centerline radius of detection around 4.5 in. Larger spacing can be used but the true effectiveness of measuring the entire plume is not equal; more distant regions have less effect. A more severe consequence of a wider spacing is the plume may reach into the surrounding soil and falsely register the concrete as bad where it actually is

measuring a lower cover thickness; there is no directionality detection of the gamma radiation pathways.

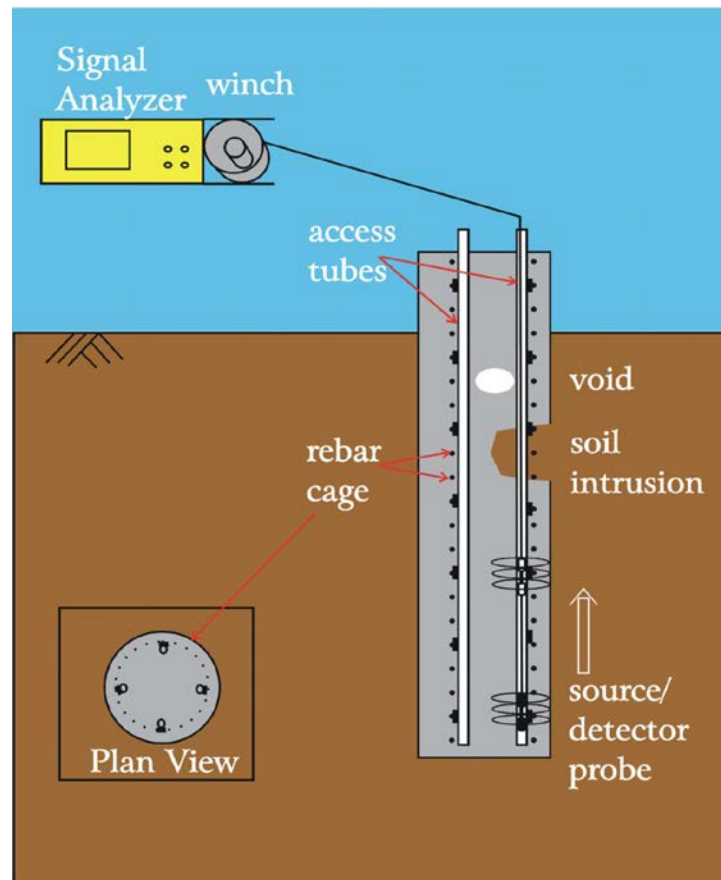


Figure 2.6. Gamma-Gamma Logging, GGL (COLOG, 2010)

Another limitation to GGL testing is in the data analysis. Unless radiation counts are correlated to actual density for similar concrete the data is almost meaningless. Most often, the quality of concrete surrounding the tube is assessed solely on the statistical percentage of gamma radiation counts detected by the receiver in that tube. If any portion of the tube profile registers above three standard deviations (higher counts), that portion is considered bad. This can lead to misleading results in several ways: (1) the average should be based on the entire shaft and not just one tube at a time, (2) if the entire tube is resting against the soil side walls, the average of the entire tube will be high, and the entire portion should be considered bad, but statistically, it would mostly fall within the normal two standard deviations which is “good,” and (3) if the entire profile is within sound concrete then the standard deviation will be small, so some of the profile will statistically fall outside two or three standard deviations and be falsely considered poor or bad, respectively. Caltrans has the only comprehensive protocol for GGL testing that incorporates calibration cells and plume radius verification (Caltrans, 2005). Finally, the radioactive nature of the device makes it subject to health, transportation and maintenance restrictions/complications.

While the depth limitations associated with surface testing are alleviated by the use of down-hole methods, limitations may still exist in the cross-sectional ranges of detection. With CSL, only the concrete between access tubes is tested, accounting for the majority of area within the rebar cage, but leaving the cover region completely untested. Assessment of the cover region is often desired however, because it is a key contributor to durability and flexural strength of a shaft as well as the bond to the surrounding soil. GGL detection extends to a radius of about 3 inches around each tube, which allows portions of concrete both inside and outside the cage to be tested, but equates to a relatively small percentage of the entire cross section. Figure 2.7 shows the testing coverage provided by CSL and GGL as a function of shaft size, assuming one tube per foot of diameter is provided. Research suggests that SSL has a maximum zone of detection similar that of GGL (Palm, 2012).

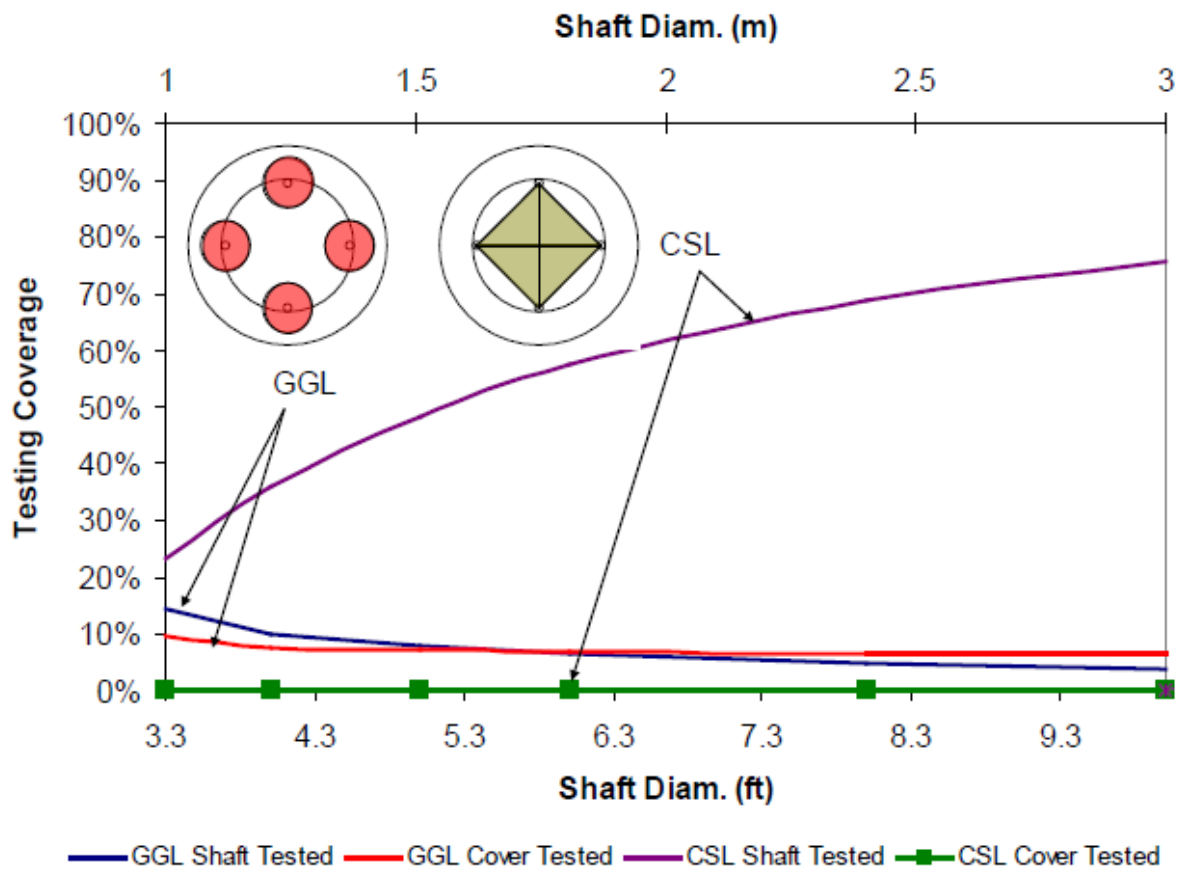


Figure 2.7. Testing coverage provided by CSL and GGL for varying shaft sizes (Mullins, 2010)

Based on the limitations of previous integrity methods to verify the as-built quality of ACIP elements, this study focused on thermal methods now applied to drilled shafts.

## 2.2 Thermal Integrity Profiling

Thermal Integrity Profiling (TIP) is a down-hole method for evaluating the post-construction quality of cast-in-place deep foundations. Developed in the late 1990's, it is the most recent of

non-destructive test methods to gain widespread popularity in drilled shaft evaluation. What distinguishes TIP from other methods, like CSL and GGL, lies in its ability to detect anomalies across 100% of the cross-section of a shaft. With the advent of thermal methods, contractors are able to assess the presence of quality concrete both inside and outside the reinforcement cage as well as the vertical alignment of the cage itself.

Concrete hydration is a highly exothermic process, and in mass concrete elements, such as drilled shafts, a significant amount of energy is released, causing elevated temperatures in both the shaft and surrounding soil, typically for several days. The amount of temperature increase at any given point depends on the volume of hydrating concrete in proximity as well as the cementitious content of that concrete, both of which help to define shaft serviceability. TIP takes advantage of this and detects anomalies based on variations in the thermal profile during the curing stages (Anderson, 2011).

### **2.2.1 TIP Methods & Equipment**

Temperature measurements can be achieved in either of two ways: down hole via probe with infrared sensors which is lowered down access tubes; or by thermal wires which are attached to the reinforcement cage and cast into the shaft. Figure 2.8 shows the testing equipment and the access tubes where measurements are taken using the probe method. A thermal probe, equipped with four infrared sensors, is lowered down each access tube (dry) at a rate of about 3-5 inch/sec. While temperature is measured by the sensors, depth is recorded by the encoder assembly. The optimal time for testing is generally between 18 and 48 hours after concrete placement. Figure 2.9 shows use of the wire method, wherein several temperature sensors are strung together at one-foot intervals and fastened to the reinforcement cage prior to concreting. With this method, data may be continually recorded over several days, but the instrumentation is disposable as it is cast permanently in the concrete (Mullins & Winters 2012).

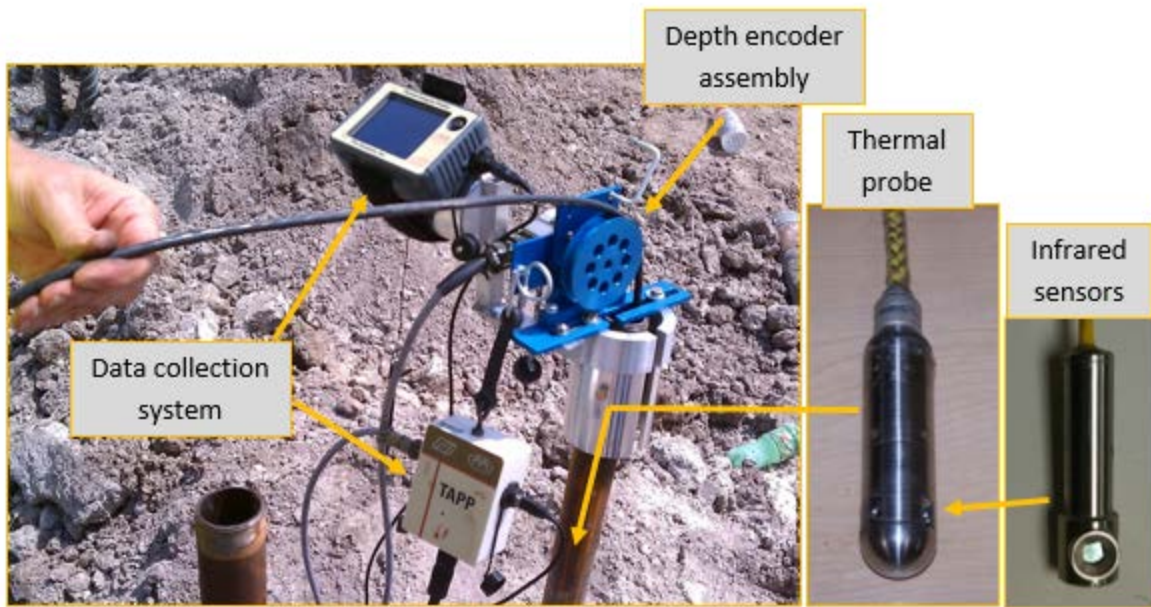


Figure 2.8. TIP setup – probe method

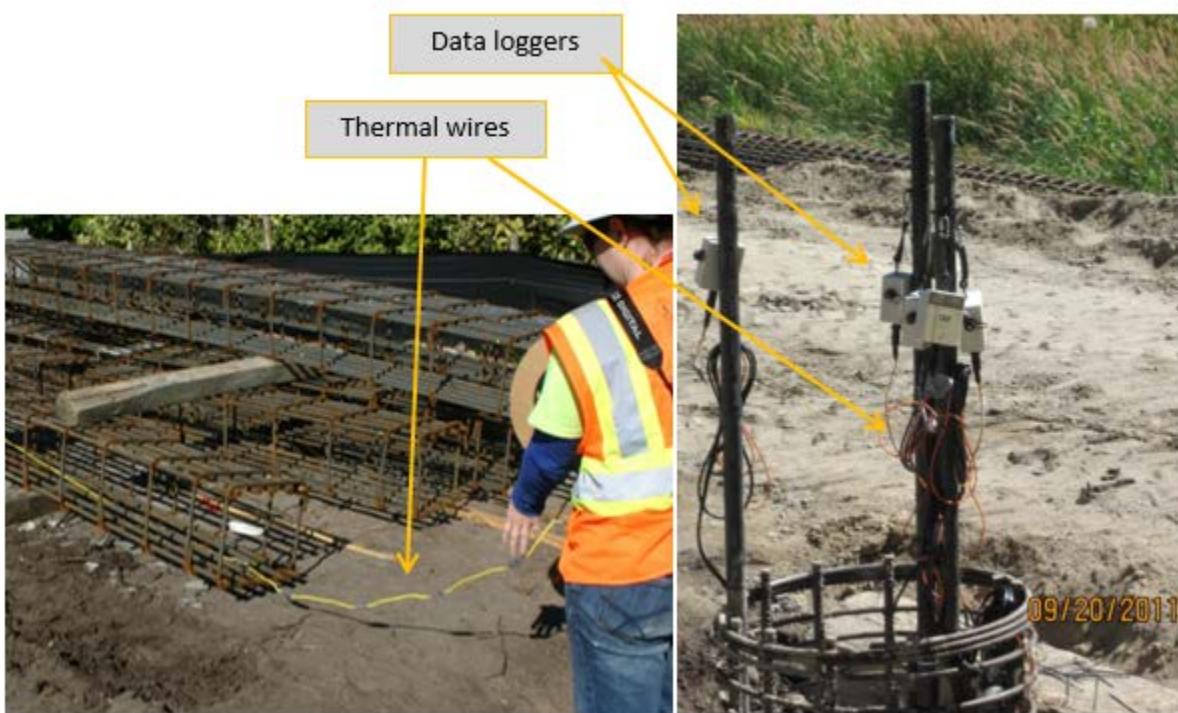


Figure 2.9. TIP setup – wire method

### 2.2.2 TIP Theory

Figure 10 illustrates the way in which heat is dissipated from a shaft to the surroundings, and the temperature distributions that result from it. For a perfectly cylindrical shaft, the vertical

distribution of temperature is nearly uniform throughout the majority of its length. The exception is near the ends where there is a distinct region of decreasing temperature. This temperature “roll-off” at the top and bottom is due to the added mode of heat loss in the longitudinal direction. The radial temperature distribution is bell-shaped, with peak temperatures occurring at the center of the shaft and decreasing radially towards the surrounding soil. With a typical configuration of access tubes, data collected from thermal integrity testing provides a continuous temperature profile vertically and discrete measurements laterally (indicated by red dots in Figure 2.10). The vertical profile reveals any bulges, necks, or inclusions that may be present, while comparison among tube temperatures indicates lateral cage alignment. (Mullins and Winters 2012)

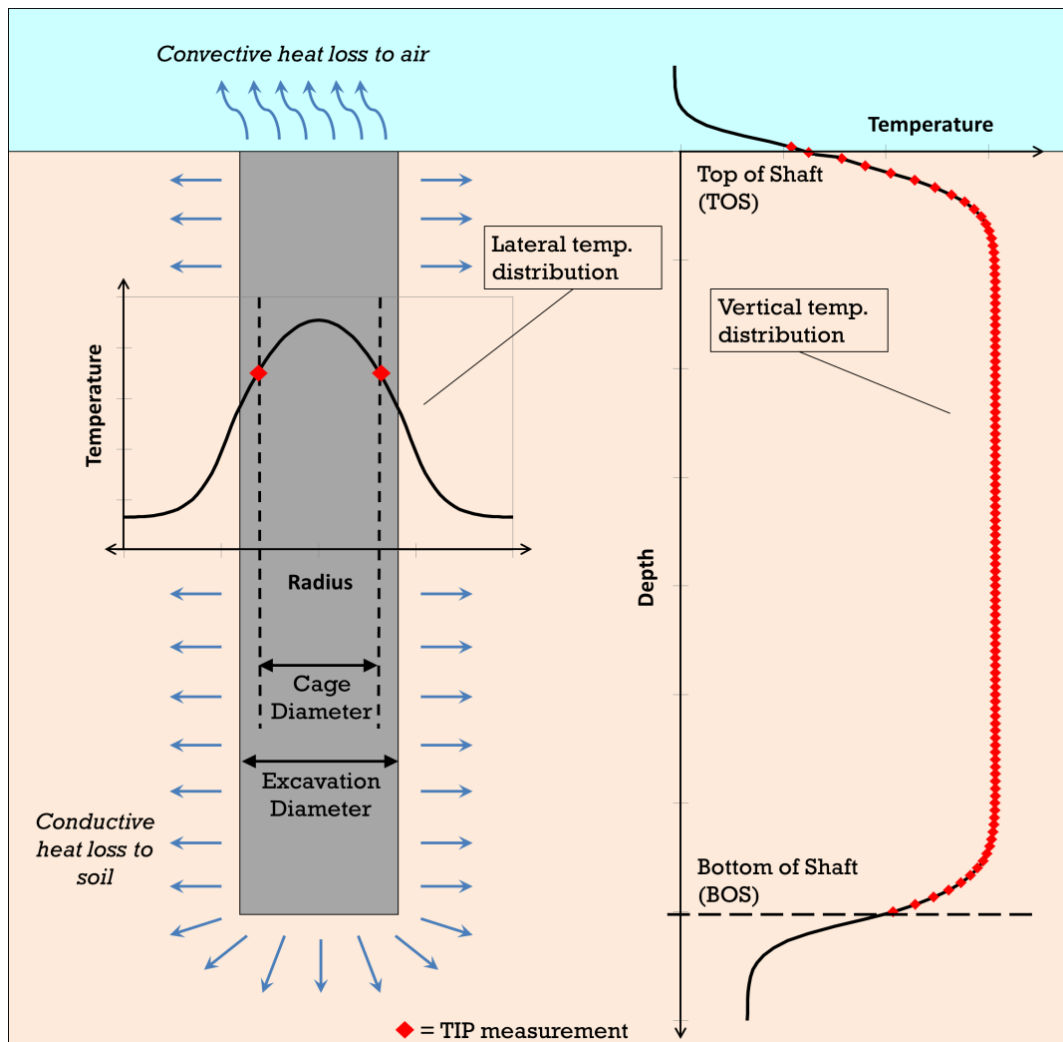


Figure 2.10. Temperature distributions in an idealized shaft

Figure 2.11 shows the effect of shaft size on radial temperature distribution. Note that the inflection point of each curve, where slope is the steepest and most linear, is at the edge of shaft, near the cage location. This makes temperature measurements at the cage highly sensitive to both shaft size and cage eccentricity. Distinction between the two can be made by comparison of cage

temperatures on opposing sides of the bell curve. Variations in temperature that are reflected by opposing sides indicate changes in overall shaft diameter, while equal but opposite variations in temperature from opposing sides indicates cage eccentricity. (Mullins, 2013)

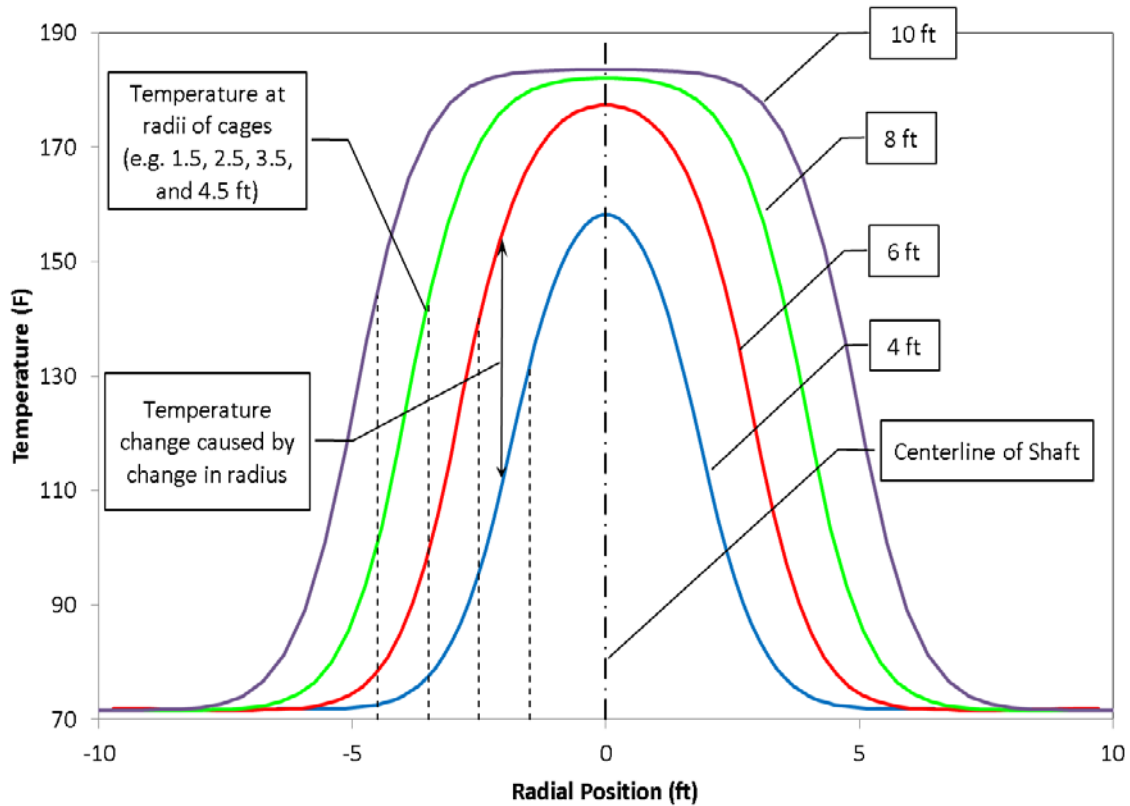


Figure 2.11. Radial temperature distribution for various shaft sizes (Mullins, 2012)

A 3-D extrusion of these curves, as illustrated in Figure 2.12, aids in visualizing the relationship between shaft radius, cage position, and measured temperatures. The dashed lines in Figure 2.12 represent cage position where measurements are taken, the bold lines represent the temperature distribution corresponding to the local shaft size, and the intersection of the lines reveals the temperature that would be measured. Note that for larger shaft sizes, temperatures near the core are not affected by size or position, but for smaller shafts, all locations are still highly sensitive to shaft radius. For a given radial position, the dashed lines in Figure 2.12 reveal the unique correlation that exists between shaft size and temperature (Figure 2.13). This relationship is asymptotic towards soil temperature and the concrete adiabatic temperature, and has an inflection point where shaft radius equals the given measurement position. Note that measurements taken at cage radius will fall near the inflection point, where the relationship between shaft size and temperature is strongly linear. (Mullins, 2013)

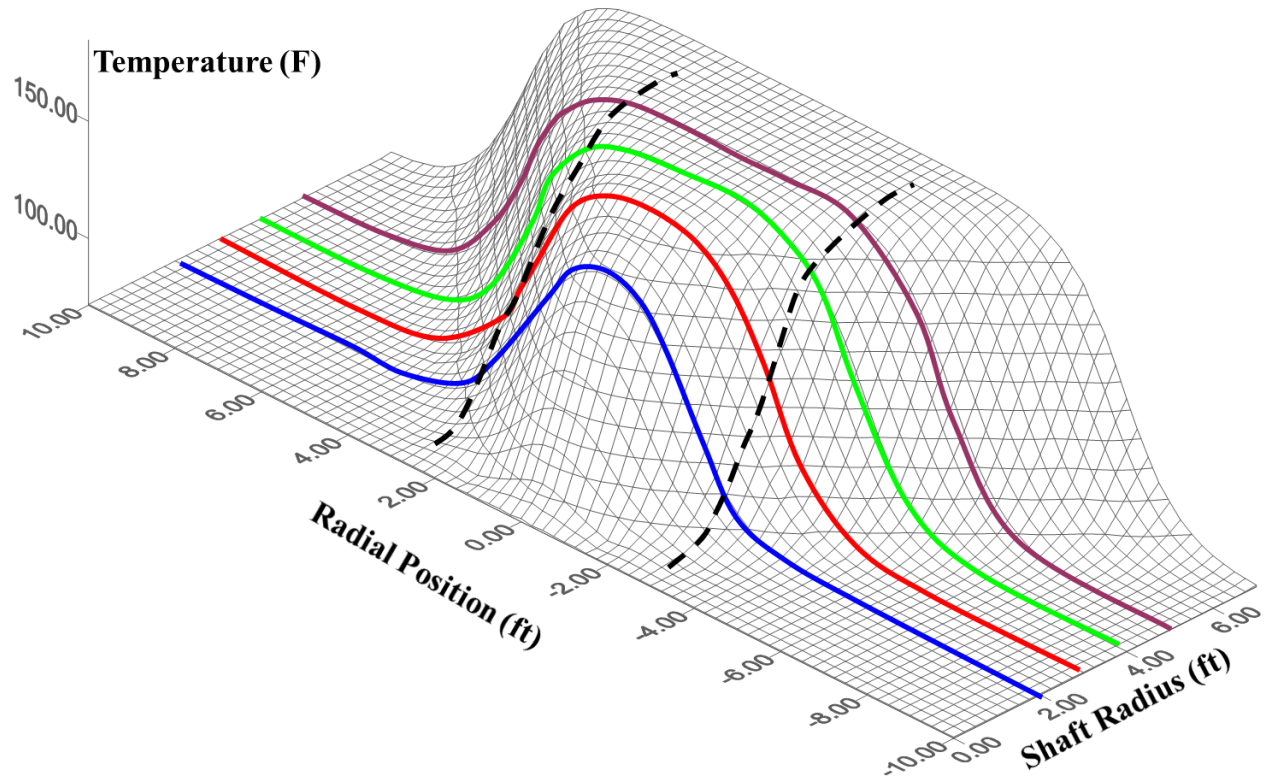


Figure 2.12. Relationship between cage position, shaft size, and temperature (Mullins, 2012)

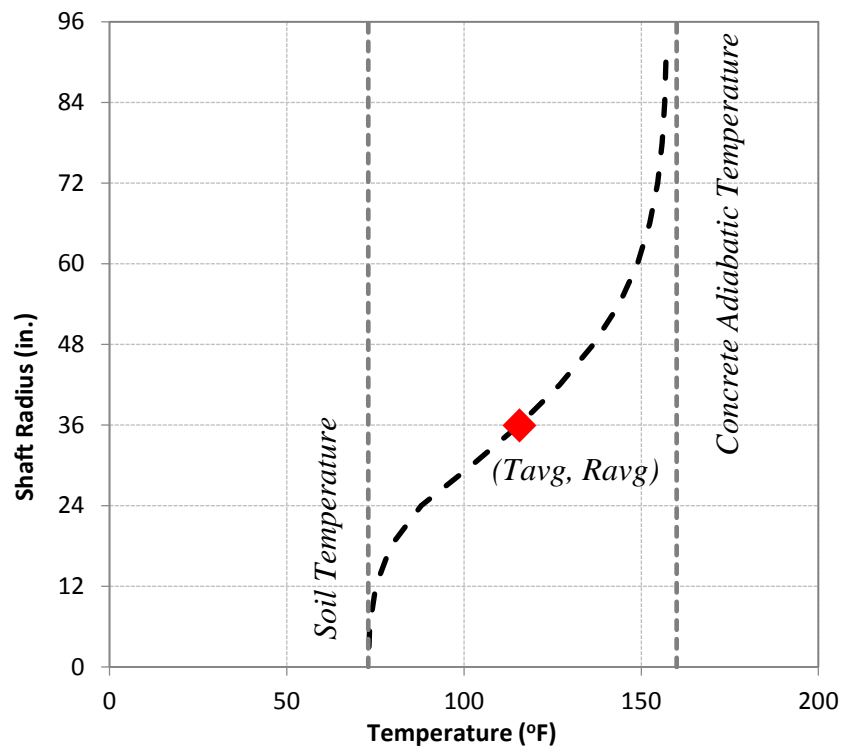


Figure 2.13. Relationship between shaft size and temperature for a given cage position (Johnson, 2014)

### 2.2.3 TIP Analysis

Direct observation of measured temperature profiles provides immediate qualitative information about a shaft, such as general shape, relative cage alignment, and the types of anomalies that may be present. As noted earlier, an increase or decrease in all tube temperatures indicates a bulge or neck in the shaft, respectively; whereas an equal but opposite variation of opposing tube temperatures indicates cage misalignment. A somewhat circular shaped temperature roll-off should extend up to about one diameter from the top and bottom of the shaft; this indicates normal end conditions. Figure 2.14 illustrates these types of observations.

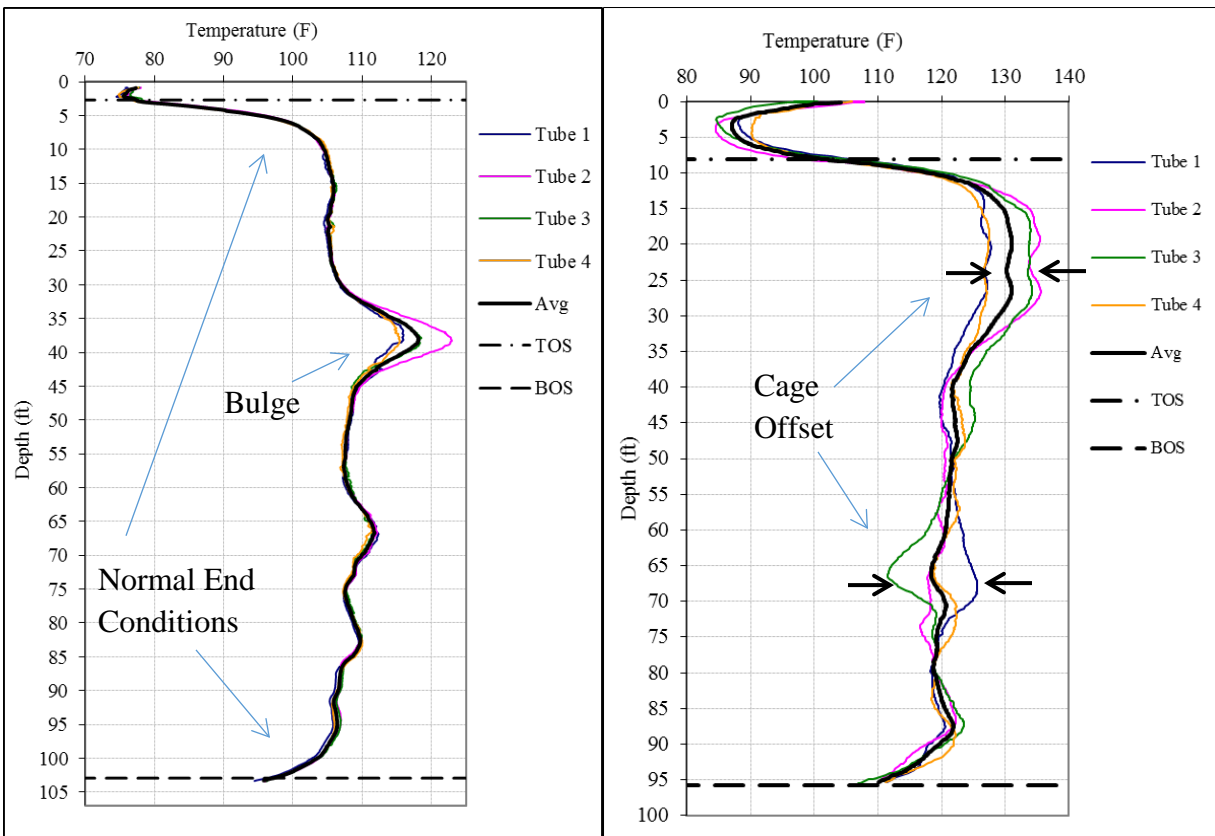


Figure 2.14. Example thermal profiles with anomalies (Johnson, 2014)

However, in order to quantify this information with actual dimensions, more rigorous methods of analysis are required. Mullins and Winters (2011) suggest the following breakdown of possible analysis techniques:

- Level 1: Direct observation of the temperature profiles
- Level 2: Superimposed construction logs and concrete yield data
- Level 3: Three dimensional thermal modeling
- Level 4: Signal matching numerical models to field data

In drilled shaft construction, it is customary to record and plot the volume of concrete placed with each truck along with the change in height to top of concrete resulting from each placement. These logs, known as yield plots, can be compared with theoretical yield calculations based on the design diameter of the shaft, and any variation therein can be used to deduce the actual effective average diameter (or radius) of the shaft over the measured height change. This information can be used to provide a series of calibration points for measured thermal data, and is the basis for the Level 2 type of analysis described above (Mullins and Winters, 2011). Figure 2.15 shows a case study from Lake Worth, Florida where both the concrete yield plot data and thermal profile are plotted together.

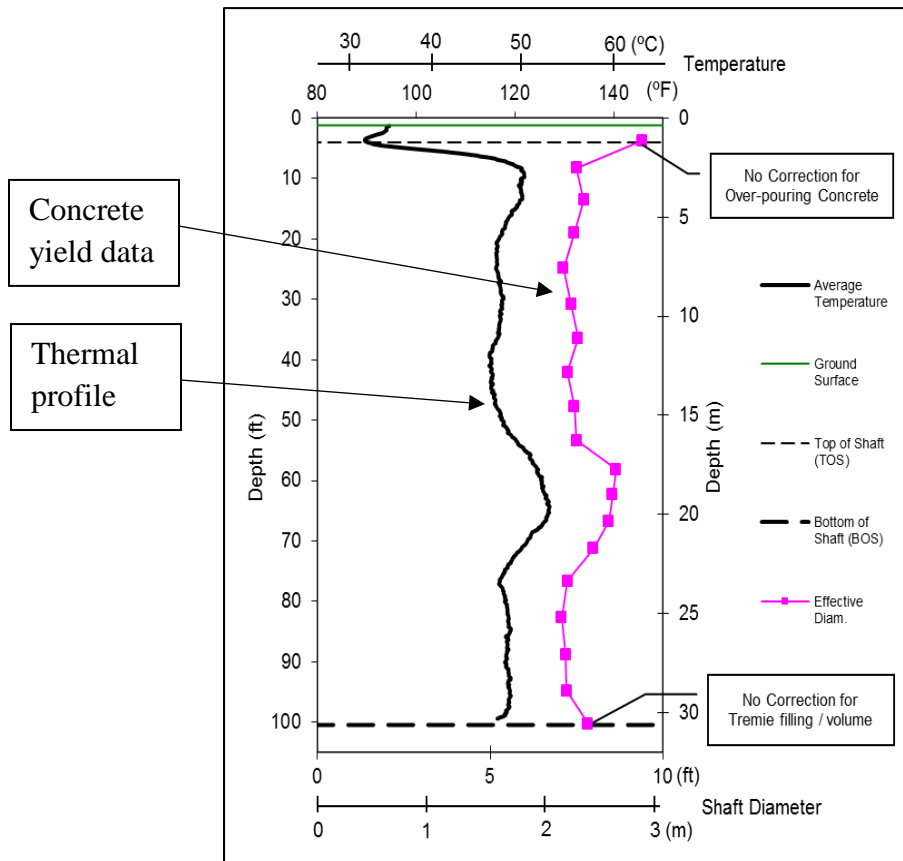


Figure 2.15. Yield plot data converted to effective diameter compared with thermal data (Mullins, 2010)

This type of calibration essentially eliminates the need to make the assumptions about thermal properties that are required for modeling analysis. By plotting the radius against measured temperature, a best-fit linear regression can be used to form a temperature-radius relationship, as shown in Figure 2.16. The assumption of linearity is valid for temperatures measurements taken in the regions near the outer radius of the shaft, as the temperature distribution is strongly linear. In either direction away from this region however, a linear relationship will tend to under-predict changes in radius greater than approximately 4 to 6 inches. (Mullins and Winters, 2011).

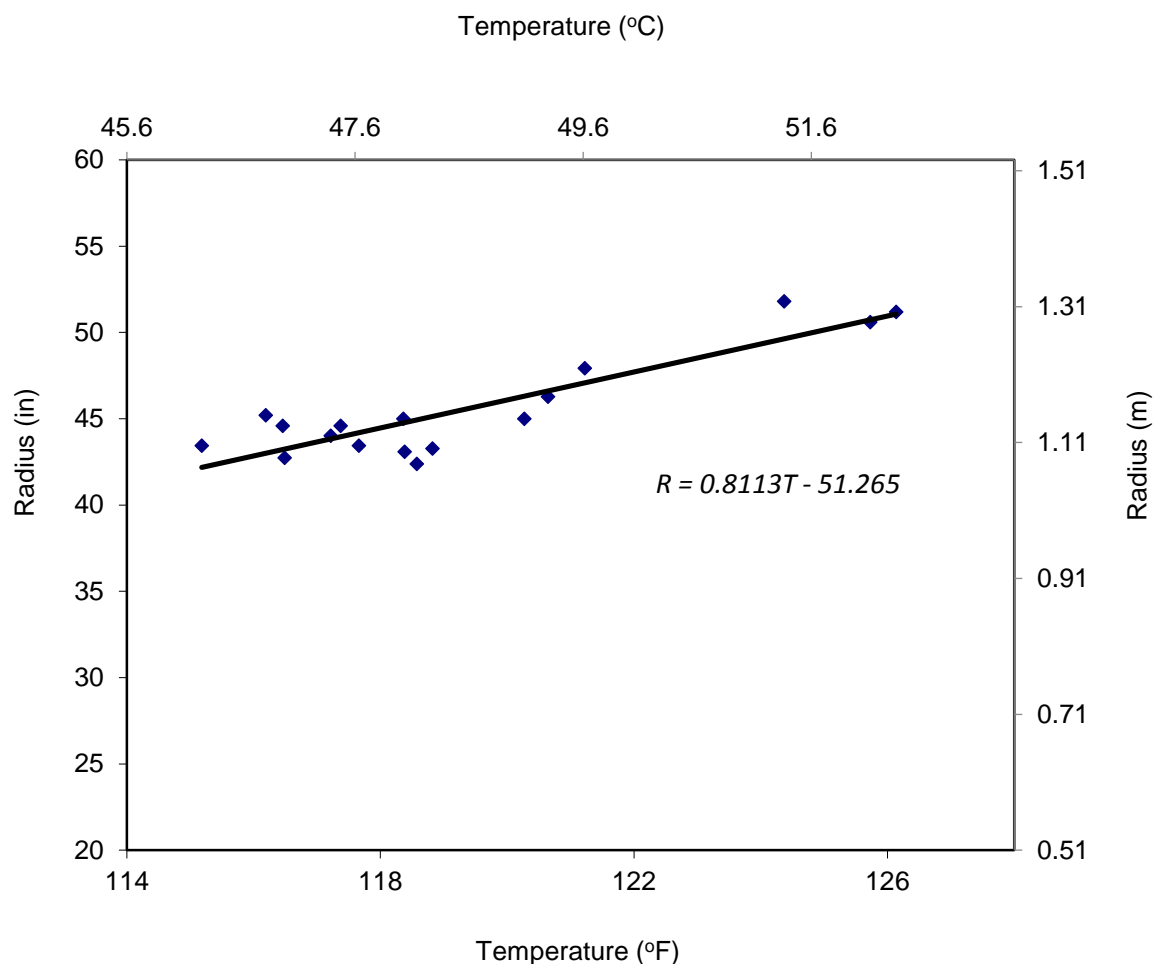


Figure 2.16. Temperature-radius relationship deduced from yield plot data (Mullins and Winters, 2012)

This temperature-radius (T-R) relationship can then be applied to the measured temperature profiles from each tube to produce a profile that reflects the effective radius of the shaft as well as the alignment of the cage. Figure 2.17 shows the effective radius profile produced from the above T-R relationship. In this case, the average temperature profile indicates that the size of the shaft meets or exceeds the design criteria in all locations, but individual tube profiles reveal areas of reduced concrete cover between 15 and 75 feet. The most severe cover defects occur at about 20ft and 48ft, where the radius of the shaft at tubes 2, 3, and 4 is equal to or less than the radius of the cage, which essentially equates to zero concrete cover and possibly exposed rebar. Note that the radius at the top of the shaft is shown to be smaller, which is actually a by-product of the temperature roll-off due to longitudinal heat loss. A method for correcting this effect is discussed later.

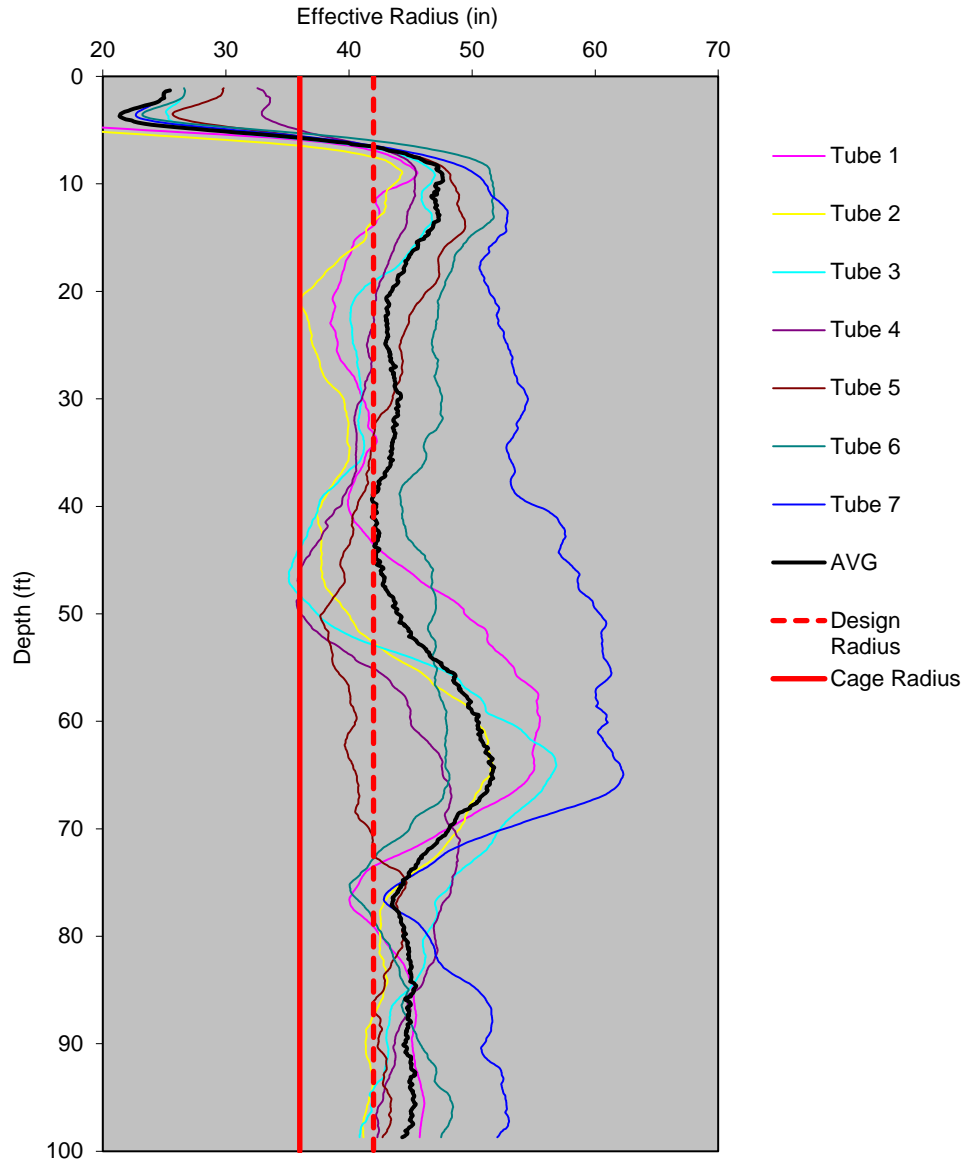


Figure 2.17. Effective radius of shaft as interpreted from TIP analysis (Mullins and Winters, 2012)

In many cases, particularly with shafts that are relatively uniform or require few trucks for concreting, yield data will not be sufficient to produce a T-R relationship by multiple data point linear regression. Alternatively, the average temperature and average radius of the entire shaft can provide a calibration point / boundary condition, and a single-point solution can be used to generate the T-R relationship. Figure 2.18 shows data from a shaft in which a single-point solution can be used. Research suggests that this type of solution yields a close approximation to true T-R relationships and is conservative against over-prediction of anomaly severity (Johnson, 2014).

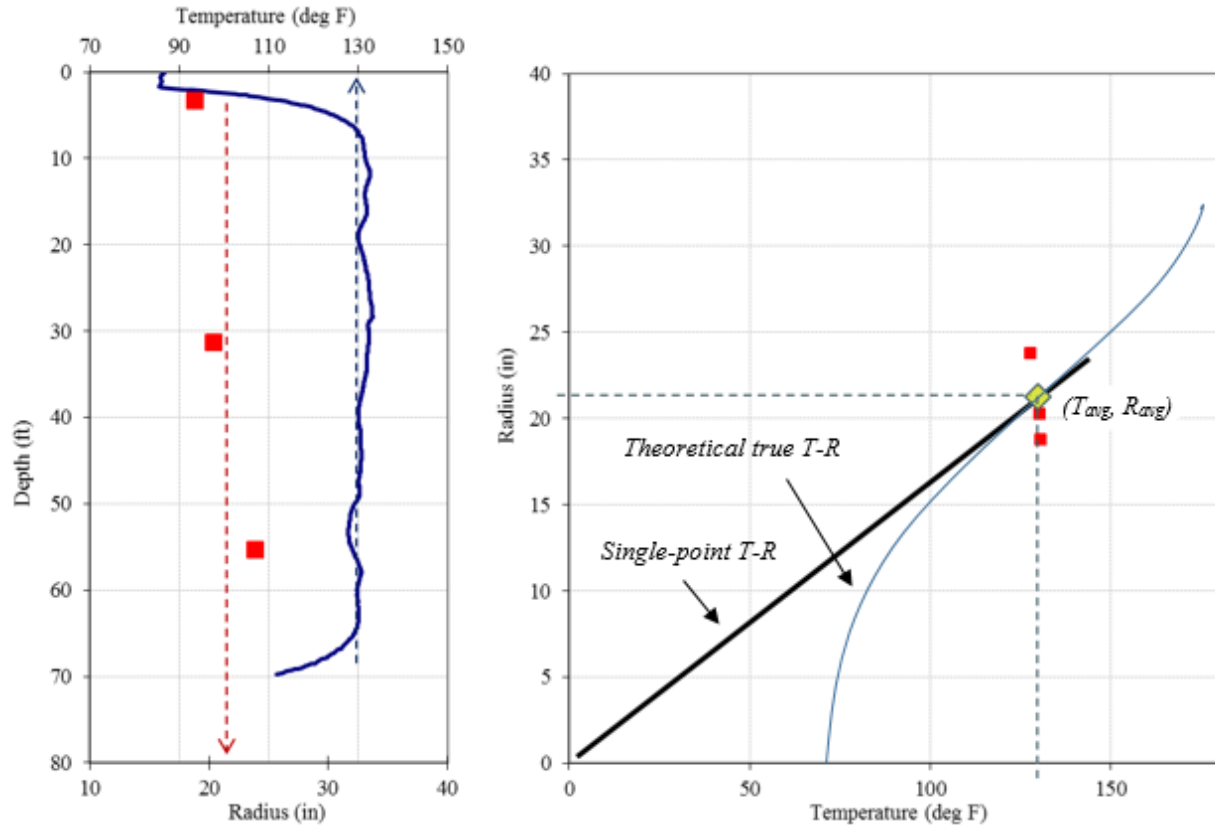


Figure 2.18. Single-point solution for determining T-R relationship based on average temperature and average radius of entire shaft, compared with theoretical true T-R relationship

It can be conceived that a given temperature measurement resulting from the anticipated shaft radius consisting of intact, good quality concrete could also be obtained with a larger radius shaft consisting of somewhat compromised or lesser quality concrete. In this regard, the term *effective radius* is defined as *the radius of intact concrete that would produce the measured temperature*. “Intact” actually refers to average quality for the given shaft as all temperature measurements are compared relative to the average temperature of the entire shaft. This also applies to average boundary conditions for the entire shaft. Corrections for changes in external boundary conditions (e.g., soil type, air, water, shaft ends) are also concerns that must be addressed.

Ideally, correlations from temperature to radius can be identified from field collection information without reliance on modeling or signal matching which have been shown to have limitations (discussed later). However, a single expression whether it is linear or hyperbolic as shown in Figure 2.18, will be limited to constant boundary conditions (e.g. no changes in environment occur, all soil, etc.). Immediately, it is apparent that the ends of the shaft do not conform to these limitations where the ends dissipate heat both radially and longitudinally (Figure 2.10). As a result, algorithms have been developed to correct end conditions (top or bottom) to account for reductions in near end temperatures that are not caused by reductions in cross-section.

Modeling reveals that the theoretical heat dissipation at the ends of a perfectly cylindrical shaft closely mimics a hyperbolic tangent curve. This was first explained by Johnson (2014) where the normal temperature of the shaft close to, but not affected by, end conditions was used to define one asymptote of the hyperbolic fit. The other asymptote was then defined by the soil below the shaft or the air above. This curve-fitting algorithm is presented in Equation 2.1. The temperature of the shaft in the “roll-off” zone near the ends can then be adjusted / corrected to remove the end effects using Equation 2.2. The radius predicted from the T-R relationship would then show the correct shape (unlike the top of Figure 17).

$$T_{fit} = -\left(\frac{T_{max}-T_{min}}{2}\right) \tanh\left(\frac{z-z_0}{\alpha}\right) + \left(\frac{T_{max}+T_{min}}{2}\right) \quad \text{Equation 2.1}$$

where for the top,

- $T_{max}$  = Nominal shaft temperature below roll-off
- $T_{min}$  = Equivalent air temperature
- $z_0$  = Top of shaft (TOS) depth
- $\alpha$  = Time factor

and for the bottom,

- $T_{max}$  = Nominal shaft temperature above roll-off
- $T_{min}$  = Soil temperature
- $z_0$  = Bottom of shaft (BOS) depth
- $\alpha$  = Time factor

$$T_{cor} = \frac{T_{measured}-T_{min}}{T_{fit}-T_{min}} (T_{max} - T_{min}) + T_{min} \quad \text{Equation 2.2}$$

The nominal shaft temperature for each end is obtained from the nearest region of relatively uniform temperature measurements within the shaft. This can usually be found at a distance into the shaft that is roughly equal to the shaft diameter. Soil temperature can be obtained by using the annual average temperature of the geographical location. As most shafts extend deeper than 10 feet, soil temperature at the toe is unaffected by seasonal temperature changes and can mostly be considered constant for a given city or location (Figure 2.20). Equivalent air temperature is a pseudo-temperature that accounts for the drastic change in diffusivity between concrete and air and is therefore usually significantly lower than actual air temperature (soil and concrete have similar diffusivity values and therefore the BOS is less affected). Its value should be set such that the inflection point of the curve is in the range of actual air temperature. TOS and BOS depths should be near reported values, but should be adjusted as needed to fit the curve (e.g. up to a foot outside the shaft). Finally, time factors should be adjusted until the best fit is achieved. These values generally range between 0.5-5ft and increase with time. Proper selection of these values is discussed at length in ensuing chapters. Once the best fit curves are determined, corrected temperatures can be found according to Equation 2.2. An example of top and bottom temperature corrections is shown in Figure 2.19 (Johnson, 2014).

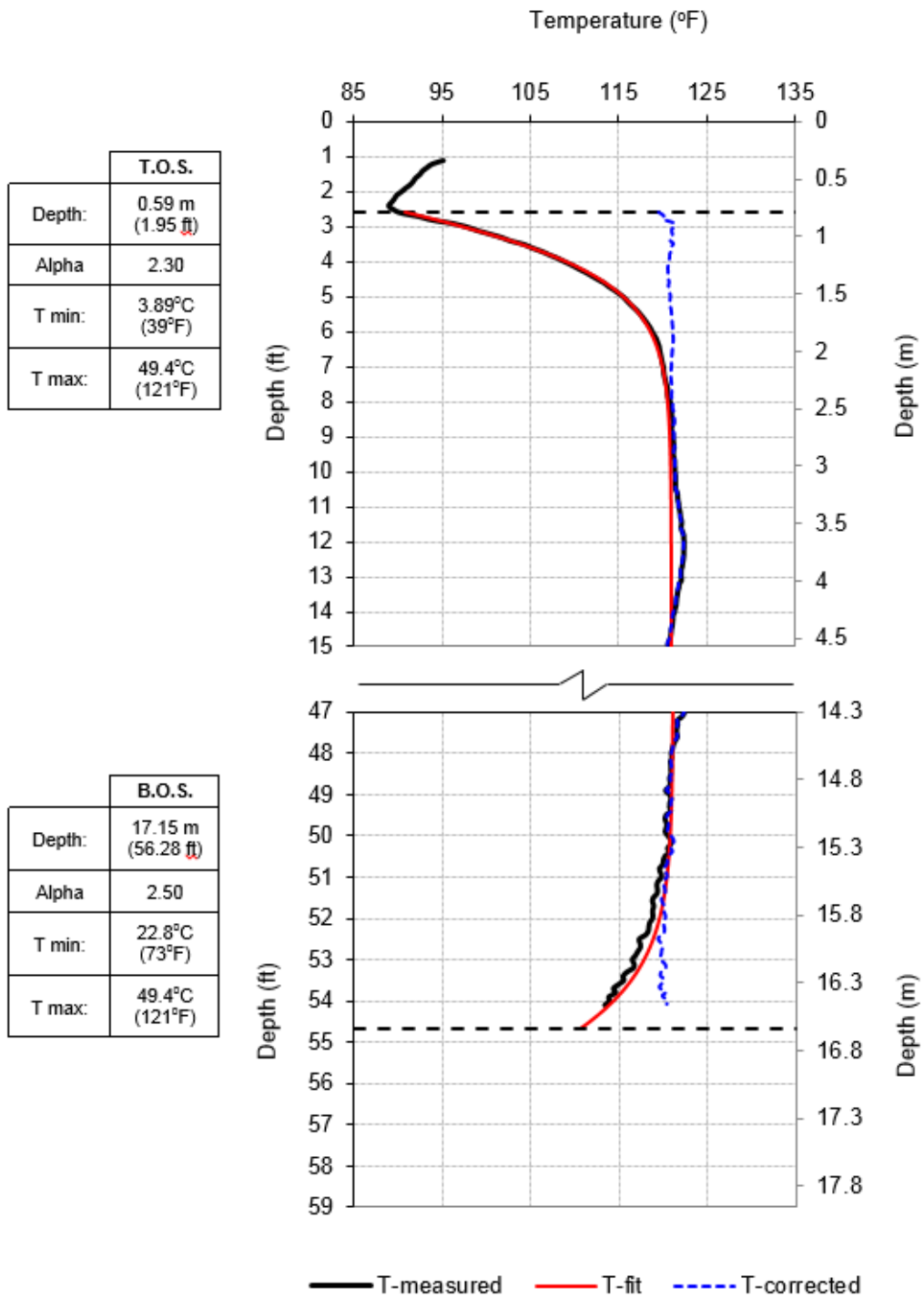


Figure 2.19. Measured, theoretical, and corrected temperatures for top and bottom of a shaft (Johnson, 2014)

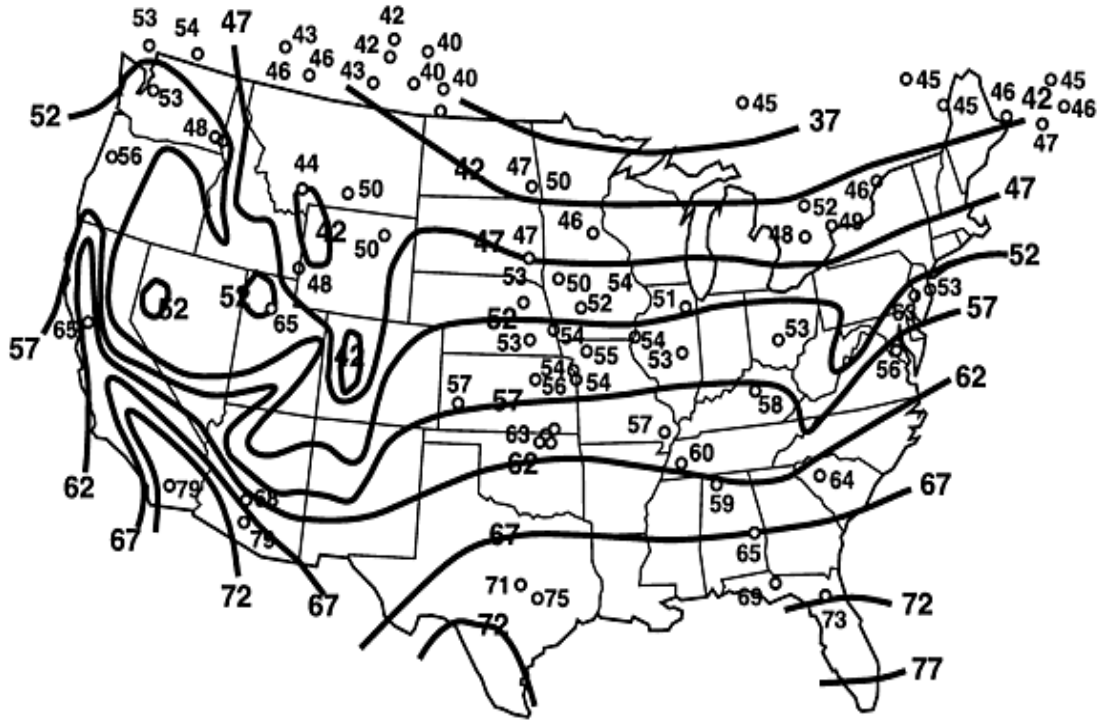


Figure 2.20. Ground temperatures in the United States (Pauly, 2010)

#### 2.2.4 TIP Modeling

For analysis of TIP data using computer models, temperature prediction software is used to solve the finite-difference form of the general heat equation (Eq. 2.3) based on input shaft dimensions, thermal properties, and boundary conditions.

$$\frac{\partial}{\partial x} \left( k \frac{\partial T}{\partial x} \right) + \frac{\partial}{\partial y} \left( k \frac{\partial T}{\partial y} \right) + \frac{\partial}{\partial z} \left( k \frac{\partial T}{\partial z} \right) + q = \rho C_p \frac{\partial T}{\partial t} \quad \text{Equation 2.3}$$

where,

- $T$  = Temperature
- $k$  = Thermal conductivity
- $\rho$  = Density
- $C_p$  = Specific heat
- $q$  = Rate of heat generation

The thermal properties of concrete vary through the curing stages and are typically expressed as a function of the degree of hydration. The hydration of Portland cement is the result of many different chemical reactions that take place, all of which release heat in the process (i.e., exothermic), though be it at separate times and magnitudes. Since the evolution of heat is a direct indication of completed reactions, it serves as a defining measure for the progression of hydration. Therein, at any given time, the rate of hydration is defined by the instantaneous rate of heat generation,  $q$  (Eq. 2.4), and the degree of hydration,  $\alpha$ , is defined as the fraction of

cumulative heat evolved,  $H(t)$ , to the ultimate amount of heat available,  $H_u$  (Eq. 2.5) (Schindler & Folliard, 2002). The variation in time and rate of the multiple types of reactions results in a hydration process that is not constant, but rather occurs in phases. In general, there are five distinguishable stages of hydration: (1) *initial hydration*, (2) *dormant period*, (3) *acceleration*, (4) *deceleration*, and (5) *steady state* (Mindess et. al., 2003). This behavior results in rate of heat generation and degree of hydration curves that follow the general pattern of those shown in Figure 2.21.

$$q = \text{Rate of heat generation} = \frac{d}{dt} H(t) \quad \text{Equation 2.4}$$

$$\alpha = \text{Degree of hydration} = \frac{H(t)}{H_u} \quad \text{Equation 2.5}$$

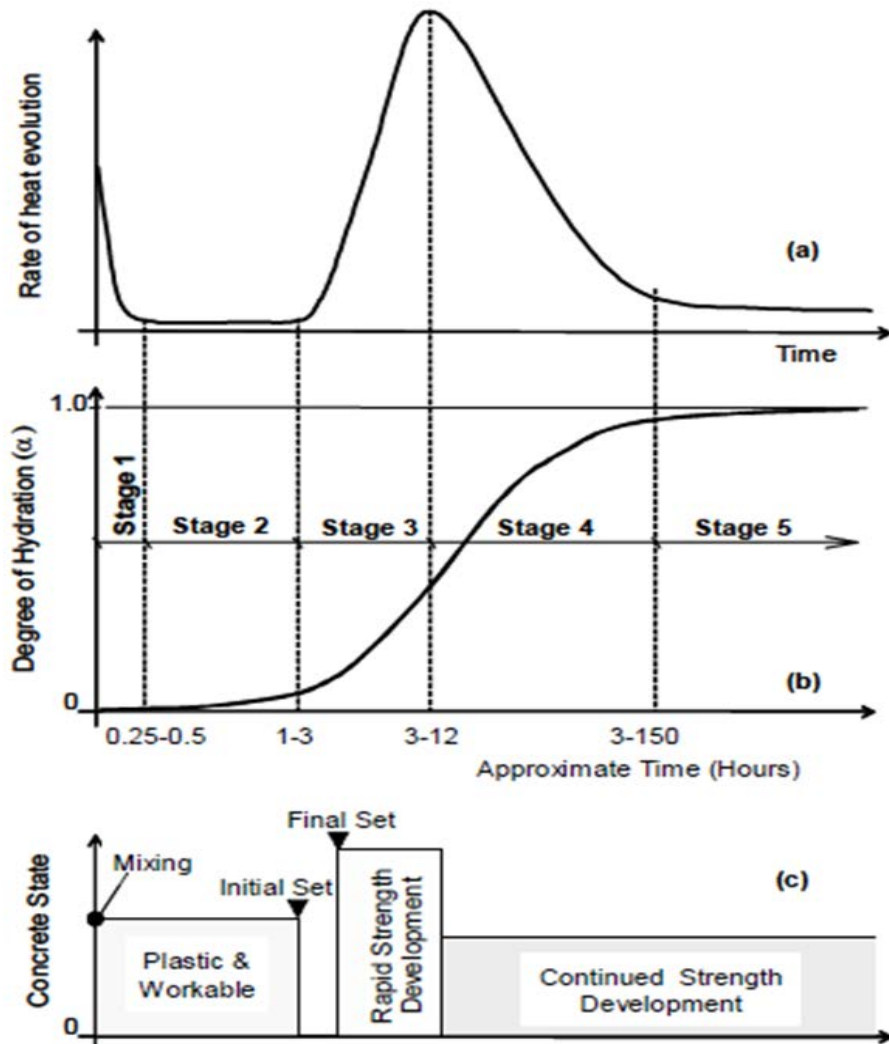


Figure 2.21. Hydration behavior of concrete (Schindler & Folliard, 2002)

The most widely accepted method for modeling this hydration behavior involves the concept of equivalent age,  $t_e$ , which invokes the Arrhenius theory for rate processes to account for the

temperature dependency of reactions (Eq. 2.6), combined with an exponential formulation and approximates the S-shaped degree of hydration curve (Eq. 2.7). (Schindler & Folliard, 2002)

$$t_e = \text{Equivalent age} = \sum_0^t e^{-\frac{E_a}{R} \left( \frac{1}{T} - \frac{1}{T_r} \right)} \cdot \Delta t \quad \text{Equation 2.6}$$

$$\alpha = \alpha_u \cdot \exp \left[ - \left( \frac{\tau}{t_e} \right)^\beta \right] \quad \text{Equation 2.7}$$

In Equation 2.6,  $R$  is the natural gas constant ( $8.314 \text{ J/mol/K}$ ) and  $E_a$  is the activation energy, a property which represents the temperature sensitivity of the hydration process.  $T_c$  is the temperature ( $^{\circ}\text{K}$ ) of concrete at time  $t$ . In Equation 2.7,  $\alpha_u$ ,  $\beta$ , and  $\tau$  are parameters that describe the shape of the hydration curve, corresponding to the ultimate degree of hydration, the rate of the acceleration phase, and the start of the acceleration phase, respectively, as shown in Figures 2.22-2.24 (Folliard et. al., 2008). These shape parameters, as well as properties  $E_a$  and  $H_u$ , are unique to every concrete batch and are best determined experimentally on an individual basis. The values can be found through a combination of isothermal and adiabatic or semi-adiabatic calorimetry testing, wherein  $T_r$  is the reference temperature ( $\text{K}$ ) at which testing is conducted.

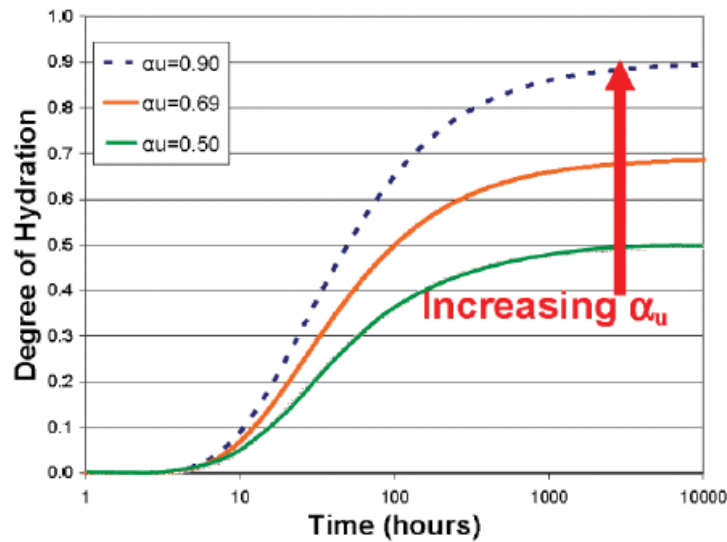


Figure 2.22. Effect of shape parameters  $\alpha_u$  on hydration curve (Folliard et. al., 2008)

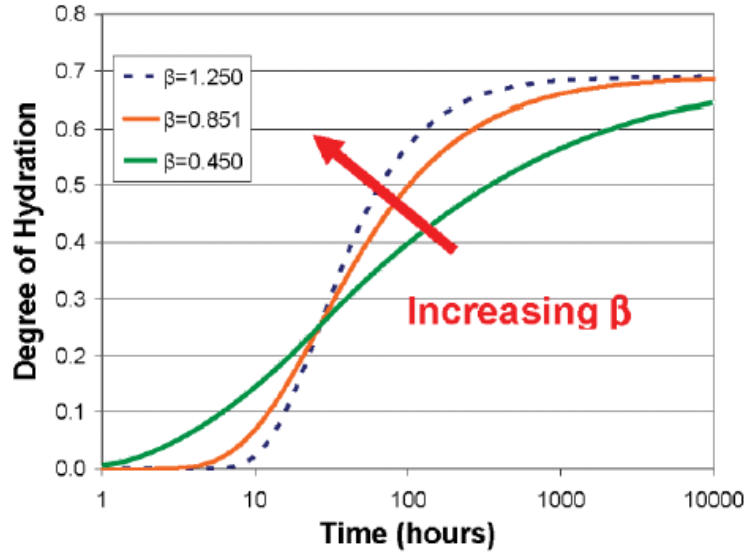


Figure 2.23. Effect of shape parameter  $\beta$  on hydration curve (Folliard et. al., 2008)

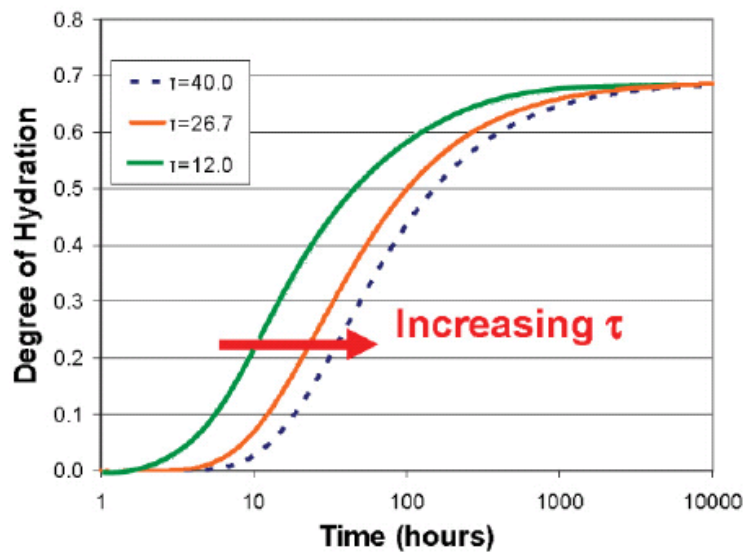


Figure 2.24. Effect of shape parameter  $\tau$  on hydration curve (Folliard et. al., 2008)

Although exact determination of a concrete hydration behavior requires laboratory testing, empirical correlations developed through past research can be used to estimate hydration parameters based on cement and concrete compositions. Bogue (1947) first correlated the total heat of hydration of Portland cement to its major compounds, producing the relationship shown in Equation 2.8.

$$\begin{aligned}
 H_{cem} = & 500 \cdot p_{C_3S} + 260 \cdot p_{C_2S} + 866 \cdot p_{C_3A} + 420 \cdot p_{C_4AF} \\
 & + 624 \cdot p_{SO_3} + 1186 \cdot p_{FreeCaO} + 850 \cdot p_{MgO}
 \end{aligned}
 \tag{Equation 2.8}$$

Several studies since then have extended this concept to correlate the additional hydration parameters used in the exponential  $\alpha$  model and to include a broader range of variables such as

supplementary cementitious materials, chemical admixtures, and cement fineness. Some of the most notable and recent work to examine such relationships includes studies from Schindler & Folliard (2005), Ge (2005), and Poole (2007), the latter of which is the most comprehensive and is presented in Equations 2.9 - 2.13. This set of equations is specific to cement compositions as determined by Bogue calculations, which are commonly found on cement manufacturer mill certificates.

$$H_u = H_{cem} \cdot p_{cem} + 461 \cdot p_{GGBFS-100} + 550 \cdot p_{GGBFS-120} + 1800 \cdot p_{FA-CaO} \cdot p_{FA} + 330 \cdot p_{SF} \quad \text{Equation 2.9}$$

$$E_a = 41,230 + 1,416,000 \cdot [(p_{C_3A} + p_{C_4AF}) \cdot p_{cem} \cdot p_{SO_3} \cdot p_{cem}] - 347,000 \cdot p_{Na_2O_{eq}} - 19.8 \cdot Blaine + 29,600 \cdot p_{FA} \cdot p_{FA-CaO} + 16,200 \cdot p_{GGBFS} - 51,600 \cdot p_{SF} - 3,090,000 \cdot WRRET - 345,000 \cdot ACCL \quad \text{Equation 2.10}$$

$$\alpha_u = \frac{1.031 \cdot w/cm}{0.194 + w/cm} + \exp \left( \begin{array}{l} -0.0885 - 13.7 \cdot p_{C_4AF} \cdot p_{cem} \\ -283 \cdot p_{Na_2O_{eq}} \cdot p_{cem} \\ -9.90 \cdot p_{FA} \cdot p_{FA-CaO} \\ -339 \cdot WRRET - 95.4 \cdot PCHRWR \end{array} \right) \quad \text{Equation 2.11}$$

$$\beta = \exp \left( \begin{array}{l} -0.464 + 3.41 \cdot p_{C_3A} \cdot p_{cem} - 0.846 \cdot p_{GGBFS} \\ +107 \cdot WRRET + 33.8 \cdot LRWR + 15.7 \cdot MRWR \\ +38.3 \cdot PCHRWR + 8.97 \cdot NHRWR \end{array} \right) \quad \text{Equation 2.12}$$

$$\tau = \exp \left( \begin{array}{l} 2.92 - 0.757 \cdot p_{C_3S} \cdot p_{cem} + 98.8 \cdot p_{Na_2O} \cdot p_{cem} + 1.44 \cdot p_{GGBFS} \\ +4.12 \cdot p_{FA} \cdot p_{FA-CaO} - 11.4 \cdot ACCL + 98.1 \cdot WRRET \end{array} \right) \quad \text{Equation 2.13}$$

where,

$H_{cem}$  = Total heat of hydration of cement ( $kJ/kg$ )

$H_u$  = Total heat of hydration of cementitious materials ( $kJ/kg$ )

$E_a$  = Activation energy ( $J/mol$ )

$\alpha_u$  = Ultimate degree of hydration

$\beta$  = Hydration slope parameter

$\tau$  = Hydration time parameter ( $hr$ )

$p_{cem}$  = Mass ratio of cement to all cementitious material

$p_{FA}$  = Mass ratio of fly ash to all cementitious material

$p_{GGBFS-100}$  = Mass ratio of grade 100 slag to all cementitious material

$p_{GGBFS-120}$  = Mass ratio of grade 120 slag to all cementitious material

$p_{SF}$  = Mass ratio of silica fume to all cementitious material  
 $w/cm$  = Mass ratio of water to cementitious material  
 $p_{C_3S}$  = Mass ratio of  $C_3S$  content in cement  
 $p_{C_2S}$  = Mass ratio of  $C_2S$  content in cement  
 $p_{C_3A}$  = Mass ratio of  $C_3A$  content in cement  
 $p_{C_4AF}$  = Mass ratio of  $C_4AF$  content in cement  
 $p_{SO_3}$  = Mass ratio of  $SO_3$  content in cement  
 $p_{FreeCaO}$  = Mass ratio of free CaO (lime) content in cement  
 $p_{MgO}$  = Mass ratio of MgO content in cement  
 $p_{Na_2O}$  = Mass ratio of  $Na_2O$  content in cement  
 $p_{Na_2O_{eq}}$  = Mass ratio of  $Na_2O$  equivalent alkalis in cement =  $p_{Na_2O} + 0.658 \cdot p_{K_2O}$   
 $p_{K_2O}$  = Mass ratio of  $K_2O$  content in cement  
 $Blaine$  = Blaine fineness of cement  
 $p_{FA-CaO}$  = Mass ratio of CaO in fly ash  
 $ACCL$  = Mass ratio of accelerator to cementitious material  
 $WRRET$  = Mass ratio of water reducer/retarder (ASTM type B&D) to cementitious material  
 $LRWR$  = Mass ratio of low range water reducer (ASTM type A) to cementitious material  
 $MRWR$  = Mass ratio of mid range water reducer to cementitious material  
 $NHRWR$  = Mass ratio of naphthalene or melamine based high range water reducer (ASTM type F) to cementitious material  
 $PCHRWR$  = Mass ratio of polycarboxylate based high range water reducer (ASTM type F) to cementitious material

With a working model for hydration behavior of concrete, thermal properties that are hydration dependent can be determined as these values vary with time. Since the rate of heat generation,  $q$ , is an inherent part of the model definition, it can be found by substituting Equations 2.5, 2.6, and 2.7 into Equation 2.4 and differentiating. The resulting expression is given in Equation 2.14.

$$q = H_u W_c \left( \frac{\tau}{t_e} \right)^\beta \left( \frac{\beta}{t_e} \right) \alpha \frac{E_a}{R} \left( \frac{1}{T_r} - \frac{1}{T_c} \right) \quad \text{Equation 2.14}$$

For estimating thermal conductivity,  $k$ , and specific heat,  $C_p$ , Schindler & Folliard (2002) suggest using the empirical models shown in Equations 2.15 and 2.16 in conjunction with values found in Tables 2.1 and 2.2.

$$k = k_{uc} (1.33 - 0.33\alpha) \quad \text{Equation 2.15}$$

where,

$k_{uc}$  = Thermal conductivity of mature concrete

$$C_p = \frac{1}{\rho} (W_c \alpha C_{ref} + W_c (1 - \alpha) C_c + W_a C_a + W_w C_w) \quad \text{Equation 2.16}$$

where,

$C_{ref} = 8.4T + 339$ , where  $T$  is temperature in  $K$

$C_{c,a,w}$  = Specific heat of cement, aggregate, & water

$W_{c,a,w}$  = Weight of cement, aggregate, & water

Table 2.1. Thermal conductivity of mature concrete based on aggregate type (Schindler & Folliard, 2002)

Aggregate Type	Moist Density of Concrete		Thermal Conductivity	
	(kg/m <sup>3</sup> )	(lbs/ft <sup>3</sup> )	(W/m/°C)	(Btu/h/ft/°F)
Quartzite	2350-2440	147-152	4.1-3.1	2.33-1.75
Dolomite	2500	156	3.3	1.9
Limestone	2450-2440	153-151	3.2-2.2	1.83-1.25
Sandstone	2400-2130	150-133	2.9	1.7
Granite	2420	151	2.6	1.5
Basalt	2520-2350	158-157	2.0-1.9	1.17-1.08

Table 2.2. Specific heat of concrete materials (Schindler & Folliard, 2002)

Material	Specific heat (J/kg/°C)	Reference
Cement	1140	Mindess and Young, 1981
Water	4187	Scanlon et al., 1994
Limestone / Dolomite	910	Trinhztfy et al., 1982
Sandstone	770	
Granite / Gneiss	780	
Siliceous River Gravel	770	
Basalt	900	

In thermal modeling of drilled shafts, equally important as the thermal properties of concrete are the thermal properties of surrounding materials. For deep foundations, this is primarily soil or rock and the dominant mode of heat transfer is conduction, thus the same thermal properties  $k$ ,  $C_p$ , &  $\rho$  apply. These properties can vary widely with soil type, moisture content, and porosity. Table 2.3 gives typical values for various soil and rock types.

Table 2.3. Conductive thermal properties of subsurface materials

Material	Density, $\rho$ (kg/m <sup>3</sup> )	Thermal Conductivity, $k$ (W/m/K)	Specific Heat, $C_p$ (J/kg/K)	Diffusivity, $k/\rho C_p$ (mm <sup>2</sup> /s)	Reference	
Granite	2630	2.79	775	1.37	Incropera & Dewitt (2007)	
Limestone	2320	2.15	810	1.14		
Marble	2680	2.8	830	1.26		
Quartzite	2640	5.38	1105	1.84		
Sandstone	2150	2.9	745	1.81		
Sandy Soil - 40% pore space	Dry	1600	0.3	800	0.23	Arya (2001)
	Saturated	2000	2.2	1480	0.74	
Clay Soil - 40% pore space	Dry	1600	0.25	890	0.18	
	Saturated	2000	1.58	1550	0.51	
Peat Soil - 80% pore space	Dry	300	0.06	1920	0.10	
	Saturated	1100	0.5	3650	0.12	
Still Water (20°C)	1000	0.57	4180	0.14		
Still Air (20°C)	1.2	0.025	1010	20.63		

In the case of deep foundation construction, Standard Penetration Testing (SPT) data and borehole information are often available, and can provide further insight into the thermal properties of subsurface materials. In situ soil density,  $\rho$ , is a property commonly needed by geotechnical designers and can be estimated directly from uncorrected SPT blow count ( $N$ ) values using the empirical correlations shown in Figure 2.25. Thermal conductivity is not typically considered a result of SPT analysis, but research has shown that it is largely dependent on soil type, density, and saturation state. Pauly (2010) investigated these relationships by accumulating results from past studies involving the thermal behavior of soil and correlating them to the information provided by boring log data. To this end, an algorithm was developed to estimate values of density and thermal conductivity of soils based on the depth, soil type, blow count, and water table elevation as determined from SPT boring logs. The correlations investigated and regressed by Pauly (2010) are presented as functions of thermal conductivity vs. dry density for variable moisture contents and for both coarse grained (sandy) and fine grained (clayey) soils in Figures 2.26-2.39.

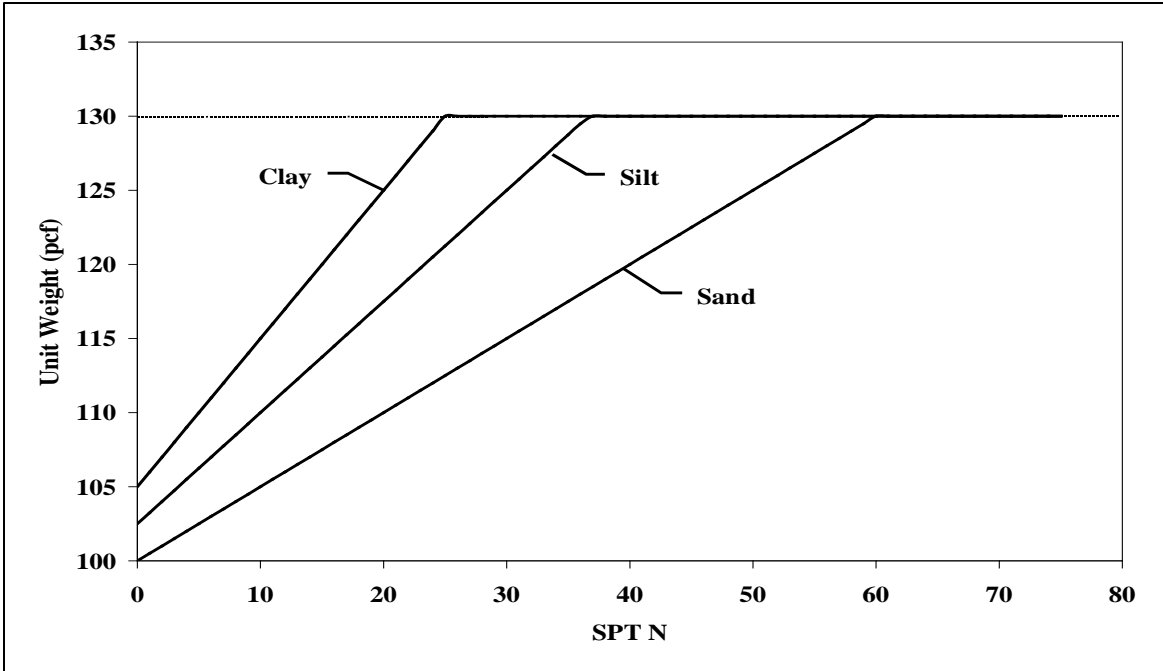


Figure 2.25. Soil density as a function of uncorrected SPT blow count (N) (Pauly, 2010)

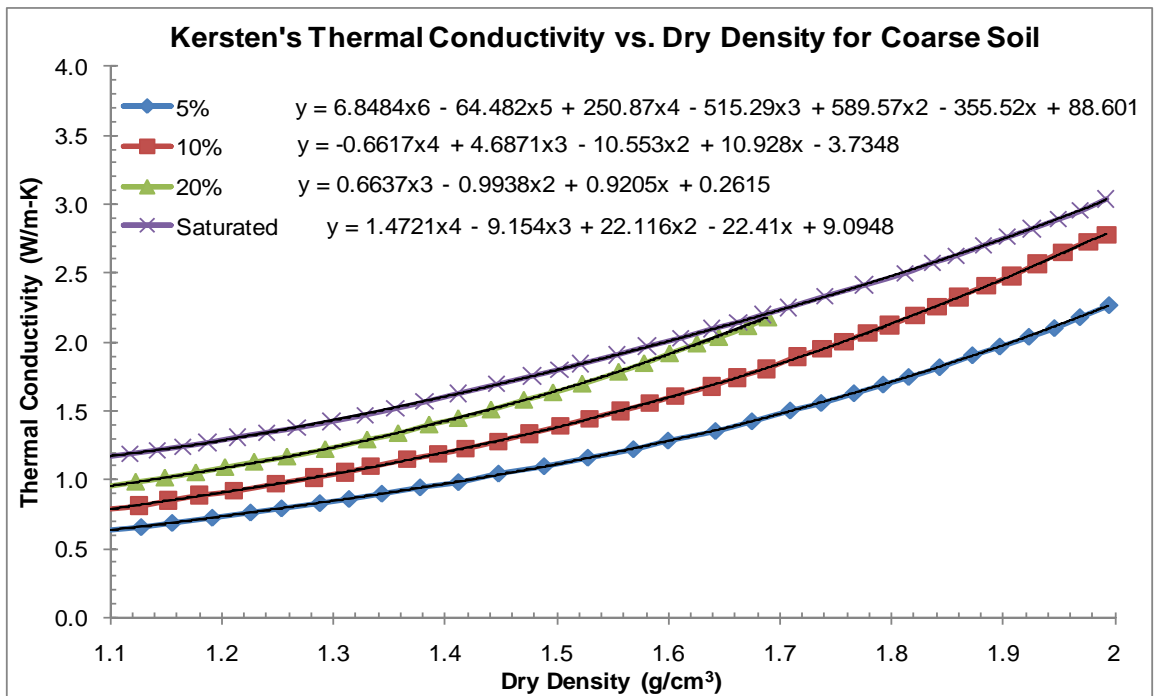


Figure 2.26. Kersten's conductivity vs. density at varied moisture contents for sandy soils (Pauly, 2010)

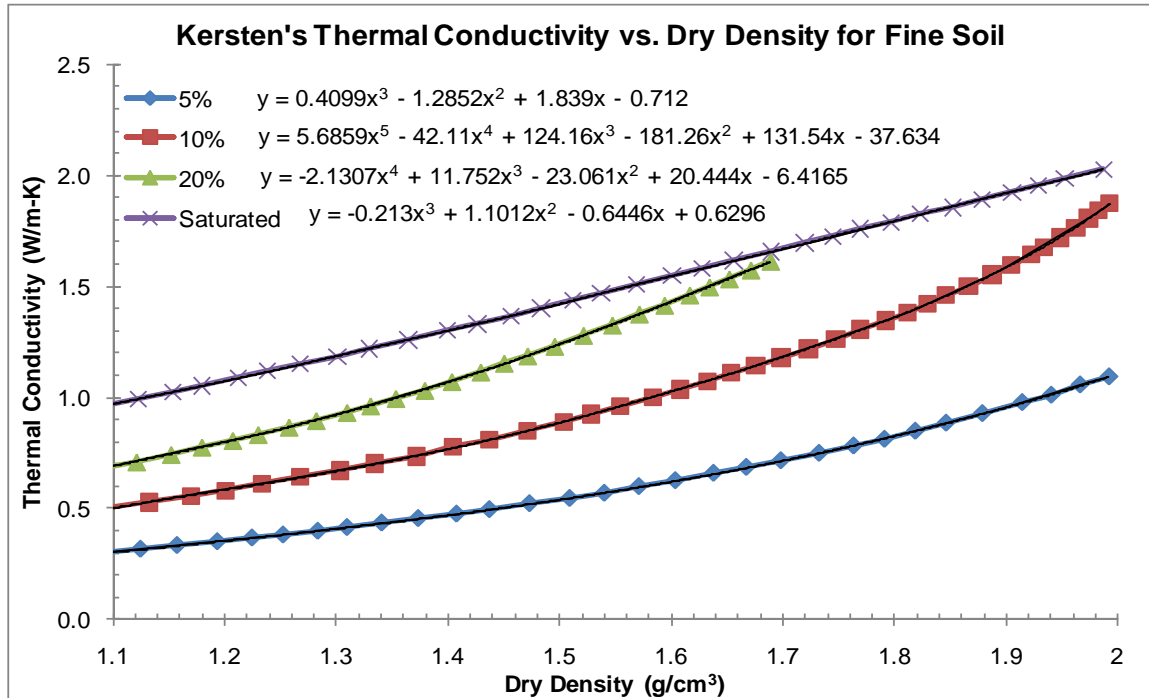


Figure 2.27. Kersten's conductivity vs. density at varied moisture contents for clayey soils (Pauly, 2010)

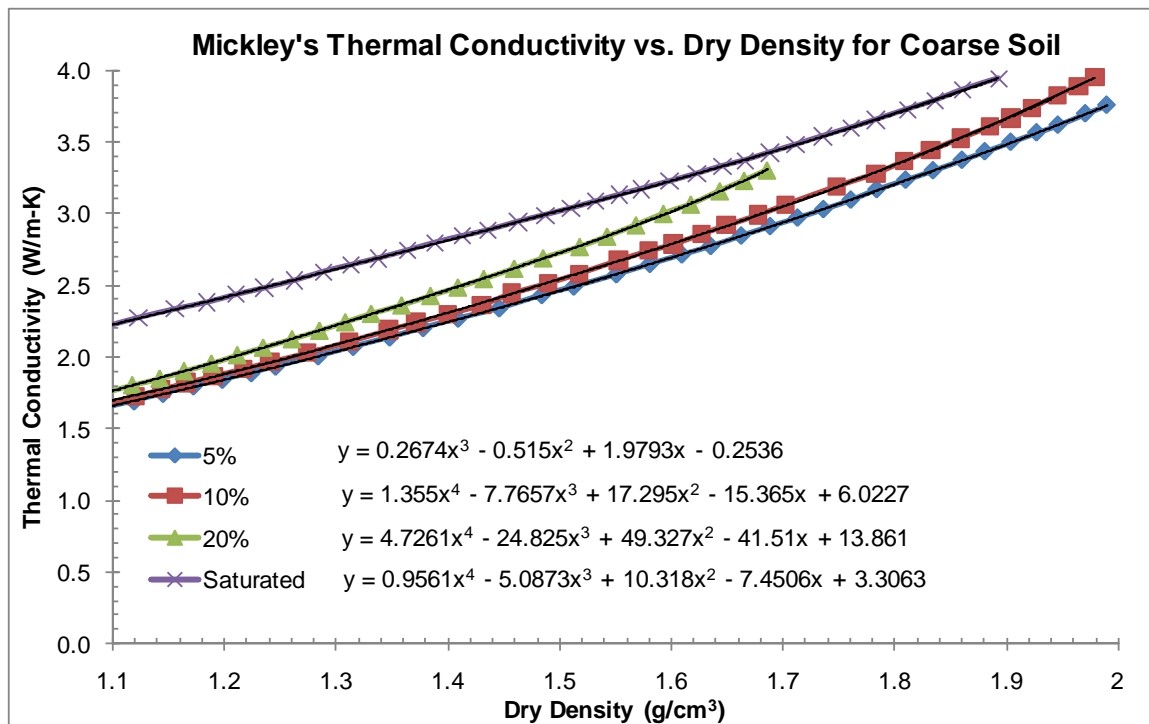


Figure 2.28. Mickley's conductivity vs. density at varied moisture contents for sandy soils (Pauly, 2010)

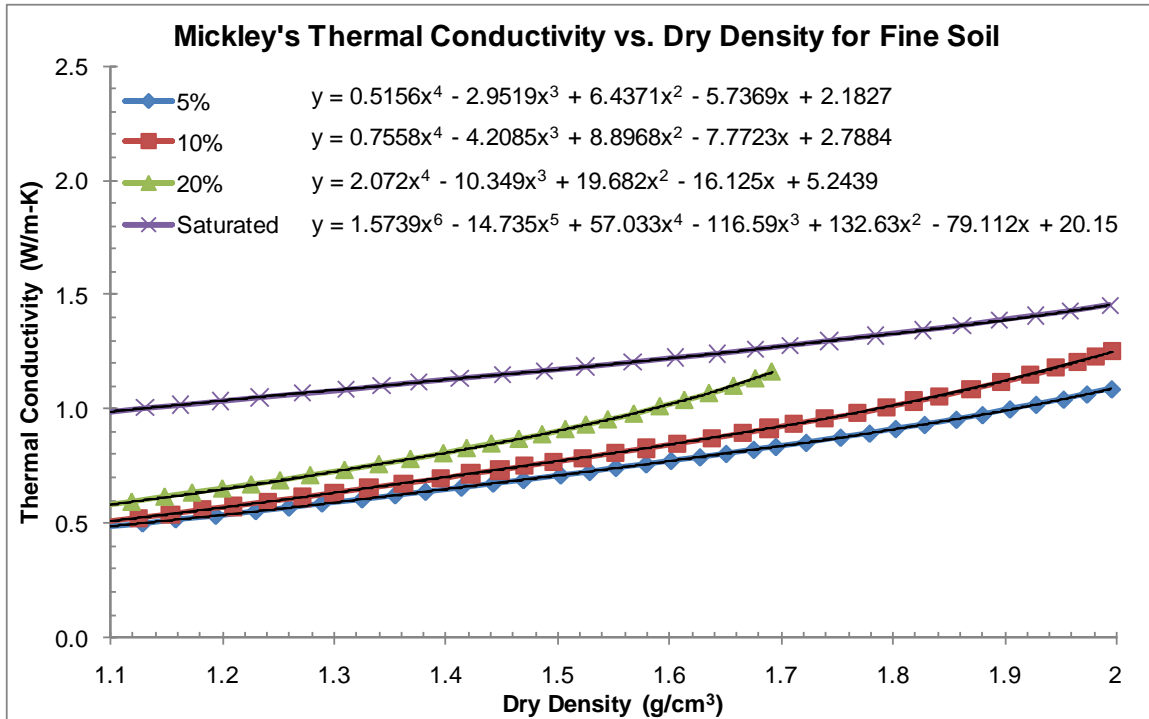


Figure 2.29. Mickley's conductivity vs. density at varied moisture contents for clayey soils (Pauly, 2010)

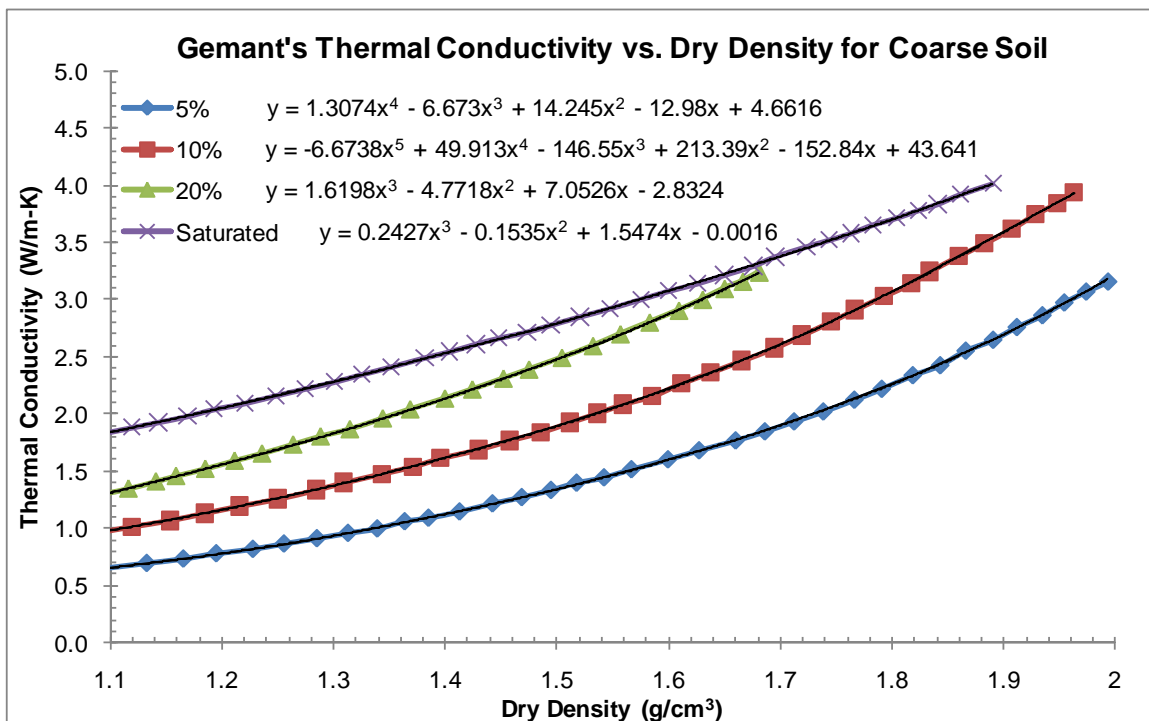


Figure 2.30. Gemant's conductivity vs. density at varied moisture contents for sandy soils (Pauly, 2010)

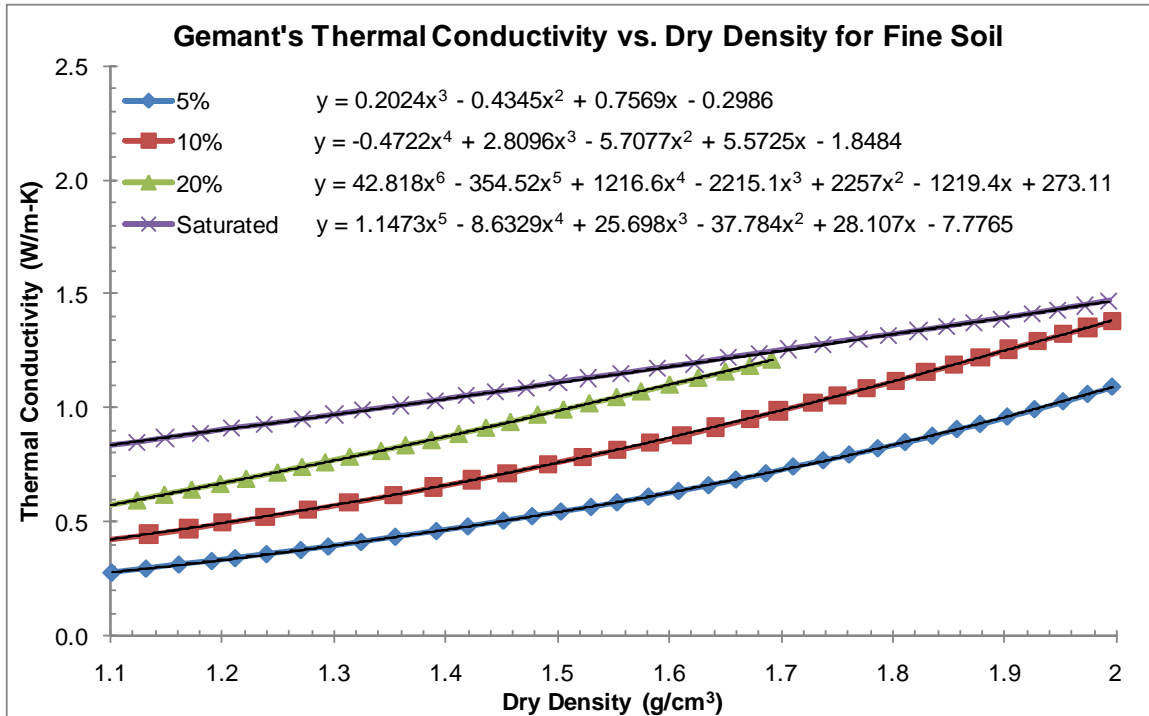


Figure 2.31. Gemant's conductivity vs. density at varied moisture contents for clayey soils (Pauly, 2010)

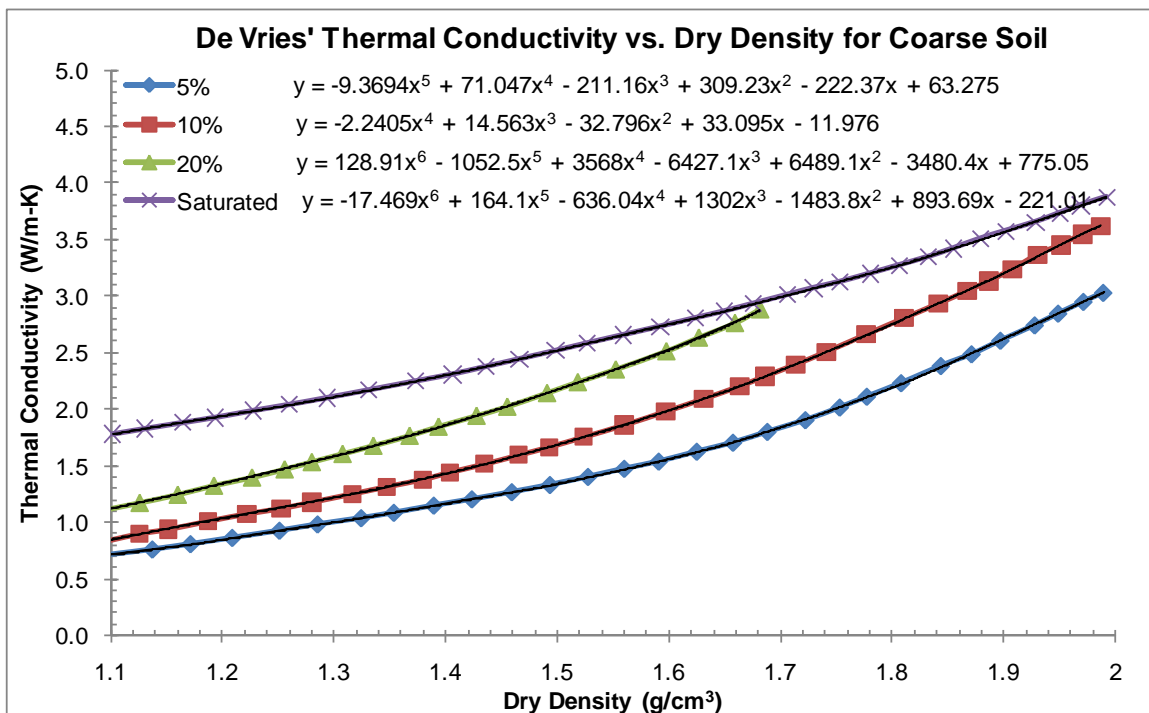


Figure 2.32. De Vrie's conductivity vs. density at varied moisture contents for sandy soils (Pauly, 2010)

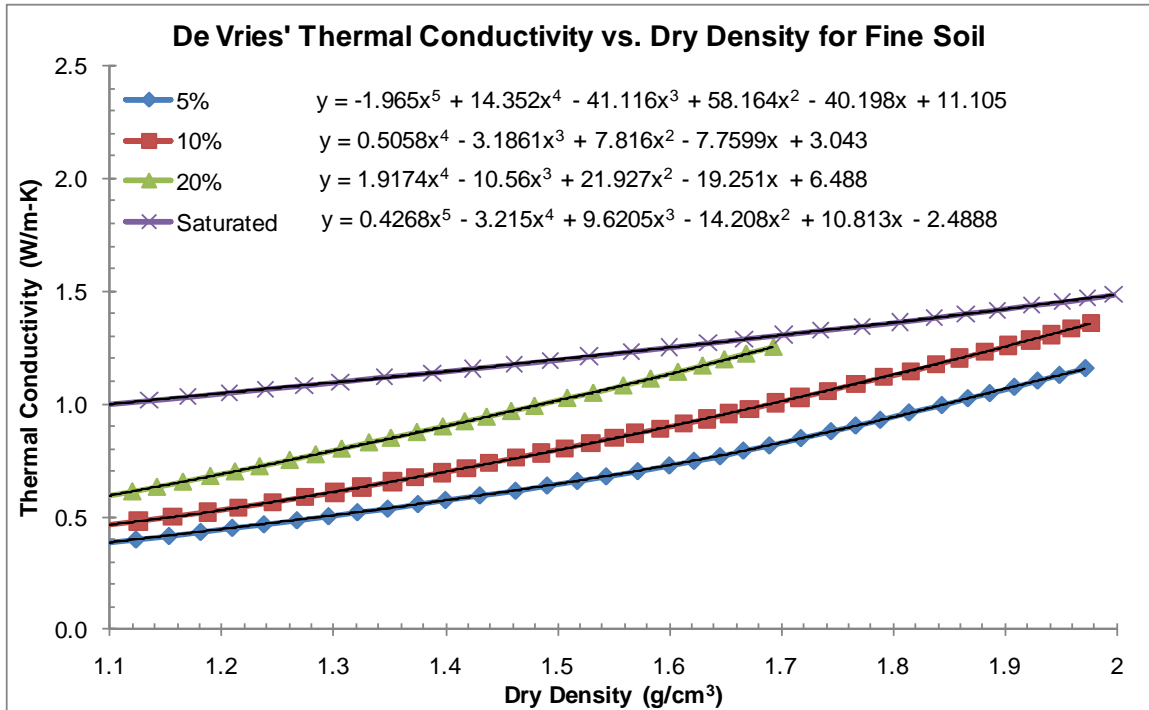


Figure 2.33. De Vrie's conductivity vs. density at varied moisture contents for clayey soils (Pauly, 2010)

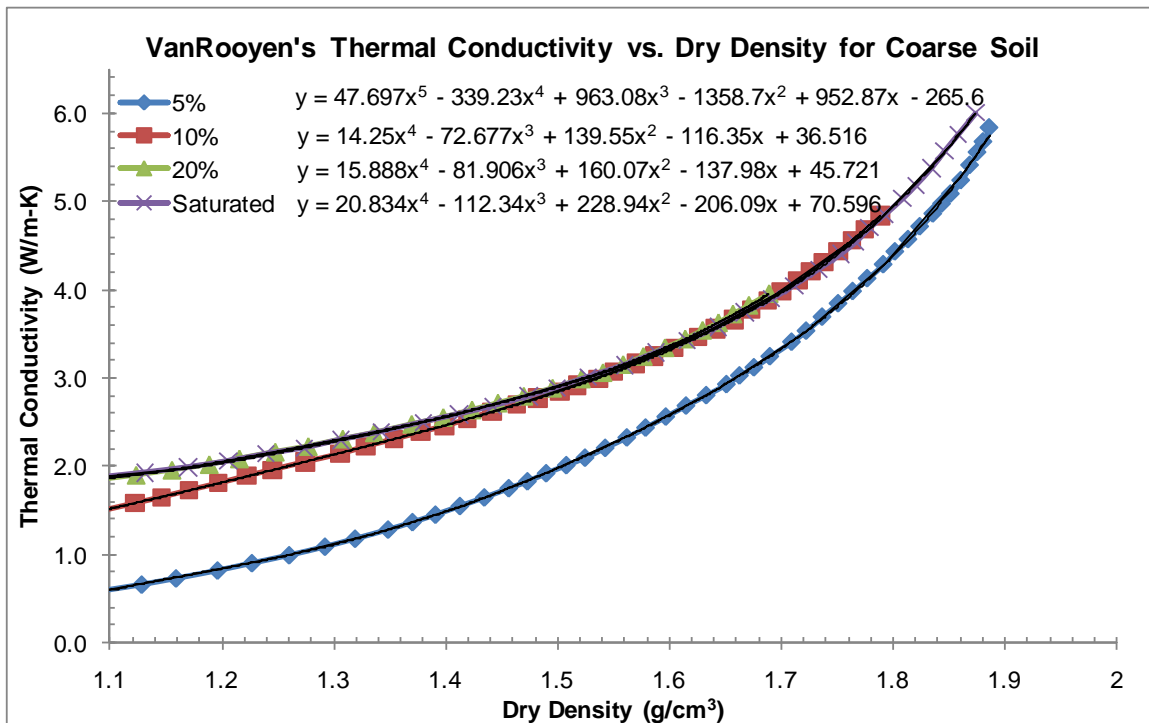


Figure 2.34. VanRooyen's conductivity vs. density at varied moisture contents for sandy soils (Pauly, 2010)

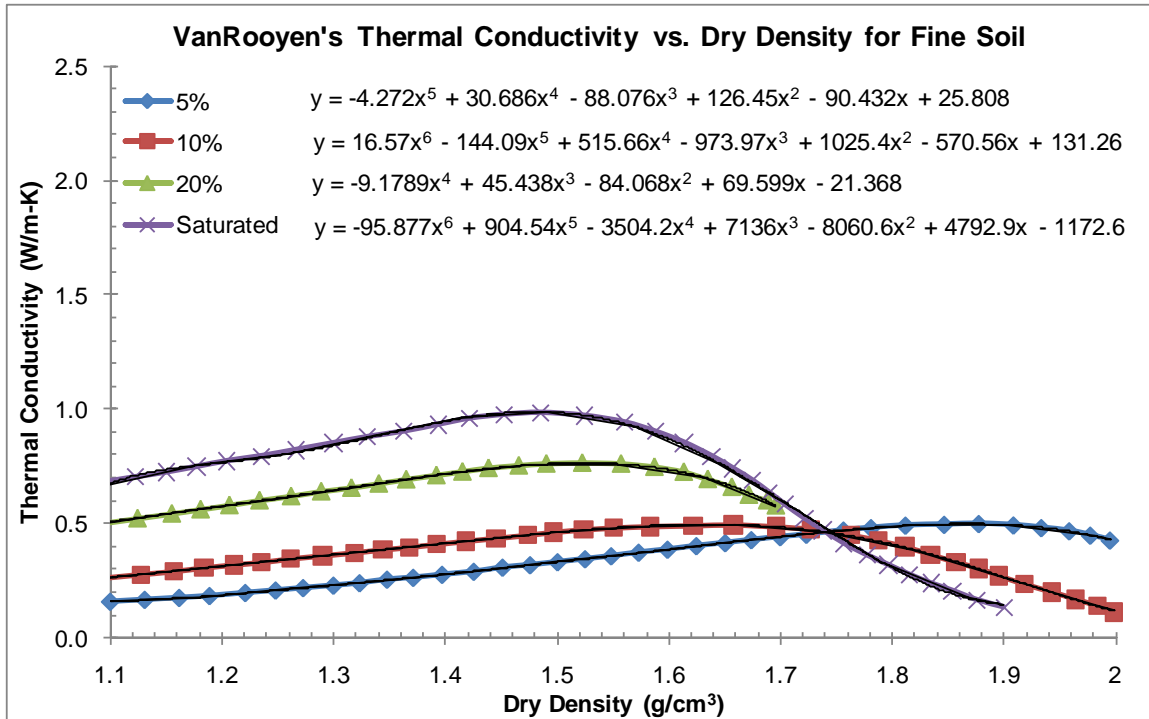


Figure 2.35. VanRooyen's conductivity vs. density at varied moisture contents for clayey soils (Pauly, 2010)

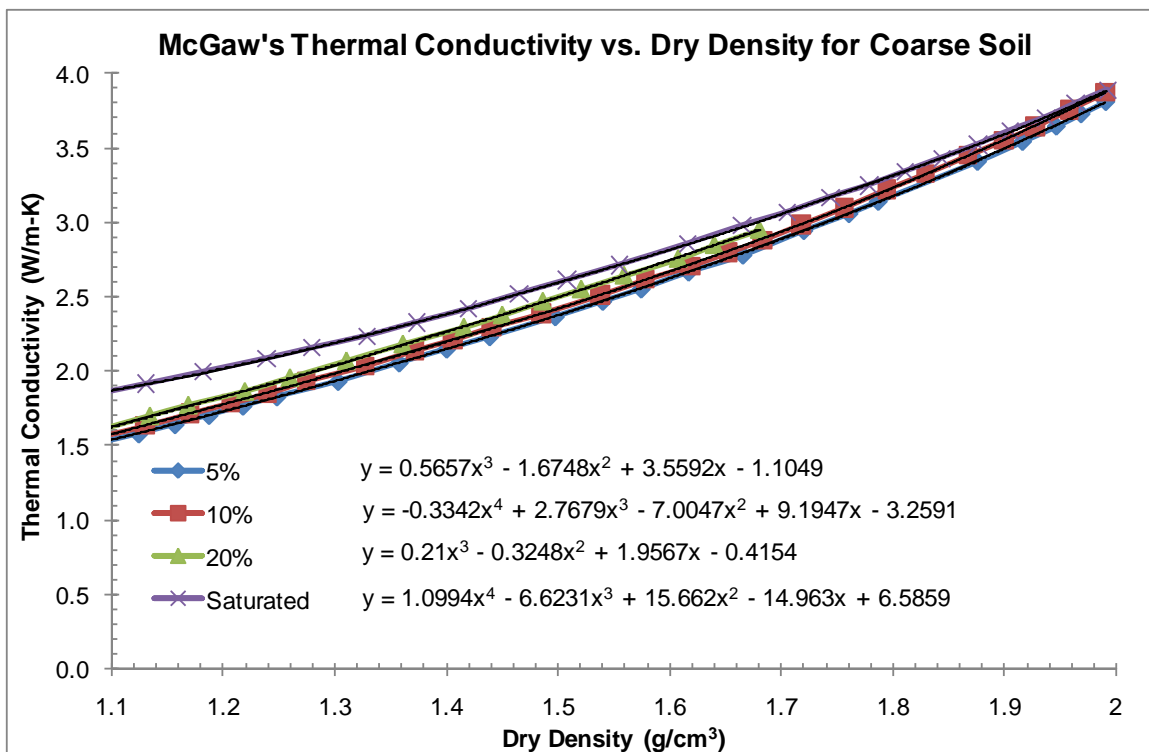


Figure 2.36. McGaw's conductivity vs. density at varied moisture contents for sandy soils (Pauly, 2010)

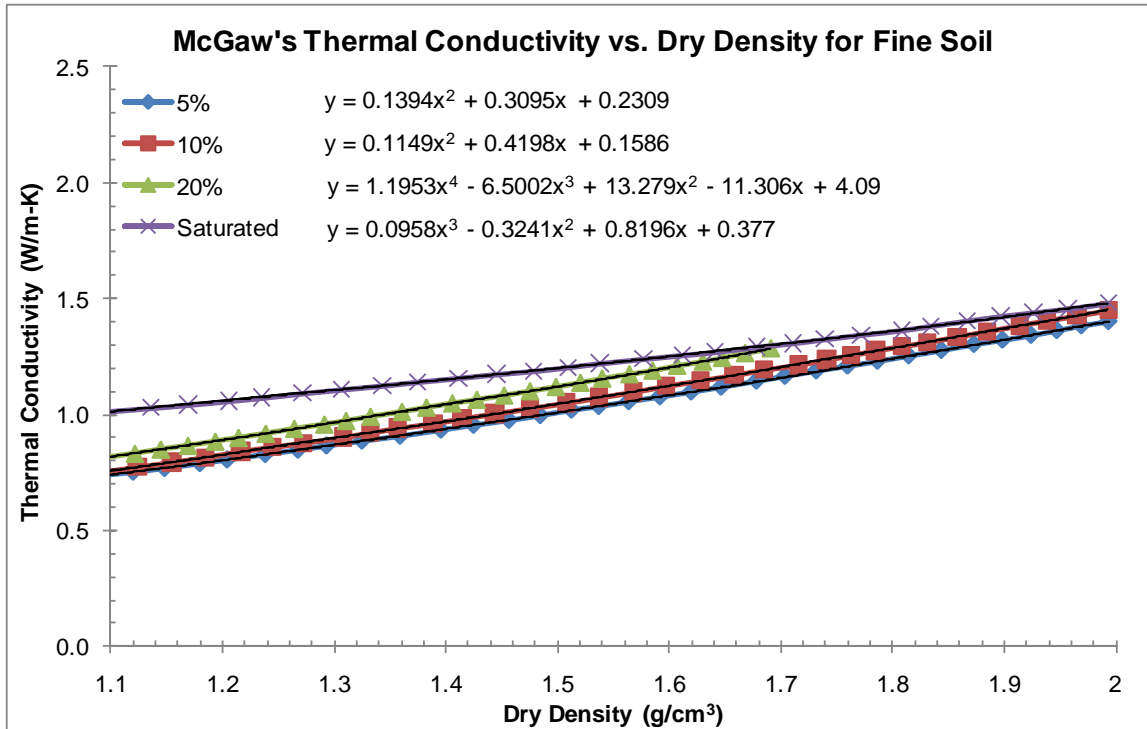


Figure 2.37. McGaw's conductivity vs. density at varied moisture contents for clayey soils (Pauly, 2010)

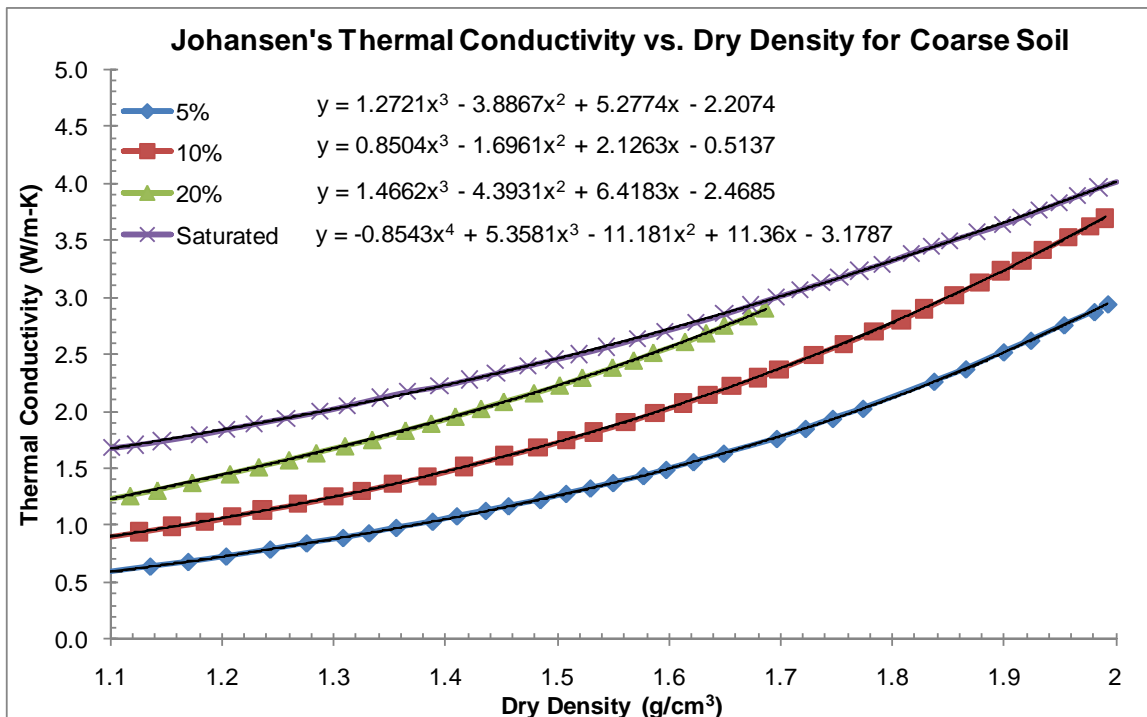


Figure 2.38. Johansen's conductivity vs. density at varied moisture contents for sandy soils (Pauly, 2010)

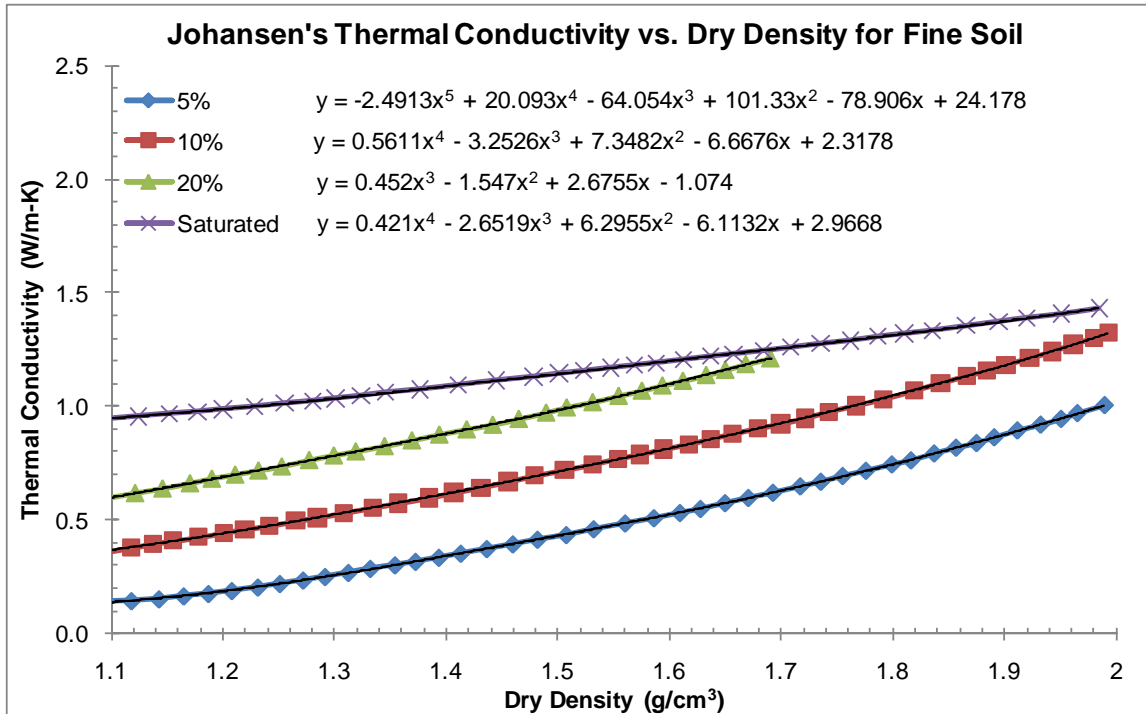


Figure 2.39. Johansen’s conductivity vs. density at varied moisture contents for clayey soils (Pauly, 2010)

In theory, a signal matching approach using modeled shafts could reveal the shaft geometry that would produce the measured thermal profiles. Figure 2.40 illustrates this, wherein results from constant soil temperature models were shown to closely match measured data (normalized to account for actual non-constant soil temperatures). However, the accuracy of models is largely dependent on input parameters such as shaft dimensions, boundary conditions, and concrete hydration behavior. Although the margins of error associated with these parameters can easily accumulate, useful trends and relationships about the temperature distributions within drilled shafts and surrounding environments can be identified. Used in tandem with traditional analysis techniques, these observations can provide enhanced levels of TIP data interpretation.

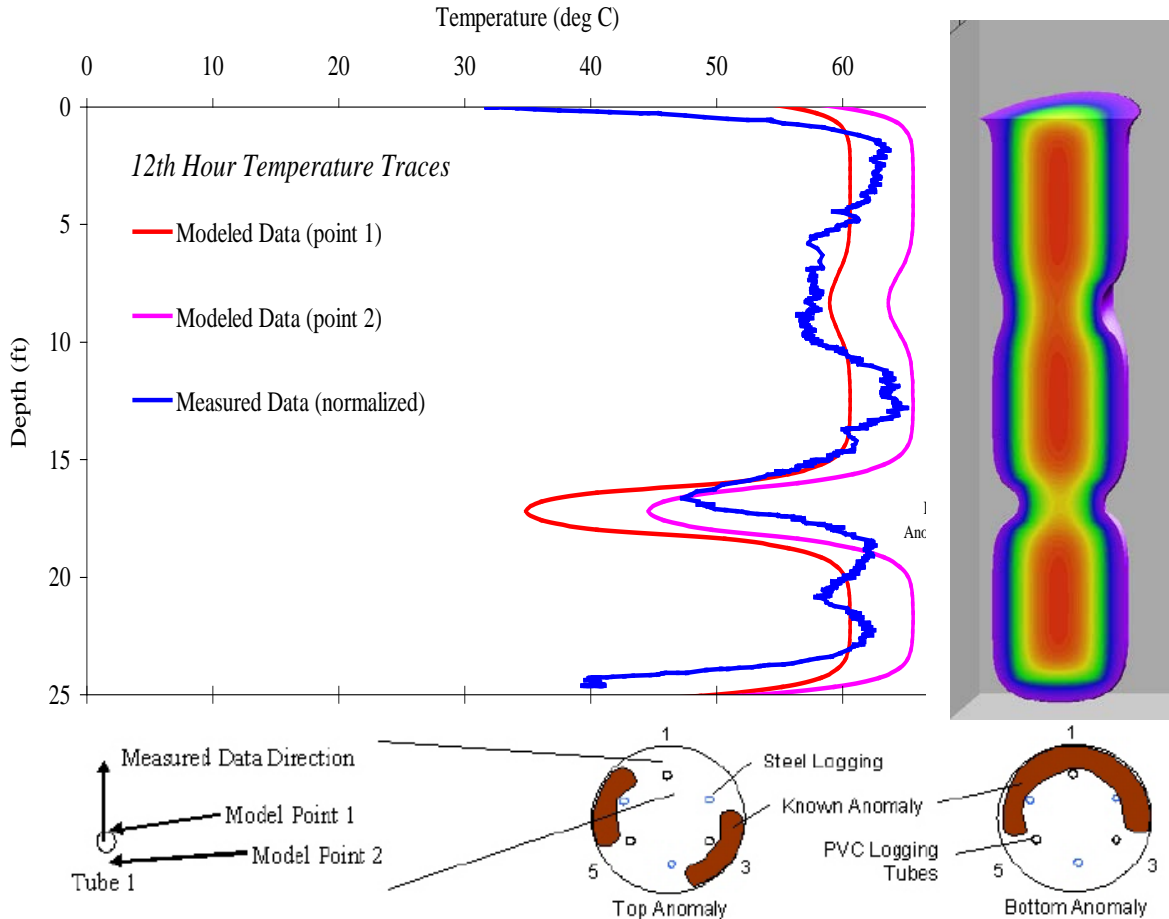


Figure 2.40. Modeled and measured temperature profiles for a tested shaft. (Mullins, 2008)

### 2.3 Use of TIP for ACIP

Because TIP is a relatively new non-destructive test (NDT) method, there are far fewer documented cases of TIP used for ACIP evaluation than for methods like Sonic Echo, CSL, SSL, and GGL. The fundamental concepts that make TIP effective with drilled shafts however, are equally as present in auger-cast piles, thus a translation of the technology between the two is conceivable.

A case study presented by Sellountou and Alvarez (2013) demonstrated the use of thermal wires with two 36cm (14in) diameter full displacement bored piles in Santa Cruz, Bolivia. Each pile was instrumented with two wires fastened to a full length reinforcing cage of 26cm (10in) diameter. The results from each pile indicated mostly uniform radius with a small bulge near the water table, which was in agreement with reduced grout pressures recorded at the same location.

Furthermore, a study by Piscsalko (2014) demonstrated the use of thermal wires fastened to a single center reinforcing bar on several 18 inch diameter CFA piles. He noted that the results were able to reveal anomalies not detected by low strain impulse methods (e.g., Sonic Echo).

In a separate study by Pisciak et al. (2014), the use of TIP to evaluate soil nails was investigated, again by fastening thermal wires to a single center reinforcing bar. Four soil nails, 6 inches in diameter by 20 feet long, were instrumented, with one containing two planned defects made of sandbags. The results showed clear detection of the two defects, indicated by sharp temperature decreases, while the other nails exhibited only slight fluctuations in temperature, likely due to misalignment of the center bar.

With trends pushing toward the increased use of auger-cast piles on larger U.S. transportation projects, the need for heightened levels of ACIP post-construction quality assurance is great. Surface testing provides very limited ranges of detection, and down-hole techniques like CSL, SSL and GGL require installation of access tubes to test only a fraction of the total pile volume. The potential for TIP to detect anomalies across 100% of the cross section, while requiring minimal accommodations for access, makes it a desirable candidate for optimization with ACIP piles. While these case studies demonstrate the ability of TIP to detect anomalies on small diameter piles, those cases were purely demonstrative and leave many theoretical concerns unaddressed, such as measuring and accounting for bar misalignment and how data analysis is affected.

### *Chapter Three: Numerical Modeling*

Use of numerical modeling was chosen as a means to identify trends in thermal profiles that in turn could be used to better evaluate field-collected measurements and to set criteria for the minimum amounts of data that are necessary to fully assess a tested foundation element. The effort put forth not only furthers the thermal evaluation of drilled shaft applications, but also focuses on the auger cast-in-place pile scenarios where fewer locations in the pile may be accessible.

#### **3.1 Modeling Hyperbolic Temperature Corrections**

Previously, in Chapter 2 hyperbolic tangent functions (Equations 2.1 and 2.2) were identified as being a reasonable approximation to the shape of the temperature profile near the top and toe of a cast-in-place cylindrically shaped concrete element. This equation is one of two equations suggested for such thermal diffusion boundaries when looking at mechanical engineering / heat transfer type solutions. The other common approximation is an error function (not discussed any further). While both present close fits to field data, the hyperbolic tangent function is more closed-form and easier to apply.

In order to evaluate the application of hyperbolic tangent function corrections, a set of thermal wire data was selected from a shaft containing clear top and bottom roll-offs as well a significant thermal transition caused by a change in soil strata (dry clay overlying saturated sand). Construction logs and interviews with field personnel indicated that the clay layer was predrilled without casing, and casing was loosely embedded (permanently), and drilling proceeded with slurry below that point. In any event, this caused a change in external boundary conditions that could conceivably be caused by any number of factors other than that explained by field information. Before applying these analysis methods to the field-collected data, a model shaft was generated with similar conditions and was analyzed to assess any trends or patterns which may prove useful. A dry clay was used in the model to cause a reduced diffusion condition which could also have been an air void. Model output was generated for times ranging up to 60 hr. The modeled profiles were analyzed using hyperbolic corrections and T-R conversions. Figure 3.1 shows the original field profile and the computer-generated model created to emulate it.

The shaft was modeled with an upper cased portion of 27in radius and a lower uncased portion of 24in radius. Top of shaft (TOS) was located at ground surface and bottom of shaft (BOS) was located at a depth of 35.4ft. Based on the input shaft dimensions, the concrete volume placed (CVP) was 19.25yd<sup>3</sup>. Also included was a drastic change in soil strata (low diffusivity overlying high diffusivity) occurring at depth of about 12ft. Ambient soil temperature was set to 60°F and air temperature was set to have a diurnal fluctuation of 66 - 83°F. Once data was generated, peak temperatures were identified at 18hr and the corresponding profile was selected for initial analysis.

The first step in applying temperature corrections is to properly identify regions of the profile where corrections are warranted. In almost all shafts, this includes the top and bottom, however any other regions of suspected changes in diffusion boundaries should be justified by strong evidence from site investigations (e.g., boring log, SPT, CPT). Also, for mid-shaft boundary changes, the boundary layer considered most normal should be identified, typically whichever accounts for the majority of the shaft length, given it is in soil, not water or air. In this case, everything in the clay layer was normalized to the underlying sand layer.

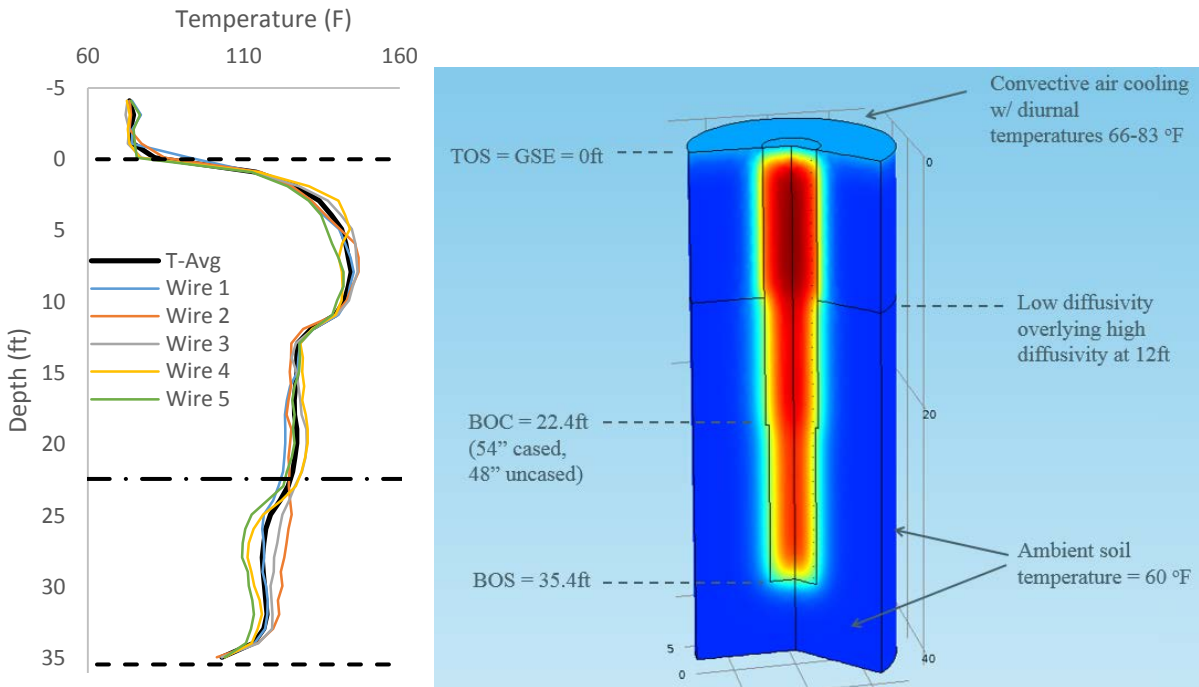


Figure 3.1. Field data (left), computer-generated model (right)

Selection of hyperbolic parameters began by setting the inflection point depths based on the known depths of TOS, BOS, and the clay-sand interface. Next, asymptotic and inflection point temperatures ( $T_{max}$ ,  $T_{min}$ ,  $T_0$ ) were selected based on observed values within the profile as well as known environmental temperatures. At the interface between soil layers,  $T_{min}$  and  $T_{max}$  can be observed in the nearest regions of uniform temperature on either side of the transition zone, and  $T_0$  is the average between them. For the top and bottom roll-offs, the temperature of both the ambient air and soil are strong pieces of information which help to define each hyperbolic temperature distribution. At the bottom, because the heat transfer characteristics of soil are similar to those of concrete, the temperature distribution in the soil is essentially a continuation of the same hyperbolic curve exhibited in the concrete. This results in a symmetrical curve with  $T_{min}$  equal to soil temperature,  $T_{max}$  equal to nearest uniform temperature in the shaft, and  $T_0$  equal to the midpoint between them. Conversely, at the top of the shaft, the modes of heat transfer between concrete and air are drastically different. The much stronger convective cooling behavior of air results in little to no temperature distribution beyond the interface and dominates the temperature at the concrete surface. Because of this effect, top roll-offs are best fit by forcing the inflection point ( $T_0$ ) to ambient air temperature. Empirical evaluation of this suggestion will

be discussed in an ensuing section. Note that doing so results in a  $T_{min}$  value that has no physical significance.

After determining depth and temperature parameters for each curve, alpha values were selected to achieve the best fit. The physical characteristic represented by alpha is the depth to which the effects of a thermal transition extend away from the interface. It has units of depth and is defined by the intersection of the asymptote and the slope at the inflection point on a hyperbolic curve. Using this definition, a rough estimate can be made by visual inspection of the profile. Past case studies suggest that alpha typically ranges between 1 - 3ft and increases with time. Theoretically, alpha ranges from zero at time zero, when no heat exchange has had time to occur, to infinity once all heat exchange has occurred and equilibrium is reached.

Table 3.1 gives the best fit hyperbolic parameter values for the model shaft at 18hr using an iterative evaluation algorithm. All depth and temperature parameters were kept in agreement with the shaft dimensions and boundary temperatures input into the model, and alpha values ranged from 1.25 - 1.4ft. Figure 3.2 shows the applied hyperbolic fits and corrected temperatures along with the resulting effective radius profile. The computed effective radius returned a maximum deviation of approximately 0.5in from the actual shaft radius.

Table 3.1. Hyperbolic equation parameters for model data at 18hr

	$Z_0$ (ft)	$T_{max}$ (°F)	$T_{min}$ (°F)	$T_0$ (°F)	$\alpha$ (ft)
Top	0	141.6	--	66.3	1.28
Transition	11.9	141.6	120.2	133.6	1.25
Bottom	35.4	110	60	94.25	1.4

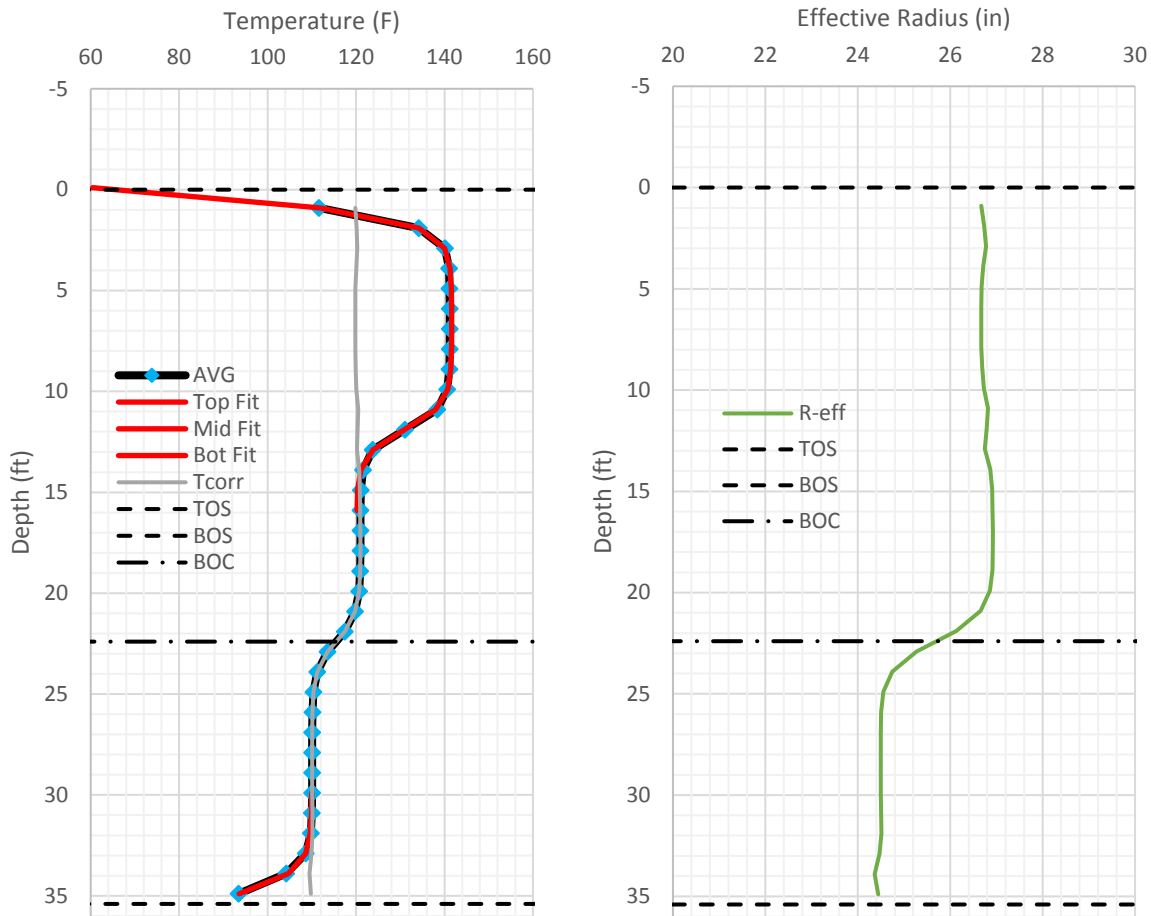


Figure 3.2. Results of model analysis at 18 hr

With the same model inputs, the same analysis procedure was performed for all times ranging from 9 - 60hr in order to examine the effects of time. In each case, best fits were achieved with the same inflection point depths ( $z_0 = \text{top or bottom of concrete}$ ) throughout, matching asymptotic temperatures within the shaft by visual inspection, and using soil temperature as the minimum for the bottom roll-off. The only parameters requiring trial and error iterations were the inflection point temperature ( $T_0$ ) for the top roll-off and all three alpha values, each of which revealed trends. Figure 3.3 shows the correlation that was exhibited between air temperatures and the inflection temperatures at the top roll-off.

The pattern of the best fit inflection temperature exhibits the same period as that of diurnal air temperature, but with a distinct lagging effect, suggesting that they are primarily influenced by the range of air temperature experienced over the previous day (or half day). Furthermore, the damping effect exhibited as time progressed suggests that inflection temperatures are less variable at later stages and could be more accurately estimated with the average of previous daily temperatures. Figure 3.4 shows the trends revealed by the best fit alpha values from the model

analysis. All three exhibit a strong linear relationship with the square root of time, and with similar slopes for the top, bottom and mid-shaft transition.

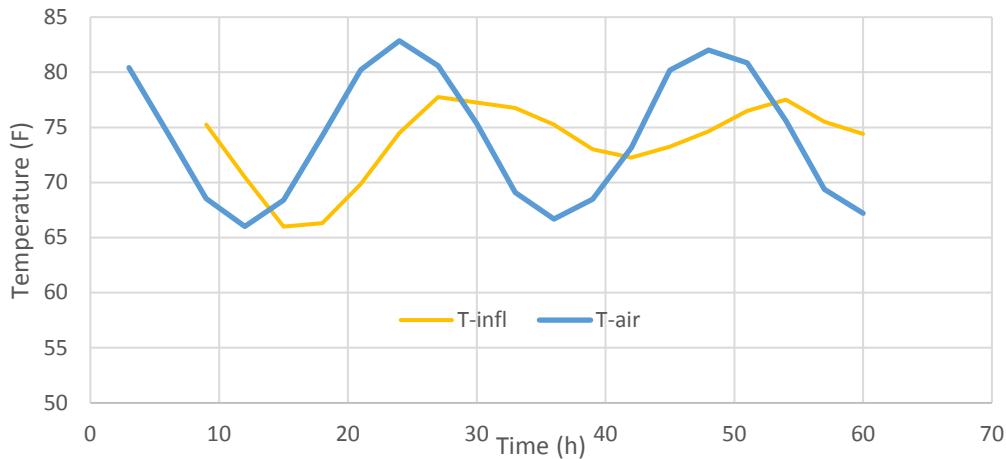


Figure 3.3. Variation of top roll-off inflection temperatures compared with air temperatures

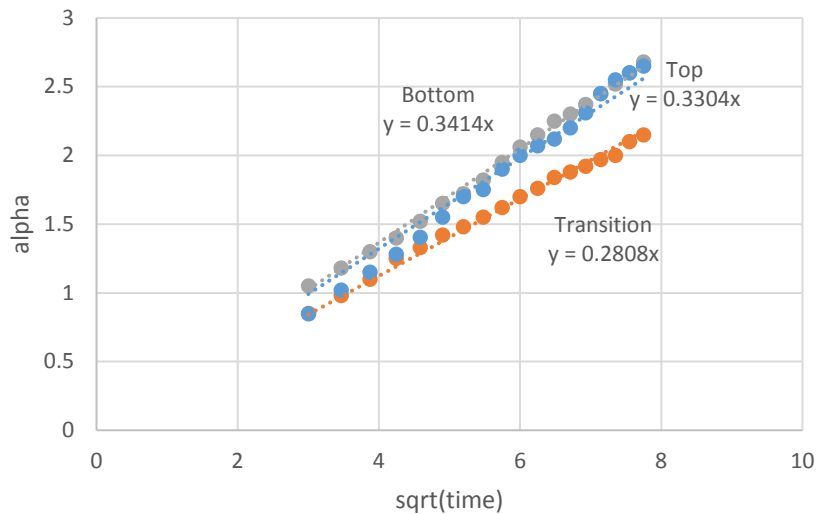


Figure 3.4. Variation of alpha with time resulting from analysis of model data

The model data analysis was used to evaluate the reproducibility of the T-R conversions. In theory, analysis performed on the same shaft at any time during the dominant stages of concrete hydration should produce a changing T-R relationship with time, but ultimately the same effective radius should be predicted. Figure 3.5 provides a comparison of the range of results obtained from the model data between 9 and 60hrs. The dashed lines correspond to the maximum and minimum effective radius that was obtained for each depth at any time.

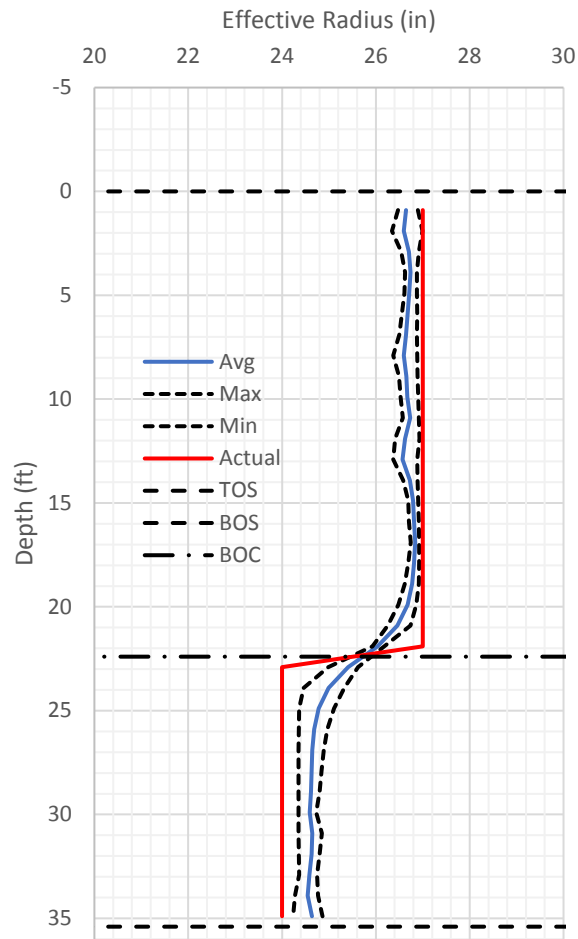


Figure 3.5. Range of results from model analysis up to 60 hr

Using the insight gained from modeling, the same analysis was performed using the data collected from a 35ft long, 4ft diameter shaft (Figure 3.1). Figure 3.6 shows the temperature profiles collected from five measurement locations around the cage circumference where thermal wires were embedded in the shaft and the fitted hyperbolic profile. As the reinforcing cage is rarely perfectly concentric, the average of all profiles should be used for determining T-R relationships. As with the model data, peak temperature was observed at 18hrs and this data was analyzed first (Figure 3.6). Hyperbolic parameters were selected using the same guidelines but were adjusted in order to obtain the best fits. Inflection point depths for the top and bottom roll-offs were adjusted from reported values up 1ft and down 0.3ft, respectively. It is not uncommon for reported TOS and BOS elevations to vary slightly depending on factors like over excavation of the bottom and the amount of overpour (or underpour) at the top. Thus, adjustment of inflection point depths up to about 1ft in either direction is not unreasonable (depending on log quality). The inflection point for the change in soil strata was set at 11.4ft based on visual inspection of the data and then compared with the nearest boring log which indicated a water table depth of 11ft. While saturation states can have a drastic effect on soil conductivity, soil saturation does not typically vary significantly just above and below the water table (Johansen,

1981). However, in regions where the water table is relatively stable, this can occur. Soil temperature was determined from the annual average air temperature of the region, which was 55°F, and was used for the bottom roll-off minimum temperature. Air temperature from the time of casting was conveniently available from the excess thermal wire sensors extending from the top of shaft. Recorded data showed a daily temperature range of 65-82°F. An inflection temperature of 77°F provided the best fit for the top roll-off. All other temperature parameters were selected from observed values in the thermal profile, and alpha was iterated by trial and error using  $\alpha = 0.3\sqrt{t}$  as an initial estimate. Table 3.2 gives the final parameter values.

Table 3.2. Hyperbolic equation parameters for field data at 18 hr

	$Z_0$ (ft)	$T_{max}$ (°F)	$T_{min}$ (°F)	$T_0$ (°F)	$\alpha$ (ft)
Top	-1.0	144	--	77	3.0
Transition	11.4	144	126.5	135.5	1.25
Bottom	35.7	117.5	55	95.75	1.33

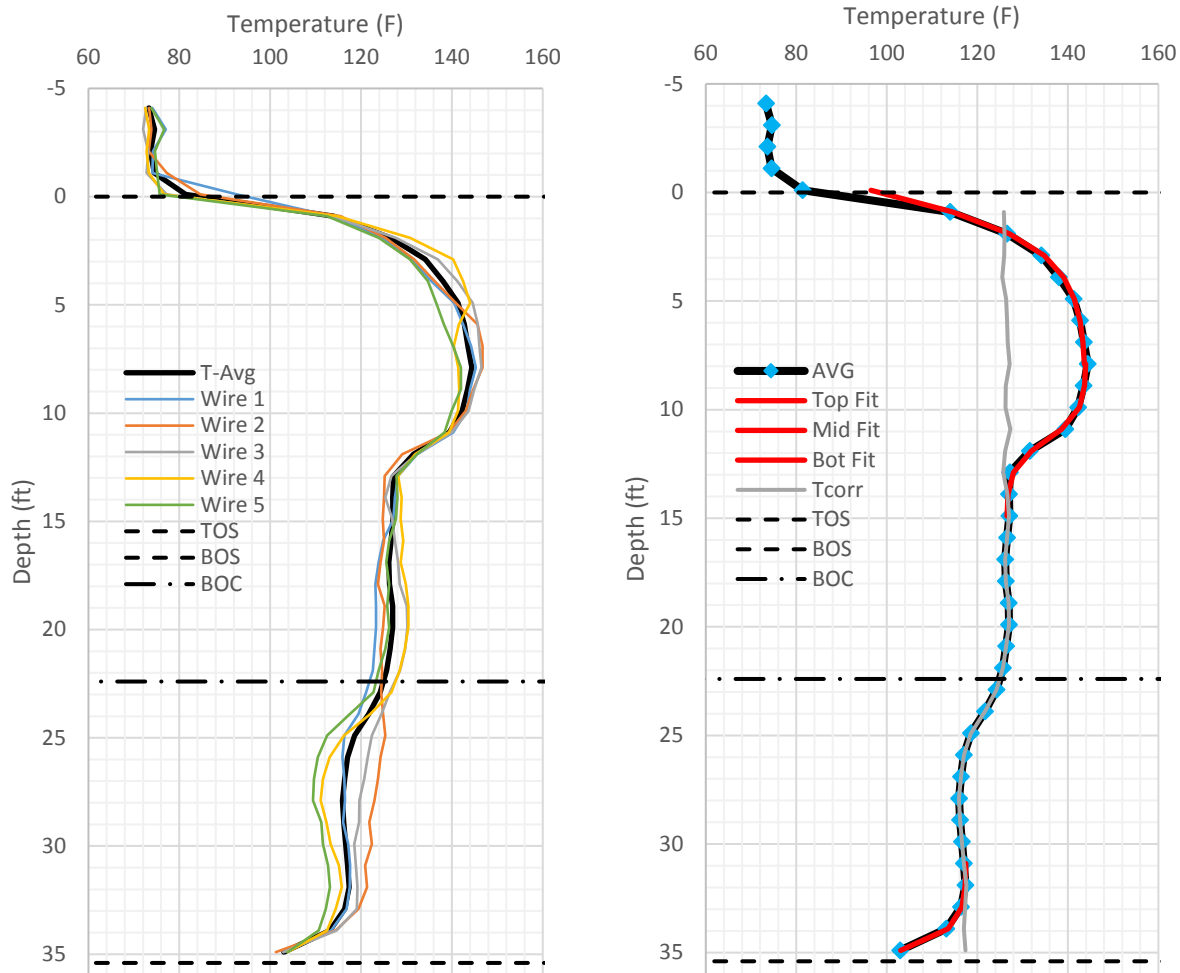


Figure 3.6. Results of analysis field data analysis at 18 hr

Analysis of the entire time range that was collected (23hr), yielded similar patterns to those revealed by the model analysis. Inflection point temperatures at the top were dominated by air temperature (Figure 3.7), and alpha values followed a linear increase with the square root of time (Figure 3.8). In fact, the alpha relationships for the bottom and middle fits adhered to a similar slope as found in modeling, however the top alpha values followed a pattern that increased at more than twice the rate of the others (may indicate other problem with shaft).

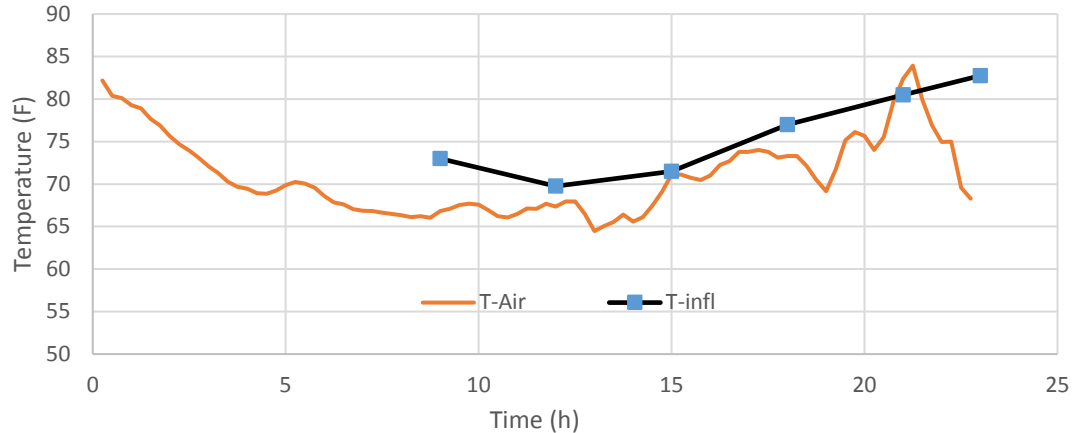


Figure 3.7. Top inflection point temperatures compared with measured air temperatures

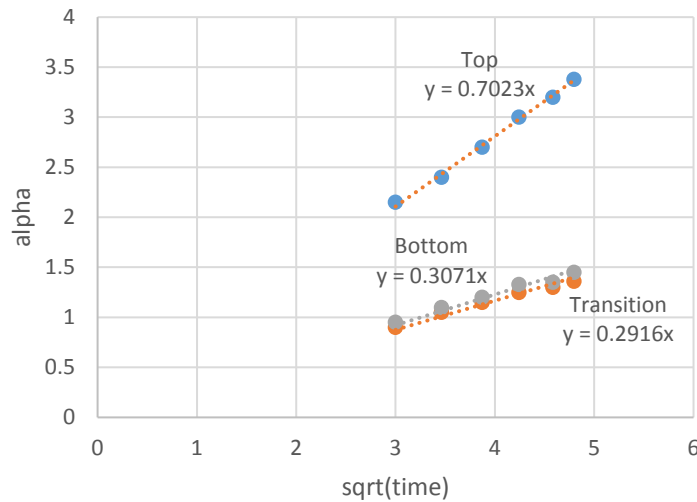


Figure 3.8. Correlation between  $\alpha$  and time

Finally, with the transitions zones corrected and the T-R conversion complete, the entire shaft was analyzed using all the temperature profiles collected from around the shaft (Figure 3.9, left). Therein, the T-R conversion was applied to each thermal wire profile to show local shaft radii from which the amount of cage offset can be determined. The reproducibility of the T-R conversions was assessed to demonstrate the variability brought about by the time chosen for analysis (Figure 3.9, right). A comparison of the maximum and minimum effective radius (average of all tubes) determined at each depth revealed very little variation from 9 to 23hr for this shaft (only 23hr of data was available). Furthermore, construction log information revealed that the upper portion of the shaft was permanently cased and that the shaft took  $1\text{yd}^3$  more

concrete than anticipated. This is strongly corroborated by the thermal results which indicate a close match to the casing radius in the upper part, and a slightly larger than intended radius in the lower uncased part.

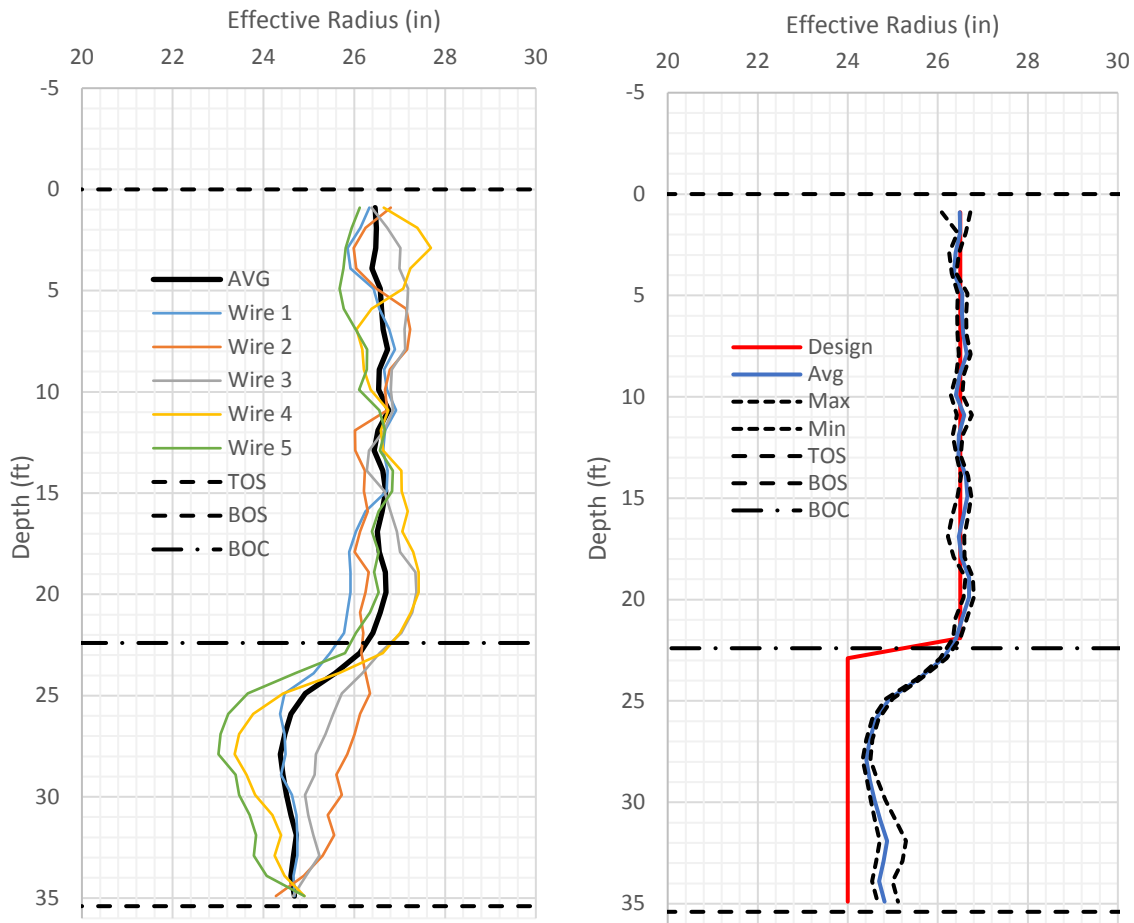


Figure 3.9. T-R results for analysis at 18hr (left) and range of results for all times (right)

### 3.2 Analysis of Field Data for Hyperbolic Parameter Selection

As with any signal matching approach, good matches can be found with physically impractical parameters. A strong sense of reasonable input values must be present when applying temperature corrections. Experience with both model and field data is useful in identifying trends and understanding the relationships involved in thermal data analysis. In the case study presented above, the modeled results agreed well with the field observed/fitted values, with the exception of the top of shaft  $\alpha$  factor. In all cases, the  $\alpha$  factor should increase with time (as it did) and has been shown to be linearly proportional to the square root of curing time. Whether or not the fitted value is appropriate is best determined from site specific experience that may show increases in the upper shaft heat dissipation modes.

The selection of the most appropriate hyperbolic fitting parameters for TIP analyses was further investigated by collectively examining the data from 232 tested shafts to identify the trends

exhibited by the best-fit hyperbolic parameters selected for each one. To do this, the data from each shaft were imported into a single spreadsheet and a curve-fitting algorithm was developed to find the best-fit solution for each top and bottom roll-offs by iterating through a range of values for each of the hyperbolic parameters (e.g.,  $T_{max}$ ,  $T_{min}$ ,  $D_{inf}$ ,  $T_{inf}$ ,  $\alpha$ , etc.). Once the best-fit hyperbolic solutions were found for every shaft, the resulting parameters were examined collectively and compared against contributing factors like concrete age and air temperature.

As noted previously, modeling shows the alpha factor to follow a strong increasing relationship with the square root of time, which was also corroborated by the above case study (Figures 3.4 and 3.8). This relationship can be expressed by Equation 3.1, where  $\alpha$  is in units of feet,  $t$  is units of hours, and the coefficient  $c$  is the subject of investigation (in units of  $\text{ft}\cdot\text{hr}^{-1/2}$ ).

$$\alpha = c\sqrt{t} \qquad \text{Equation 3.1}$$

Figure 3.10 shows the  $\alpha$  values resulting from the best-fit top and bottom hyperbolic solutions versus the age of concrete at time of testing for the 232 shafts analyzed. Since testing on this project was typically performed either one or two days after concreting, much of the data is clustered around the 24 and 48 hour timeframes, however some tests were performed as early as 12 hours and as late as 96 hours after concreting, providing a wide enough range of data to examine the time dependent trends.

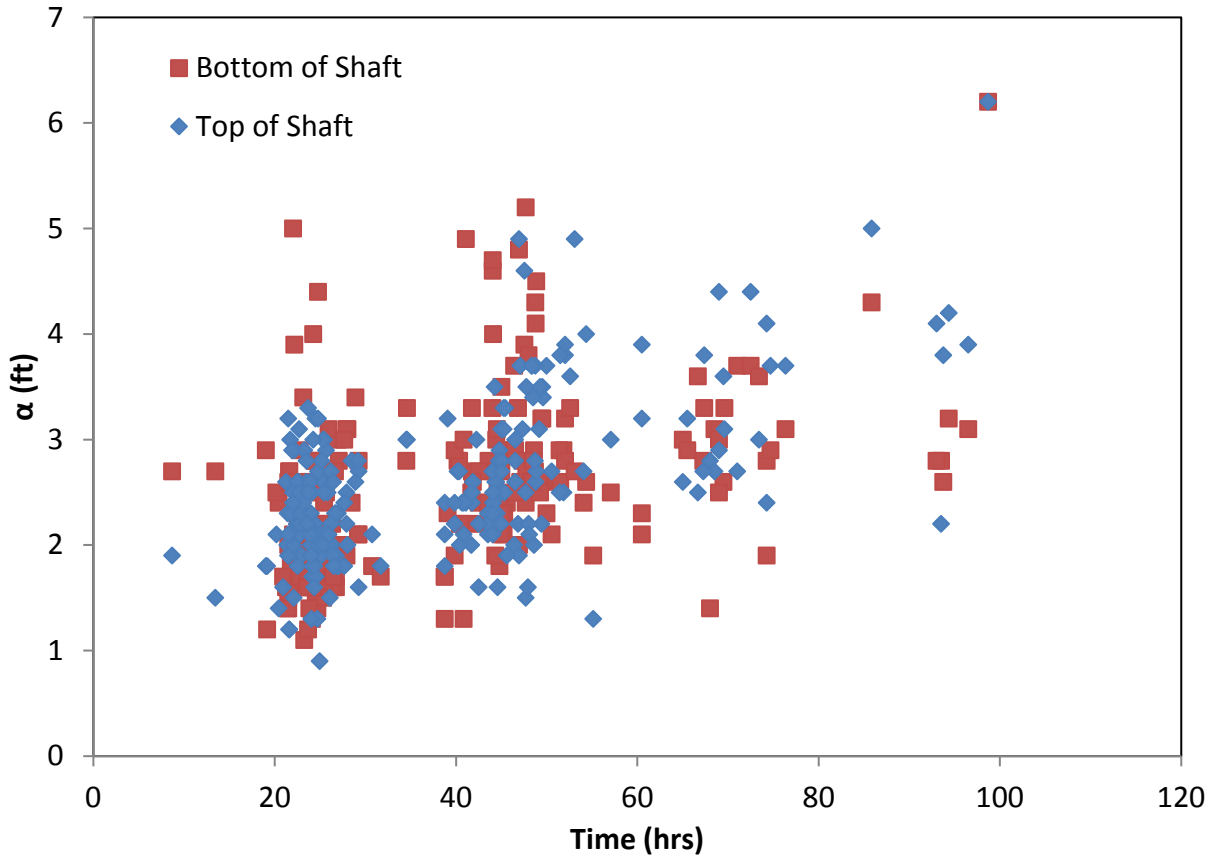


Figure 3.10. Best fit  $\alpha$  values for both the top and bottom of shaft

For each data point in Figure 3.10, the coefficient  $c$  was back calculated and rounded to nearest multiple of 0.025 for the purpose of creating the frequency distribution curve shown in Figure 3.11. The result is a positively skewed distribution, as opposed to a normal distribution, due to the hard boundary on the lower side imposed by the concept that  $c$  cannot equal zero. This is not uncommon for data with such a condition, but it results in a statistical average that is heavily weighted by the outliers on only one side of the distribution. Instead, the central tendency of the data is better represented by the median value, which in this case yielded a value of  $c = 0.4$ . The variability of the data is measured by the standard deviation ( $\sigma$ ). Figure 3.12 shows the  $\alpha$  vs. time relationship resulting from the statistical analyses.

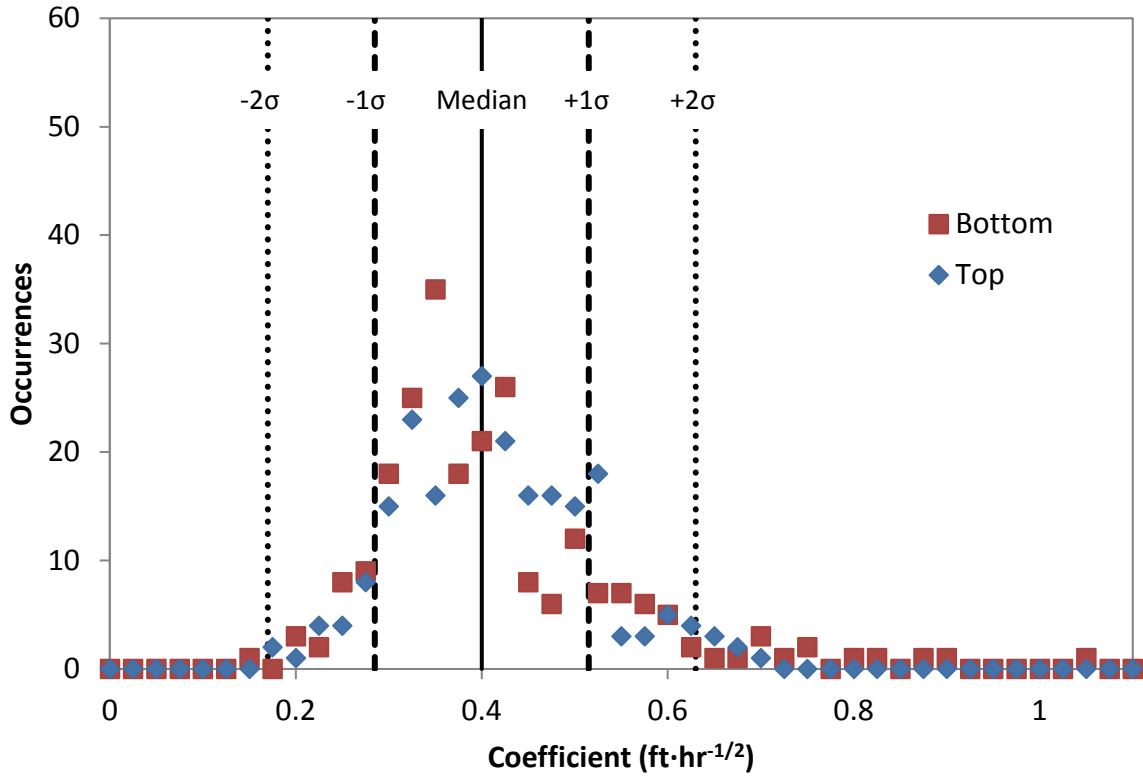


Figure 3.11. Probability density distribution for the coefficient  $c$  in the equation  $\alpha = c\sqrt{t}$

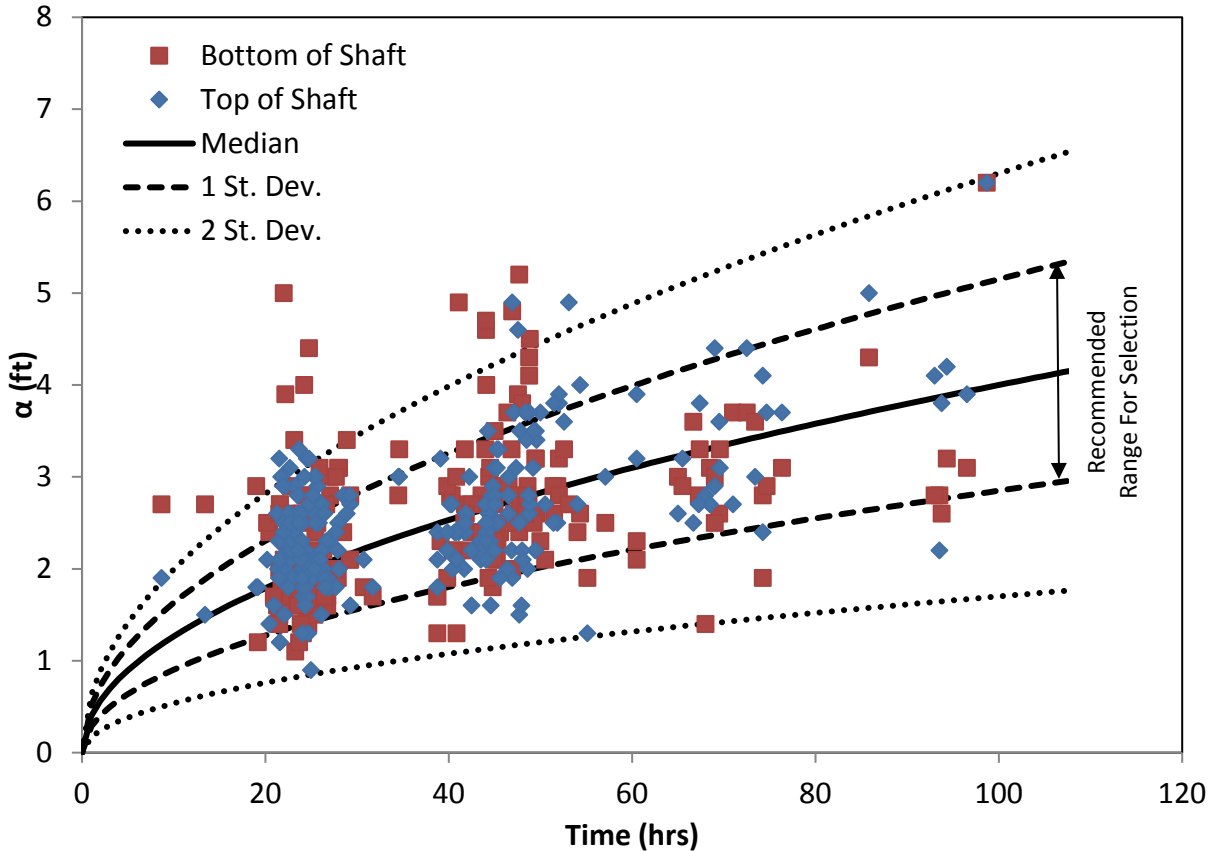


Figure 3.12. Statistically derived boundaries for  $\alpha$  selection

Note that the occurrence of  $\alpha$  values less than one standard deviation below the median is less frequent than those more than one standard deviation above the median. This demonstrates the effects of a positively skewed probability distribution where  $\alpha$  values for bullet shaped shaft tips or misshaped tops are more likely than oversized tops or bell-shaped toes. A lower than expected  $\alpha$  value only occurs in the presence of a significant belled shaft tip or bulge. At the surface this occurs when over pour concrete is left on the ground surface around the shaft top.

Further investigation of the fitted field data is aimed at proper selection of the inflection point temperature at the top of shaft. Because the convective cooling behavior of free air is much stronger the conductive heat transfer in soil, it directly influences the temperature at the top surface of a shaft. Figure 3.13 shows the best-fit top of shaft inflection point temperatures along with the daily high and low recorded air temperatures.

NOTE: The 232 shafts were all cast up to ground surface, but did not extend above. For shafts that are terminated well below ground (low cutoff elevation), there is less effect from air and those cases tend to be more aligned with bottom of shaft conditions.

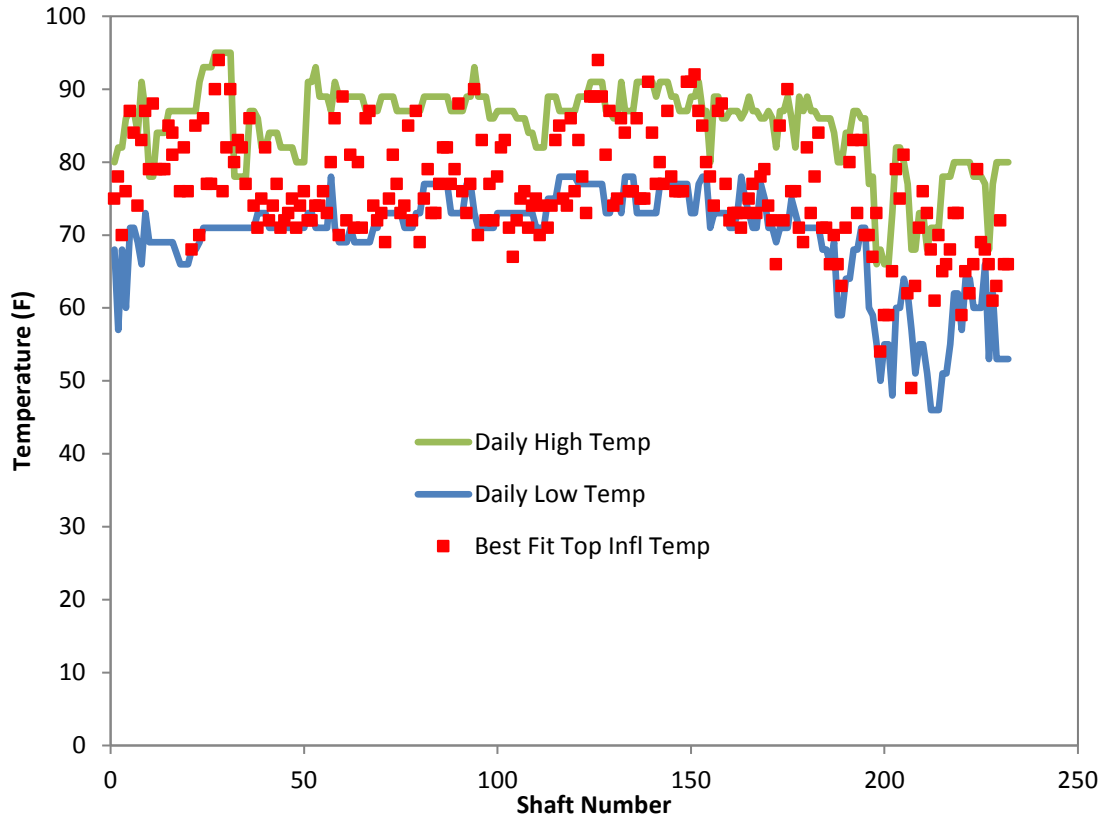


Figure 3.13. Top of shaft inflection temperature along with max. and min. daily air temperature

One quick observation is that in warmer summer months, the inflection temperature more closely aligns with the lower daily air temperature and in winter months it aligns with the warmer daily air temperature. It should also be noted that the trend could also be affected by the regional deep soil temperature which was 73°F for that site. Recall, the deep soil temperature is a constant that reflects the average annual air temperature for the geographical region. A further extension of this evaluation could be performed which would look more closely at the exact time of testing relative to the recent air temperature history (e.g., within the previous 4 to 24hrs, etc.).

The best fit algorithm also varied the inflection depth to account for known or unknown variations in construction details (e.g. where the excavation stopped or where the top of concrete truly concluded after the pour); bleed water can cause a slight reduction in the effective top of shaft elevation. Figure 3.14 shows that bottom of shaft inflection depths were virtually always within 1ft of the actual measured/reported shaft tip but rarely above. An inflection point above the reported tip indicates a problematic shaft that could only be “best fit” with a physically unreasonable condition. This can occur where the shaft is drastically bullet shaped for example. Only five of the 232 shafts exhibited this condition.

Similarly, the top of shaft inflection depth consistently showed the hyperbolically fitted solution to inflect above the shaft (negative refers to a depth less than top of shaft). Future evaluation showed that the TOS and BOS inflection points move slight outside the shaft, increasing with

time. This is a numerical curve fitting artifact that accounts for the difference in diffusivity between the concrete and air or concrete and soil, respectively.

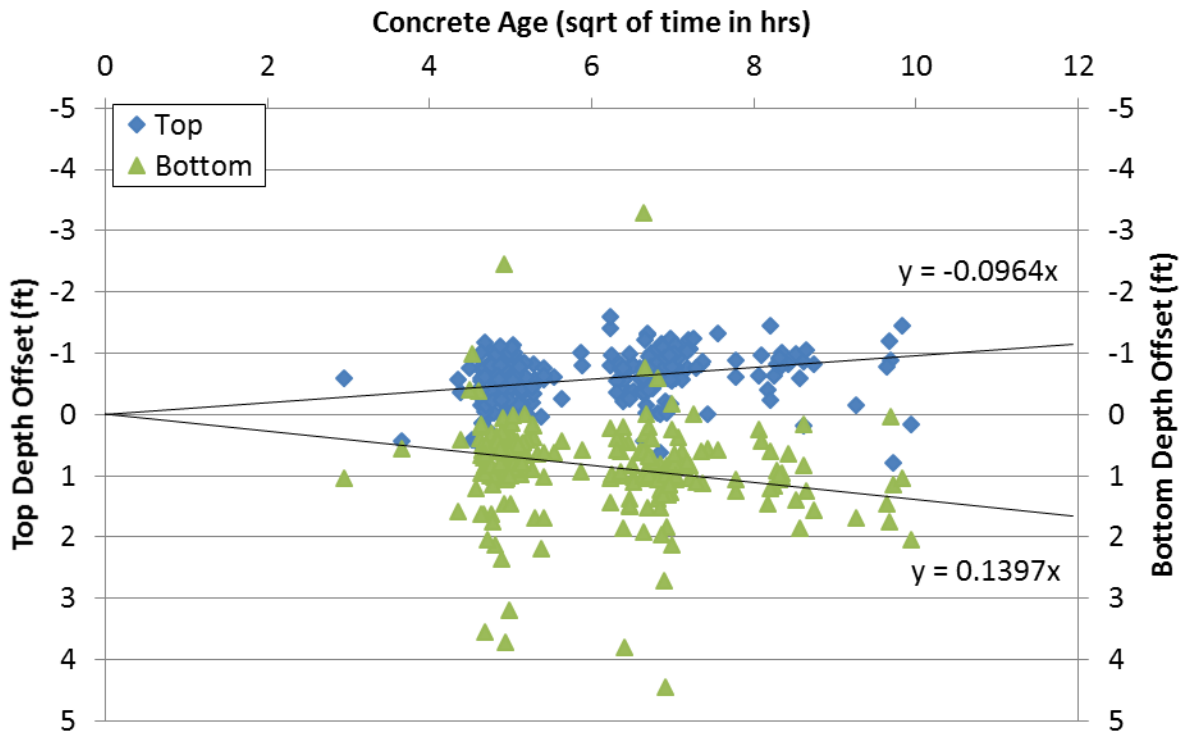


Figure 3.14. Hyperbolic inflection point offsets for top and bottom of shaft fits

### 3.3 Modeling for Time and Spatial Sensitivity of Measurements

A primary concern in translating TIP methods from drilled shafts to auger-cast piles is determining the best time and locations for taking measurements and performing analyses. To examine this, modeling was performed to identify the effects of shaft size on aspects related to TIP analysis methods.

Figure 3.15 shows the temperature versus time curves for various shaft diameters using drilled shaft concrete, while Figure 3.16 shows the same but for a typical ACIP grout mix. In all cases, the optimal time for testing any shaft is near the occurrence of peak temperatures, but testing is also acceptable for the period of time that the heat generation effects of concrete hydration are dominant. In large shafts this can be up to several days, but the window shrinks to only 1 - 2 days for 2 - 3ft shafts, the typical size range for auger-cast piles.

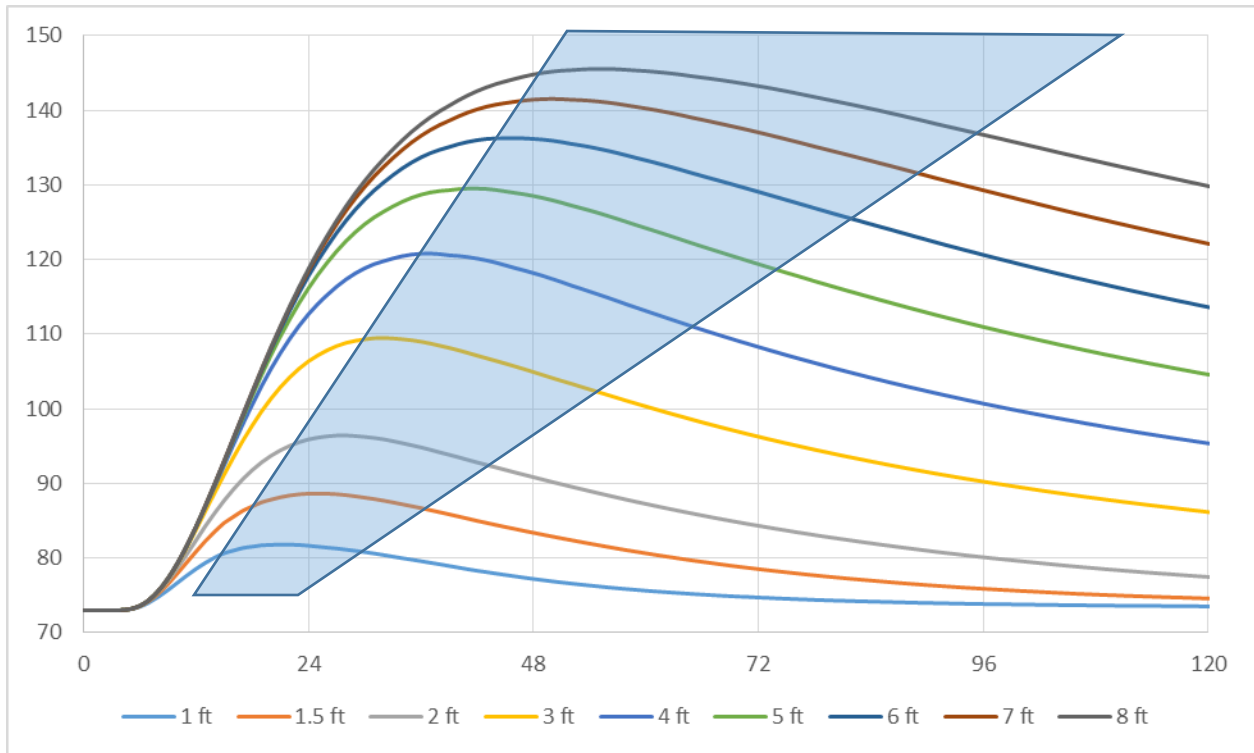


Figure 3.15. Optimum testing/analysis time for different size shafts with drilled shaft concrete

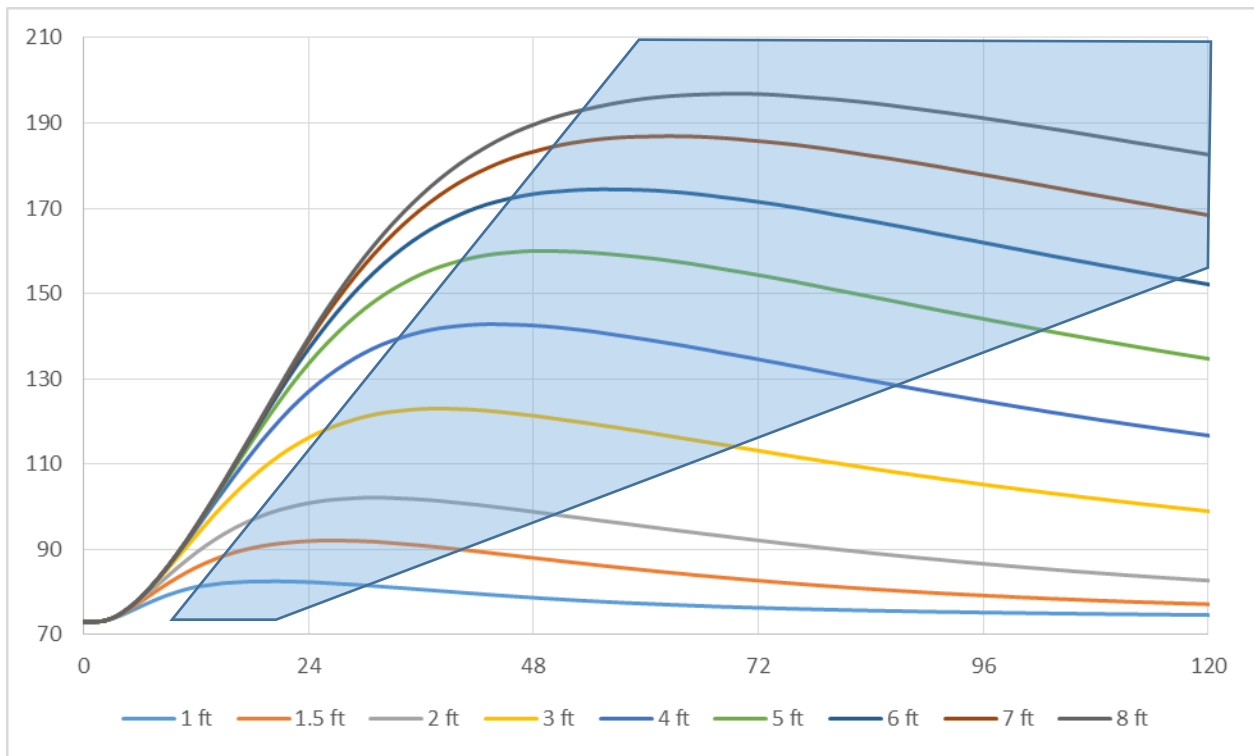


Figure 3.16. Optimum testing/analysis time for different size shafts with ACIP grout

Figure 3.17 shows the lateral temperature distribution for different size shafts, which reveals the acceptable positions for temperature measurements to be effective. For thermal integrity measurements to produce meaningful results, measured temperatures must correlate to a unique shaft diameter. In larger shafts (e.g., greater than 8ft), temperatures at the center of shaft approach adiabatic conditions and exhibit a plateau, rather than a peak, in the radial temperature distribution. In this region, large shafts will produce the same temperature regardless of variations in diameter, thus thermal integrity measurements here would be blind to edge of shaft anomalies. The ideal location for thermal integrity measurements in large shafts is near the edge of shaft, where temperature measurements yield a largely linear correlation with shaft diameter. This is conveniently available via cage attached measuring fixtures (tubes or wires). In smaller shafts, the entire cross section is acceptable for taking measurements.

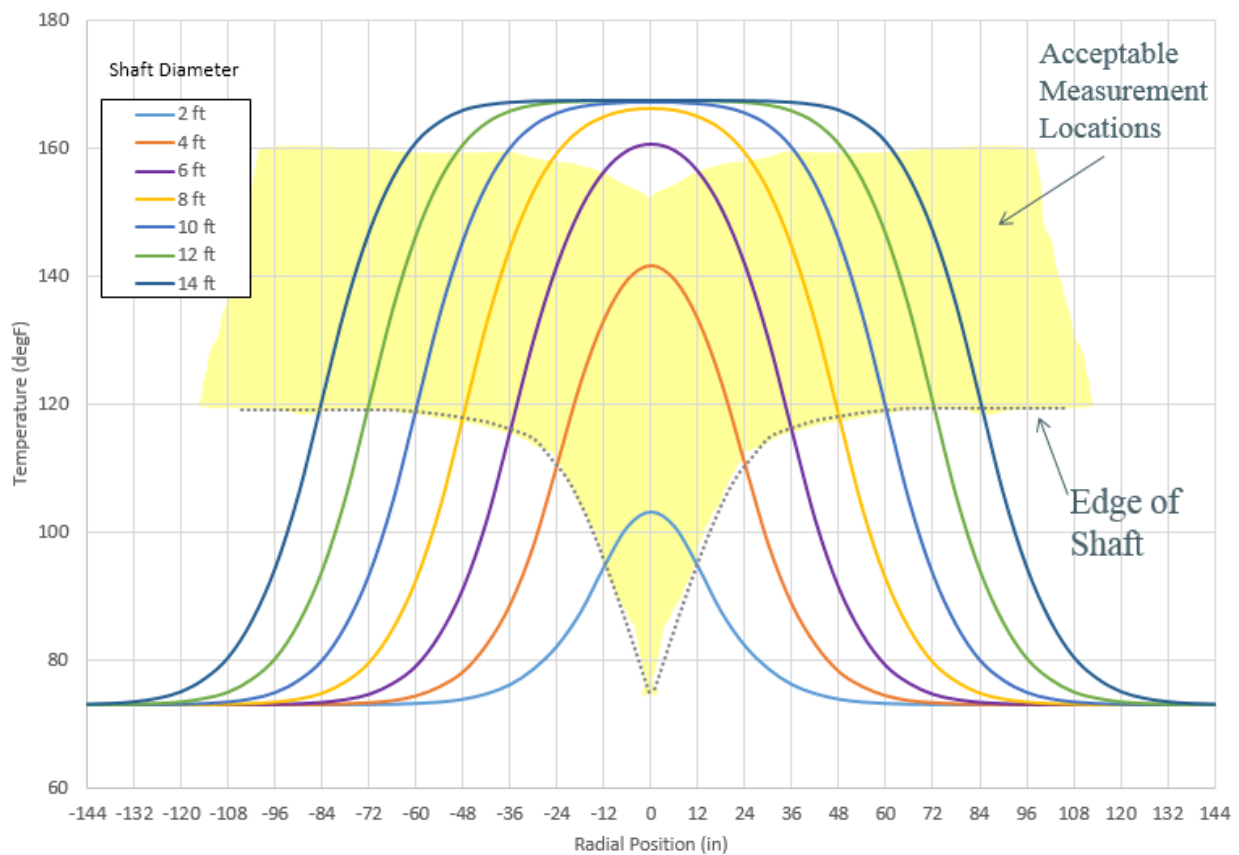


Figure 3.17. Acceptable measurement locations based on shaft size

Figure 3.17 shows the relationship between shaft radius, measurement location, and measured temperature. The shaded yellow region indicates the portions of curves that would be included in the analysis of auger-cast piles. The T-R curve for center of shaft measurements is represented by the black dashed line in Figure 3.18, which is also shown in Figure 3.19.

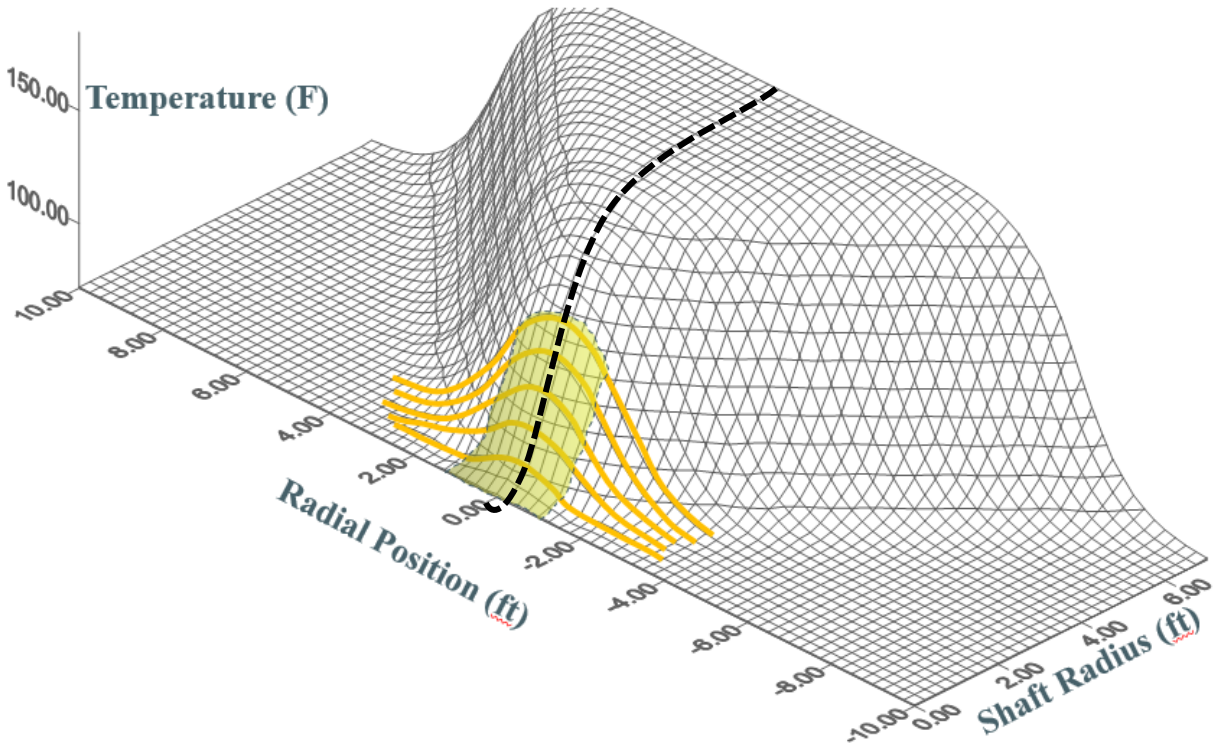


Figure 3.18. Temperature-radius relationship zone for ACIP piles

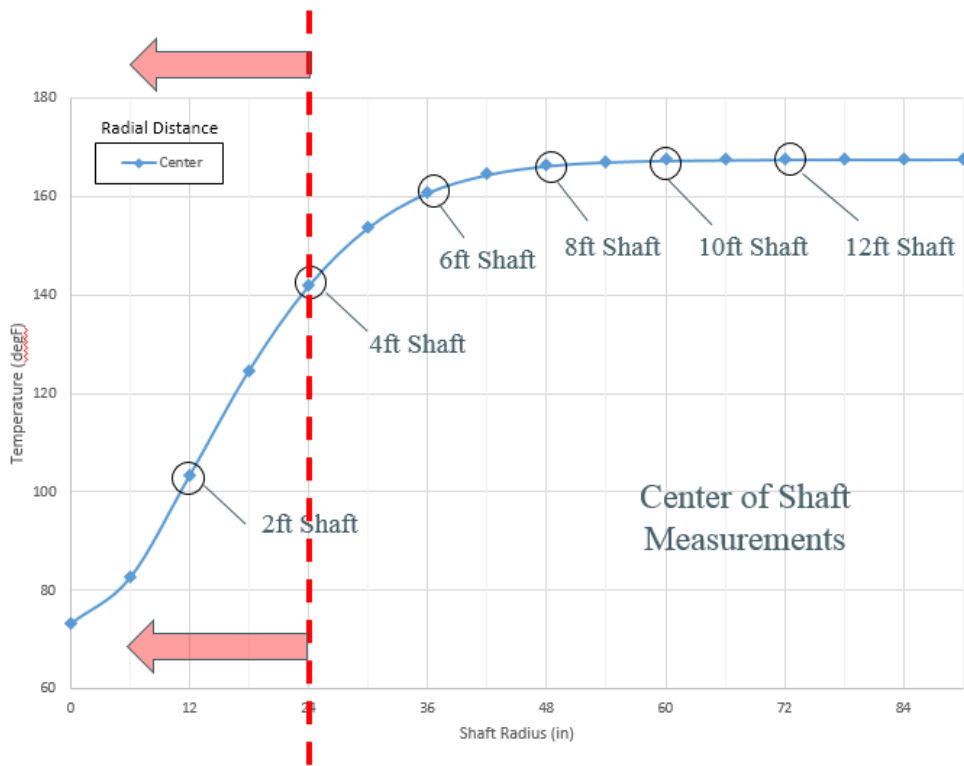


Figure 3.19. T-R curve for center of shaft measurements

To further investigate the ability of thermal measurements to detect anomalies in auger-cast piles, three different shaft sizes were modeled, with diameters of 4, 3, and 2ft, each with three different hemispherical edge anomalies, with diameters of 2, 6, and 10in (Figure 3.20). After generating model-predicted temperature profiles for each shaft, two cases of hypothetical locations for TIP measurements were examined – one case in which only a single center profile is measured (Figure 3.21), and one in which four profiles, equally spaced around the cage radius (assumed here to be 6in from edge of shaft), are measured (Figure 3.22).

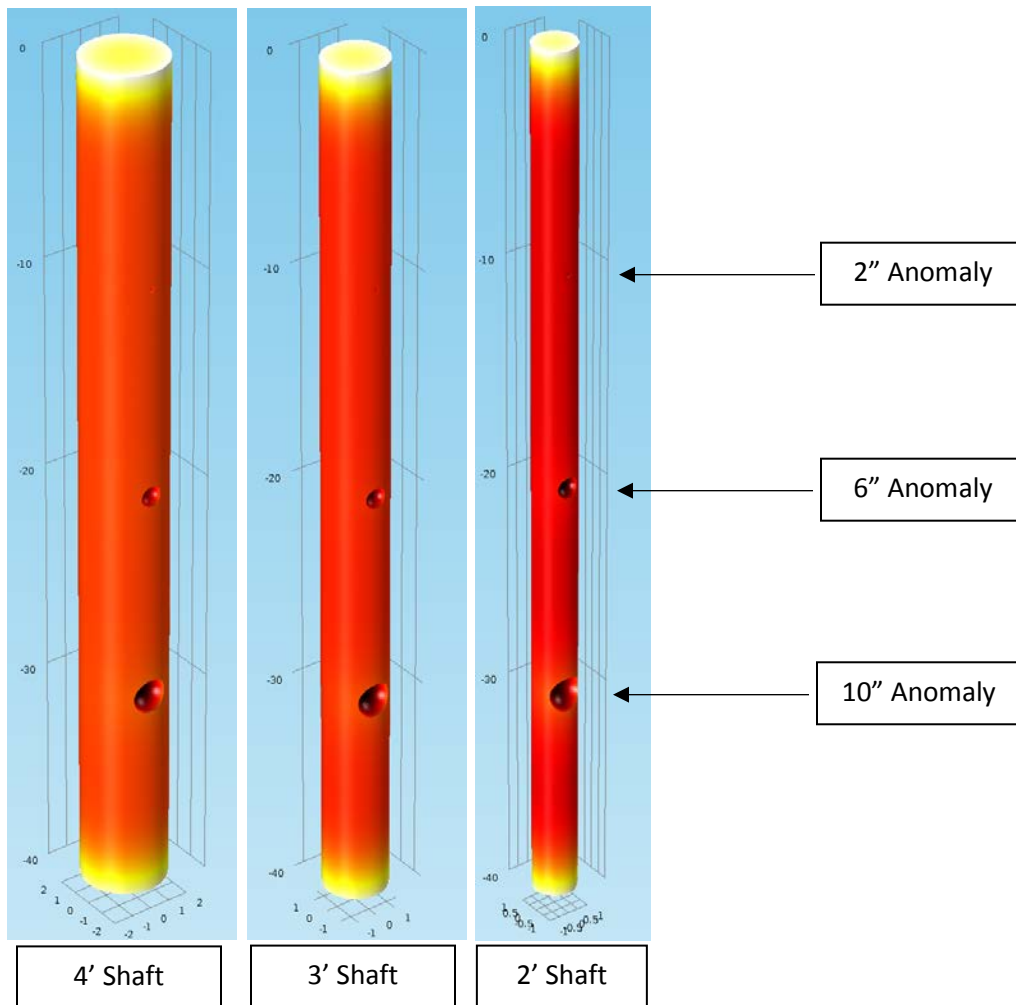


Figure 3.20. Computer-generated models for anomaly sensitivity

In Figure 3.21, it can be seen that the single center profile was unable to detect the 2in and 6in anomalies at all in the 4ft diameter shaft, and that the 10in anomaly had a virtually insignificant effect on the measured temperature. In both the 3ft and 2ft diameter shafts, the 10in anomaly was easily detected, and the 2in anomaly was not detected at all. The 6in anomaly had a moderate effect on the profile of the 2ft shaft, but an insignificant effect on that of the 3ft shaft.

Figure 3.22, on the other hand, shows that both the 10in and 6in anomalies are easily detected by at least one of the profiles within each of the three shafts. The 2in anomaly, however, is still

undetectable in all cases. Note that in Figure 3.22, each of the four profiles is shown, and the one nearest the anomalies exhibits the largest temperature variation. Also note that the 2in anomaly only accounts for a half ice cream scoop size loss of concrete which has no serious consequence.

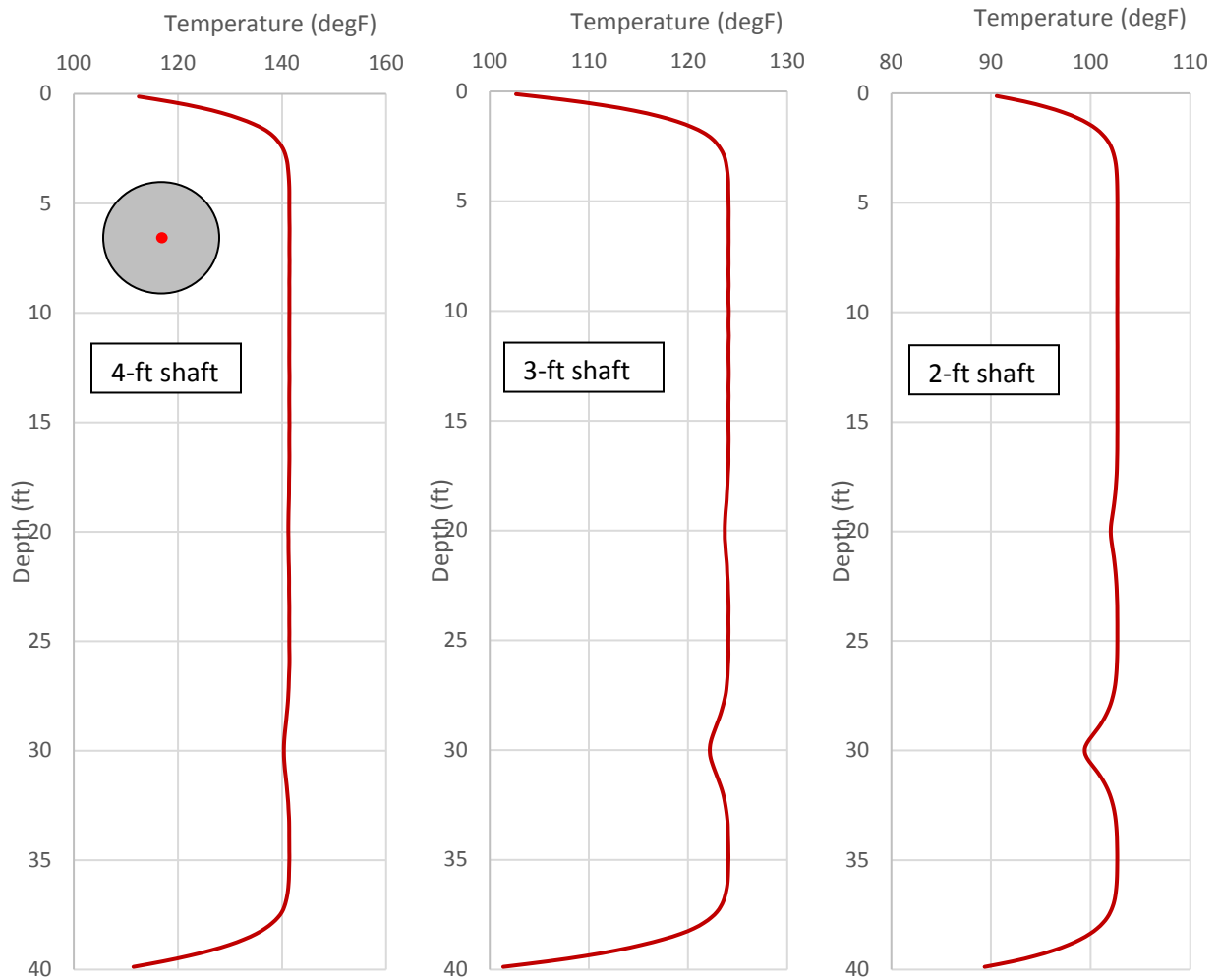


Figure 3.21. Model results for single centerline of shaft measurements

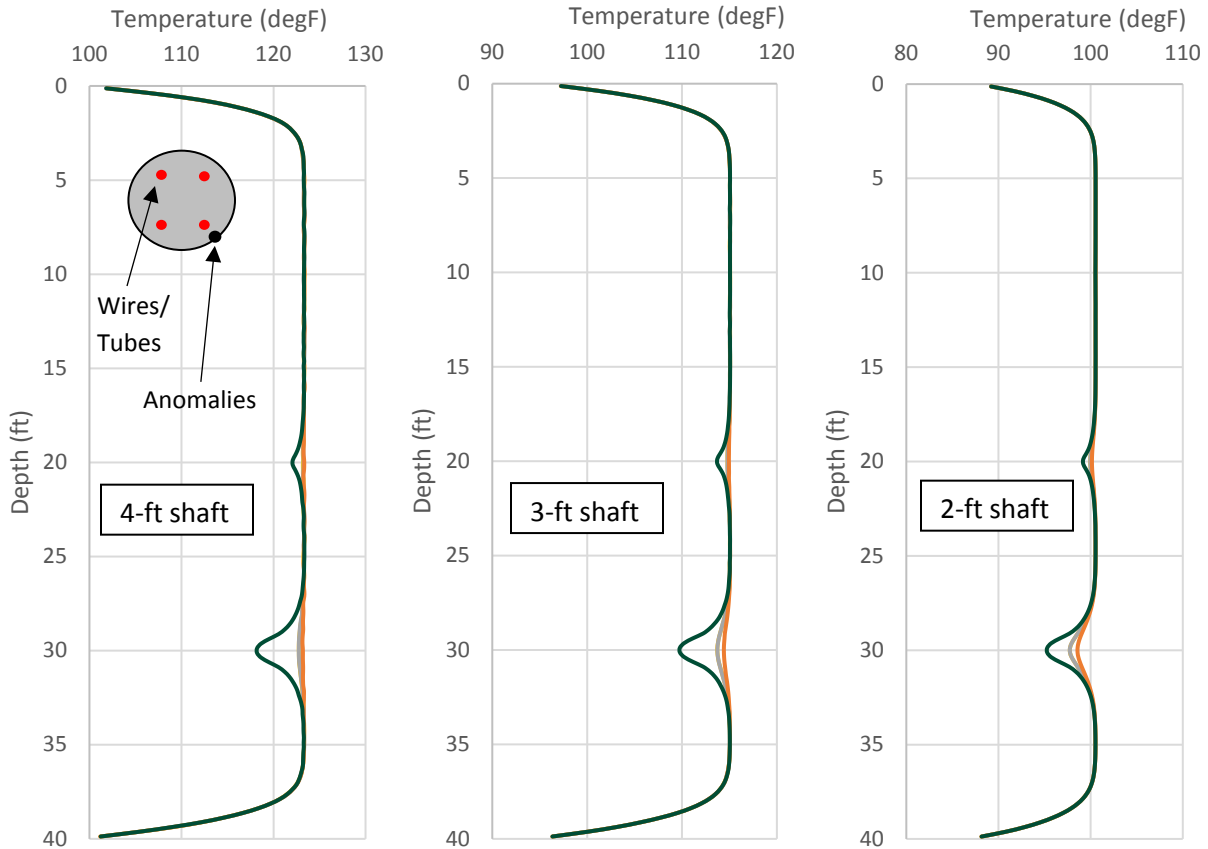


Figure 3.22. Model results for four perimeter measurements taken 6 in from edge of shaft

Figure 3.23 shows the same type of analysis, but for an 8ft diameter shaft, and with an additional 24in diameter anomaly (12in inclusion). These results show that centerline measurements have even less detection capabilities on large shafts, as even the additional 12in radius anomaly causes an almost negligible change in temperature at this location. With the four profiles measured around cage location, though, the 6, 10, and 24in anomalies are all detected. However, note that they are only detected by the one profile nearest to them, while the other three profiles are completely unaffected.

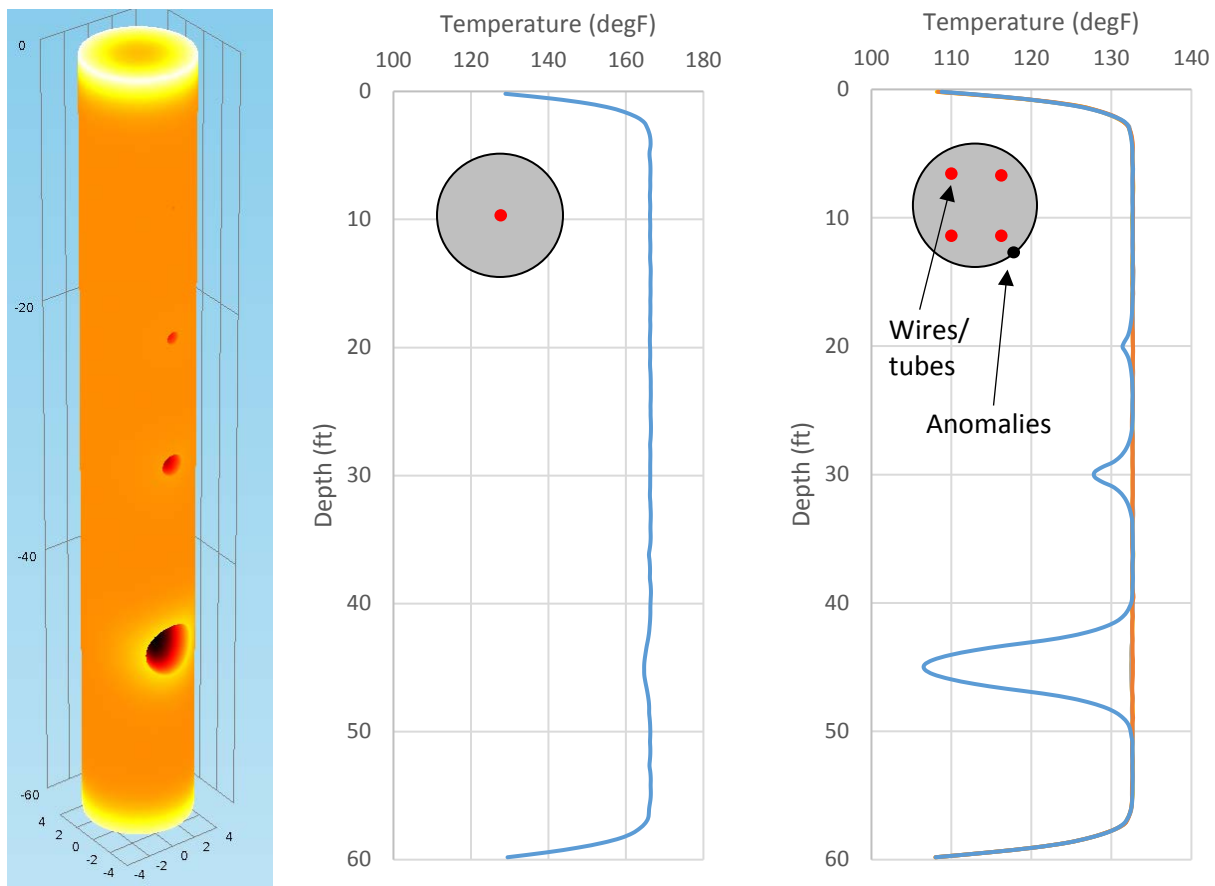


Figure 3.23. Center vs. perimeter measurements for 8 ft shaft with 2-, 6-, 10-, & 24-inch anomalies

Figures 3.24 – 3.26 show the effects of wire/tube misalignment. When only a single center profile is measured (Figure 3.24), the temperature profile for a straight shaft should appear as a straight line (except at the ends) representing the peak of the lateral temperature distribution. Any movement away from the center location will cause a decrease in the temperature profile, regardless of direction. However, without a complementary profile measured somewhere else in the cross-section for comparison, it is impossible to discern between wire/tube misalignment and actual variation in shaft size.

Using only two profiles, where profiles are located on opposing sides of center, the ability to distinguish between cage movement and diameter changes is greatly enhanced. The case illustrated in Figure 3.25 shows two profiles which experience cage movement in the direction parallel to the line between them. While one profile moves away from the center and measures colder temperatures, the other profile moves towards the center and records warmer temperatures. Because the lateral temperature distribution in this region of the cross-section is strongly linear, the variations in temperature between the two profiles is equal and opposite, and the average between the two is the same as the temperature profile that would be measured if no misalignment had occurred.

Figure 3.26 considers the case in which the same two profile system experiences cage movement in the direction perpendicular to the line between them. In this scenario the two profiles do not exhibit equal and opposite temperature variations, and distinction between cage movement and changes in shaft diameter are less discernable, as in the case of a single center measurement. The difference however is that the temperature variations that are experienced are less than those deviating from a centerline profile, and almost negligible when compared to a perfectly aligned two profile system. This was the by-product of the “12:00” position of the cage hitting the sidewall to the north preventing the temperature to reduce as much. Obviously, including two more profiles in the orthogonal direction would alleviate this completely.

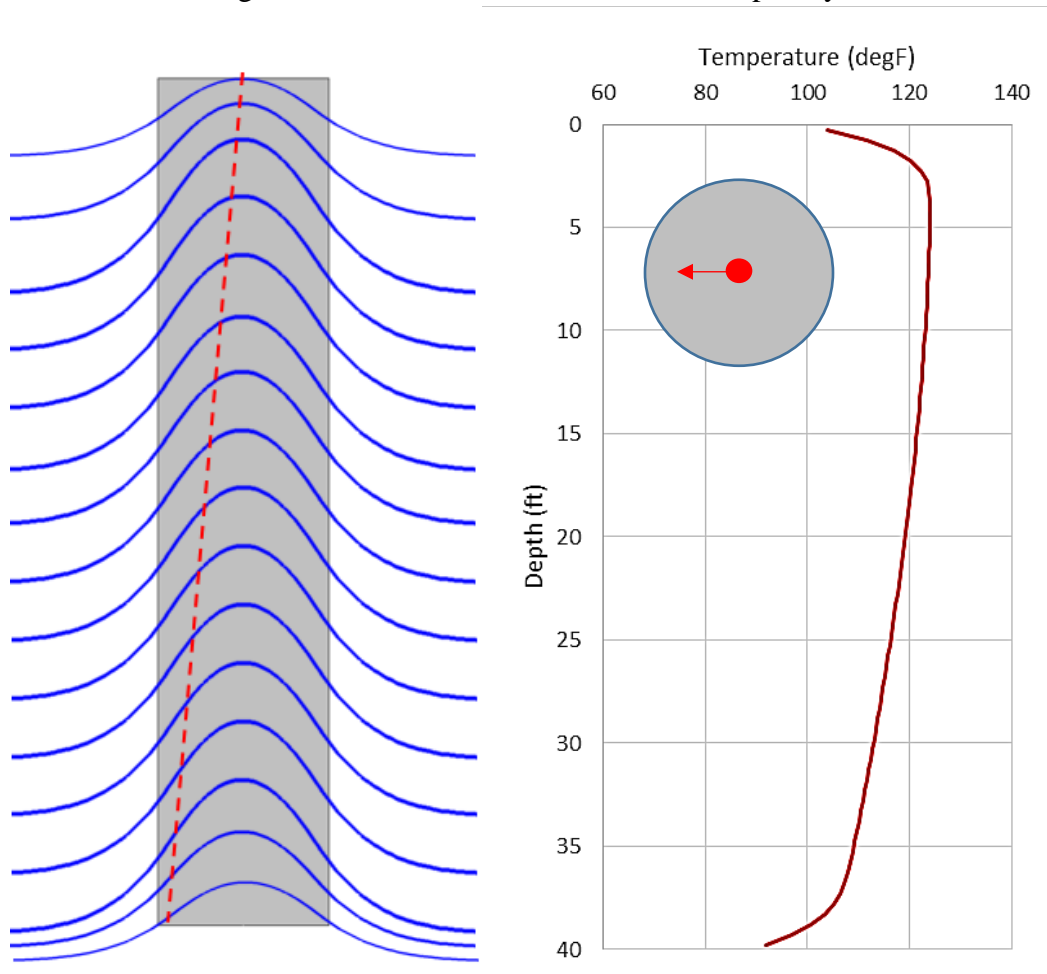


Figure 3.24. Effect of a misaligned single center measurement location

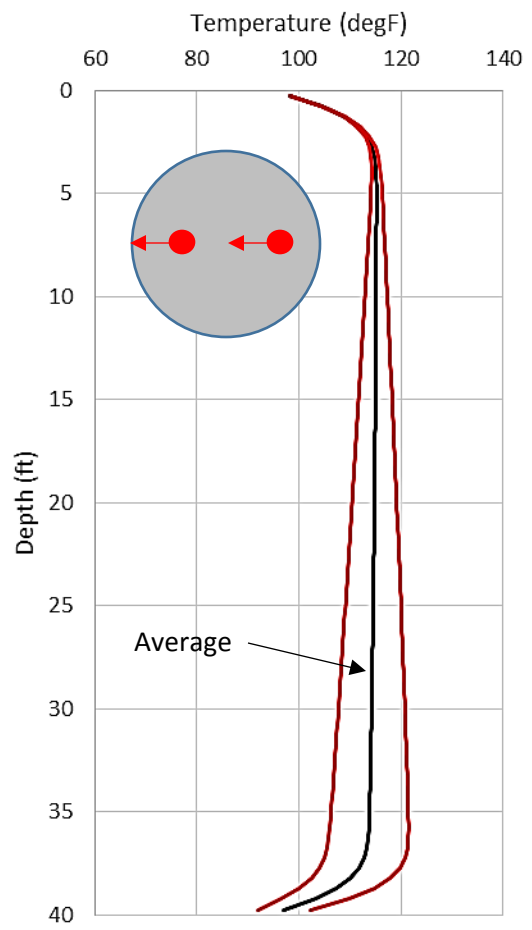
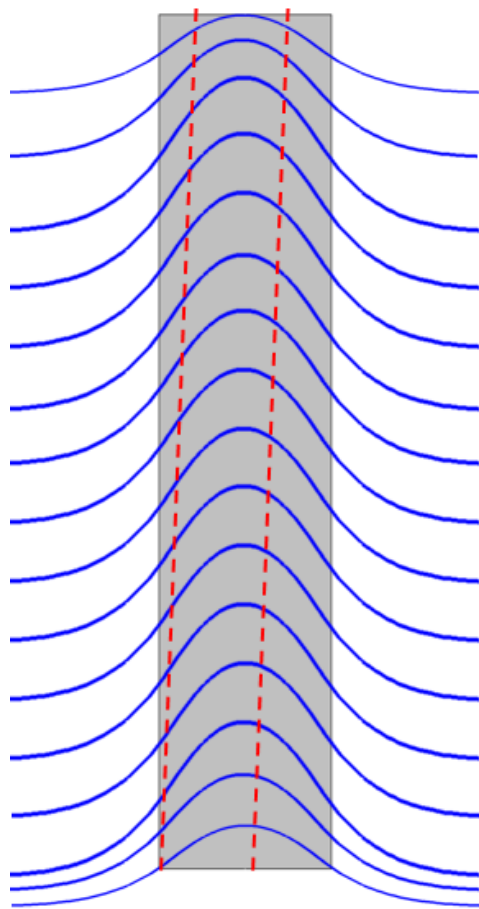


Figure 3.25. Effect of two measurement locations misaligned in the x-direction (per drawing)

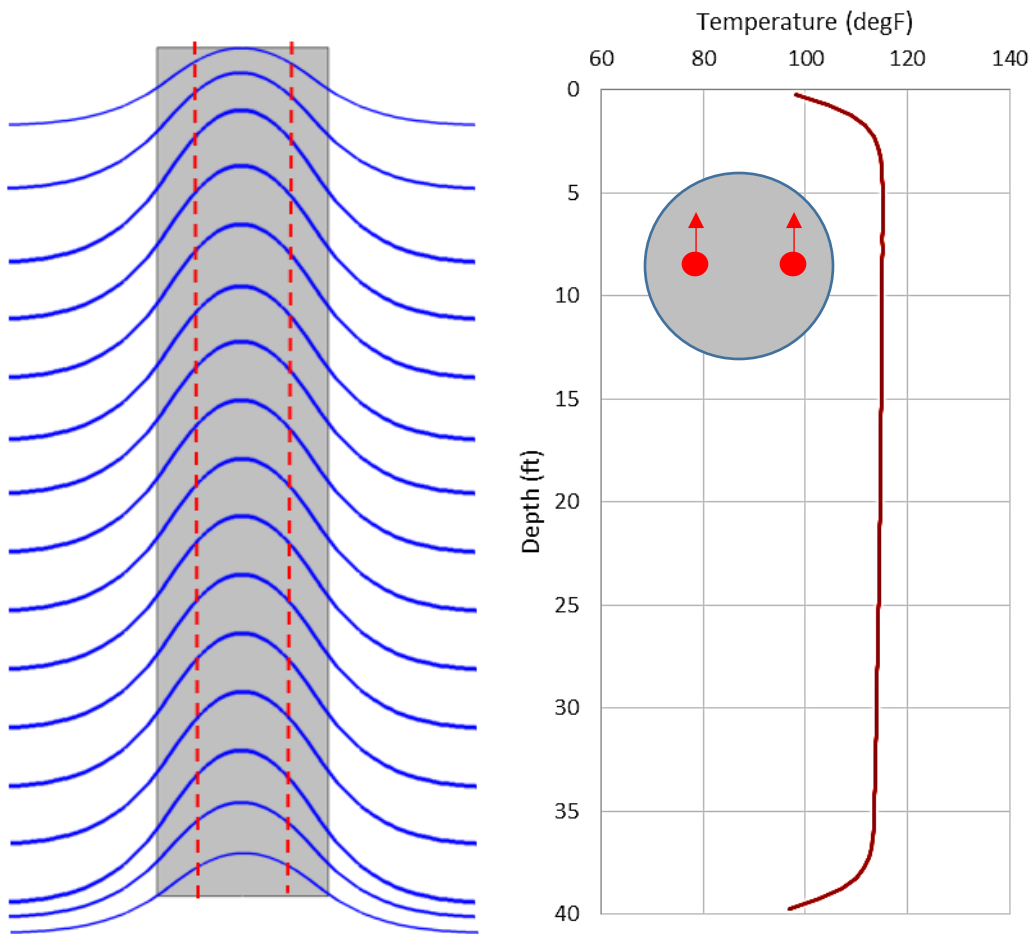


Figure 3.26. Effect of two measurement locations misaligned in the y-direction (per drawing)

### 3.4 Chapter Summary

Use of 3-D thermal dissipation modeling provides insights into how a wide range of variables might affect a measured temperature profile. This is a forward modeling type condition that was used to bolster the ability to perform inverse modeling whereby the shape of a constructed foundation element can be predicted from measurements. Modeling showed the following outcomes:

- The time of testing has virtually no effect of the computed effective shaft radius/shape. This finding, however, is limited to a reasonable timeframe that stays within the previously stated rule-of-thumb whereby testing/evaluation time should be performed within a 1 day per foot of shaft diameter upper limit, but after or very near peak temperature has occurred.

- Temperature to radius algorithms require several input parameters to correct for increased diffusion near the ends of the shaft which should be selected on the basis of reasonable limits. These parameters include:
  - Bottom of shaft elevation/depth (inflection depth)
  - Top of shaft elevation/depth (inflection point to air)
  - $\alpha$  values that are a function of time
  - Soil temperature which serves as  $T_{min}$  for the bottom of shaft hyperbolic tangent fit
  
- Bottom and Top shaft elevations were observed to be slightly outside the shafts increasing with time when compared to empirically observed data sets and best fit hyperbolic tangent solutions.
  
- The  $\alpha$  values can be estimated to be 0.4 times the square root of the hydration time in hours. While difficult to show with modeling, the hydration start time should consider any delays caused by retarders added to the concrete. Top of shaft  $\alpha$  values may be slightly higher to account for additional modes of heat transfer that include convection. This phenomenon is more pronounced in shafts that extend above ground via permanent casing or other similar means.
  
- The minimum temperature used in the bottom of shaft hyperbolic fit can be estimated using the average annual air temperature for that geographical region. In essence, long-term thermal dissipation has occurred wherein the temperature at depth has reached equilibrium with the past years or decades of seasonal temperature fluctuation. This is one of the strongest input parameters the user has at their disposal and should rarely be adjusted to be something other. In regions of volcanic/geothermal sources this value may be strongly influenced otherwise.
  
- While the ASTM standard for thermal profiling recommends using no fewer than four temperature profile locations positioned equidistance around the shaft perimeter, auger-cast piles have restricted cage volumes that may present problems when preparing the cage for subsequent testing. Use of two locations at 180° separation can show movement in one direction but not in the orthogonal direction. The concern is whether or not a misaligned cage with only one centrally located sensor could produce a false positive anomaly.
  
- Sensitivity analyses were performed to show what size of anomaly could be detected by a center bar sensor group (or tube). In short, a one-half tennis ball size anomaly on the outside of a shaft or auger-cast pile may not be detectable regardless of the wire or tube layout unless it coincided directly with or radial positioned at the measurement location (wire or tube). A half-soccer ball or half basketball sized anomaly was detected by four

wire (or tube) configurations in shafts or piles up to 4ft diameter and even with center locations up to 3ft.

Statistical evaluation of 232 previously tested shafts showed that the selection of the most appropriate  $\alpha$  value may vary between 0.29 and 0.51 times the square root of time in hours. This finding was in keeping with model findings and should serve as a limiting range in which future integrity evaluation is performed. Near perfect fits of all shafts were achieved, but when the fit requires unreasonable input parameters, the shaft had a flaw (deviation from normal).

## *Chapter Four: Feasibility of Probe-Based Inclination Measurements*

The present approach to cage alignment computations (for drilled shafts) is to compute the cage position relative to the edge of concrete where the local radius is calculated relative to the rest of the shaft. This limitation means that (1) the cage may be moving within a perfectly plumb excavation, (2) the cage is perfectly plumb and the excavation is moving away from the cage, or (3) a combination of both. To this end, this measurement affects acceptable tolerances for cage movement and concrete cover, but excavation deviations from vertical/plumb are difficult to assess below ground. Inclination of the access tubes (cage) is one way of differentiating cage movement from shaft movement, and so on. For single wire ACIP applications, it is impossible to precisely differentiate between temperature reduction caused by center bar movement and overall section loss (discussed in Chapter 3, Figure 3.24).

### **4.1 Past Case Studies**

Several cases have arisen where the suspected verticality of the cage or excavation was questioned. In one case the integrity access tubes were observed to have spun during casing removal. In those instances, a linked-rod inclinometer assembly was used to identify the severity of the as-built cage misalignment (Figure 4.1).



Figure 4.1. Groove-less casing with wheel-less inclinometer

Most inclinometers use specialized casing with internally scribed grooves in which a wheel-type accelerometer probe is lowered. These devices take relative measurements whereby the change in slope is equated to the progressive displacement away from a datum location (the top or bottom of the casing). If only one measurement is taken for the purposes of defining the as-built inclination of the casing, the absolute inclination (not relative) must be determined. Therefore, all

measurements must be performed twice (180 degrees apart) to remove the inherent equipment offsets. Wheel-less inclinometers are subject to the same errors. All data shown in Figures 4.2 and 4.3 used this analysis technique and the equipment shown in Figure 4.1.

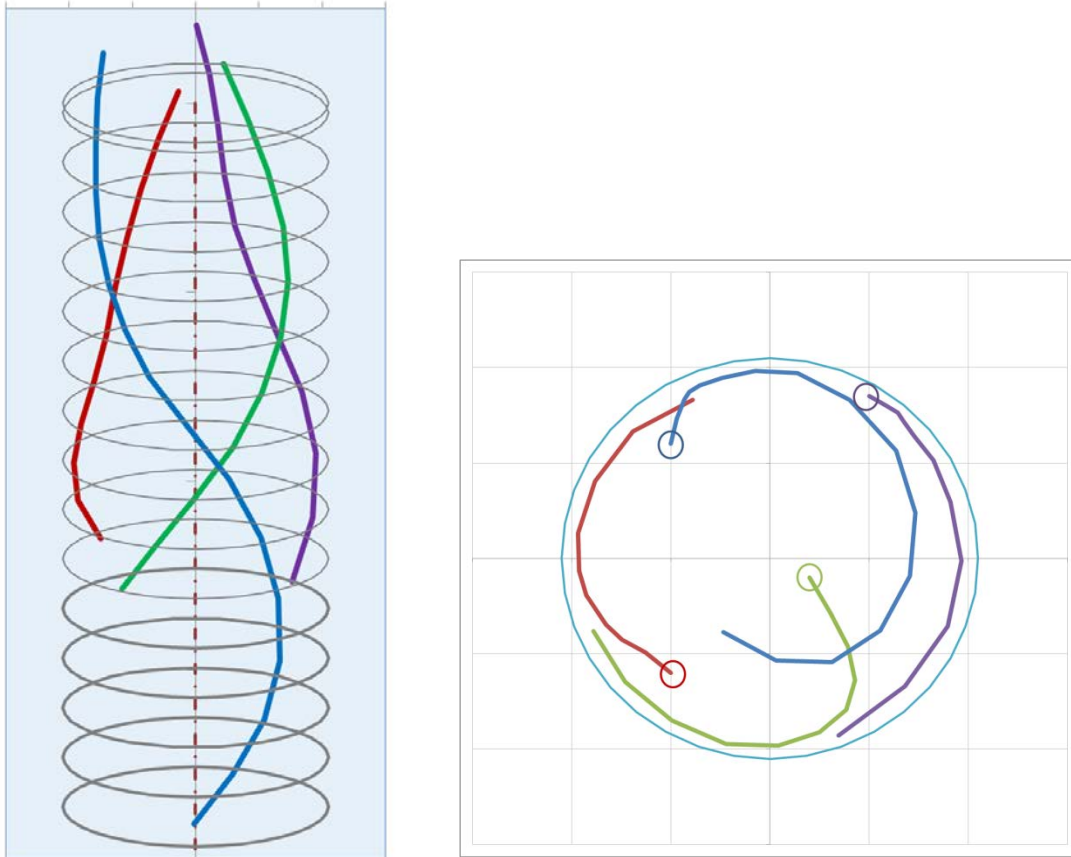


Figure 4.2. Defected shape of access tubes and cage distorted by casing removal (Crosstown Connector Project, Tampa, FL)

Thermal profiling of the shaft shown in Figure 4.2 could not be performed below the point where the access tubes were sheared or severely bent approximately 60ft down. One tube was tested to a deeper depth but still could not be fully tested to the bottom of shaft.

Figure 4.3 shows the results of both inclination and thermal profiling wherein the thermal results showed the cage sloping at a somewhat constant rate for most of the shaft length. Due to the length and inflexibility of the wheel-less inclinometer, couplings and drastic changes in tube linearity caused two of the tubes to restrict passage part way down. Inclination results corresponded well to the thermal predicted alignment.

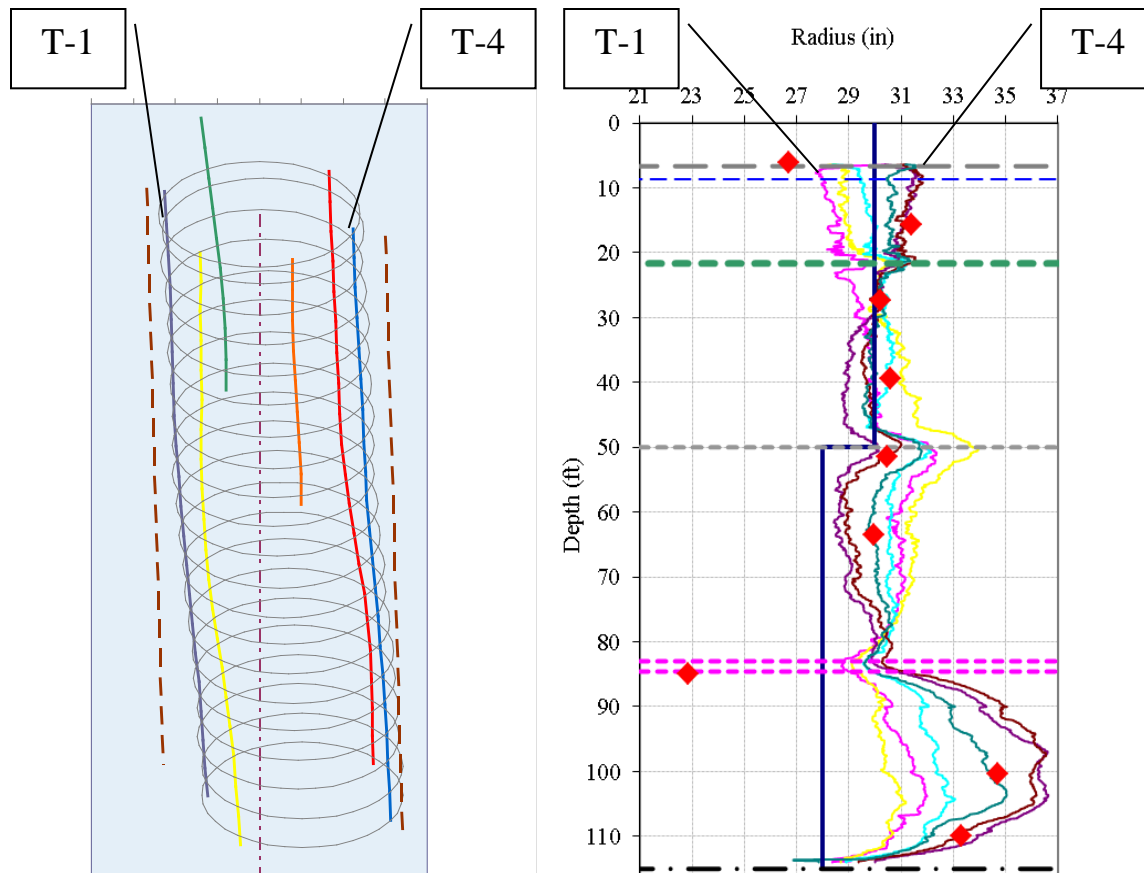


Figure 4.3. Inclined cage from inclinometer measurements (left) and thermal alignment measurements (right) (Jolley Bridge Project, Marco Island, FL)

Smart phone technology has raised the bar for accelerometer-based software (games, celestial applications, mapping programs, etc.). More recently, manufacturers have latched onto the capability/availability making the once extremely expensive drones affordable and now commonplace. Therein, multi-axis axial and rotational (gyroscopic) acceleration equipment is small (lightweight) and the associated computational algorithms are often incorporated as part of the purchase. Inclinometers of all kinds may benefit from these advances. It is conceivable that a probe lowered without alignment grooves and wheels or without linked rods could incorporate three-dimensional (orthogonal) accelerometers as well as three-axis rotational acceleration measurements or gyroscopic devices. In concept, a probe equipped with these features could be lowered without a depth encoder, and the spacing between access tubes could be determined by relative movement between tubes. A thermal probe equipped with this information could track cage movement, tube spacing variations, and verify whether changes in measured temperature profiles are due to movement in the cage, excavation walls or both.

A simplified version of the above concept was implemented recently at the Choctawhatchee Bay Causeway Project (US331), where only two axial acceleration measurements were used to define the degree of inclination of settlement plate rods. Standard settlement plate details start with a 24in x 24in steel or wooden plate to which a series of 5ft rods (1in ID pipe) are attached as an

embankment is built. The rationale for use is to monitor vertical movement (settlement) as an increased embankment load is applied. The procedure dictates that periodic (e.g. daily) surveys of the top of rod are used as the measurement. Additional lengths of pipe are added as the embankment level rises and exceeds the already present pipes. Ideally, the pipes are coupled and the height re-surveyed and that the pipe segments remain vertical. Occasionally, however, the act of compacting the embankment around the settlement pipes causes a disproportional amount of compaction on one side resulting in a tilted settlement rod assembly (Figure 4.4).



Figure 4.4. Two of four settlement rods that exhibited excessive tilting

As the settlement pipes were too small to permit access from commercially available inclinometers like that shown in Figure 4.1, a miniature wheel-less version was fabricated from a three-axis accelerometer circuit board (Figure 4.5). The circuit board was epoxy sealed in the aluminum housing and secured into the end of a ½-in thin-walled PVC pipe with the X-axis direction aligned with the PVC manufacturer stenciling down one side of the pipe. The resulting device was ¾-in O.D. and 20ft long to fully define the inclination of the system throughout the 19ft embankment. Data cables were run inside the PVC pipe to the data collection system. Table 4.1 shows the specifications of the circuit board.

Table 4.1. DE-ACCM3D Tri-axis Accelerometer Specifications

Measurement range	$\pm 3\text{ g}$
Resolution	333mV/g
Sampling rate	500Hz
Communication	Analog
Power source	3.5 - 15V (regulated onboard to 3.3V)



Figure 4.5. Circuit board installed in PVC delivery rod

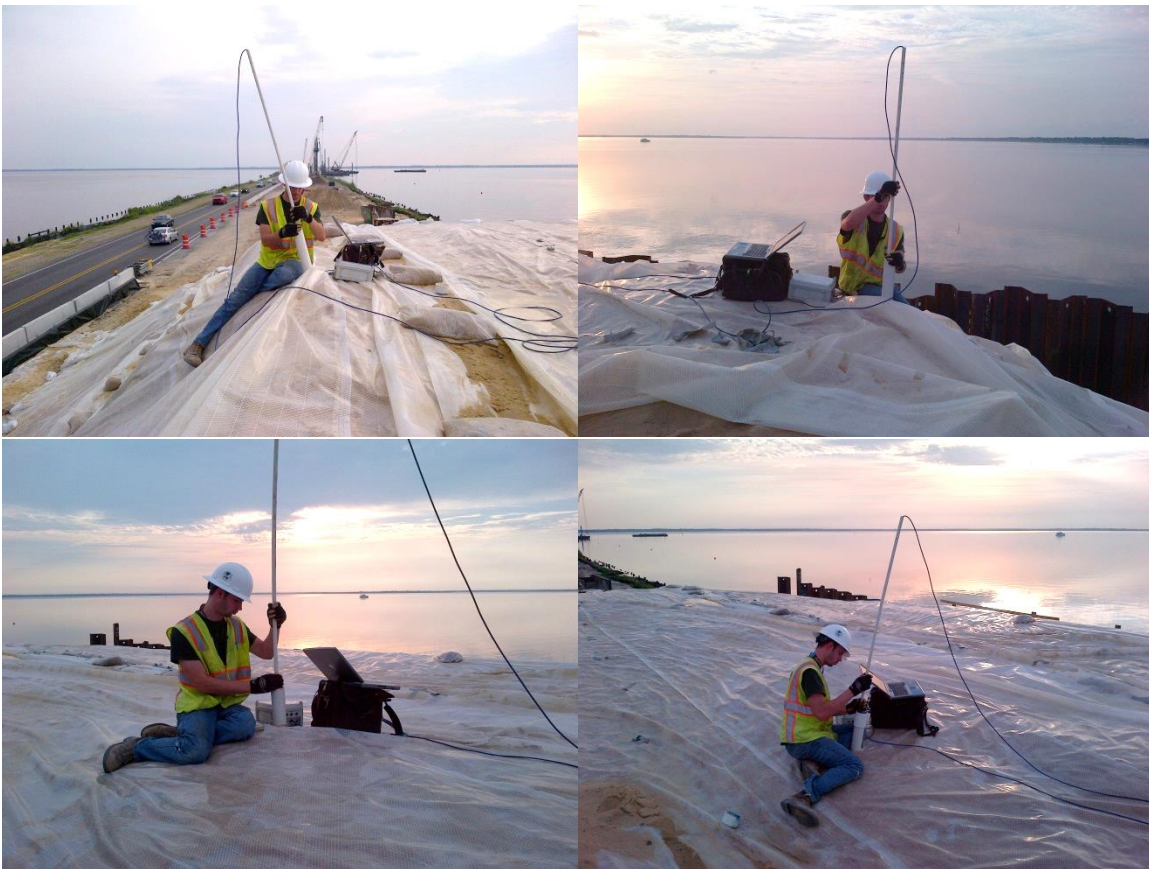


Figure 4.6. Inclination measurements taken from four settlement rods at various degrees of inclination severity

Data was collected at prescribed depth intervals of 1ft and used to determine the amount of lateral offset and vertical error that could be expected from that amount of progressively increasing tilt (Table 4.2). Figure 4.7 shows the simple data collection scheme from each of the three axes of inclination based on voltage measurements. As with the previously used linked system, measurements were replicated at 180 degrees to cancel out the effects of an electrical offset voltage.



Figure 4.7. Data collection from 3-axis accelerometer

Table 4.2. Top of settlement rod movement

Settlement Rod ID	Top of Settlement Rod Lateral Offset (ft)		Vertical error (in)
	Survey	Inclinometer	
1	0.58	0.56	0.14
2	2.32	2.10	1.06
3	1.36	1.40	0.61
4	2.41	3.00	3.32

## 4.2 Thermal Probe-Based Inclination Systems

Thermal integrity profiling equipment with the added features for inclination / lateral position measurements were reviewed as part of this study. This type of additional feature augments the lateral cage alignment predictions and helps to differentiate between a bent cage in a straight hole and a straight cage in an irregular shaft excavation. However, as this is a free probe based device, there are no wheels (typical of most inclinometers) or aligning lined rods. Rather, these device options use gyroscopic sensors in concert with conventional accelerometers to determine how much rotation has been imposed by the wire on the probe. The accelerometers detect the amount of tilt and the gyro detects the rotation/compass heading.

### 4.2.1 Basic System

For downhole navigation of vertical access tubes, with a free spinning probe as described above, a minimum of 3 degrees of freedom (DOF) must be measured – tilt about the two horizontal axes (X and Y), and rotation about the vertical axis (Z), which can be recorded by two accelerometers and one gyro, respectively. While only a three-DOF system is required for this application, sensors are commonly packaged together and marketed as six-DOF inertial measurement units (IMUs), which are widely used in applications like unmanned vehicle navigation. Since integrated units like this are readily available off-the-shelf, one was purchased and tested as a stand-alone system for its practicality in measuring vertical alignment of access tubes. A prototype TIP probe equipped with gyro is discussed later.

The IMU selected for this investigation was the LORD MicroStrain® 3DM-GX4® Attitude Heading Reference System (AHRS). This unit incorporates a tri-axial accelerometer and tri-axial gyroscope to make a six-DOF system, as well as a tri-axial magnetometer for global heading reference, and temperature and pressure sensors for compensation of thermal and altitude effects. It also houses an onboard A/D converter, so that all data is output as a digital signal, and signal conditioning circuitry special pre-computed outputs (e.g., roll, pitch, yaw angles). With all of this, the overall dimensions of the unit are still small enough to fit comfortably inside a 1.5-in access tube. The IMU is shown in Figure 4.8 and important features are outlined in Table 4.3. The full datasheet is provided in Appendix A.

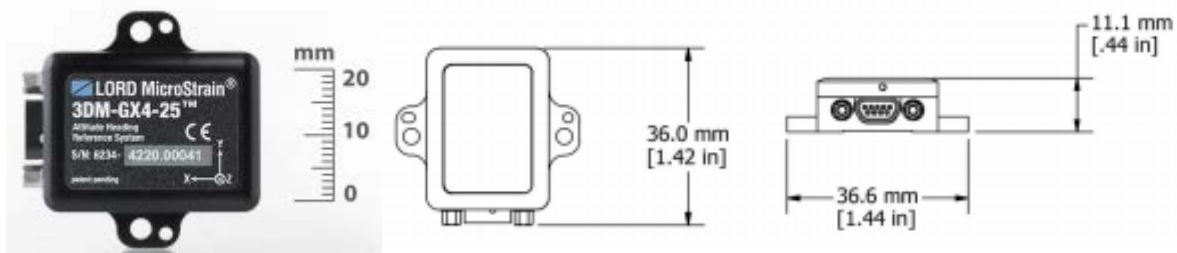


Figure 4.8. LORD MicroStrain® 3DM-GX4®

Table 4.3. LORD MicroStrain® 3DM-GX4® Specifications

	Accelerometer	Gyroscope
Measurement range	$\pm 5g$	300°/sec
Resolution	<0.1mg	<0.008°/sec
Sampling rate	4kHz	4kHz
Communication	USB 2.0	
Power source	+3.2 to +36Vdc	
Operating temperature	-40°F to +185°F	
Mechanical shock limit	500g (calibration unaffected) 1000g (bias may change) 5000g (unpowered survivability)	

As noted above, only two accelerometer axes and one gyroscope axis were needed for downhole navigation measurements. While the magnetic compass output could theoretically replace the gyroscope output and simplify the post-test analysis algorithms, the accuracy and reliability of such measurements would be greatly affected by the presence of steel access tubes and the steel reinforcing bars, so this was not considered a viable option. In the future though, it may be possible that this type of feature be used to obtain a rotational starting point for the gyroscope by beginning data collection outside of each tube, provided the proximity of steel is not enough to still hinder the magnetometer readings. This would be a luxury however, not a necessity.

#### 4.2.2 Probe-Based System

A complete prototype probe based system was provided by Pile Dynamics, Inc. (PDI) which incorporated an even smaller six-DOF IMU into a traditional TIP probe. The IMU used in this system was the InvenSense MPU-6000™ (Figure 4.9), which consists of a tri-axial accelerometer and tri-axial gyroscope. Specifications for this unit are given in Table 4.4 and the complete datasheet is also provided in Appendix A.



Figure 4.9. InvenSense MPU-6000™ (left), probe system (middle and right)

Table 4.4. InvenSense MPU-6000™ Specifications

	Accelerometer	Gyroscope
Measurement range	$\pm 2g$	250°/sec
Resolution	0.06mg	0.0076°/sec
Sampling rate	1kHz	8kHz
Communication	Serial (I <sup>2</sup> C or SPI)	
Power source	2.375 – 3.46Vdc	
Operating temperature	-40°F to +221°F	
Mechanical shock limit	10,000g for 0.2ms	

### 4.3 Thermal Gradient Method

Another conceivable way to detect the effects of wire spin is to measure the direction of the thermal gradient within the access tube with respect to the four orthogonal infrared sensors that make up a TIP probe. In an ideal shaft, the direction of this gradient should always point from the edge of shaft toward the center, thus providing a fixed reference from which the relative rotation of the probe can be determined. Figure 4.10 illustrates this concept, showing a relative probe rotation of about 45° counter-clockwise if the initial datum angle is taken as IR-1 pointing toward the center of shaft.

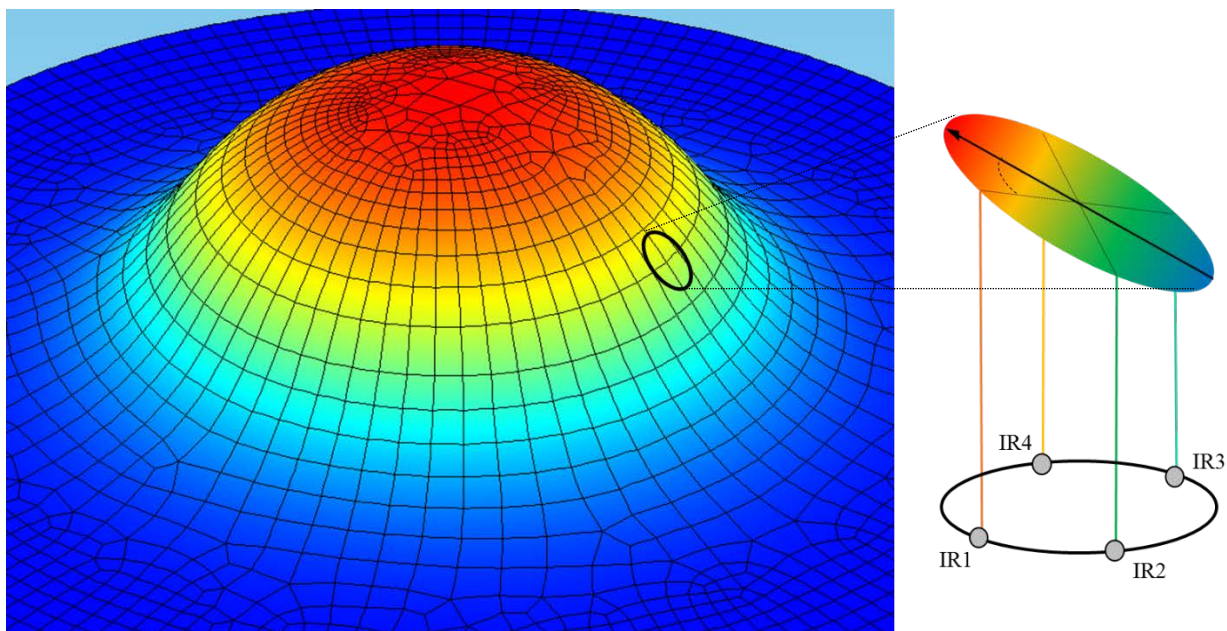


Figure 4.10. Probe rotation based on direction of thermal gradient with respect to probe infrared sensors

Figure 4.11 shows the rotation experienced by a probe during one run of a thermal test in a shaft. Since only three points are needed to define a plane, the direction of maximum temperature increase with respect to IR-1 was computed using sensors 1, 2, and 3. In this case, the probe

experienced a total of almost five full rotations over a depth of about 40ft. It is also interesting to note the horizontal jump in the curves that occur about once every rotation. This is likely due to a jerk-like rotation of the probe once it has built up enough stored energy to overcome the hump formed by the spiraled arrangement of the wires in the cable. The effect is less noticeable at depth because it is dampened by the available amount of elastic torsional energy over the length of the cable. For the same reason, a somewhat cyclic back-and-forth motion becomes noticeable with increased cable length.

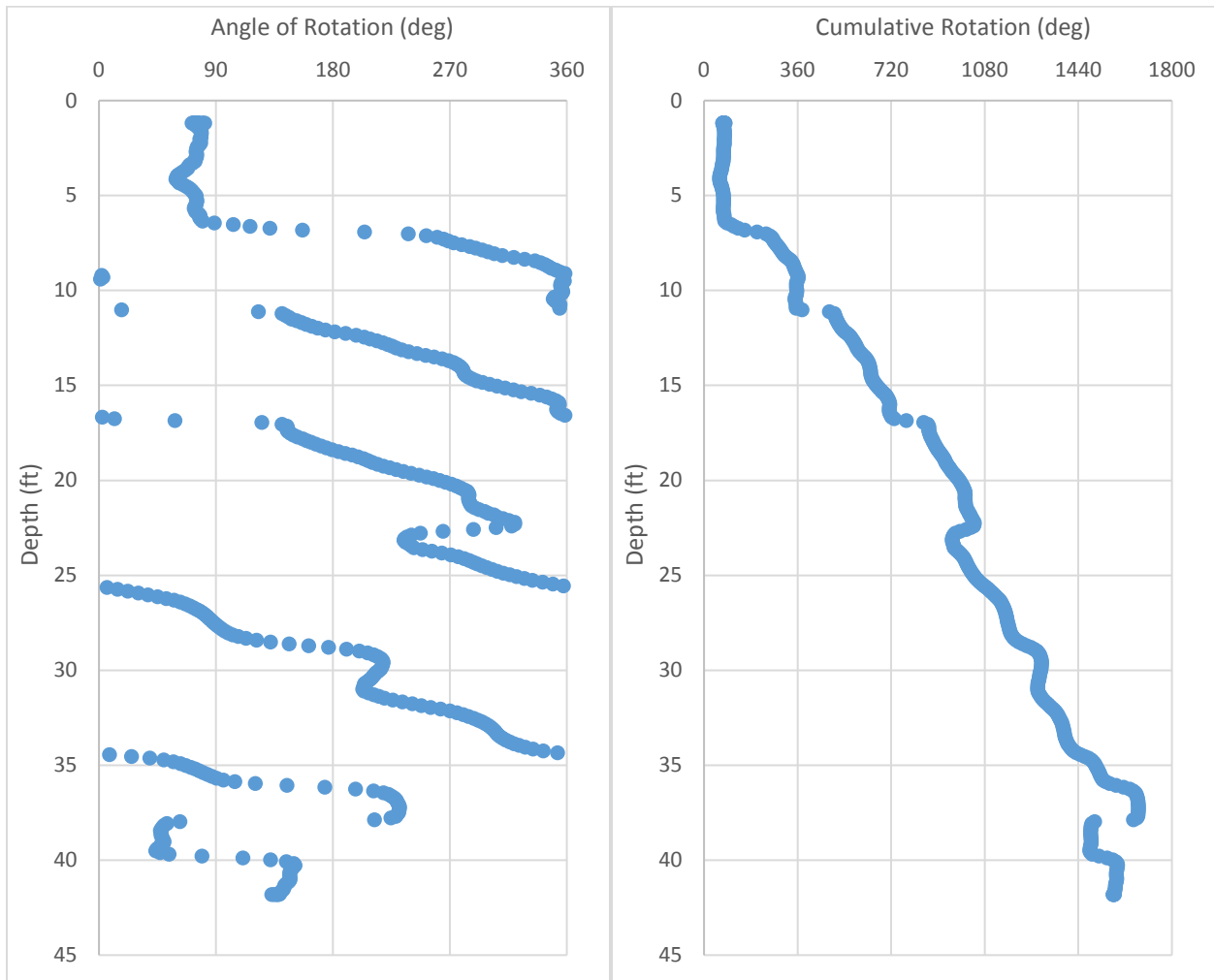


Figure 4.11. Computed probe rotation based on thermal gradient calculations during testing

While in theory this method could replace the need for a gyroscopic sensor to measure probe rotation, it would only be reliable under the assumption of a shaft with a perfect heat signature, which is not valid as soon as any anomaly is introduced. It is conceivable however that this concept, coupled with probe rotation and inclination provided by a gyroscope and accelerometers, could open the doors to a wealth of untapped information and analysis techniques for TIP data. One example would be the ability to indicate the location or direction of a localized anomaly based on the location of the tube and the direction of the thermal gradient. Another is the possibility of coupling exact cage coordinates with the magnitude and direction of

the thermal gradient to determine the distance to the edge of shaft (i.e. an alternative or supplementary method to traditional T-R conversions for determining effective radius).

Furthermore, in ACIP piles with only a single center line of measurements, the direction and magnitude of thermal gradient can be used to estimate the direction and distance of tube/bar eccentricity from center of pile. This will be discussed in the next Chapter where field data from four wires on a center bar were collected.

#### 4.4 Lab Testing of Inclination Systems

Three forms of testing were adopted to assess the feasibility of a wheel-less inclination system for thermal applications. These included probe rotation, wire spin / gradient, and 3-D position tracking tests.

Rotation Tracking. The two systems under review were subjected to rotational reliability experiments that induced a controlled amount and rate of rotation. The outputs from the probe-based devices were then compared to the known inputted motion to assess the stability of the rotation tracking methodology.

The controlled rotational movement was provided using a digitally controlled stepper motor system which required the stepper motor, a micro-step driver, and a programmable step motor controller (Figure 4.12 left to right, respectively). The programming feature allows the user to prescribe a rotational movement, rate and duration of test. Figure 4.13 shows the two systems attached to the programmable stepper motor system.



Figure 4.12. Stepper motor system components (Anaheim Automation, Anaheim, CA)



Figure 4.13. Gyro probe (left) and IMU (right) attached to stepper shaft assembly

A wide range of rotational rates and degrees of rotation were applied to both units. The probe based system (in its prototype state) could not maintain digital communication and would time-out after no more than 15 minutes and did not accurately account for the amount of rotation. Figure 4.14 shows the results of three trials. The first two spun approximately five revolutions in one direction and then back while the second spun 150 degrees and then back but at a faster rotational rate.

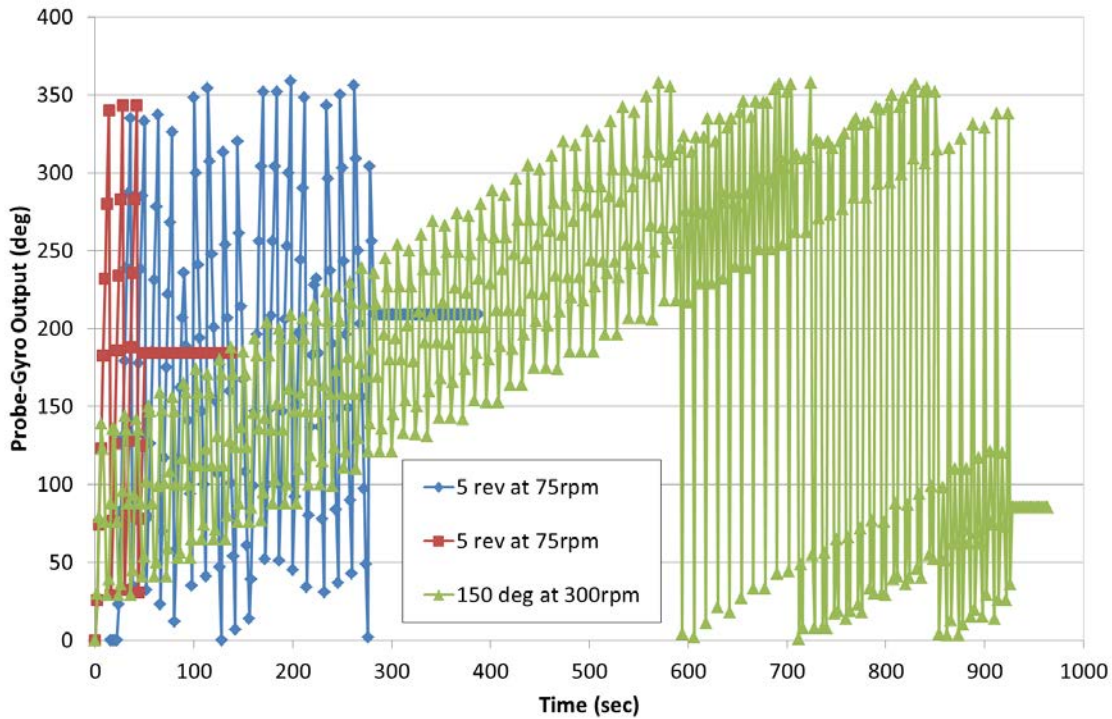


Figure 4.14. Rotational trials with probe-based gyro sensor

Due to the higher number of revolutions in the first two trials, drift in the computed azimuth ( $0^\circ$  to  $360^\circ$ ) could not be detected. The second set up (only  $150^\circ$ ) clearly showed a progressive offset (drift) over time. Note as the sensor output (after drift) crossed over  $360^\circ$  (at approximately 590 seconds of elapsed test time) the error was more pronounced as it jumped across the zero degree point. In the 15 minute test, the drift accumulated to almost a  $360^\circ$  error.

Correction of acceleration drift can often be accomplished by adjusting the zero offset such that the true zero acceleration results in no velocity drift. For the gyro (angular acceleration) data, the output has already been transformed to radial position and the sampling rate (2sec/sample) does not allow for this type of correction.

Similar testing was performed on the IMU unit to assess the validity of output signals for downhole navigation. Specifically, the angular rate output about the sensor x-axis and the gravity vector output of the other two axes were tested because these are the minimum necessary pieces of information for tracking downhole tube deformations. Ideally, data should be monitored and interpreted at high frequencies and stored and slower more reasonable sampling rates. The effect of sampling rate on integration is well known to affect the resultant velocity and displacement. However, balancing the needs of the interpretation algorithms with that of reasonable storage rates requires knowledge of the event duration and/or frequency of the event. Therein, slowly occurring movements can be sampled slowly and recorded slowly. Faster events require faster sampling. The spin of the thermal probe can be approximated by past observations like that shown in Figure 4.11. In that case, approximately  $1800^\circ$  of probe rotation were computed to occur over a 40ft descent. Typical descent rates for TIP measurements range from 0.3 to 0.5ft/sec making the average rotational velocity of the probe used to collect the Figure 4.11 data somewhere in the neighborhood of 13-22deg/sec.

Rotational tracking tests were performed at both high and low rates of angular motion as well as both fast and slow sampling frequencies. The results shown in Figures 4.15 – 4.19 show the differences in final computed values between each combination rotational speed and sampling rate for various types of motion about each axis. In all cases, the 100Hz sampling rate yielded undesirable errors, although slight at lower rotational rates. The 500Hz sampling rate also produced large errors at high rotational speeds, but was very accurate at lower speeds (those in line with typical free spinning probe motion).

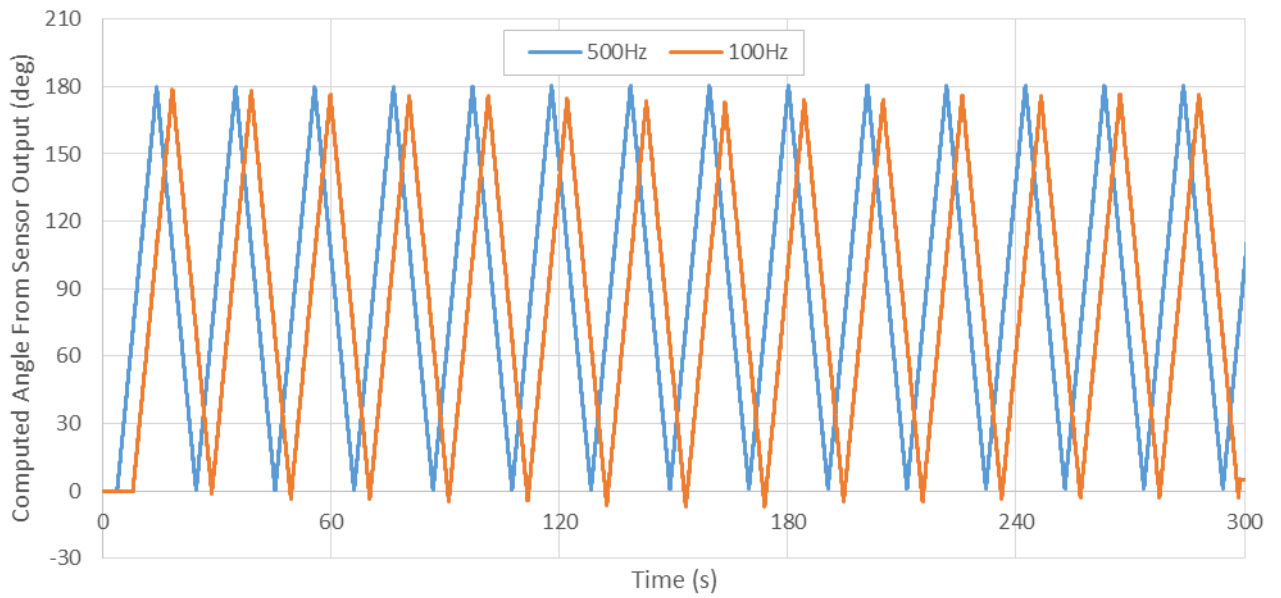


Figure 4.15. Rotational trials with IMU sensor – 180° oscillations at 17 deg/sec

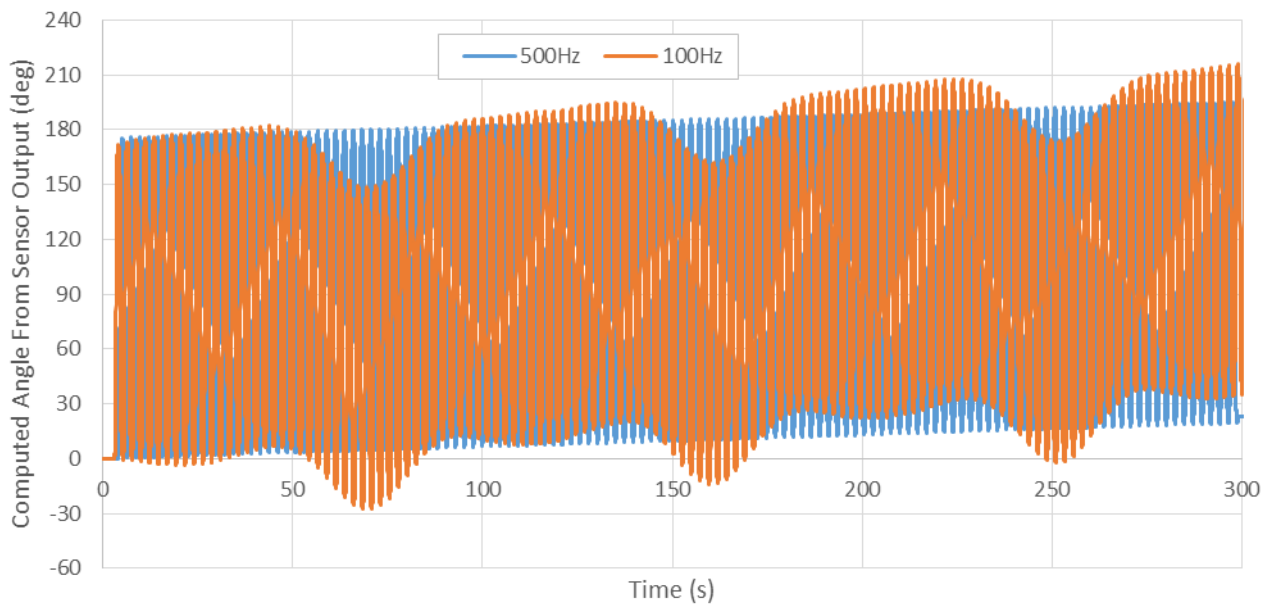


Figure 4.16. Rotational trials with IMU sensor – 180° oscillations at 450deg/sec

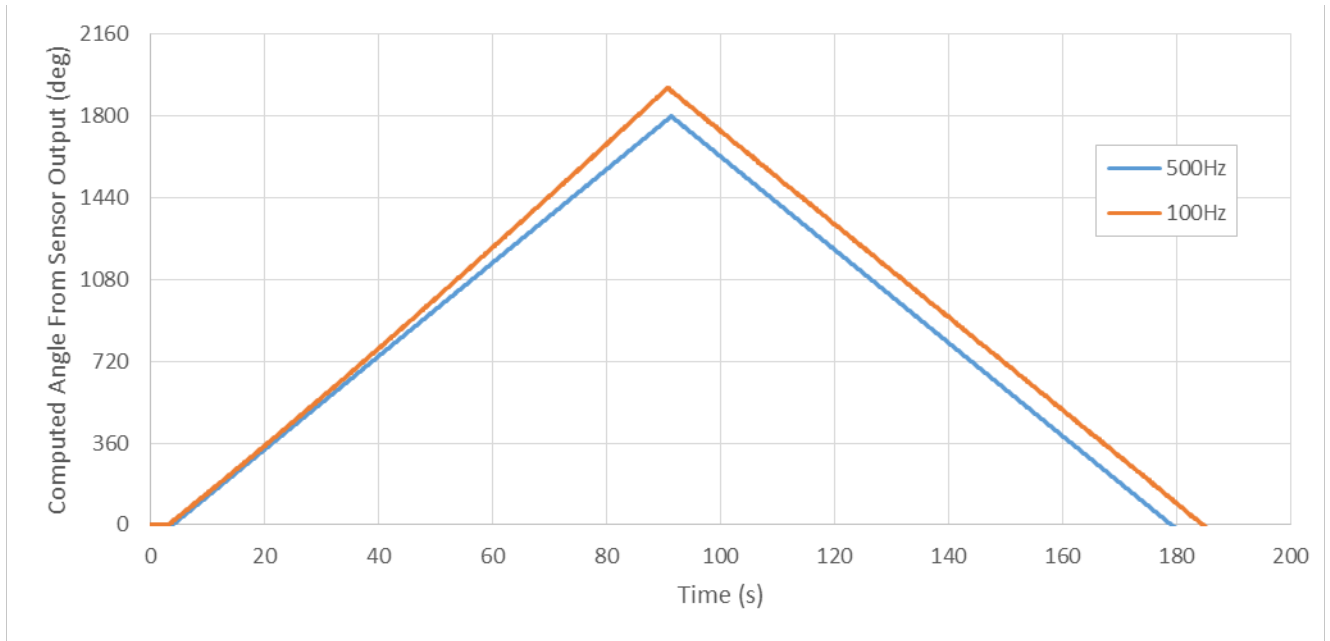


Figure 4.17. Rotational trials with IMU sensor – 5 revolutions CW then CCW at 20deg/sec

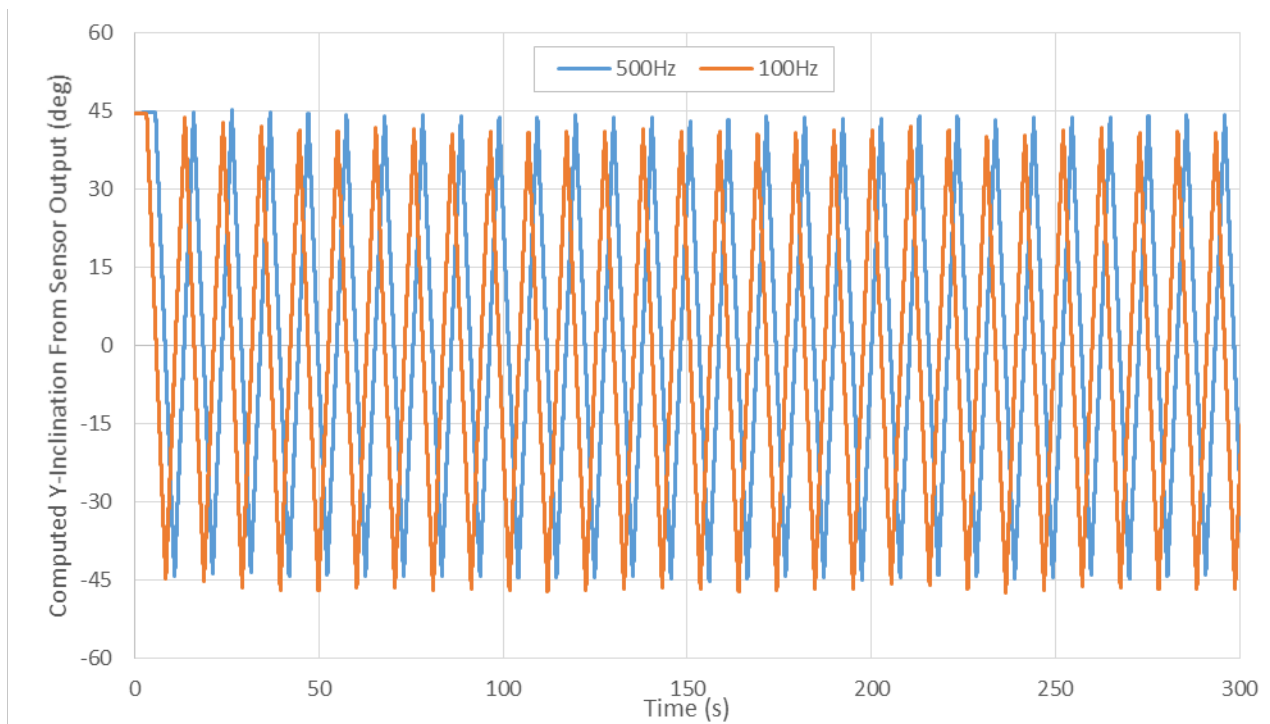


Figure 4.18. Inclination trials with IMU sensor – +/-45° oscillations at 17deg/sec

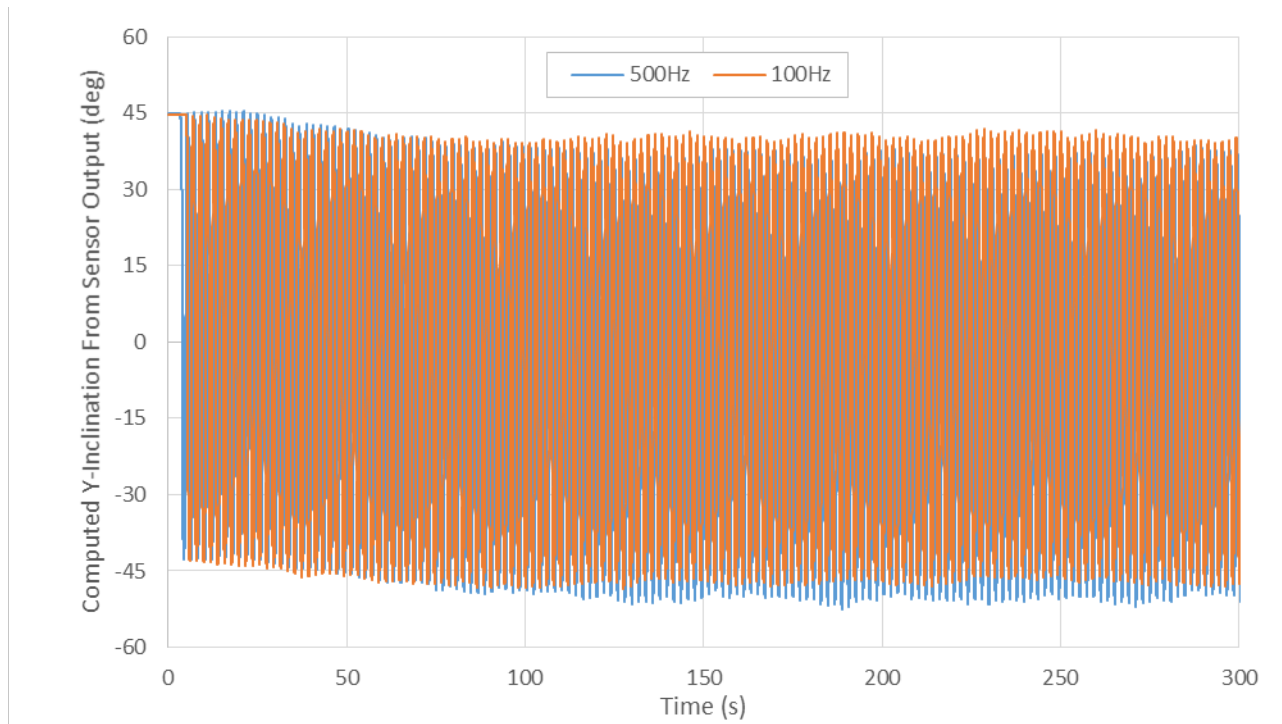


Figure 4.19. Inclination trials with IMU sensor –  $\pm 45^\circ$  oscillations at 450deg/sec

#### 4.4.1 Wire Spin / Gradient Monitoring

This series of tests highlights the capabilities of probe-based systems that incorporate multiple sensors directed in opposite directions. This type of analysis differs from rotational velocity or direction measurements in that the gradient is highly dependent on the normal radially decreasing temperature distribution. If the gradient vector is defined as the magnitude of the temperature to distance ratio and in the direction of increasing temperature, then the opposite direction allows points to cooler regions. In this way, the opposite gradient vector either points to the concrete soil interface or an anomaly. While Figure 4.11 showed the wire can and does rotate. This series of tests was designed to further define the algorithms with a constant gradient test setup.

A 30ft length of 1.5in ID SCH40 pipe was oriented vertically in indoor conditions (air conditioned 75°F) and a Frost King electric pipe heater strip was attached down the entire length excepting the top 2ft and only on one side (simulating the side of an access tube facing the center of shaft). In this test, a standard thermal probe was lowered into the standard sized tube while monitoring depth and all four infrared temperature sensors. Figure 4.20 shows the temperature measurements from each of the four infrared sensors alongside the computed angle of probe rotation per each three sensor combination.

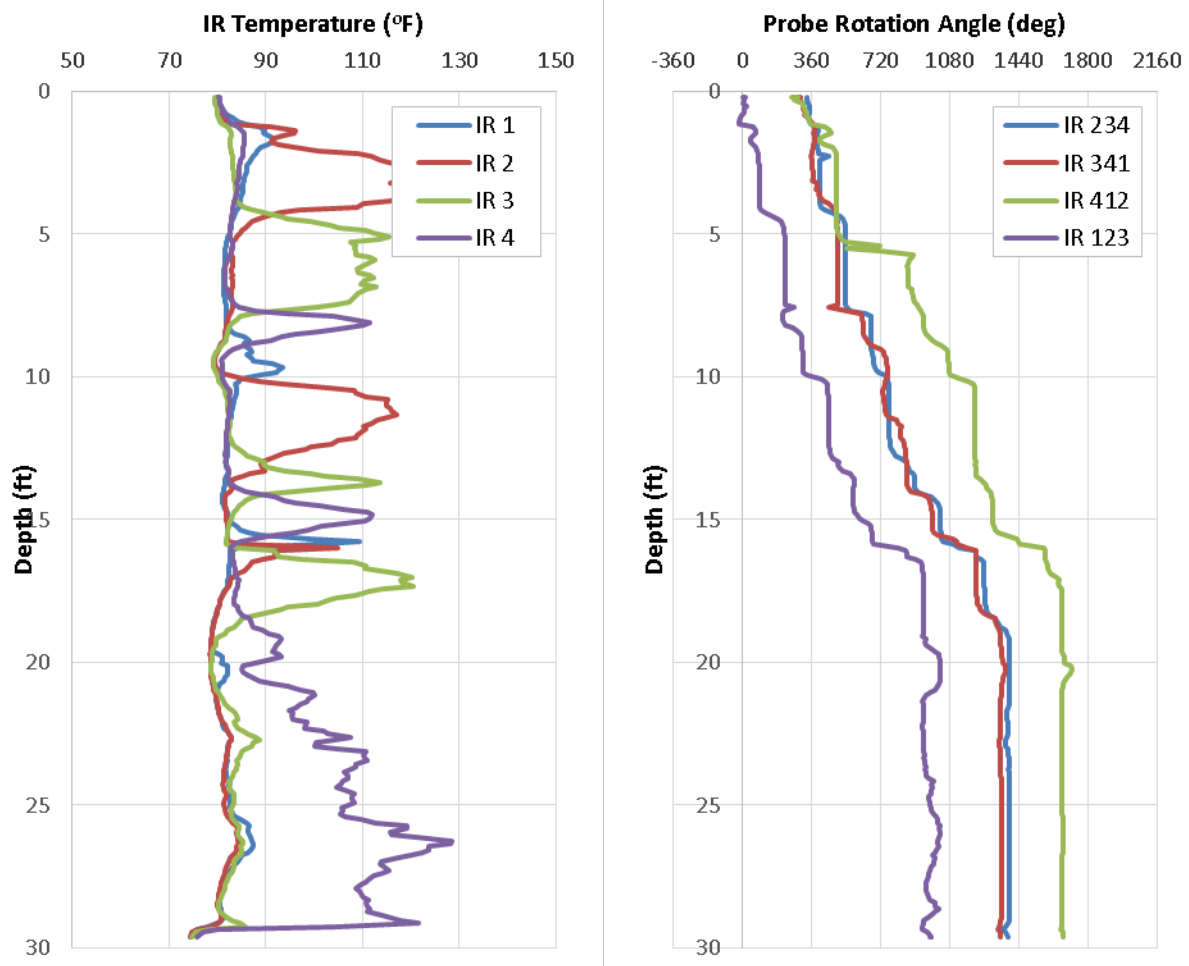


Figure 4.20. Temperature measurements from each IR sensor (left) and computed probe rotation based on thermal gradient from each three-sensor combination (right)

Immediately apparent from the results in Figure 4.20 is that each combination of IR sensors used to compute the gradient angle produces the same general pattern of probe rotation, but not identical. In this case, the most drastic discrepancies occur at the top of the run (0ft) and around 6ft deep. Closer investigation reveals that the reason for these discrepancies is a lack of a clear and distinct gradient to be determined when the IR sensor closest to the heat source is excluded from calculations. In this test setup, the heat strip was terminated about 2ft below the top of tube, therefore any thermal gradient computed above this point is virtually meaningless and theoretically non-existent (same basic temperature from all sensors). However, the slight variability in sensor outputs still allows for the computational algorithm to determine some gradient direction for each IR combination, albeit random and meaningless thus resulting in a discrepancy of starting angles from the beginning. At a depth of about 6ft, the IR-412 combination appears to compute a full revolution that the other combinations do not pick up. Again, closer examination of the individual IR measurements reveals that at this depth the probe was oriented such that IR-3 was closest to the heat source, thus combinations including IR-3 provide the most distinct thermal gradient calculation; but the IR-412 combination at that depth

became confused. This singularity-like phenomenon actually occurs at several points throughout the run, but the effects are only noticeably consequential when they result a full revolution ( $360^\circ$ ) of discrepancy. The temperature field around a normal tube in a shaft or pile is better defined by all sensors and not just one that registers a single warm strip.

#### **4.4.2 3-D Position Tracking**

Using the software and built-in algorithms provided by the IMU manufacturer, the position tracking capabilities of the sensor were tested by lowering it down 30ft of 1.5in SCH40 pipe with prescribed degrees of lateral deflection (Figure 4.21). To keep the x-axis of the sensor aligned and as parallel as possible with the direction of the tube at all times, it was housed in a specially fabricated probe body measuring 3.62in in length and 1.50in in diameter (actual ID of 1.5in pipe measured 1.59in). The probe is shown in Figure 4.22.

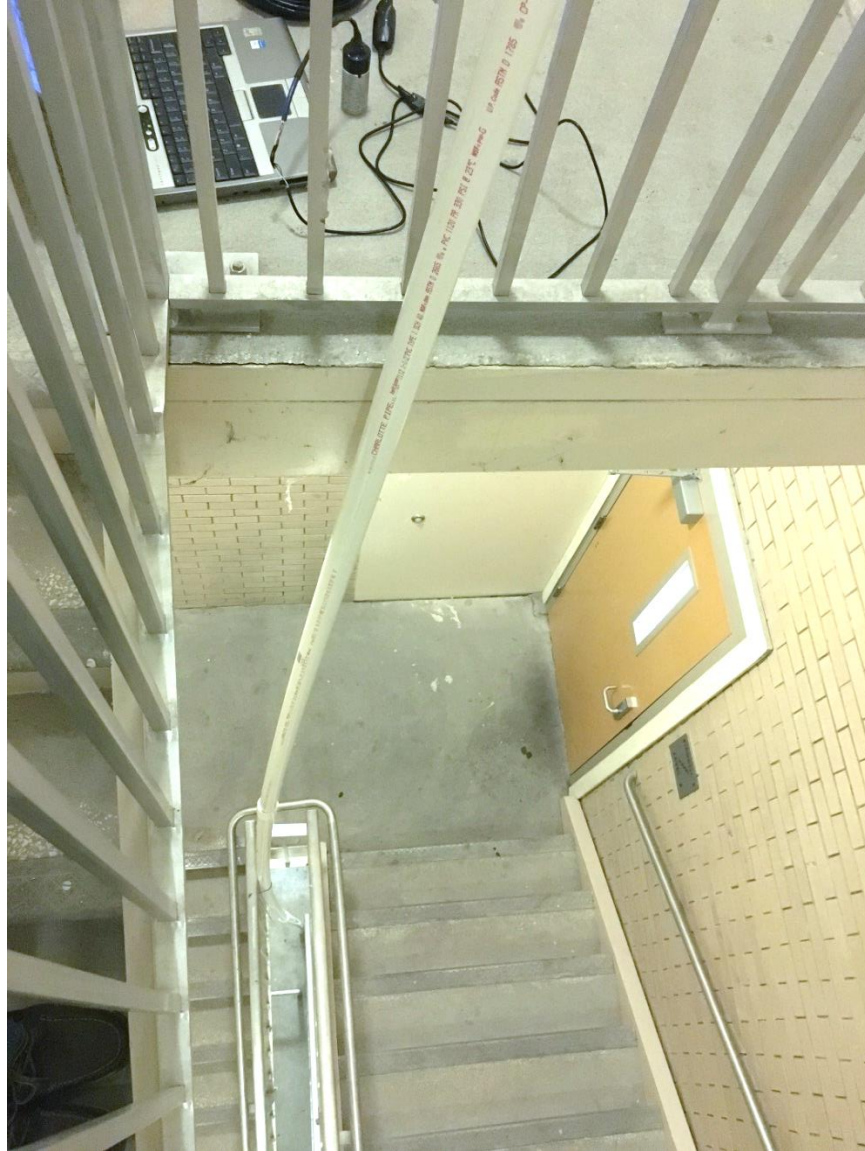


Figure 4.21. 30ft PVC pipe with prescribed lateral deflections



Figure 4.22. Aluminum probe body with housed IMU sensor

The IMU was then lowered into the pipe to determine the level of certainty to which the amount of lateral movement could be determined. Figures 4.23 and 4.24 show the measured versus actual deflection of the pipe in X-Z, Y-Z, and X-Y planes. Data was continuously collected at 500Hz through both the downward lowering and upward return paths of the probe. While the sensor was able to detect the general shape of the deformed pipe, the exact lateral deflection at any given depth was off by as much 4 inches. Multiple runs yielded similar results.

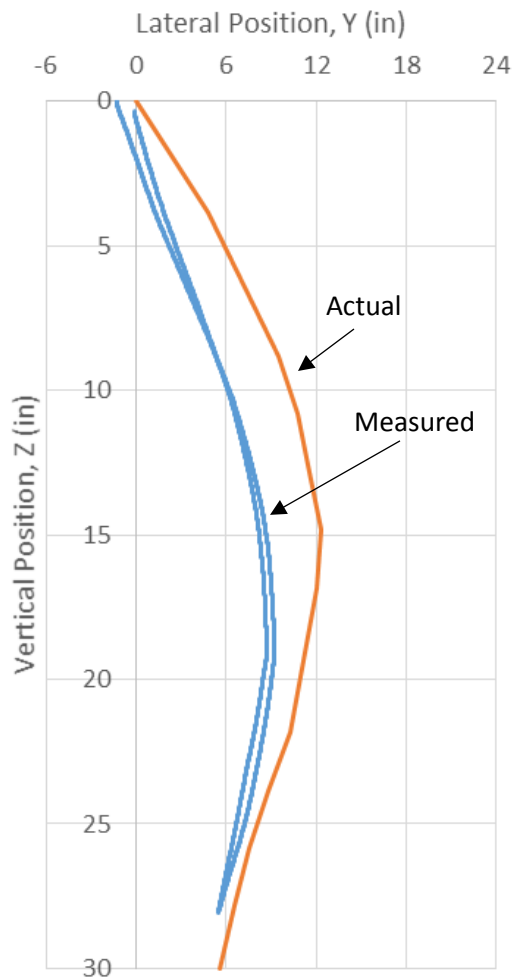
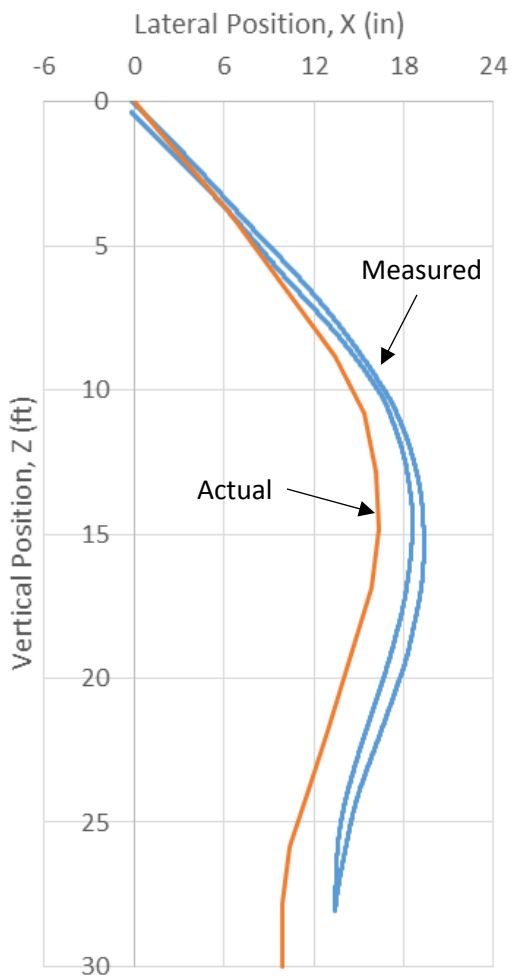


Figure 4.23. Measured vs. actual pipe deflection in the X-Z (left) and Y-Z (right) planes

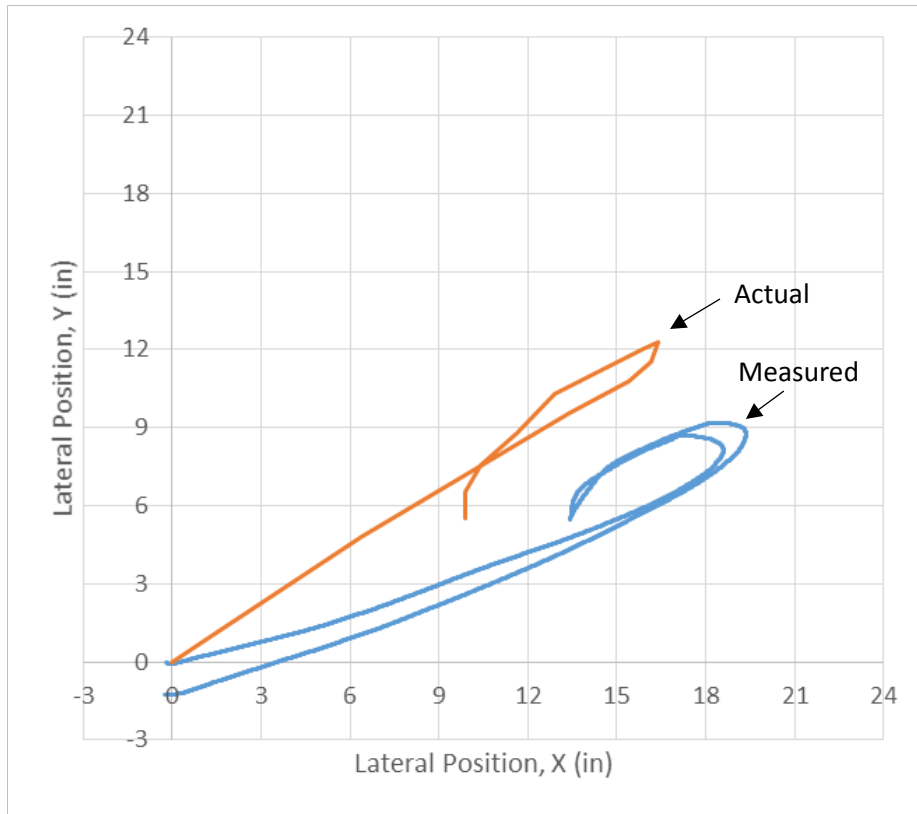


Figure 4.24. Measured vs. actual pipe deflection in the X-Y plane

After further investigation, the discrepancy between actual and measured deflection was found to be primarily due to the diameter tolerance between the probe and the pipe. Because of the tendency of the probe to hang completely vertical, any gap between the probe body and inner wall of the pipe resulted in a sensor inclination which was less than that of the pipe, as illustrated in Figure 4.25.

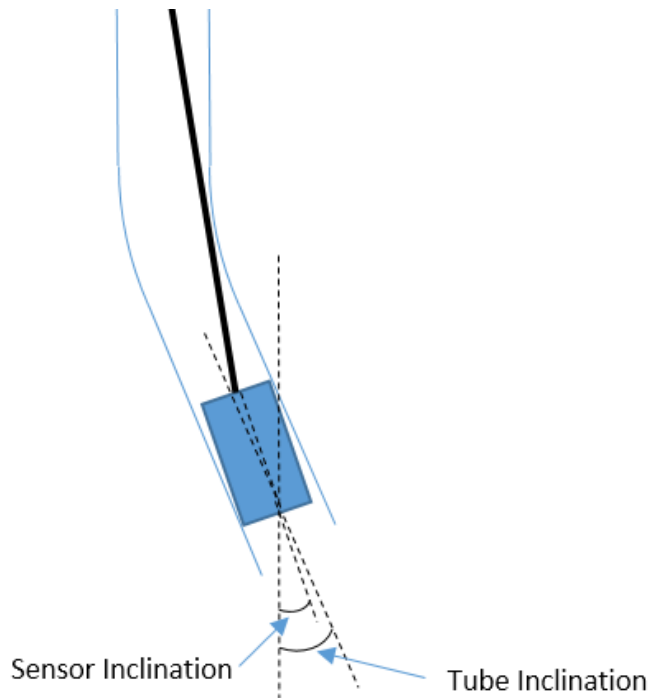


Figure 4.25. Inclination error due diameter tolerance between probe and tube

Figure 4.26 shows the results from a test in which the probe was purposely wiggled within the tube to show the possible amount of inclination error between the fabricated probe and 1.5in PVC pipe. The results revealed approximately  $\pm 1.25^\circ$  of inclination difference between the tube and probe, which, over 15ft, equates to about 4 in of lateral displacement error. This was corroborated by the results in Figures 4.23 and 4.24.

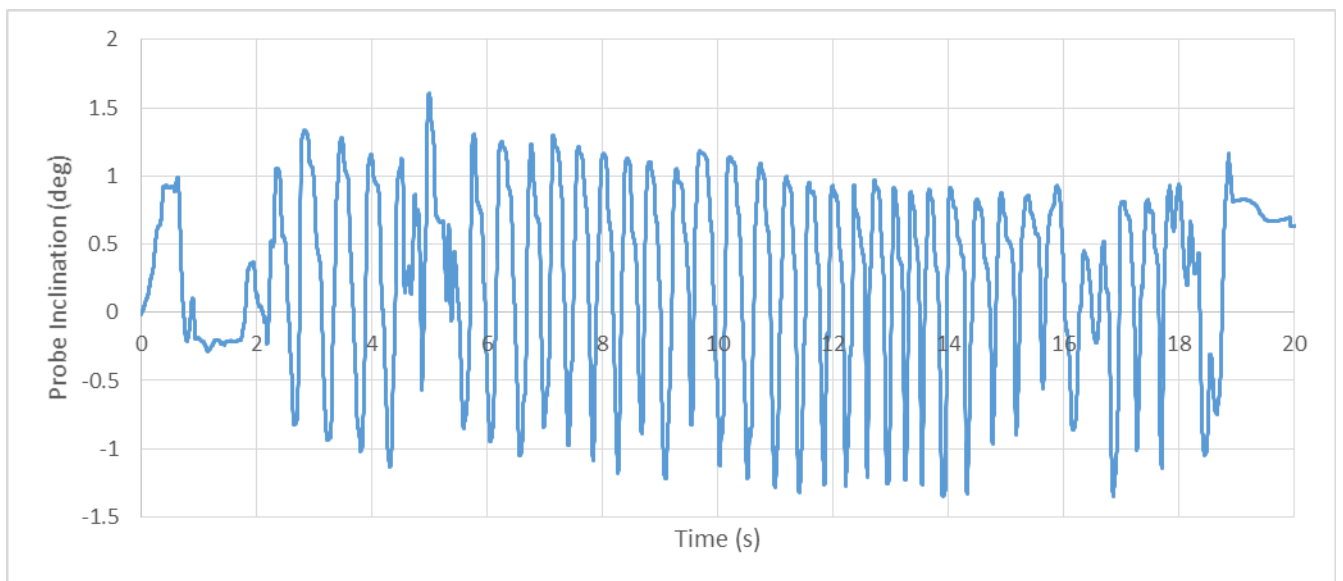


Figure 4.26. Measured inclination error between fabricated probe body and PVC pipe

While the consequences of this effect were understood prior to testing, the severity of errors, which compounded with depth, was not expected to be as significant. The degree of inclination of the probe within a tube is affected by both the diameter tolerance between the two, as well as the length of the probe. Increasing either of the diameter or length of the probe will reduce the degree of possible inclination, but will also decrease the ability of the probe to navigate around bends in the tube. Although the probe body was specifically dimensioned to have as tight a tolerance as possible (0.09in) while still allowing unrestricted navigation through the tube, the short length of the probe proved to allow even a tight radial tolerance to yield a large enough inclination to produce undesirable results. To mitigate this and maintain a balance between possible error and navigability, a new probe design, like that shown in Figure 4.27, was envisioned. The 1.5in diameter ends coupled with the lengthened distance between them reduced inclination error, while the reduced diameter center link allowed for navigability around bends.

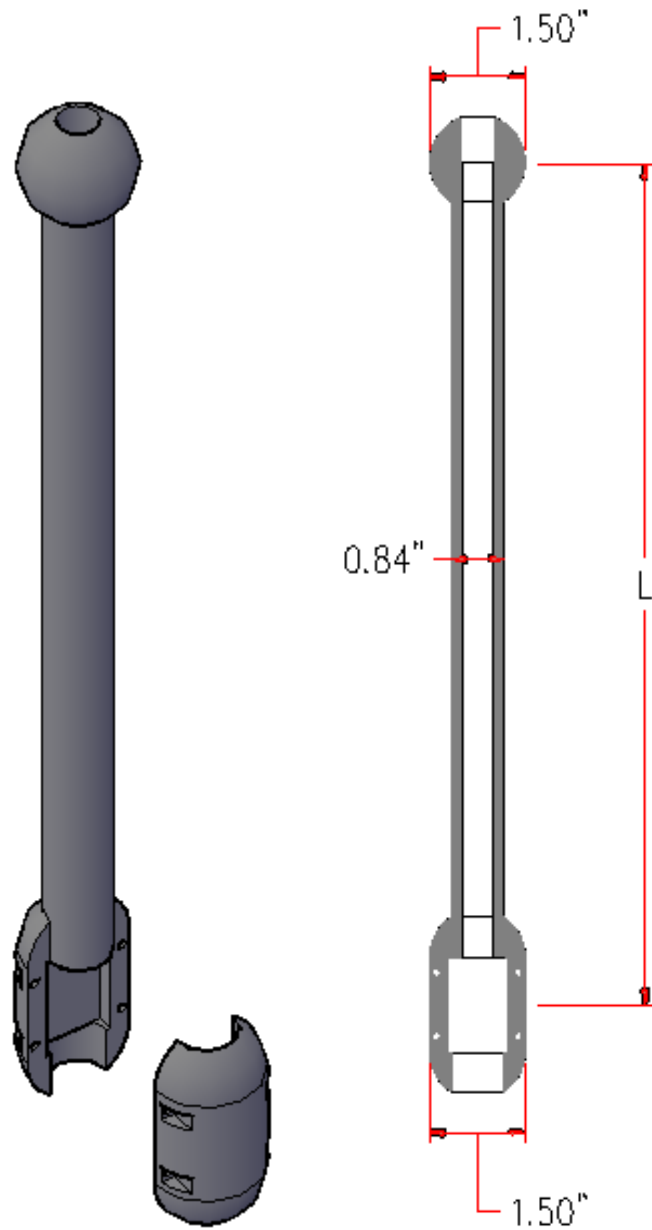


Figure 4.27. Design of probe to aid in alignment and reduce inclination error

Based on the diameters of probe and tube, the maximum possible degree of inclination can be determined as a function of probe length, which in turn can be converted to maximum possible lateral error over a given depth. This curve is shown in Figure 4.28 with lateral error expressed as a percentage of depth. Likewise, with the same geometry, the minimum radius of curvature that can be navigated by the probe was also determined as a function of probe length and is also shown in Figure 4.28. Using the above probe design with a 36in length, the maximum possible error is approximately 0.25% and minimum navigable radius of curvature is about 5ft. This is almost a ten-fold increase in accuracy from the probe used in the tests discussed above, but at the

expense of navigability. As a frame of reference however, the severe deformations experienced by the access tubes shown in Figure 4.2 were computed and yielded a minimum radius of curvature of 72ft, therefore it is conceivable that a 5ft minimum capability would be more than sufficient for typical access tube navigation.

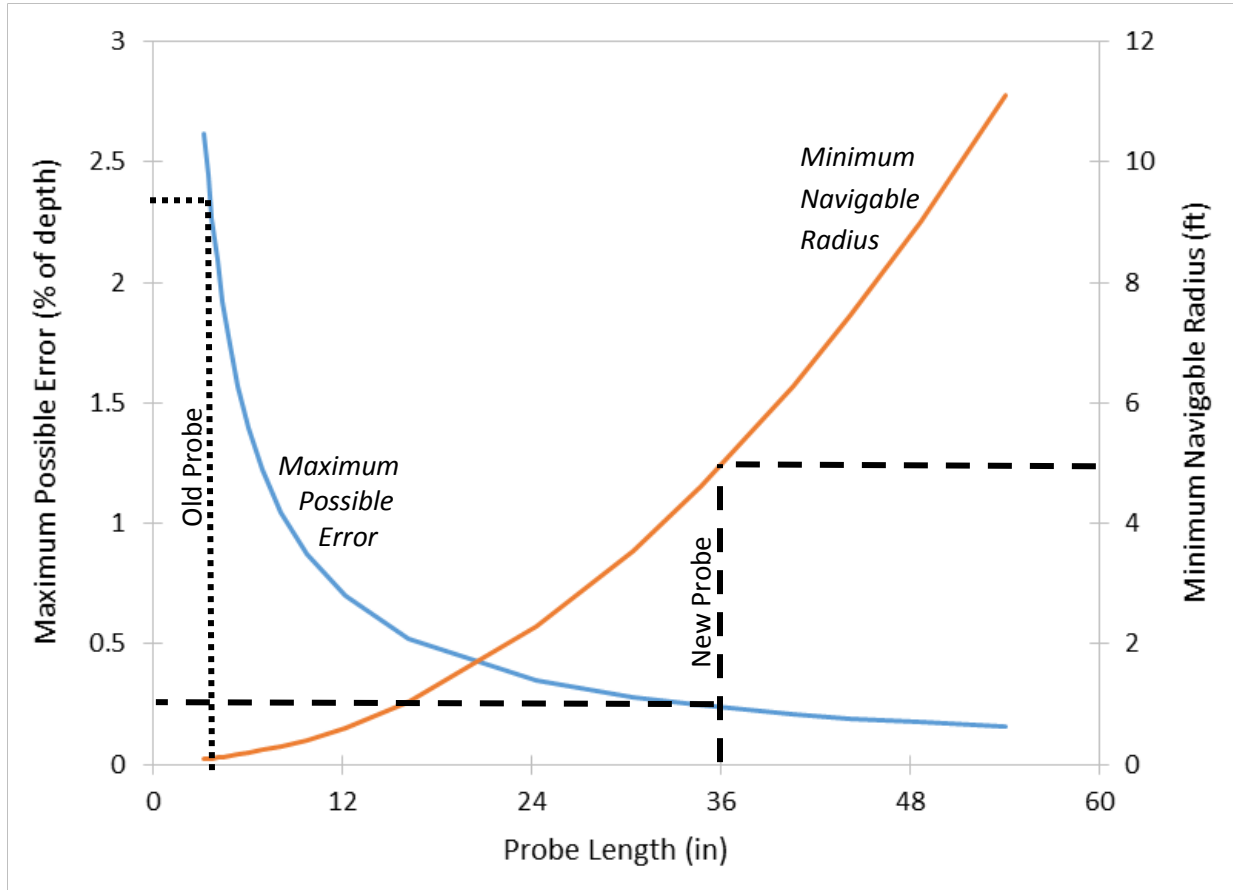


Figure 4.28. Reduced error and increased navigable radius with increasing probe length

#### 4.5 Chapter Summary

The investigation and testing of various gyroscopic inclination measuring systems concluded with encouraging results. The prototype probe assembly provided increased accuracy while maintaining reasonable accessibility to account for bends in access tubes. Although single wire/tube instrumentation schemes may never be used by FDOT for ACIP pile applications, the development and/or eventuality of this technology will bring significant amounts of valuable information. The increased insight into ACIP pile integrity is accompanied by increased quality assurance for all sizes of drilled shafts as well.

## *Chapter Five: Field Testing*

### **5.1 Overview**

This chapter outlines the data analysis of field-collected data from four different sites, where a total of 28 auger-cast piles were assessed using some form of thermal integrity evaluation. The data types varied in the instrumentation scheme, testing method used, and analysis technique developed which specifically targeted applications with auger-cast piles (or small shafts).

Instrumentation schemes included: (1) embedded wire sensors where one, two or four locations within the pile were monitored, (2) single access tube (centered), and (3) a cluster of four embedded thermal sensors located around a center bar. This means that both probe and data logging systems were used to collect data. A wide range of analysis methods were used, which are discussed in detail for each case study. But in all cases, the basic temperature to radius conversion was used to show when and where it was applicable without further evaluation.

### **5.2 Case Studies**

#### **5.2.1 Case Study 1: 22in drilled shafts with single center access tube, tested with probe**

This site consisted of six 22in diameter, 15 - 20ft long drilled shafts. The reinforcement was similar to auger-cast piles where only a single center bar was installed within a steel access tube for TIP testing using the probe method (Figure 5.1). The shafts were drilled using an 18in auger with 2in tip extensions, and a 27in ID temporary surface casing was used. While construction methods and concrete type were those of conventional drilled shafts, the size and reinforcement scheme resemble that of many auger-cast piles. The advantage of this study was that the shafts were later exhumed and measured, allowing for comparison of actual radius to that computed from TIP results. Diameter measurements were taken on 4in intervals along the length pile, using a large caliper to measure diameter in orthogonal directions, as well as using a soft tape measure circumference. The measurement values shown Figures 5.2 - 5.6 are an average of the two methods.

The center bar which was threaded into a base plate was removed immediately after casting, leaving the 1.5in steel access tube in place for probe testing. Each shaft was tested (via probe) on 3hr intervals for 18hr after concreting. In each case, peak temperatures were observed at 15hr, and these profiles were selected for analysis. Analysis was performed using traditional single-point T-R conversions after applying hyperbolic top and toe corrections. The measured temperature profile for each shaft is shown in Figures 5.2 - 5.6 (left), along with the resulting TIP computed radius and actual measured radius of each shaft (right).



Figure 5.1. Shaft with single center access tube for TIP probe testing

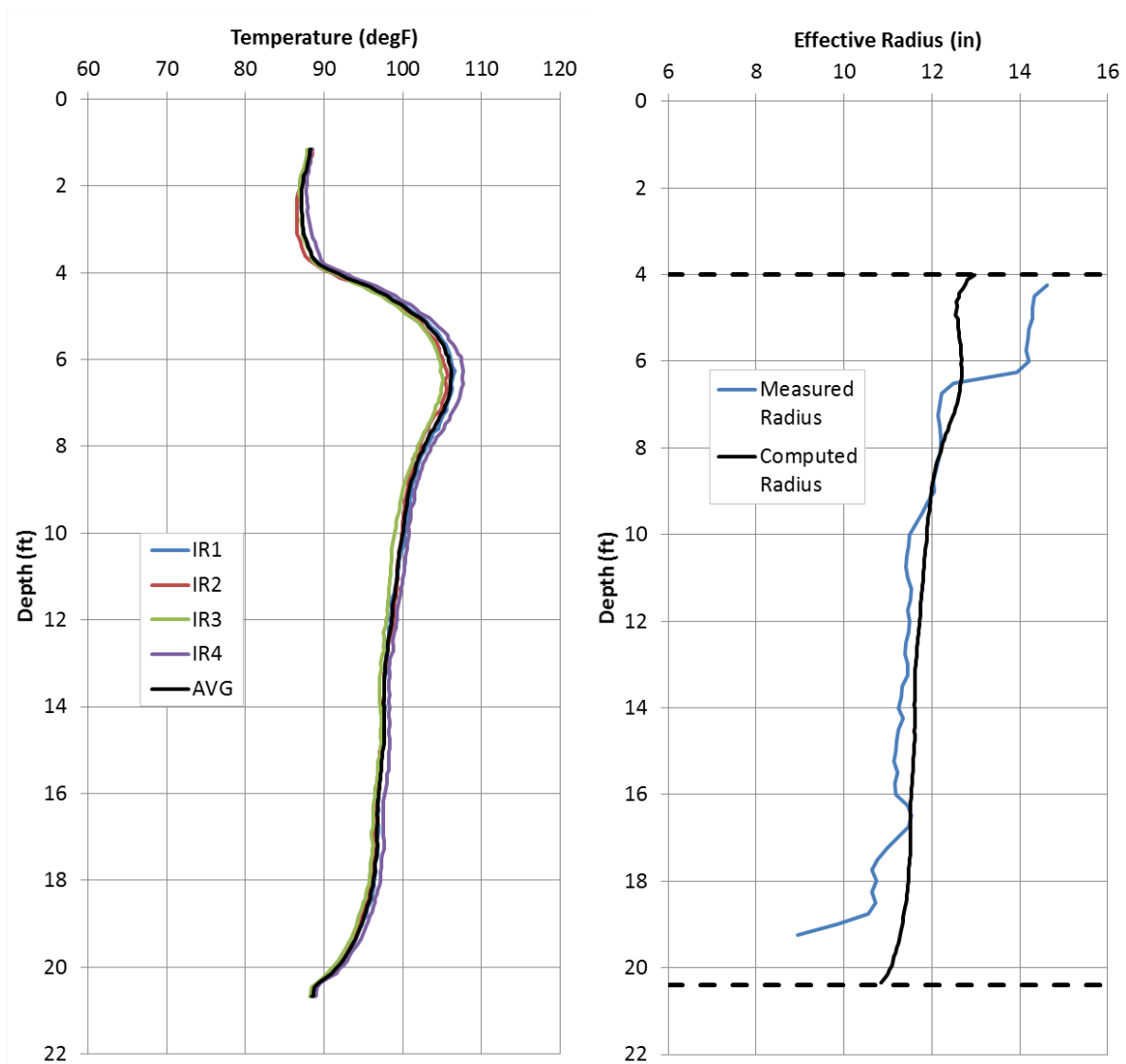


Figure 5.2. Shaft B4 raw temperature profile (left); interpreted results (right)

Observations:

- Thermal data shows both top and bottom of pile
- Computed radius reflects general shape of pile, but with little definition
- Bottom of profile indicates wire run-on at end of test (probe touches bottom and some extra wire is passed over depth wheel)

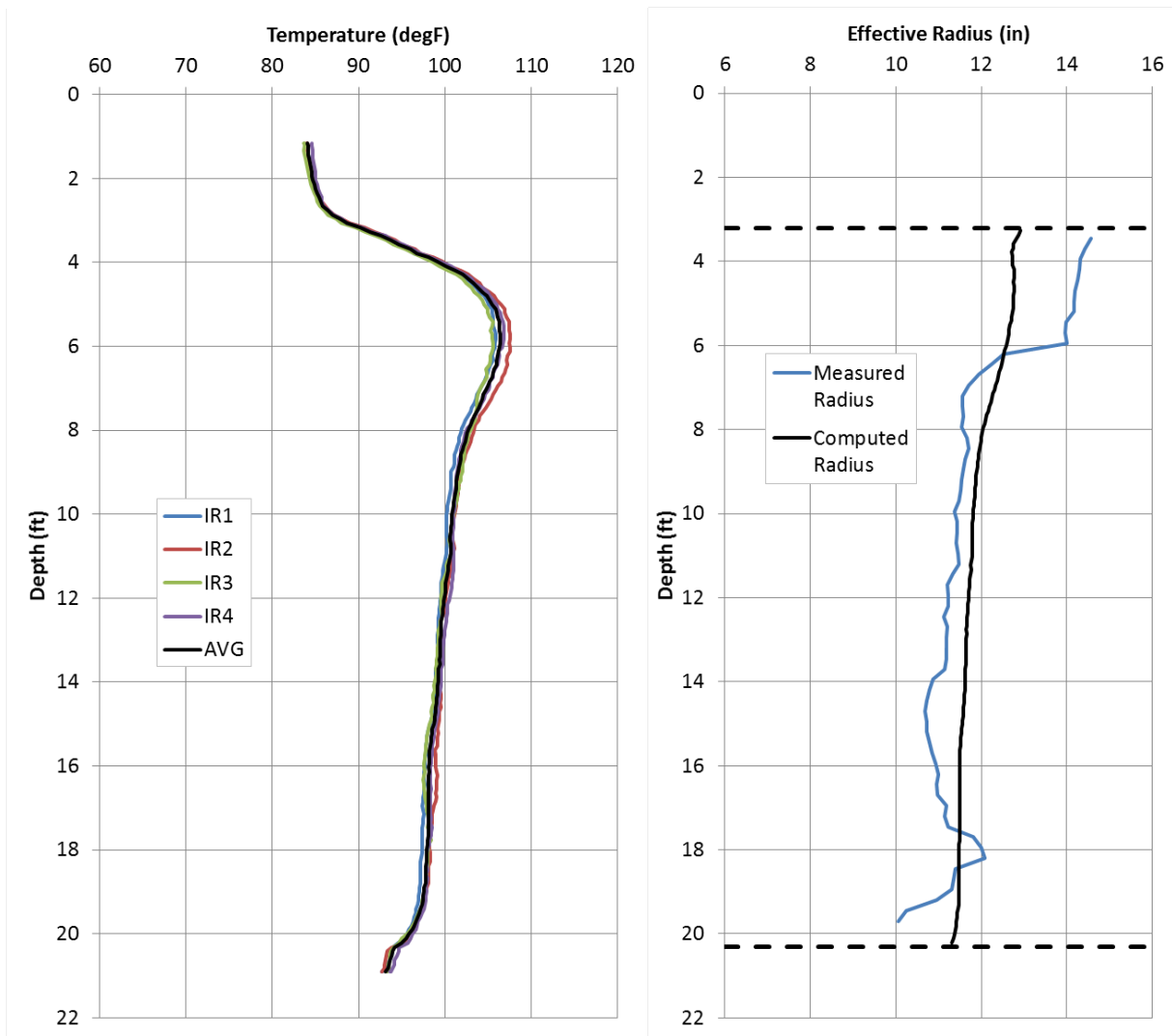


Figure 5.3. Shaft B5 raw temperature profile (left); interpreted results (right)

Observations:

- Thermal data shows both top and bottom of pile
- Computed radius matches general shape of pile, but with little definition
- Bottom of profile indicates wire run-on at end of test

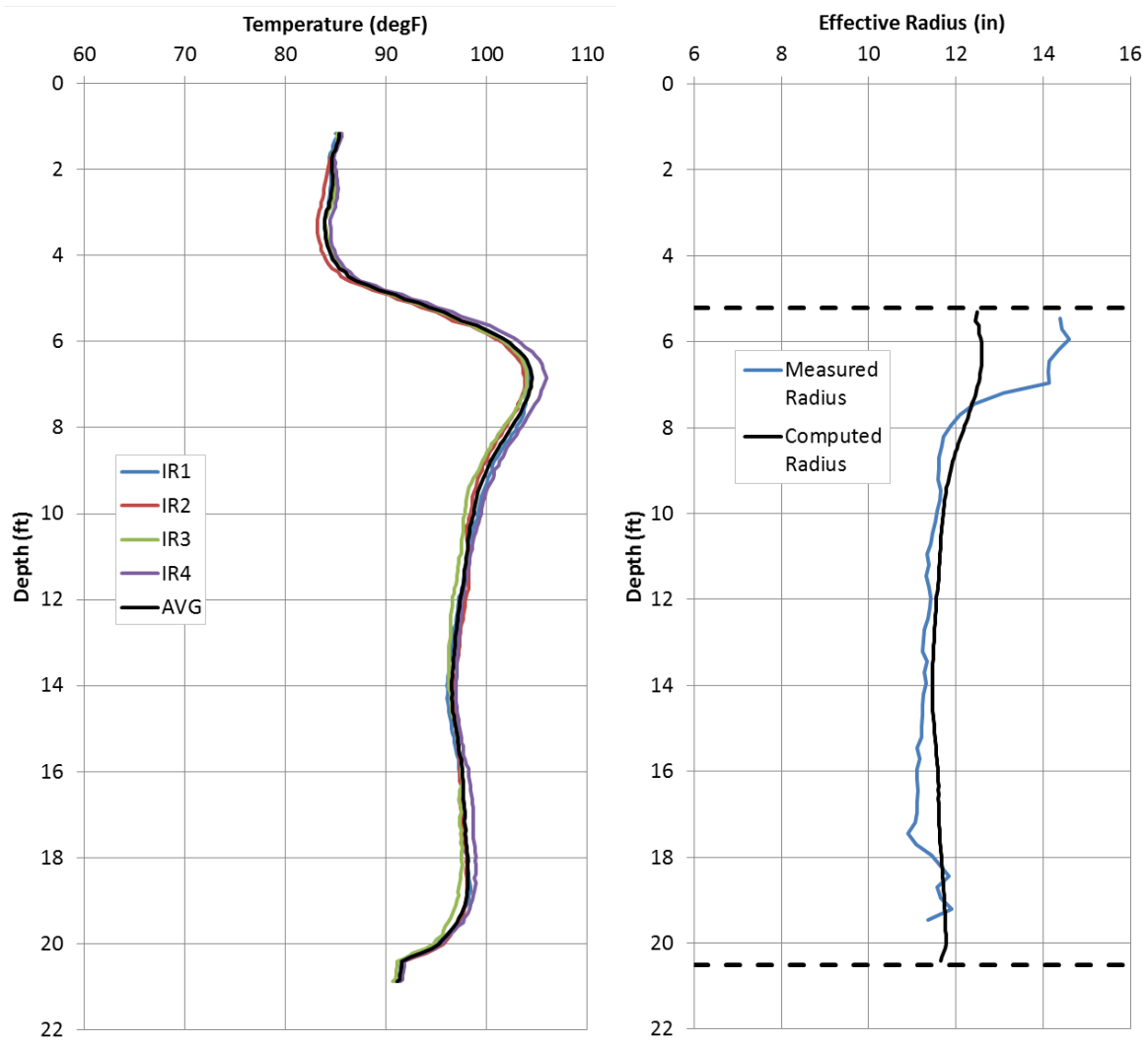


Figure 5.4. Shaft B6 raw temperature profile (left); interpreted results (right)

Observations:

- Thermal data shows both top and bottom of pile
- Computed radius matches general shape of pile, but with little definition
- Bottom of profile indicates wire run-on at end of test (probe touches bottom and some extra wire is passed over depth wheel)

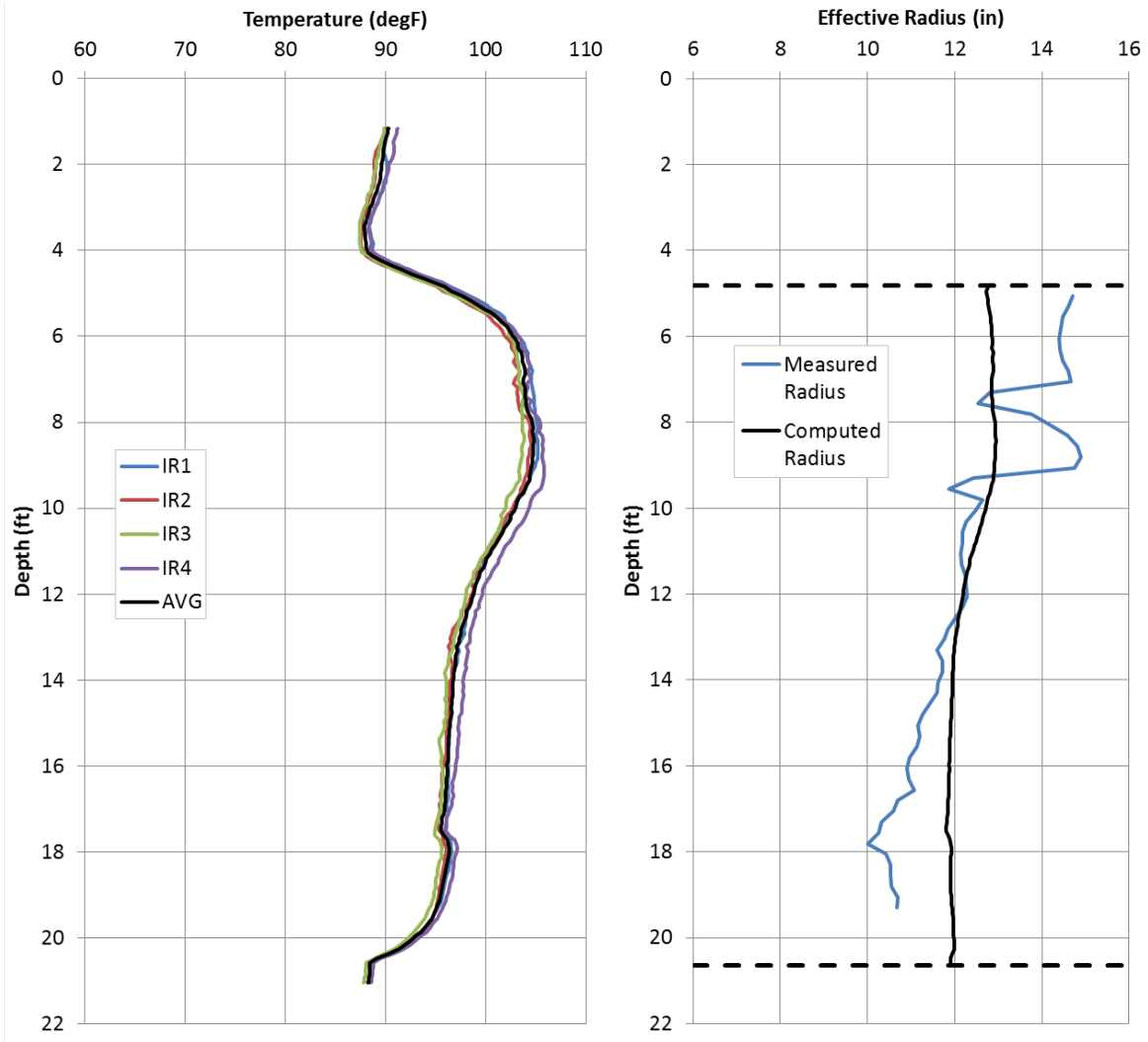


Figure 5.5. Shaft P6 raw temperature profile (left); interpreted results (right)

Observations:

- Thermal data shows both top and bottom of pile
- Computed radius matches general shape of pile, but with little definition
- Bottom of profile indicates wire run-on at end of test (probe touches bottom and some extra wire is passed over depth wheel)

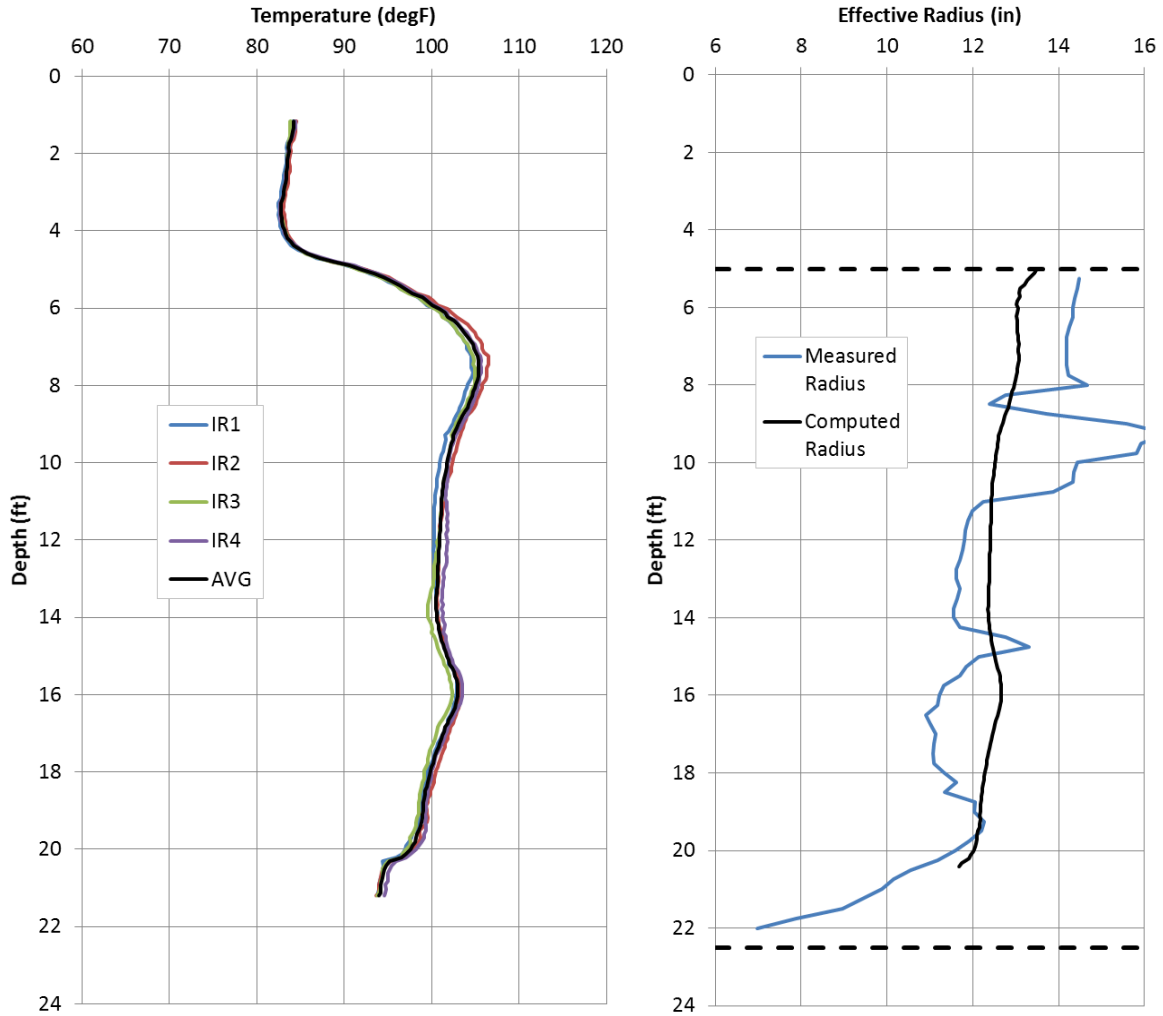


Figure 5.6. Shaft P5 raw temperature profile (left); interpreted results (right)

Observations:

- Thermal data shows both top and bottom of pile
- Computed radius matches general shape of pile, but with little definition
- Bottom of profile indicates wire run-on at end of test (probe touches bottom and some extra wire is passed over depth wheel)

From these results, it appears that the thermal profiles did somewhat reflect the general shape of each shaft, but was unable to detect, with any clear definition, any of the localized bulges or anomalies that were present (using shaft analysis methods). In each case the computed radius profile shows a slight increase at the top due to the increased dimensions of the temporary surface casing that was used, but the true degree of radius increase was never really captured. The most notable example of whether or not TIP results were able to detect localized anomalies is seen in Figure 5.6 (Shaft P5), where distinct bulges (other than that directly corresponding to surface casing) are seen at depths of around 10ft and 15 - 16ft. At 15 - 16ft, the thermal profile

does show a local temperature increase which corresponds to the measured concrete bulge at roughly the same depth. The slight discrepancy in depth of the measured and computed bulges is likely due to small differences in datum reference between TIP testing and measurement of the exhumed shafts. The large bulge shown in the measured profile at a depth of about 10ft, however, was not detected by the thermal profile. Closer examination of the photos taken of the exhumed shaft show that while this anomaly protruded a great amount, it was confined to a very small portion of the shaft circumference (Figure 5.7, left). A complete catalog of photos of each shaft is provided in Appendix B.

The conclusions drawn from this study were that a single set of center measurements were not sufficient to detect local anomalies for this size of shaft (i.e. 22in) using standard analysis methods.



Figure 5.7. Top, middle, and bottom (left to right) of exhumed shaft P5

### 5.2.2 Case Study 2: 22in drilled shafts with four thermal wires fastened around a single center bar.

This study consisted of six 22in diameter, 15ft long drilled shafts constructed similarly to those in Case Study 1. However, instead of providing access tubes for probe testing, each shaft was instrumented with four thermal wires (with sensors spaced on 1ft intervals) fastened orthogonally around a 1.5in SCH40 PVC pipe placed in the center of the shaft (Figure 5.8). The wires were left to collect data for approximately 24hr after concreting. Peak temperatures were observed around 12hr and these profiles were selected for analysis. Figure 5.9 shows the temperature history for each shaft over the 24hr period. As in Case Study 1, each shaft was later exhumed and measured, allowing for comparison between TIP computed radius values and actual shaft dimensions.



Figure 5.8. 1.5in PVC instrumented with four orthogonal thermal wires placed in center of shaft

Analysis was performed using the same methods as in Case Study 1. Hyperbolic corrections were applied to the top and toe roll-offs, then traditional T-R conversions were used to convert the average thermal profiles to effective radius profiles. The results for each shaft are shown in Figures 5.10 – 5.14.

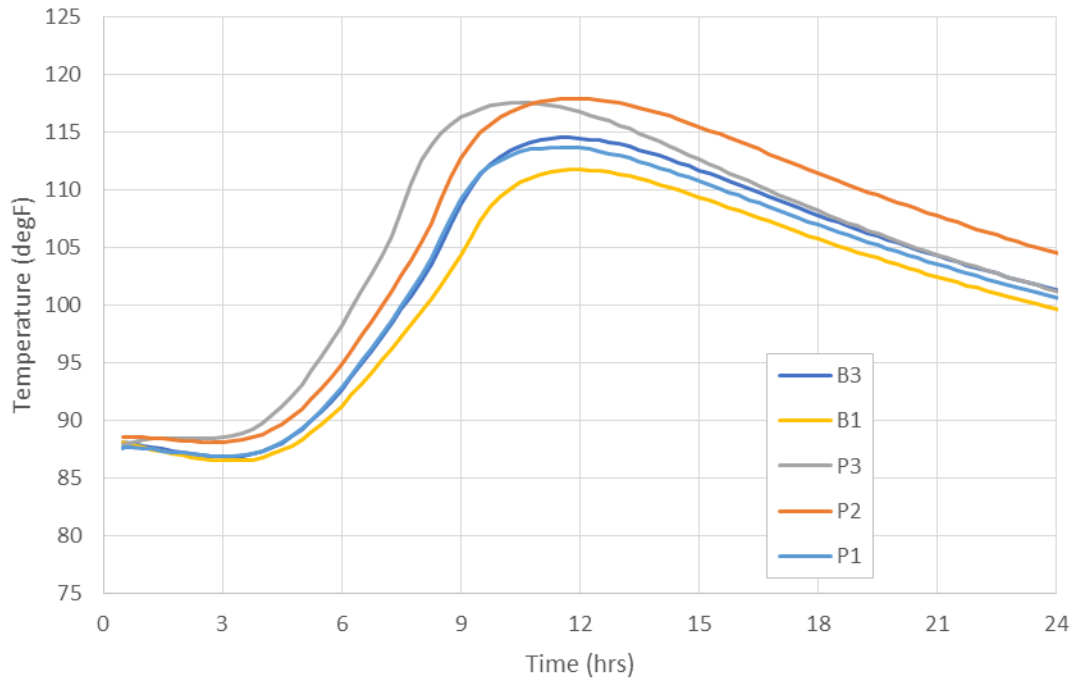


Figure 5.9. Temperature history for each shaft

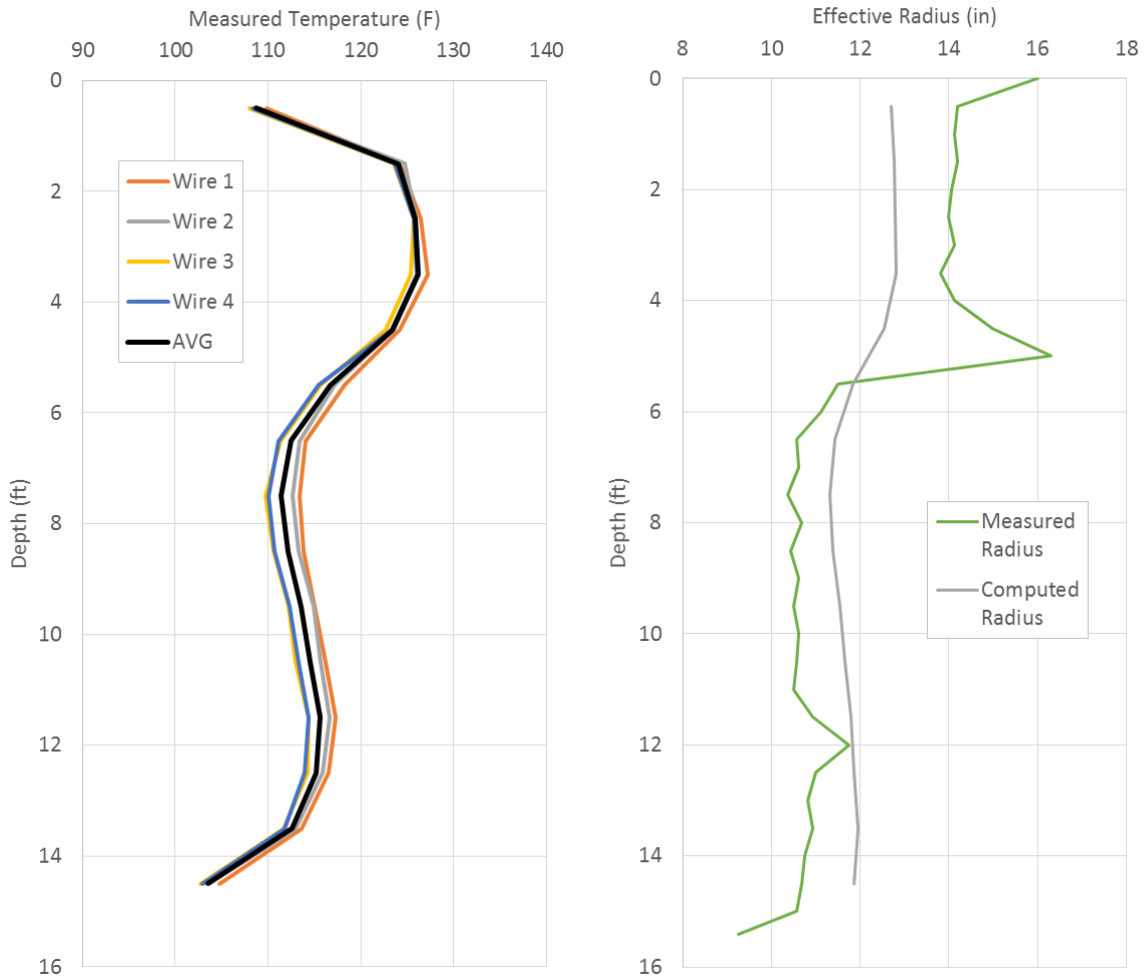


Figure 5.10. Shaft P1 raw temperature profile (left); interpreted results (right)

Observations:

- Thermal data shows top of shaft location and part of bottom roll-off (shaft deeper than last sensor)
- Computed radius matches general shape of pile, but with less definition
- Center bar eccentricity indicated by variations from sensors with 2in separation; requires more advanced analysis to define magnitude of lateral movement
- Integrity assessment reasonably successful; pile is good

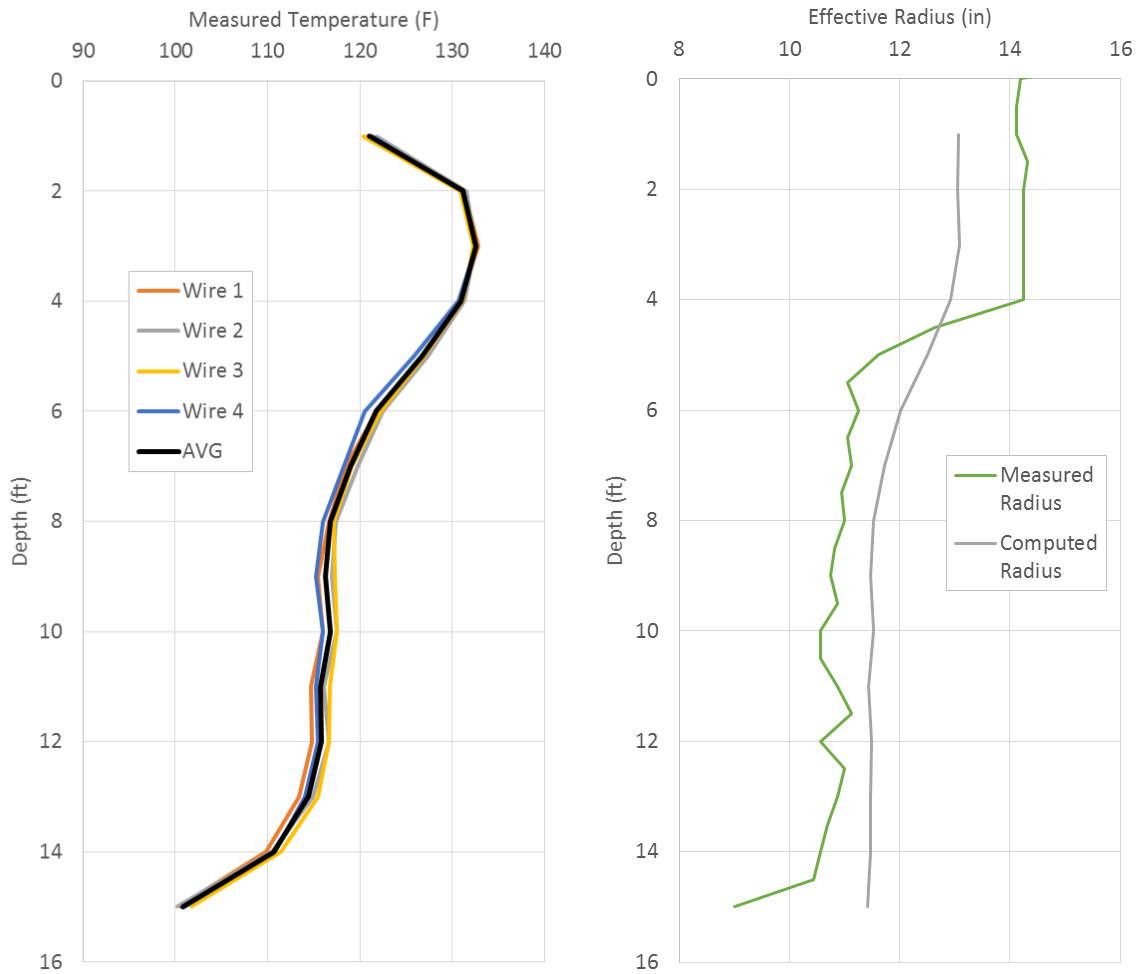


Figure 5.11. Shaft P3 raw temperature profile (left); interpreted results (right)

Observations:

- Thermal data shows bottom of pile, top-most sensor too far from top of shaft to precisely locate its location (full top roll-off not seen)
- Computed radius matches general shape of pile, but with less definition
- Center bar eccentricity less than previous pile.
- Integrity assessment reasonably successful; pile is good

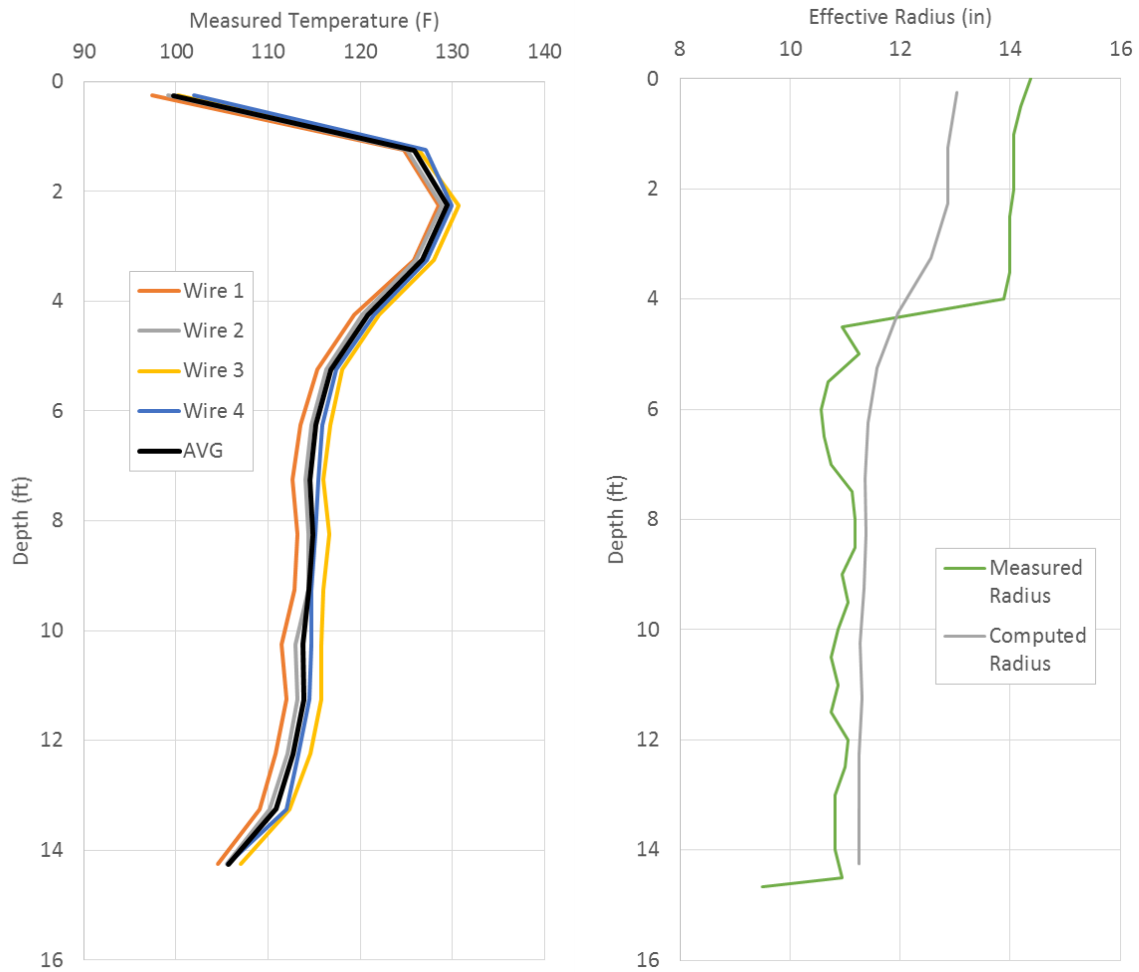


Figure 5.12. Shaft B3 raw temperature profile (left); interpreted results (right)

Observations:

- Thermal data shows both top and bottom of pile
- Computed radius matches general shape of pile, but with less definition
- Center bar eccentricity indicated by variations from sensors 1 and 3 which indicate primary direction of movement.
- Integrity assessment reasonably successful; pile is good

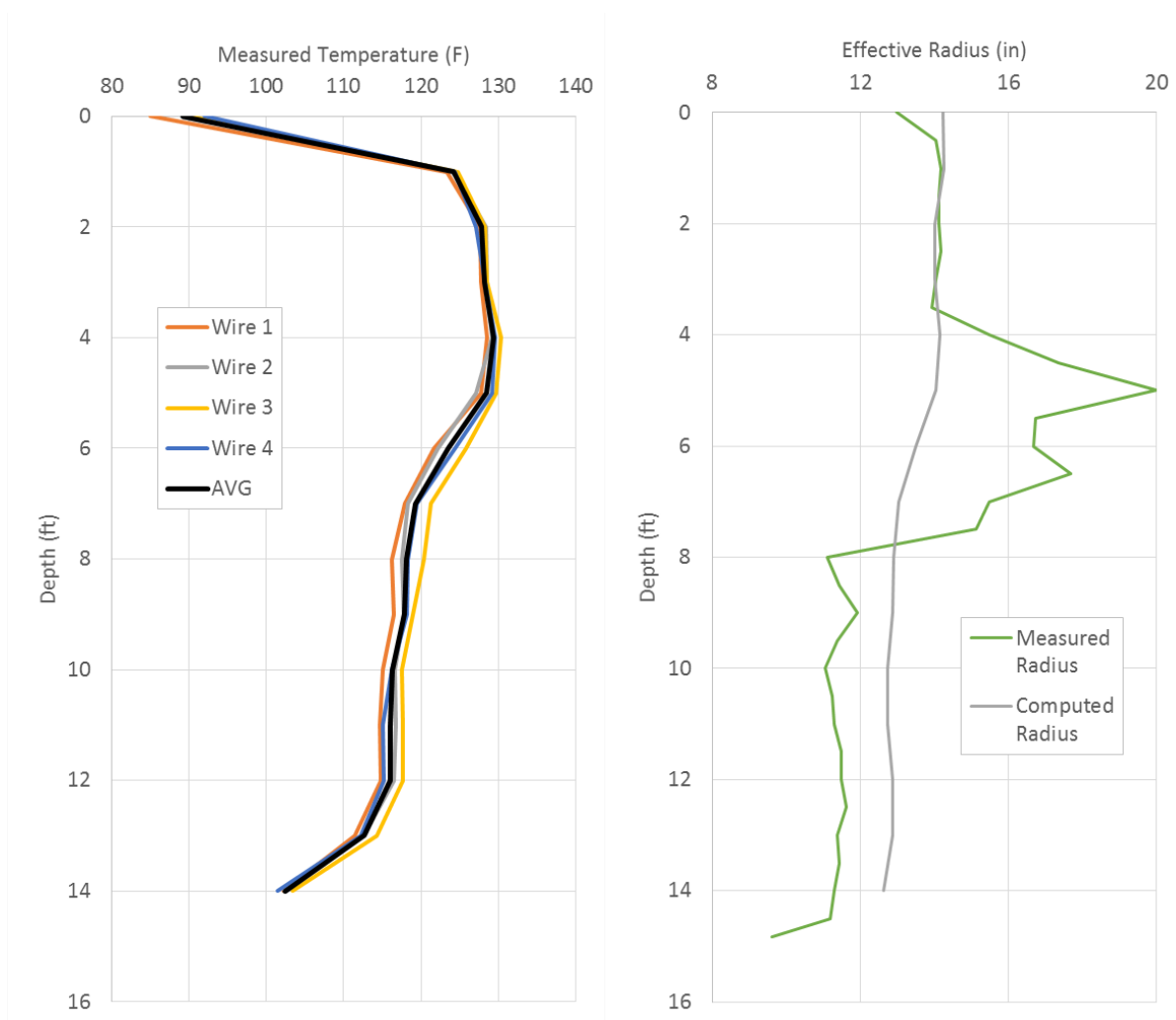


Figure 5.13. Shaft P2 raw temperature profile (left); interpreted results (right)

Observations:

- Thermal data shows both top and bottom of pile
- Computed radius shows top of shaft is larger than bottom, but did not detect large bulge
- Center bar eccentricity indicated
- Integrity assessment reasonably successful; pile is good

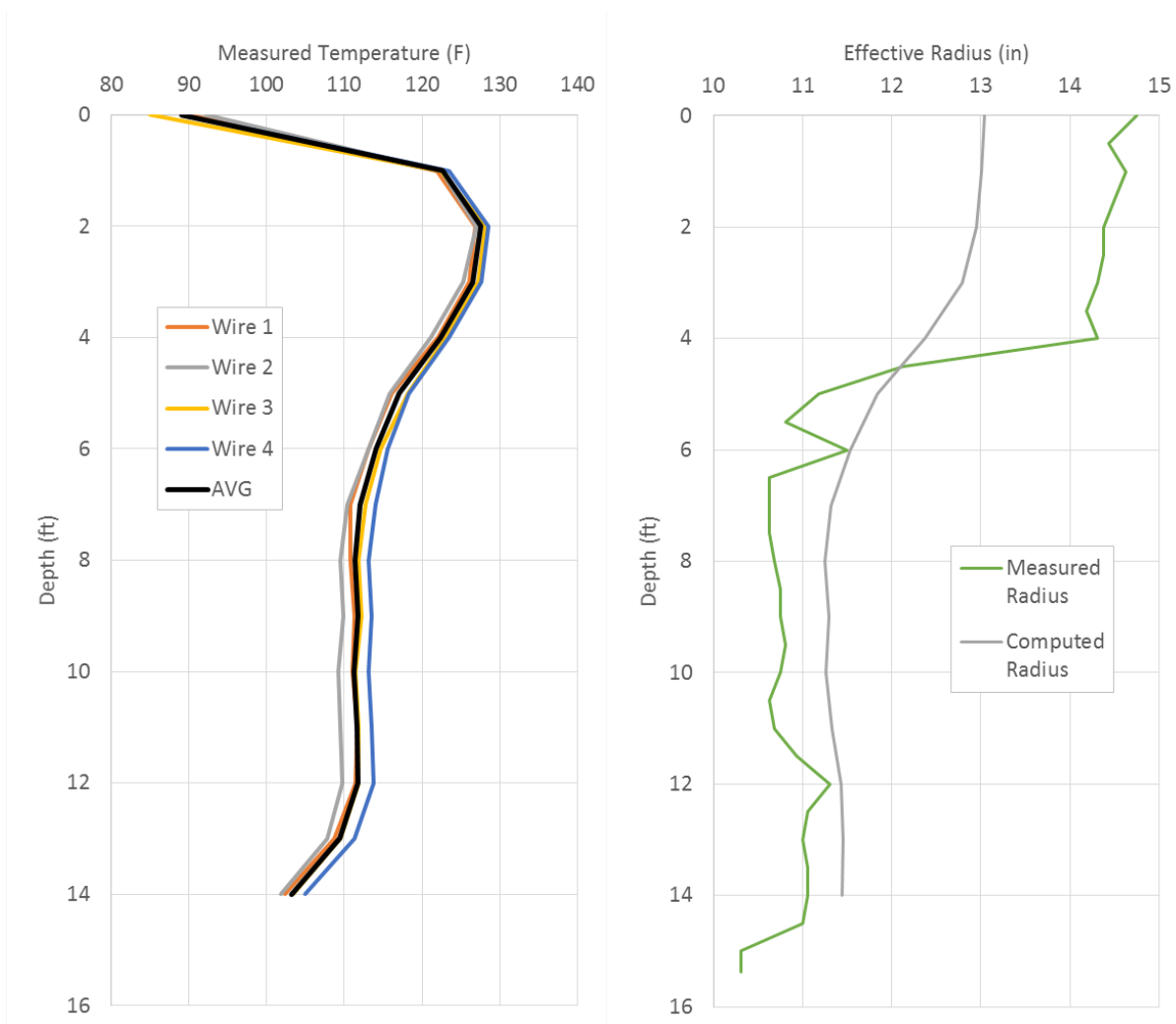


Figure 5.14. Shaft B1 raw temperature profile (left); interpreted results (right)

Observations:

- Thermal data shows top of shaft location and part of bottom roll-off (shaft deeper than last sensor)
- Computed radius matches general shape of pile, but with less definition
- Center bar eccentricity indicated by variations from sensors with 2in separation
- Integrity assessment reasonably successful; pile is good

From comparison of the TIP computed radius profiles and the measured radius profiles, many of the same conclusions from Case Study 1 can be drawn. The thermal profiles were able to detect the drastic change in radius between the lower uncased portion and the upper portion where temporary casing was used, but not to the degree which actually occurred. In each case, the computed profiles returned radii that were about 1 - 2in smaller than measured in the upper portion and 0.5 - 1in larger than measured in the lowered portion. Photographs of each shaft after extraction are included in Appendix B.

This reoccurring effect seen in Case Studies 1 and 2, of computed radius profiles returning a seemingly ‘dampened’ or ‘condensed’ version of the measured radius profile, is a result of using traditional T-R conversion methods on small shafts (e.g. < 30in) combined with centerline measurements. As described in Chapter 2, the traditional method for determining a T-R relationship is to use the average temperature of the shaft and the average radius of the shaft (determined from concrete logs) to generate a linear pole-point solution (i.e., a line defined by the points  $T_{avg}$ ,  $R_{avg}$  and  $0,0$ ). For most drilled shafts with cage radius measurements, this produces a line with a similar slope to that of the S-shaped T-R curves shown by models. However, when the highest temperature (i.e., that at the center of a shaft) is combined with a small radius, the pole-point solution yields a line with a much shallower slope (Figure 5.15).

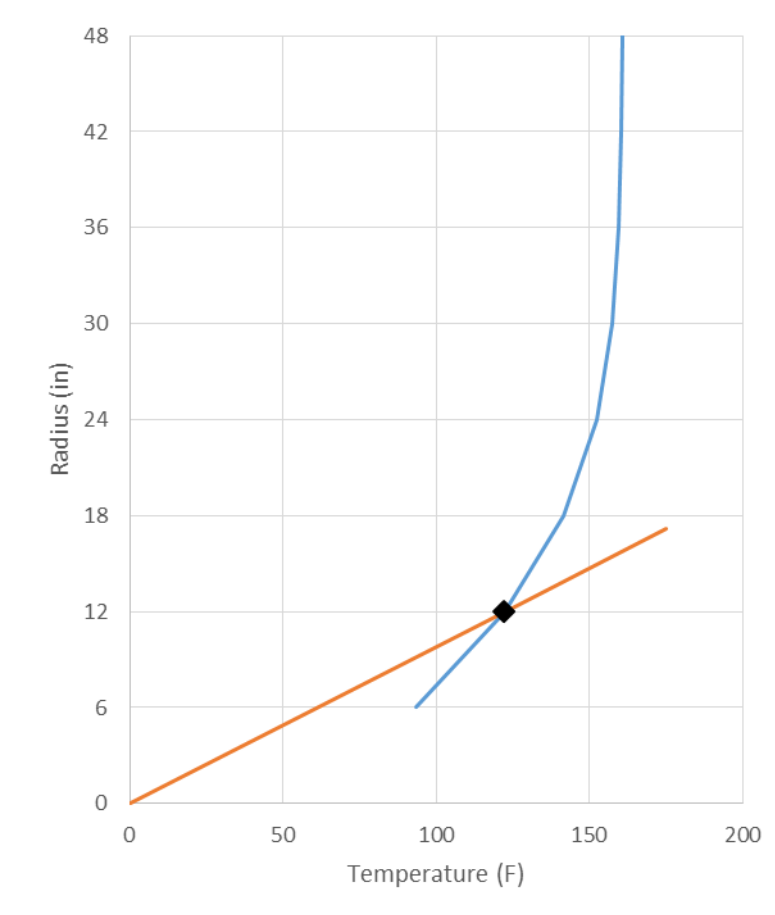


Figure 5.15. Discrepancy between true T-R relationship and pole-point solution when center measurements are used on a small radius shaft

Ideally, a T-R relationship should be defined by a function which mimics the S-shaped curve shown by models. The S-shaped curve is closely approximated by the same hyperbolic tangent function which is used to approximate top and toe roll-offs. The equation is of the same form as that shown in Equation 2.1, except the dependent variable depth is replaced with radius. The parameters which define the shape of the curve are the same – inflection point, asymptotic

temperatures, and vertical stretch – but now are influenced by different factors and in different ways.

$$T = \left( \frac{T_{max} - T_{min}}{2} \right) \tanh \left( \frac{R - R_0}{\alpha} \right) + T_0 \quad \text{Equation 5.1}$$

where,

$T_{max}$  = Upper asymptotic temperature = concrete adiabatic temperature

$T_{min}$  = Lower asymptotic temperature

$T_0$  = Inflection point temperature

$R_0$  = Inflection point radius = radial location of measurements

$\alpha$  = Time factor

As an exercise, this type of analysis was attempted with the thermal profile from Figure 5.14 (Shaft B1), using the basic concepts that are well understood combined with information provided by models that were signal matched to best represent the shaft. Once parameters were selected based on theoretical concepts and modeling, they were adjusted so that the calibration point ( $T_{avg}$ ,  $R_{avg}$ ) was satisfied by the curve.

Since measurements were taken at the center of shaft, the inflection point radius was set to zero. The inflection point temperature was then defined by the temperature that would be measured at this location on a shaft of the same size (i.e., at the edge of shaft). In this case, a zero radius shaft would produce no heat, so the measured temperature would be that of the surrounding soil, 73°F. The maximum asymptotic temperature is defined by the adiabatic temperature of the concrete. Since there is no way of knowing this from field test data (without calorimetry testing of the specific concrete mix), it was determined from model results. A signal matched model was generated by inputting all known properties of the shaft and surrounding environment, then adjusting the concrete hydration parameters,  $\alpha$ ,  $\beta$ , and  $\tau$ , until the temperature vs. time curve matched that which was measured by the thermal wires. These parameters were then used to generate model results for the concrete under adiabatic conditions, which returned a temperature of 161°F. As an initial guess, the hyperbolic time factor, alpha, was set equal to the alpha that was used for the toe roll-off correction, 21.6in (1.8ft). Remarkably, this selection of parameters produced a curve which satisfied the calibration with no need for adjustment, and the resulting effective radius profile showed good agreement with the measured profile.

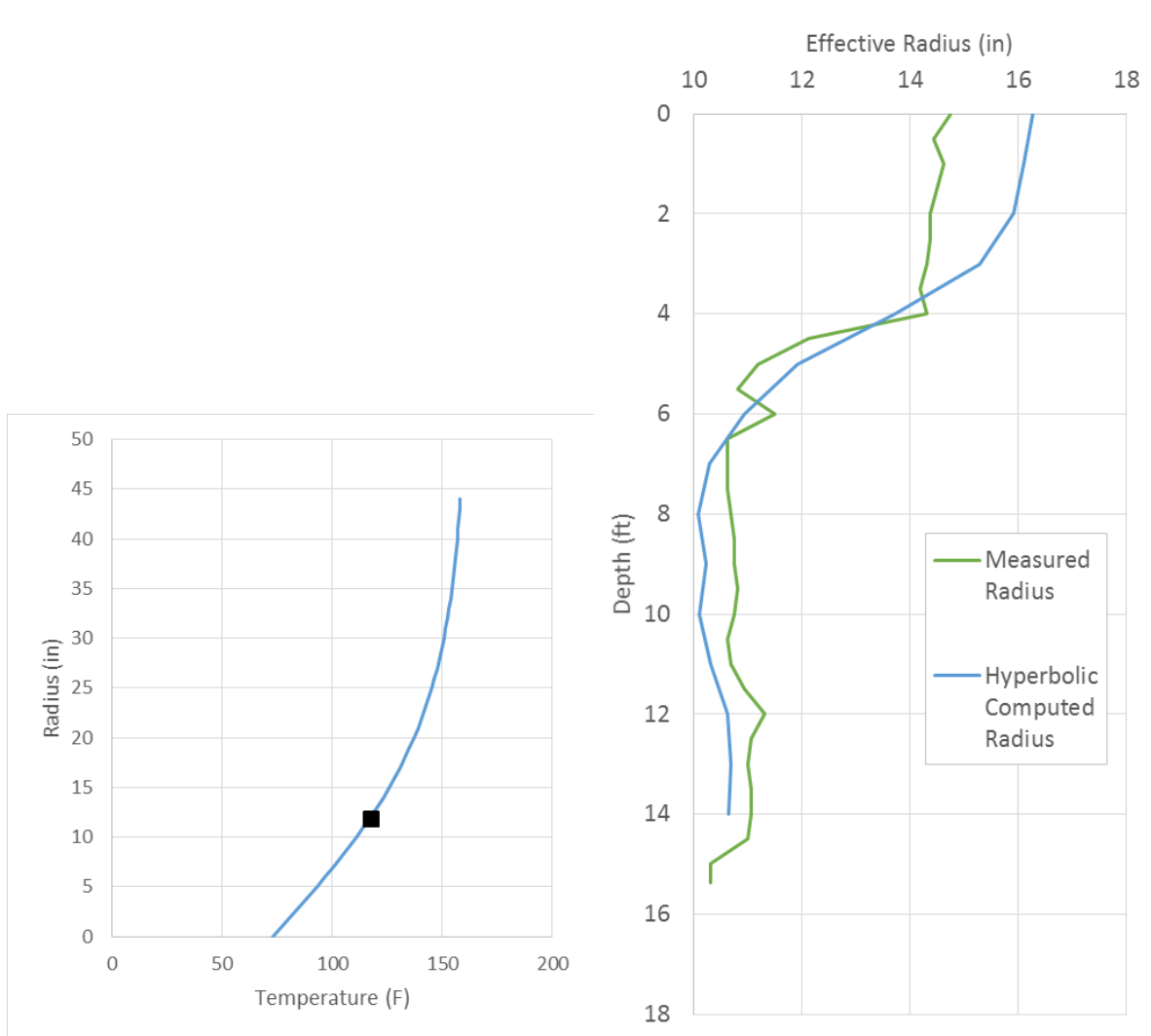


Figure 5.16. Shaft B1 interpreted results using hyperbolic T-R relationship

To further examine the effects of parameter selection, the inflection point radius and alpha value were adjusted until the agreement between computed and measured radius was optimized with a T-R curve which still satisfied the calibration point. The result was an adjustment of the inflection point radius from 0 to 3.5in, and of alpha from 21.6in to 15in (1.25ft). The curve and corresponding radius profile are shown in Figure 5.17. Note that although the profiles appear to be in better agreement and the calibration point is still satisfied, the resulting hyperbolic T-R curve yields a zero radius temperature of about 55°F. Theoretically, the zero radius temperature should correspond to regional soil temperature, which, for the location of this pile, is 73°F. Having not satisfied this boundary condition, this solution may be another example of forcing a good fit with physically impractical parameters.

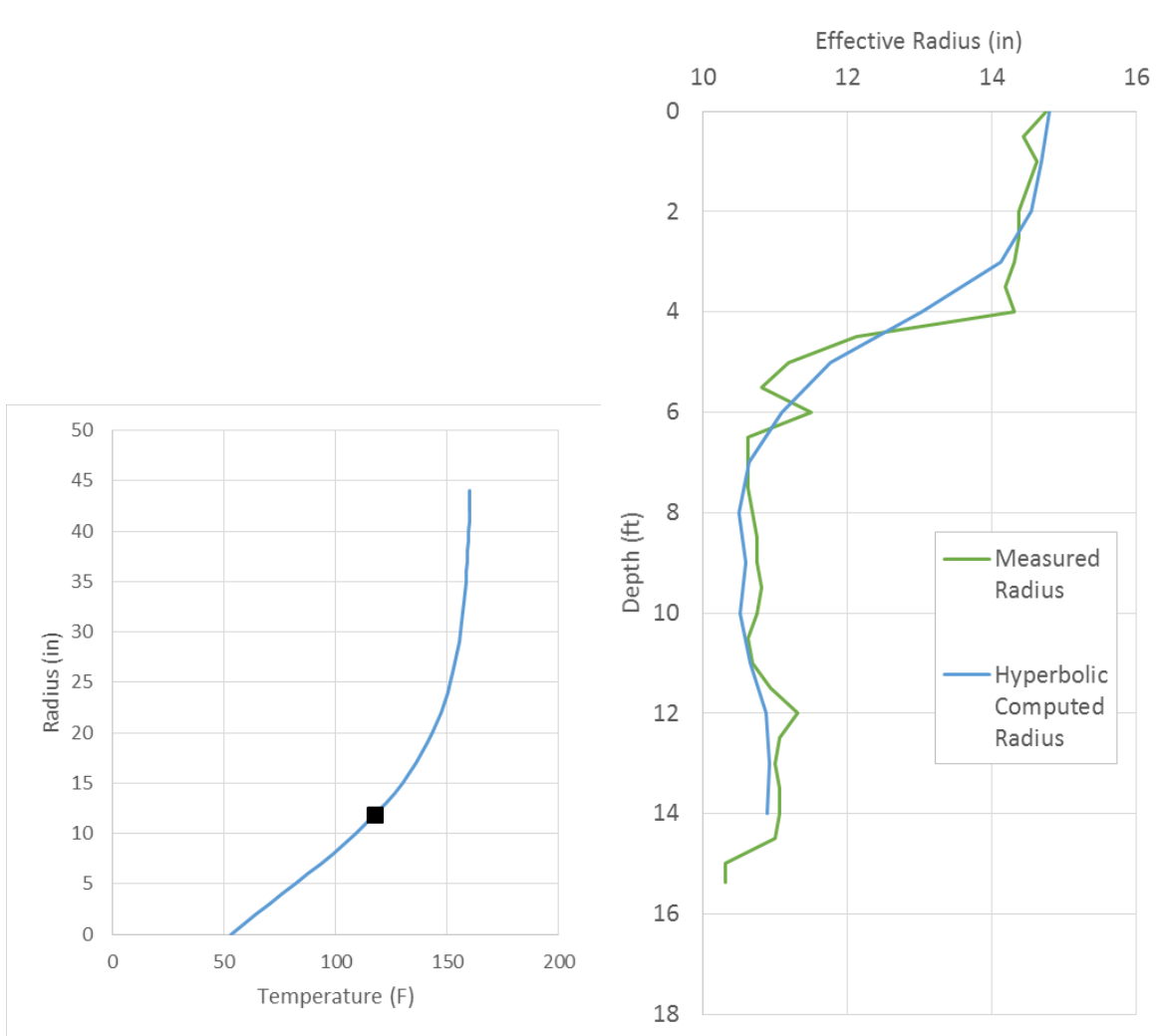


Figure 5.17. Shaft B1 interpreted results using hyperbolic T-R relationship with parameters adjusted for optimum fit

While this type of analysis has potential to help mitigate some of the problems associated with single center measurements, it still leaves the problem of unknown cage / bar offset unaddressed. While the results do not appear to suffer from error due bar movement, the temperature variation among opposing wires in Figure 5.14 does indicate eccentricity. To account for this, another advanced analysis exercise was performed in which the temperature gradients between opposing wires at each depth were compared against data generated from the signal matched model for that shaft.

Figure 5.18 shows the radial temperature distributions for shaft sizes ranging from 10 - 20in in radius. Also shown are the temperatures recorded by wires 2 and 4 at a depth of 10ft from shaft B1, separated by a distance of 2in (OD of the 1.5in PVC pipe). By plotting the two temperatures with the correct lateral spacing, the gradient line between them is drawn. From this information, the bar offset and shaft size is determined by shifting temperature pair left and right until they fall on the bell curve which satisfies both points as well as the slope between them (gradient).

This procedure is illustrated in Figure 5.18. When the points are shifted too far to the left, they fall onto bell curves which have too shallow of a slope. Likewise, a shift too far to the right puts them on bell curves with too steep of a slope. The only position which satisfies the two points is the one shown in green, which corresponds to a 6.6in offset on a 23in diameter shaft. This approach provides a simultaneous solution of both bar offset and shaft radius, and assuming the model data is the most accurate representation of the shaft, there is only one unique solution for each pair of temperatures. Of course, this approach, as with any which relies on modeling, is only as strong as the level of confidence in model input parameters like concrete mix and hydration properties.

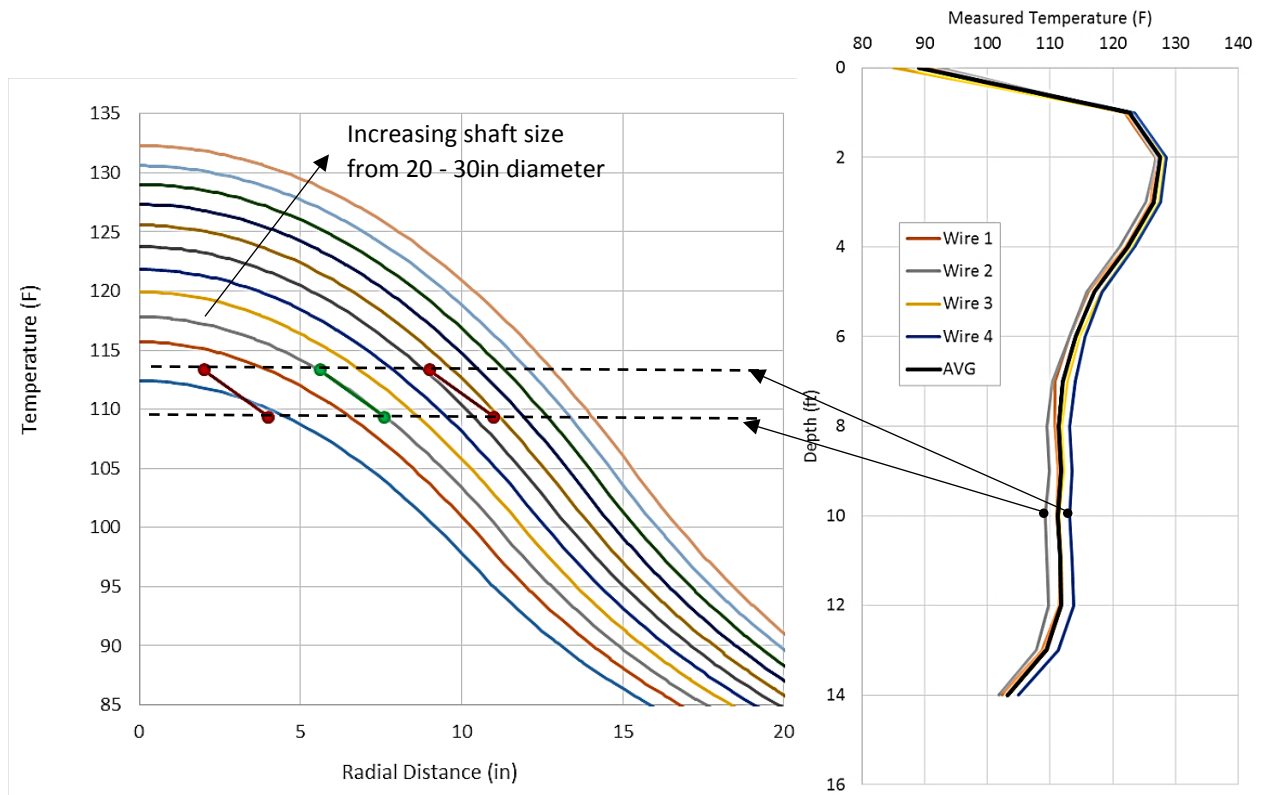


Figure 5.18. Model generated bell curves used to match measured temperature gradient between opposing wires from shaft B1 at 10ft

For the shaft in Figure 5.14 (Shaft B1), this type of analysis was performed at each depth using wires 2 and 4, shown in Figure 5.19. Note that the best fit for many of the pairs does not fall directly on top of plotted bell curve. In these cases, the corresponding shaft size was estimated by visual interpolation. Ideally, a simple algorithm would be in place to make this procedure both more accurate and less iterative. Figure 5.20 shows good agreement between the resulting effective radius profile and the measured radius profile.

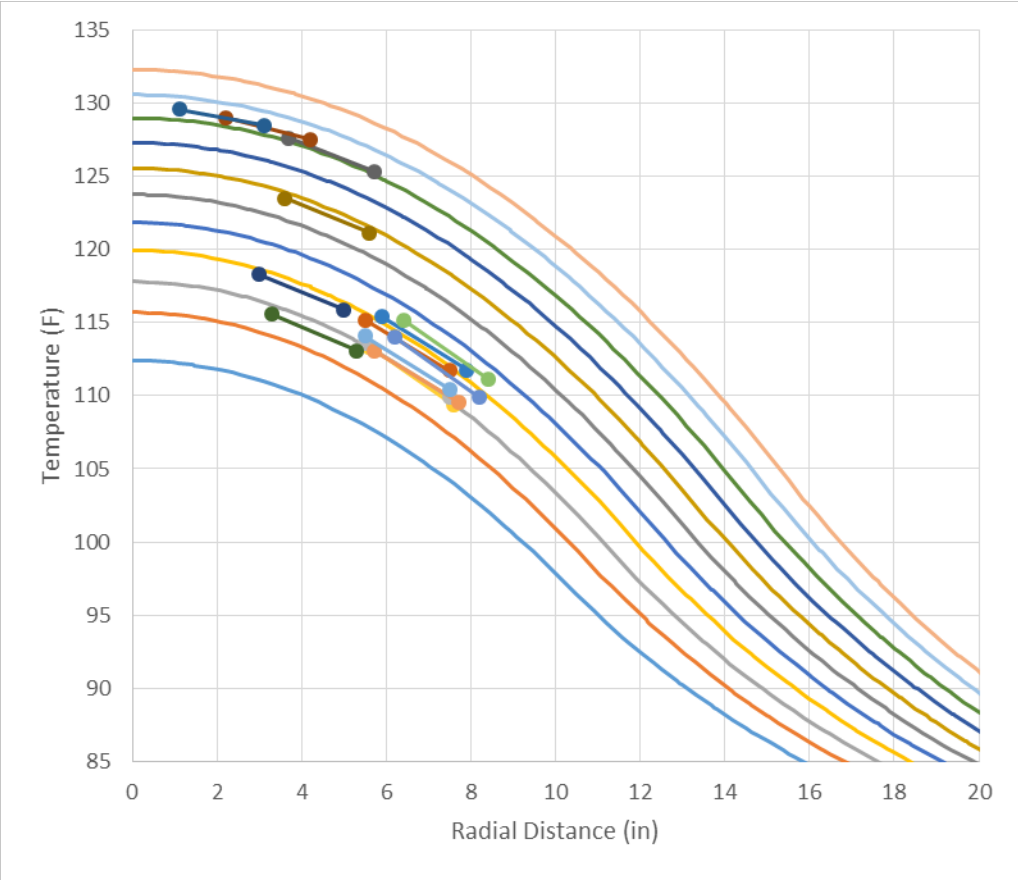


Figure 5.19. Thermal gradients at each depth matched to corresponding bell curves

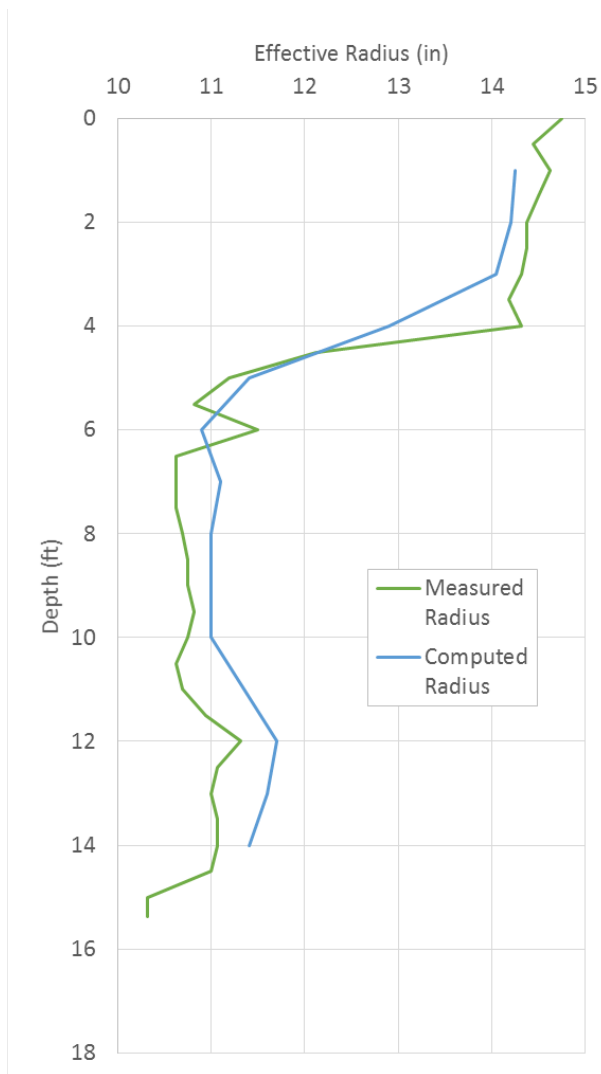


Figure 5.20. Shaft B1 interpreted results using thermal gradient method

### 5.2.3 Case Study 3: 14in auger-cast piles instrumented with a single wire on single center reinforcing bar.

This study consisted of fourteen 14in diameter, 60ft long auger-cast piles with a full length single center reinforcing bar along with an upper 25ft full reinforcing cage. TIP data was collected via a single thermal wire attached to the full length center bar. Unlike the shafts in Case Studies 1 and 2, these were true ACIP piles, constructed using typical ACIP methods and materials.



Figure 5.21. 14in ACIP pile instrumented with single center thermal wire

Aside from data analysis, it should be noted that of the 14 instrumented piles, full length data was only able to be recovered from seven. Partial length data was recovered from four piles, and no data was able to be recovered from three of the piles. It is believed that the wires in these cases were possibly damaged by protruding internal hook bars of the upper reinforcing cage. This type of complication is a special consideration for use of wires in ACIP piles, as the use of multiple reinforcing schemes is common and the post-concreting installation method makes any attached wires susceptible to damage. Figure 5.22 shows the reinforcing cage with internally protruding hooks (left), and the instrumented center bar with centralizing rods at the bottom and a temporary protective sleeve made from PVC pipe along the entire length (right).



Figure 5.22. Reinforcing cage with internal hooks (left) and instrumented center bar with centralizing device and temporary protective PVC sleeve (right)

As for the data that was recovered, direct observation of thermal profiles indicated mostly straight shafts with normal end conditions and minimal bar movement. While bar movement cannot be observed by comparison of lateral temperatures when only one wire is present, any large degrees of distortion would be evident by an overall distortion of the profile (e.g., consistent taper from high to low temperatures over the entire length). The only pile showing any significant evidence of this type of bar movement is Pile 10. Coincidentally, this is also one of the piles from which only partial data was recovered, advancing the notion that excessive movement of the bar caused conflict with the reinforcing cage, resulting in damage to the wires.

Aside from Pile 10, a few of the other profiles exhibited a slight taper that could be interpreted as bar movement, but without inclination measurements or additional thermal measurements, there is not enough information to discern this from shaft dimensions, so all piles were analyzed the same, using hyperbolic end corrections and traditional T-R conversions. The results of these analyses are shown in Figure 5.23 - 5.33. Also shown in each figure, is the radius of each pile as determined from construction logs, which provided the number of pump strokes for every one foot of auger withdrawal. As a rough means of comparison with TIP computed radius profiles, the pump strokes were grouped into 10ft segments and converted to pile radius based on the field calibrated volume of concrete for each stroke (square marker data points on right in Figures 5.23 - 5.33). Unlike the shafts in Case Studies 1 and 2, these were production piles thus were not extracted and measured for verification.

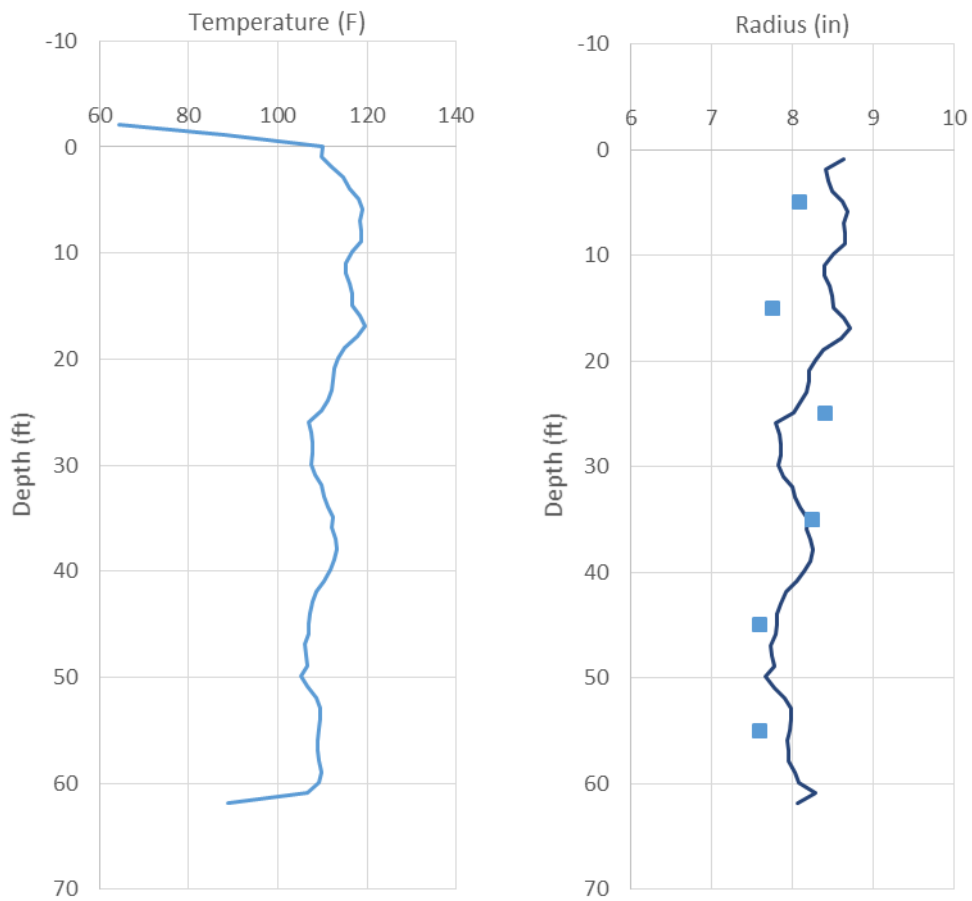


Figure 5.23. Shaft EP1 raw temperature profile (left); interpreted results (right)

Observations:

- Thermal data shows both top and bottom of pile
- Only subtle variations in temperature versus depth; no bar inclination evident
- Pump stroke computed radius generally agrees with predicted radius
- Integrity assessment reasonably successful; pile is good

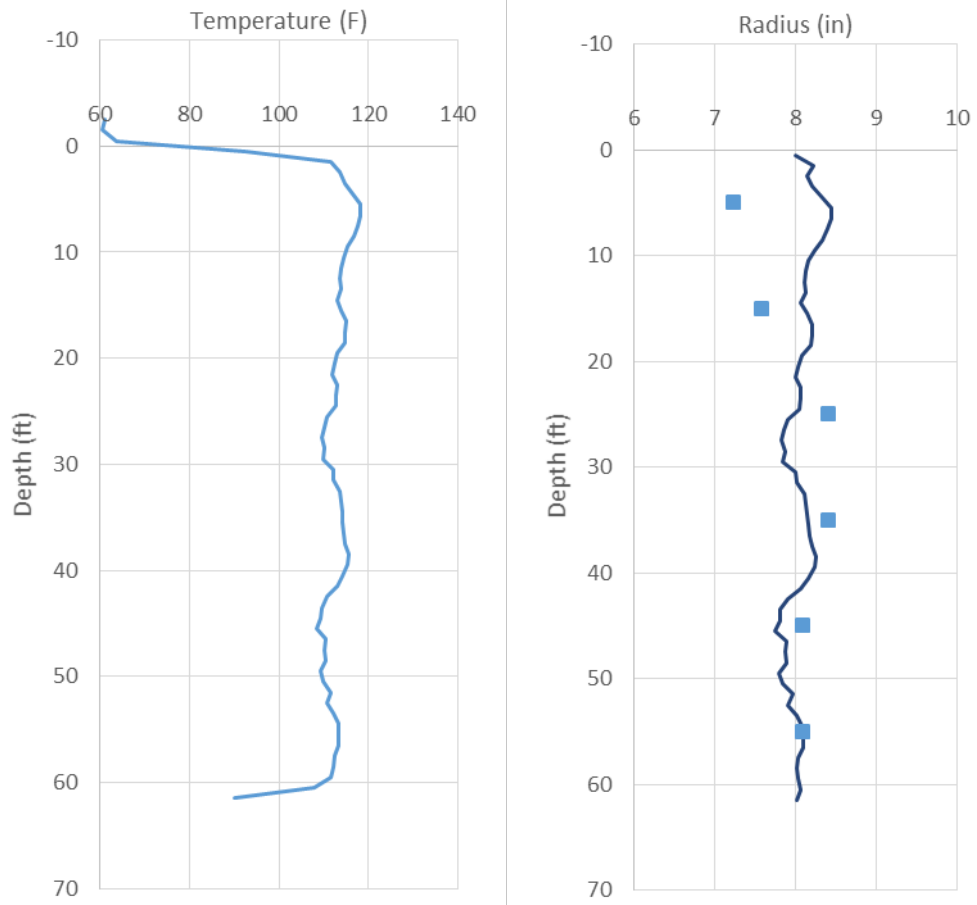


Figure 5.24. Shaft EP2 raw temperature profile (left); interpreted results (right)

Observations:

- Thermal data shows both top and bottom of pile
- Only subtle variations in temperature versus depth; no bar inclination evident
- Pump stroke computed radius generally agrees with predicted radius
- Integrity assessment reasonably successful; pile is good

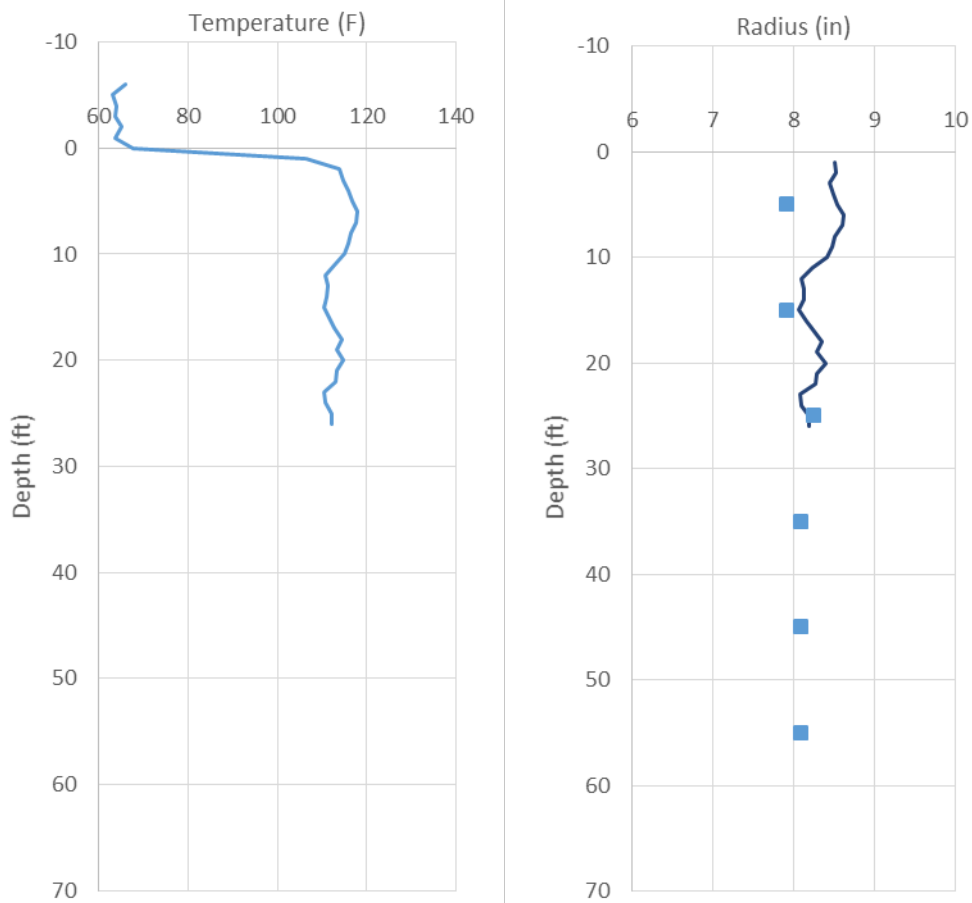


Figure 5.25. Shaft EP4 raw temperature profile (left); interpreted results (right)

Observations:

- Thermal data only shows top of pile which appears normal
- Only subtle variations in temperature versus depth for first 25ft; no bar inclination evident
- Pump stroke computed radius generally agrees with predicted radius
- Integrity assessment unsuccessful; broken wire prevented full analysis

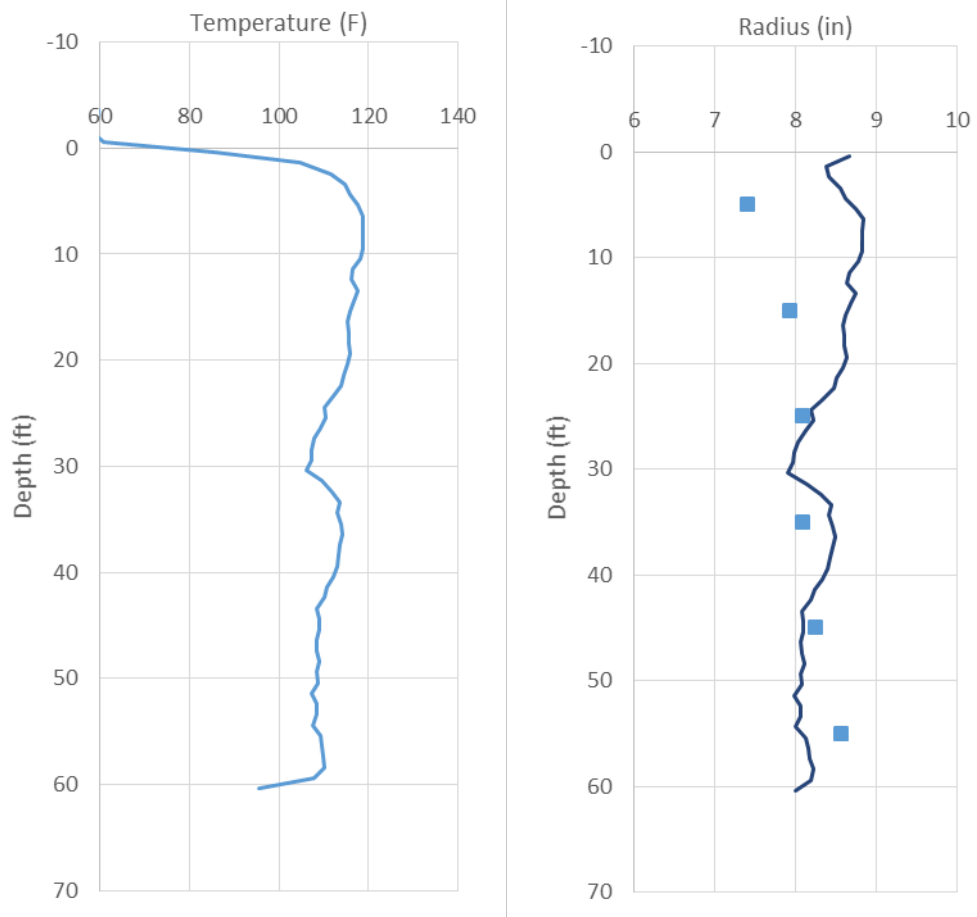


Figure 5.26. Shaft EP6 raw temperature profile (left); interpreted results (right)

Observations:

- Thermal data shows both top and bottom of pile
- Some variation in temperature with depth; bar inclination may be present
- Pump stroke computed radius maybe in conflict with predicted radius
- Integrity assessment was reasonably successful; pile is good based on 7-in nominal design radius and predicted effective radius exceeds that value throughout.

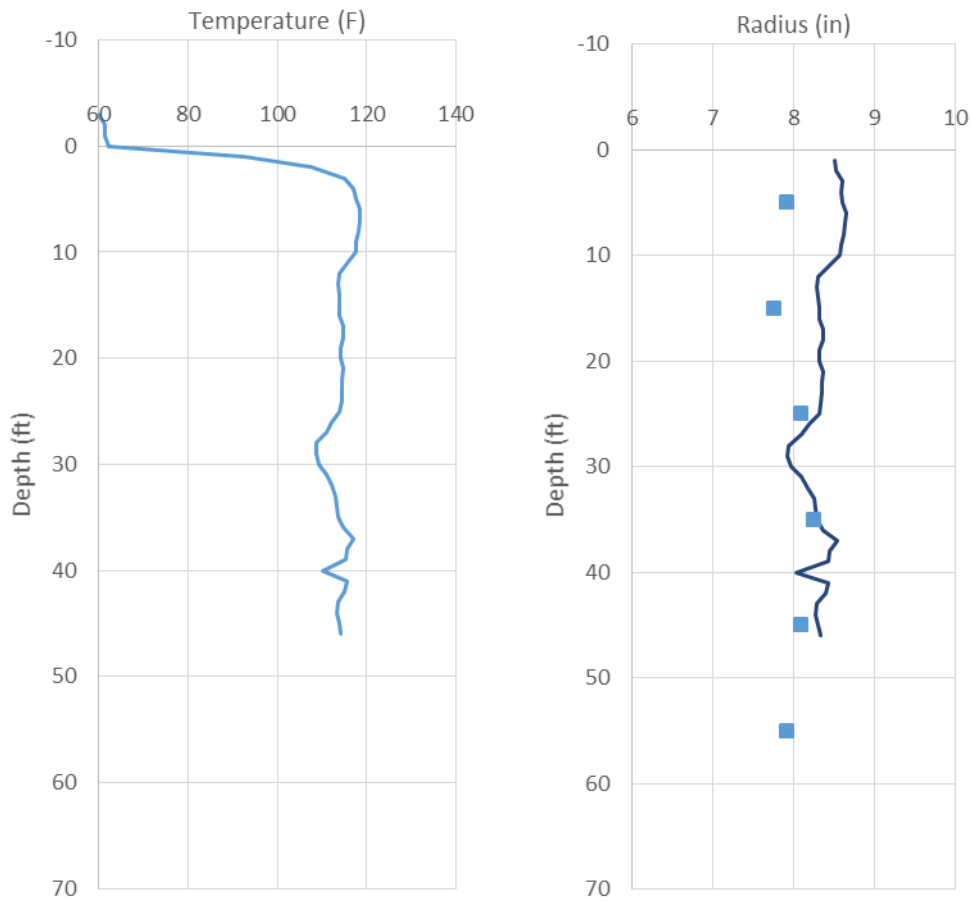


Figure 5.27. Shaft EP7 raw temperature profile (left); interpreted results (right)

Observations:

- Thermal data only shows top of pile which appears normal
- Only subtle variations in temperature versus depth for first 45ft; no bar inclination evident
- Pump stroke computed radius generally agrees with predicted radius
- Integrity assessment unsuccessful; broken wire prevented full analysis

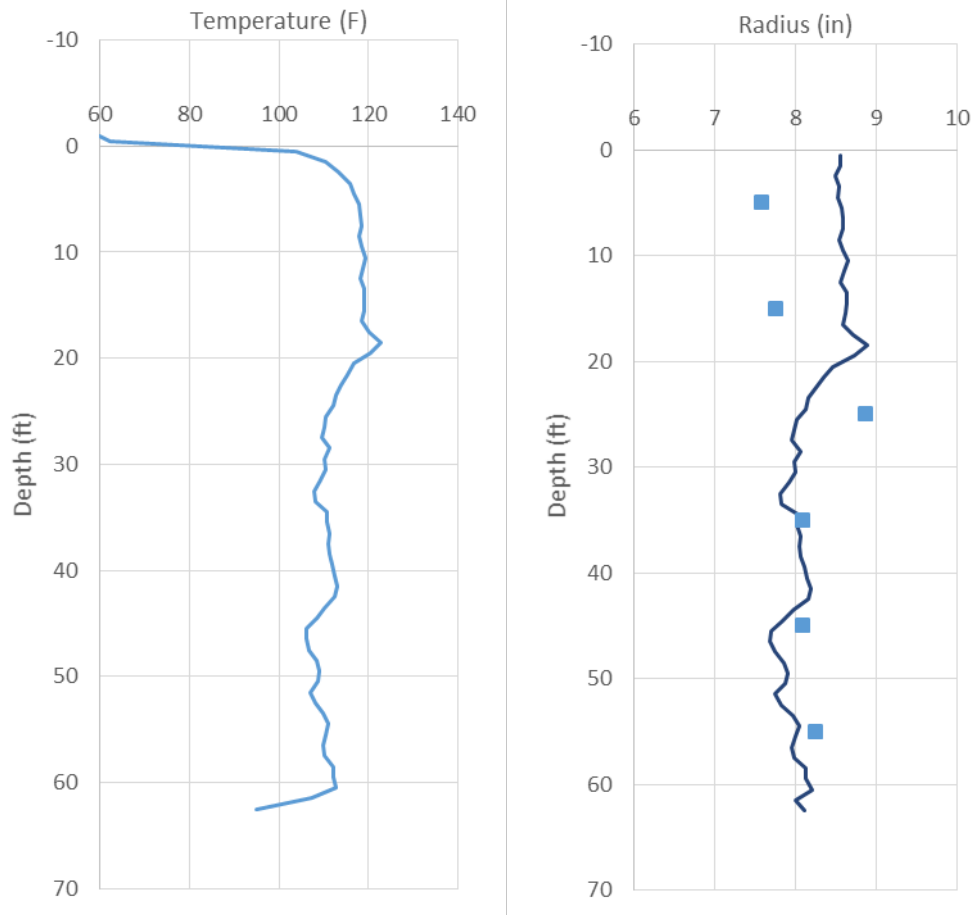


Figure 5.28. Shaft EP8 raw temperature profile (left); interpreted results (right)

Observations:

- Thermal data shows both top and bottom of pile
- Some variation in temperature with depth; bar inclination may be present
- Pump stroke computed radius generally agree with predicted radius
- Integrity assessment was reasonably successful; pile is good based on 7in nominal design radius and predicted effective radius exceeds that value throughout.

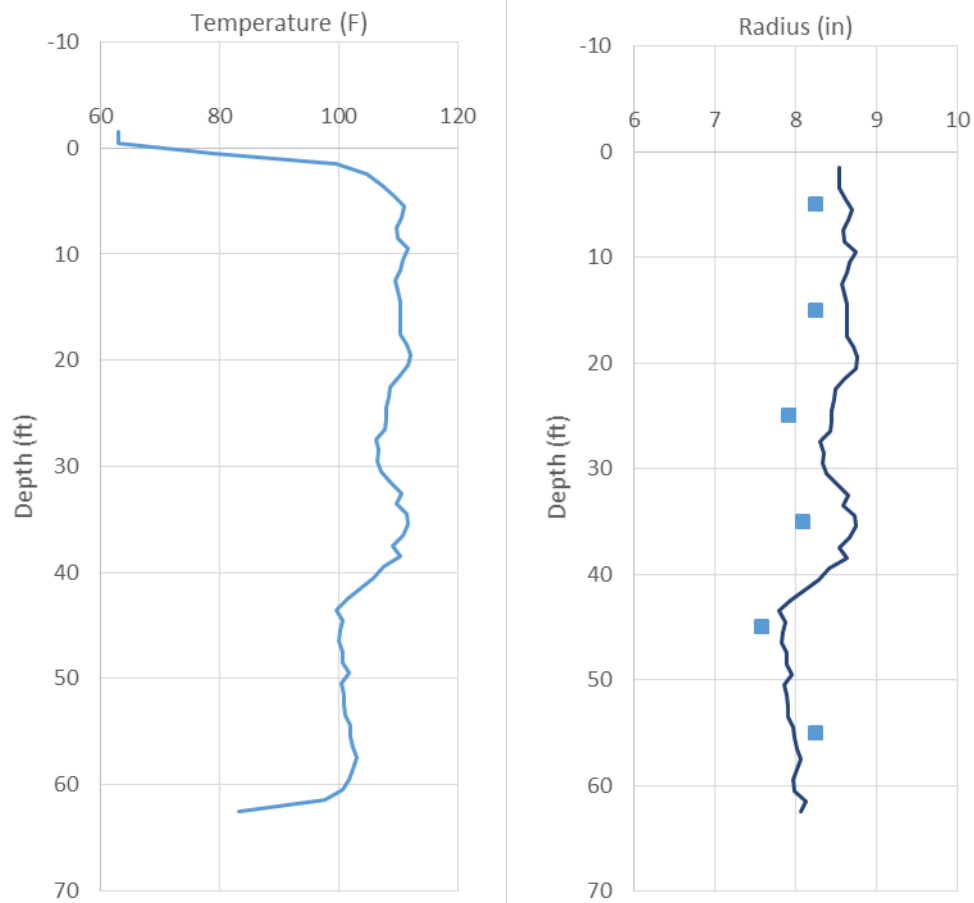


Figure 5.29. Shaft EP9 raw temperature profile (left); interpreted results (right)

Observations:

- Thermal data shows both top and bottom of pile
- Straight/vertical temperature profile; no bar inclination evident
- Small step in pile at 45ft; profile still straight thereafter
- Pump stroke computed radius generally agrees with predicted radius
- Integrity assessment reasonably successful; pile is good

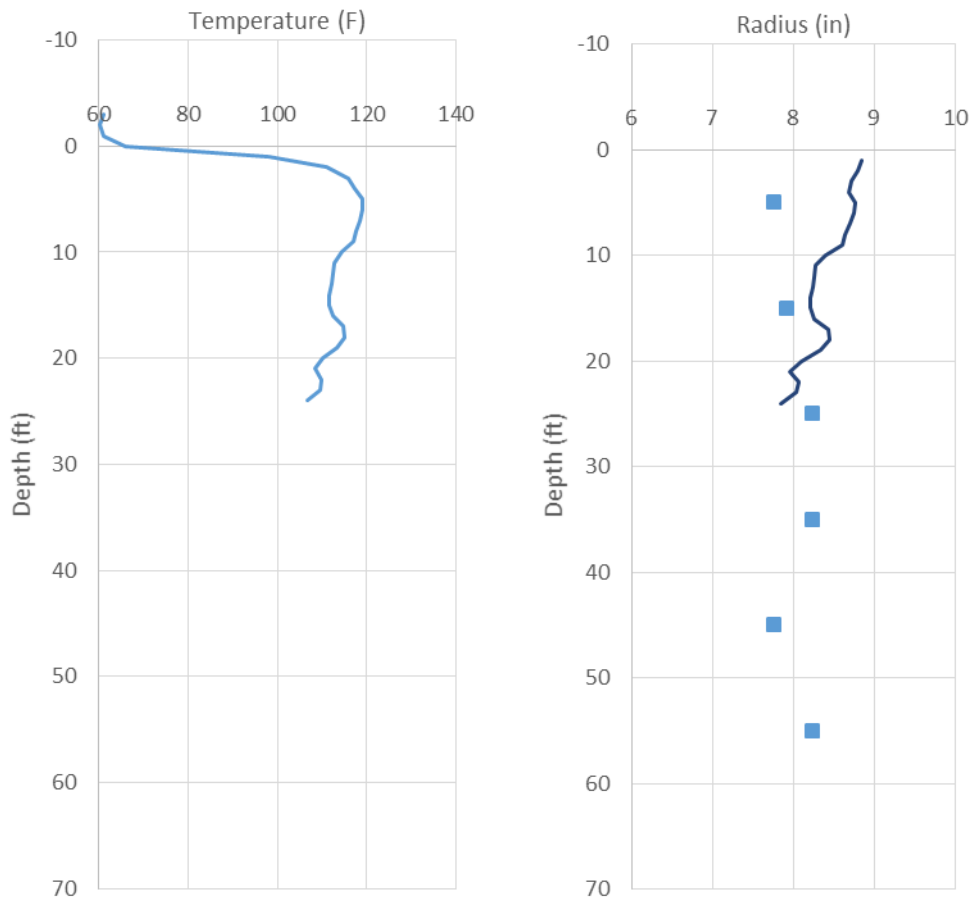


Figure 5.30. Shaft EP10 raw temperature profile (left); interpreted results (right)

Observations:

- Thermal data only shows top of pile which appears normal
- Variations in temperature versus depth for first 25ft; may indicate bar inclination
- Pump stroke computed radius versus predicted radius inconclusive
- Integrity assessment unsuccessful; broken wire prevented full analysis

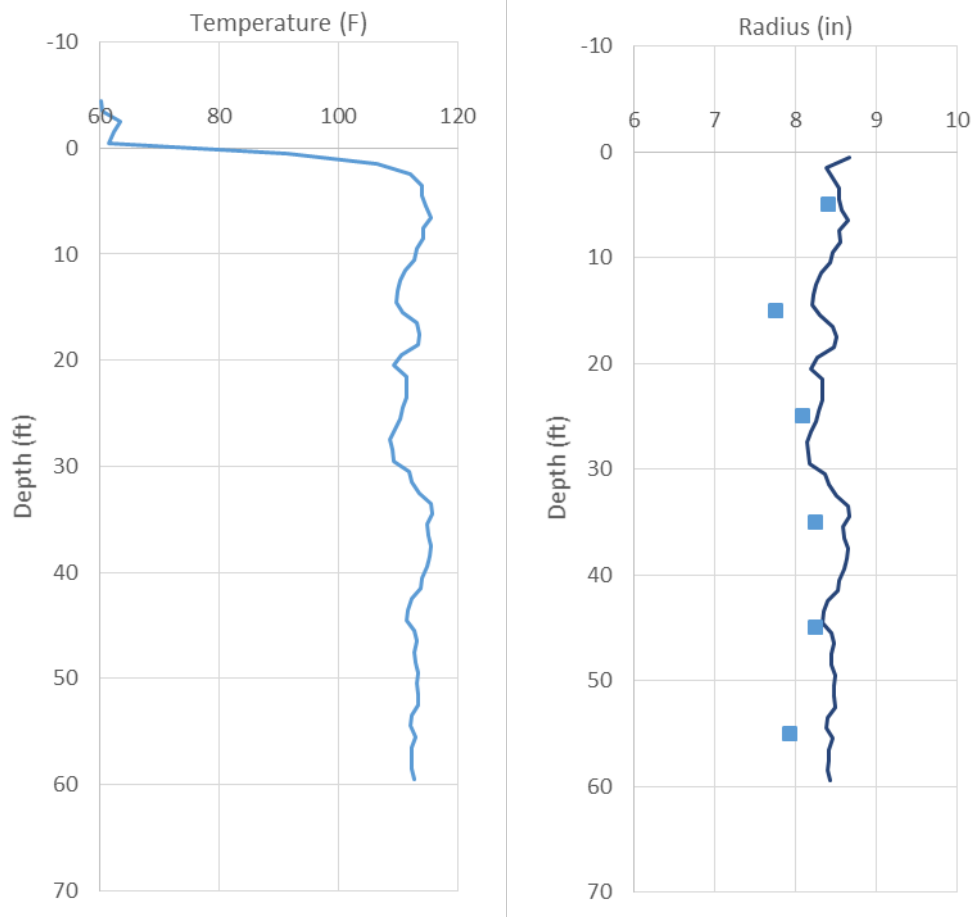


Figure 5.31. Shaft EP11 raw temperature profile (left); interpreted results (right)

Observations:

- Thermal data shows top but not the bottom of pile
- Pile extends deeper than reinforcing bar (bottom most thermal sensor)
- Straight/vertical temperature profile; no bar inclination evident
- Pump stroke computed radius generally agrees with predicted radius
- Integrity assessment reasonably successful; pile is good

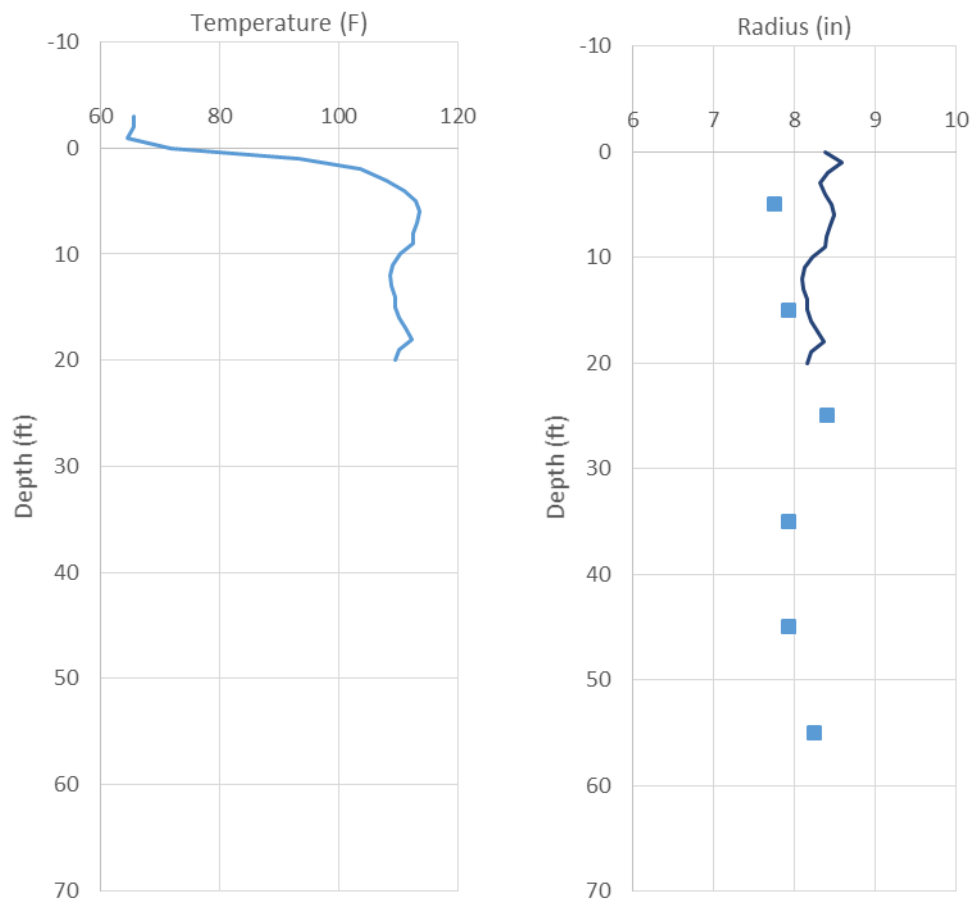


Figure 5.32. Shaft EP12 raw temperature profile (left); interpreted results (right)

Observations:

- Thermal data only shows top of pile which appears normal
- Only subtle variations in temperature versus depth for first 20ft; no apparent bar inclination over that depth
- Pump stroke computed radius versus predicted radius inconclusive
- Integrity assessment unsuccessful; broken wire prevented full analysis

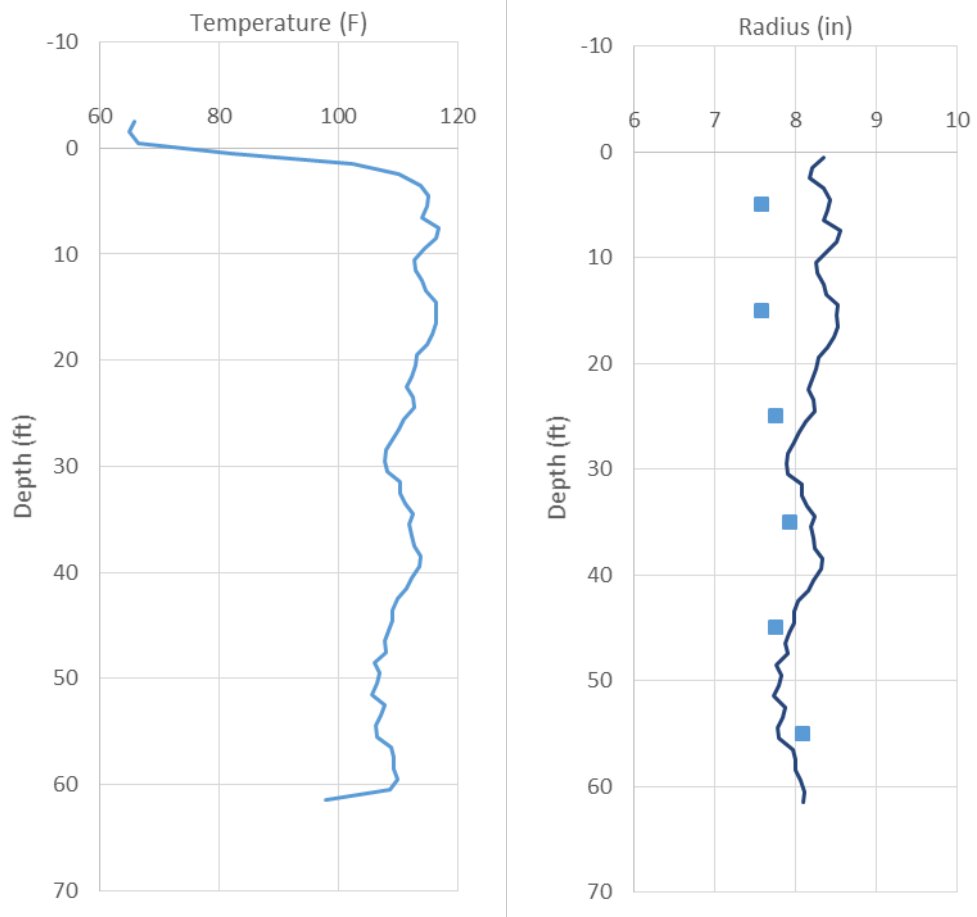


Figure 5.33. Shaft EP13 raw temperature profile (left); interpreted results (right)

Observations:

- Thermal data shows both top and bottom of pile
- Straight/vertical temperature profile; no bar inclination evident
- Small step in pile at 45ft
- Pump stroke computed radius generally agrees with predicted radius
- Integrity assessment reasonably successful; pile is good

**5.2.4 Case Study 4:** 30in auger-cast piles with full reinforcing cage – comparison between 2- and 4-wire instrumentation.

This site consisted of two 30in diameter, 20ft long auger-cast piles constructed with full-length 14in square reinforcing cages which protruded from the bottom of pre-cast concrete columns for a sound wall. One of the piles was instrumented with four thermal wires fastened to each corner of the square cage and the other with only two wires fastened to opposite corners of the cage. Figure 5.34 shows the cage instrumented with four wires and Figure 5.35 shows the cage with only two wires being placed in the grout.



Figure 5.34. ACIP reinforcing cage instrumented with four thermal wires



Figure 5.35. Cage instrumented with two wires being placed into grout

Figures 5.36 and 5.37 show the analysis results of the four and two wire systems, respectively. Note that in each case, the top two sensors were located inside the pile, thus are included in the results, however they were displaced away from the cage due to the 1.5ft portion of the pre-cast column that extended into the grout. Aside from this, the analysis of the four wire system yielded a reasonably straight pile with a radius between 15 - 16in and cage movement of just under an inch in the direction of wires 1 and 3 from 6 - 10ft, transitioning to just over an inch of movement in the direction of wires 2 and 4 at the bottom of the pile. Conversely, analysis of the two wire system yielded a pile radius that tapers from 16.5in at the top to 15in at the bottom with cage movement, in the direction of the two wires that were present, increasing from zero at the top to almost 2in at the bottom (Figure 5.37). In both piles, the reinforcement cage (and last thermal sensor) did not extend to the bottom of the piles as no temperature reduction typical of bottom conditions was present.

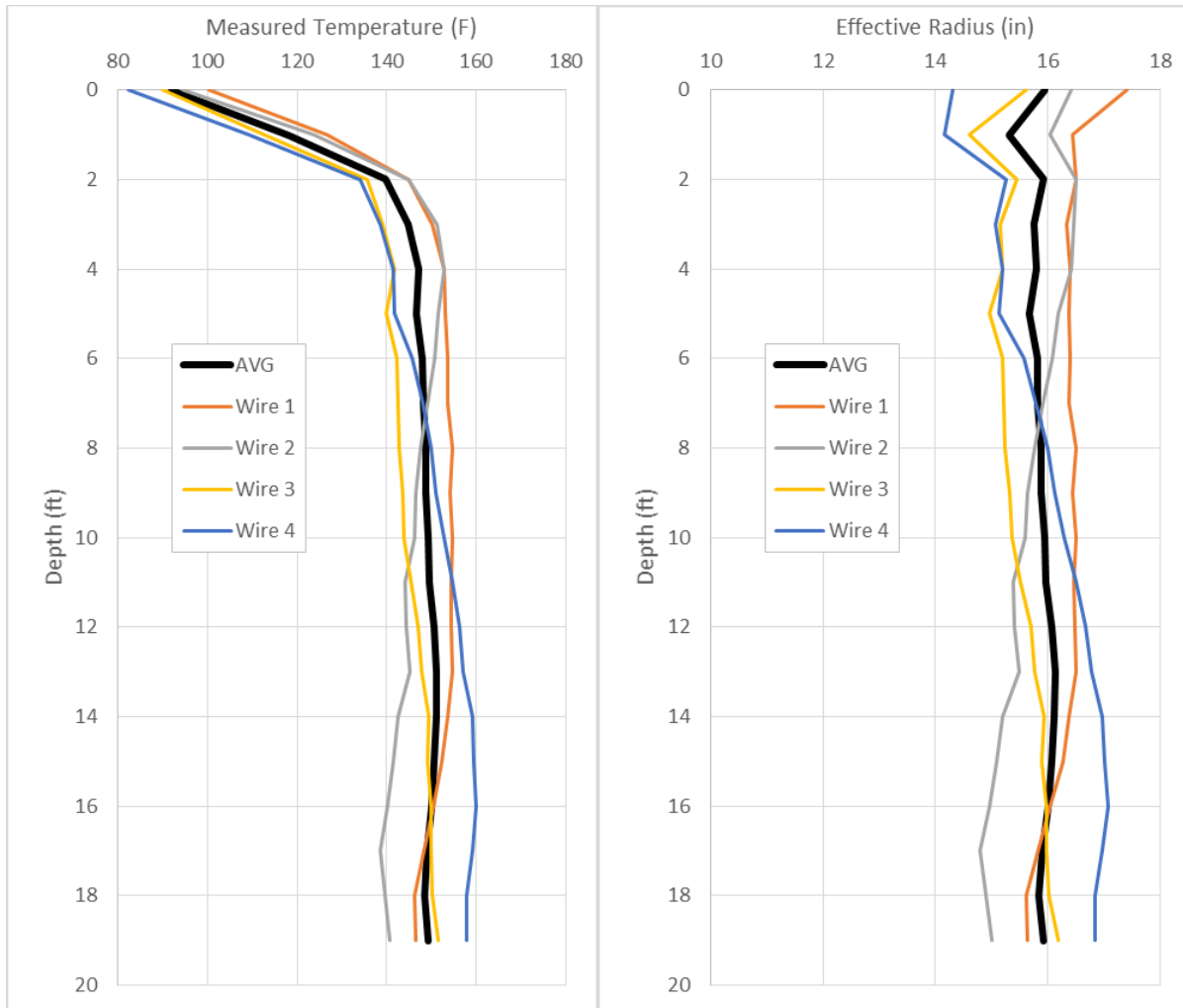


Figure 5.36. ACIP with full reinforcing cage instrumented with four thermal wires

At first glance, it appears that the two wire system is simply not sufficient, and that if two more orthogonal wires had been present, they would have counteracted the one directional tapering effect and produced a normal average, as in Figure 5.36. Closer examination however, reveals that this is not necessarily the case. Looking back at the results of Figure 5.36, which does show cage movement in both directions, it is easy to imagine that if either of the two pairs of wires were removed from analysis, the resulting average profile and cage offset would be the same as what is already shown, dispelling the notion that only two wires would yield a wildly inaccurate profile like that shown in Figure 5.37. Conversely, the two wire pile may have experienced significant cage movement in both axes throughout the entire length of the pile even though one side temperature remained constant. Figure 5.38 illustrates this type of cage movement overlaying the isothermal contour model for a 30in pile.

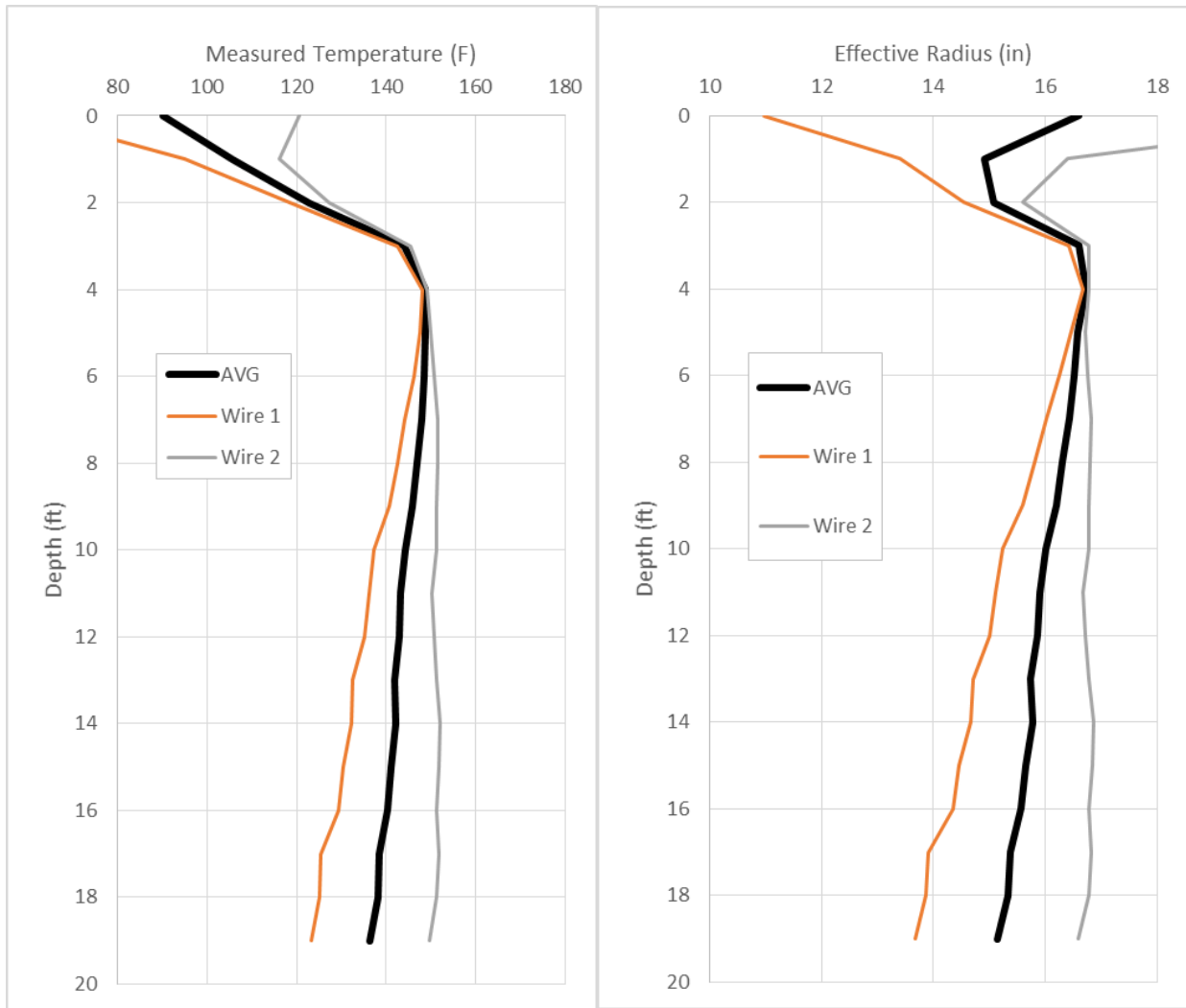


Figure 5.37. ACIP with full reinforcing cage instrumented with two thermal wires

Figure 5.38 shows the isothermal contours from a 30in auger-cast pile model, overlain with the cage of fixed physical dimensions. The initial position of the cage is shown centered within the pile, with wires 1 and 2 both measuring 148°F, as shown in Figure 5.37 at a depth of about 4ft. The illustrated cage was then moved over the contour lines to the only two positions that would have the temperatures measured at the bottom of the pile, which was approximately the same for Wire 2 and about 25°F cooler for Wire 1. This exercise produced a reasonable amount of cage movement, given the size of the shaft and cage, but the results also revealed the temperatures that the other two wires, had they been present, would have measured temperatures of 118°F and 151°F making the average 135°F which is the same as the two wire average from the field data.

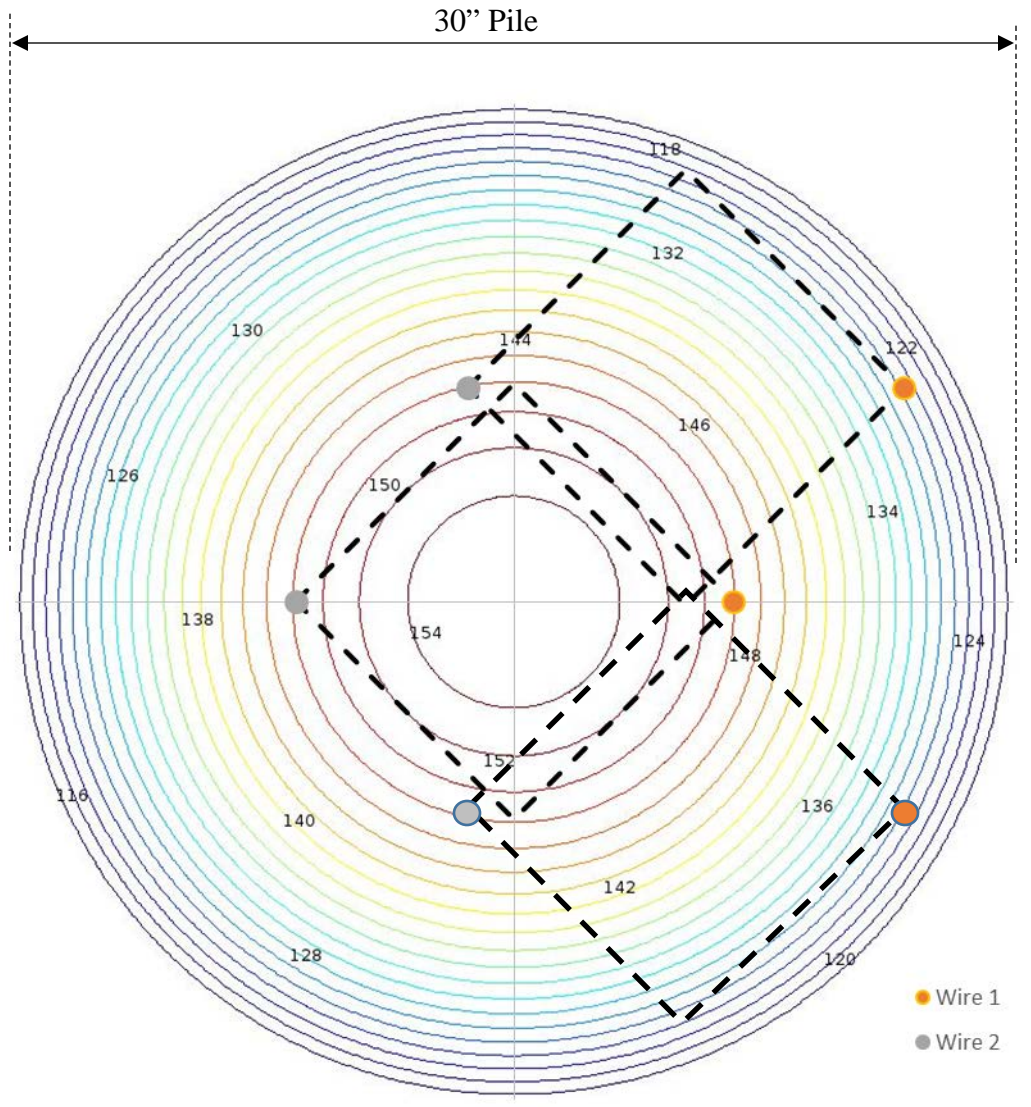


Figure 5.38. Isotherms for 30in diameter auger-cast overlain by a centered square cage and the only two possible positions that produce the two opposite side temperature measurements from the bottom of the pile

The inability to use the average temperature profile in this scenario is a phenomenon directly related to the cage-shaft diameter ratio where the cage boundaries reside in the non-linear portion of the radial temperature distribution (regions of uniformly spaced isotherms).

## *Chapter Six: Conclusions*

Drilled shafts and auger-cast piles have virtually no commonalities excepting that they are both cast-in-place, reinforced concrete deep foundation elements. The design, construction, inspection, reinforcement scheme, quality assurance, and quality control all differ and therefore do not exhibit the same types of problems or anomaly formation. Post-construction non-destructive test methods for auger-cast piles are less robust in assessing the overall element and hence this study focused on increasing the acceptance confidence via new thermal integrity methods.

The thermal integrity test has proven to be an effective method to evaluate newly constructed drilled shafts where anomalies inside and outside the reinforcing can be detected, rebar cage alignment can be confirmed, and cross sectional dimensions as well as concrete cover can be determined. However, relative to shafts, very few auger-cast piles have been tested with this method as the plurality of standard integrity access tubes typical of drilled shafts are not commonplace. It was the goal of this research to identify the limits of thermal integrity technology with regards to auger-cast pile applications. The project involved four tasks involving: literature review, numerical modeling, development and feasibility assessment of probe based inclination measurements, and field testing (with analysis). A summary of the latter three tasks is presented below.

### **6.1 Numerical Modeling**

Numerical evaluations consisted of two types of analyses: forward finite difference models that produced the anticipated temperature distribution within an auger-cast pile and curve fitting of field collected data to identify statistical trends.

While numerical models are often fraught with limitations associated with accurately inputted parameters, such models are a convenient mechanism to identify trends that will occur regardless of actual field conditions. Forward models vary from inverse models where: forward models input a system or set of conditions and predict the outcome; inverse models input field measurements (outcomes) and predict what input would be needed to create the outcome. In this case, forward models were used to both qualitatively and quantitatively assess: the effects of changing environmental boundaries, the locations and plurality of locations required to provide enough information to satisfactorily assess integrity, and trends in proper inverse modeling parameters from field data.

Information obtained from forward models was then compared to curve fitted parameters from field data collected from past projects involving drilled shafts and the same trends were observed. The field data was first fitted with hyperbolic tangent models and the parameters from each of the shafts was statistically reviewed to determine the best practice for analyzing field data. Discussed in detail at the conclusion of this chapter.

Numerical modeling also showed that shaft mixes and auger-cast pile mixes do not vary significantly when it comes to thermal analysis and that the time of testing criterion used for shafts is essentially unchanged for ACIP piles (Figure 3.15 and 3.16). Piles should be tested between 18 and 24hr for most cases due to the small diameter of ACIP piles. However, results from test data taken and analyzed over a large time period (up to one day per foot of shaft diameter) showed no appreciable difference in the predicted radius profile. Practical limits to the age of the concrete used in a given analysis should be observed thereby staying within the optimum testing/analysis timeframe.

## **6.2 Probe-based Inclination Measurements**

Eccentricity computations from thermal measurements are based on changes in opposing side local radius values. This is confirmed by noting that a decrease in local radius on one side of the shaft/pile occurs at the same point where the opposite side experiences an increase. In general, these can be interpreted as no changes in shaft dimensions, but rather only cage alignment. Recall, the average temperature profile from temperature measurements taken at the cage location closely reflects the actual shape. This was shown to be true in shafts 3ft in diameter and larger where the cage based measurements are located within the linear portion of the bell shaped temperature distribution curves. Nevertheless, eccentricity predictions assume the cage has moved from a perfectly vertical alignment and the shaft stayed straight. It is conceivable however; that the shaft may not be drilled straight and the cage is vertical after all. Or, there could be some combination of both deviating from vertical. It is in this vein, that probe-based inclination systems were tested which could distinguish between cage movement and shaft verticality changes.

Two inclinometer systems were reviewed that did not use alignment wheels or grooved casing to maintain orientation. Rather, the probe was free to rotate in response to normal wire twist, etc. The systems made use of gyroscopic, rotational accelerometers and 3-D linear acceleration measurements to track the amount of probe rotation and the angle of inclination in a given access tube, respectively. Several prototype thermal probe systems were developed and the limitations of each were noted. Based on the limitations, a modified probe assembly was proposed that could accurately track extreme undulations in an access tube over a 40ft length.

## **6.3 Field Testing and Evaluation**

Data collected from several drilled shaft and auger-cast pile projects were analyzed where the data was collected in a variety of instrumentation schemes including single central wire, single central tube, two wire and four wire systems. The analysis methods also varied from presently used simplified algorithms to more numerical/model-intensive approaches that are not known to the practicing engineering arena. Regardless of data collection method, the data should be collected from all portions of the pile such that both the top and bottom of pile can be identified and analyzed.

Single Wire Systems. In general, single centrally located embedded wire measurements can confirm the integrity of a pile but only when there is no problem with the pile, bar location and the data. This means that if the central bar moves from a straight/vertical position, there is not enough supporting data to quantify the degree of bar eccentricity or whether reduced temperature readings are caused by bar movement or from actual changes in the pile cross section. Additionally, if the wire has been severed or for some reason fails to provide data, there is no redundancy or means to retrieve the necessary information. Qualitatively, when a single wire shows a reduction in temperature with a strong trend (which may be linear) it is reasonable to assume that this could indicate a sound pile with a deviated center bar. These types of subtle transitions are not in itself indication of a bad pile; it is further reasonable to assume that drastic changes from such a trend/transition would be indication of a local bulge or neck. Note that a linear or slightly curved trend is simply an indication of the bar location relative to the center of pile; if curved, the bar may have taken on a curved final position. No such cases were found in the data analyzed.

Single Tube Systems (probe). Single tube systems can have the same limitations if standard drilled shaft analysis methods are used. However, given the plurality of infrared sensors in probe systems, the gradient formed by measurements on four sides of the central tube can be used to show tube eccentricity and therefore explain why the average temperature at a particular depth is higher or lower than other portions of the pile. For instance, when all sensors read the same, the tube is centered in the concrete/grout mass at that depth. If the average of all sensors is lower or higher than the rest of the shaft (again with all sensors reading the same) then this confirms a neck or bulge, respectively. When the average is lower than the rest of the pile, but the sensors are not registering the same temperature, then the lower average can be qualitatively explained by eccentricity of the tube relative to the center of pile. Quantitative determination of the amount of eccentricity requires thermal modeling. A quantitative approach was attempted in Chapter 5, wherein the gradient between temperatures on opposing sides of a center tube were signal matched to computer-generated bell curves for the shaft to determine both radius and bar offset simultaneously. The results were promising, however the process was tedious and required extensive modeling to produce the signal matched bell curves.

Single wire and single tube thermal systems do not produce a temperature to radius conversion that is easily approximated by a linear relationship (Figures 5.15 - 5.17), due to the small size and the location of the measurements. Some users have suggested introducing the soil temperature as a zero radius coordinate which increases the linearity of the T-R relationship for small shafts/piles (e.g., less than 3ft diameter). For all diameter shafts/piles, the true relationship between temperature and local radius is a hyperbolic tangent function which to date has not been easily defined from field measurements. An approach to try to define this function for a particular shaft was attempted in Chapter 5, again with promising results, but again, modeling was required in order to define some of the parameters.

Some of the unknowns associated with single tube systems can be offset through the use of 3-D inclination measurements discussed earlier in Chapter 4. No field tests were performed with the

new inclination system, so the true applicability has not been fully vetted, however continued research in this area could lead to enhanced TIP capabilities not only with auger-cast piles, but for all drilled shafts. These types of measurements would not only provide an additional set of known boundary conditions to reinforce the analysis process of TIP data, but could also be used as a means of detection for the severe types of cage misalignment/distortion that TIP cannot easily quantify, such as that in Figure 4.2 (twisted cage).

Double Wire Systems. Where the ASTM D7949 standard suggests that a single wire can be used for small diameter shafts/piles, results of single and double wire systems suggest that more should be used. For two measurement locations (plan view) in drilled shafts (not typical auger-cast piles), the cage radius places the locations far enough from the center that a simple average profile of the two is representative of the shaft shape. For example, a four location data set will produce essentially identical average profiles from the 1 - 3 and 2 - 4 locations as these locations lie in the linear portion of the temperature distribution with respect to radius. The location of cages in smaller diameter auger-cast piles often do not exist within the linear region and therefore the simple average profile may not represent the shaft shape. A complex method of analyzing the cage eccentricity and overall pile integrity was shown to be possible for two wire systems, but which required thermal modeling to fully understand the meaning. Similar to single wire or single tube systems, however, if the thermal profile is straight and does not show trends of decreasing temperature, the pile can immediately be accepted without further analysis.

Four Wire Systems. As noted, smaller cages do not produce meaningful average profiles with two wires, but four wires were shown to provide enough information to do so. The four wire pile tested (with small diameter cage) showed the average profile could prove the pile to be good despite having significant cage eccentricity. The data set analyzed was in keeping with Figures 3.25 - 3.26 which showed that two wires would produce a reasonable average when the eccentricity aligned with the direction of the two wires. So perhaps coincidentally, this data set was a special case where the two wire averages (e.g. 1 - 3 and 2 - 4) were essentially identical and both were straight.

## **6.4 Summary**

While single wire systems can provide some insight, it is not likely to be a robust method to always ascertain the integrity of auger-cast piles. Single tube systems are slightly better but require a higher level of analysis not presently included in commercially available systems. However, note that a single tube does not provide reinforcement so it requires a side-by-side reinforcing bar which may be adversely affected by the tube presence. Two wire systems are only marginally better than single and perhaps not worth the extra cost. Finally, four measurement location systems are the most robust; however, most commonly used auger-cast piles are too small to afford the space for the cage required (e.g. single bar piles). Therefore, a minimum of 24in diameter pile is recommended for FDOT applications that require a more robust QA/verification program. This is based on a 4.5in minimum cover which makes the cage-based measurement locations (4 minimum) to be approximately 14 - 15in diameter (Figure 6.1).

Note that the location of the cage just barely falls in the linear portion of the bell curve for a 24in pile.

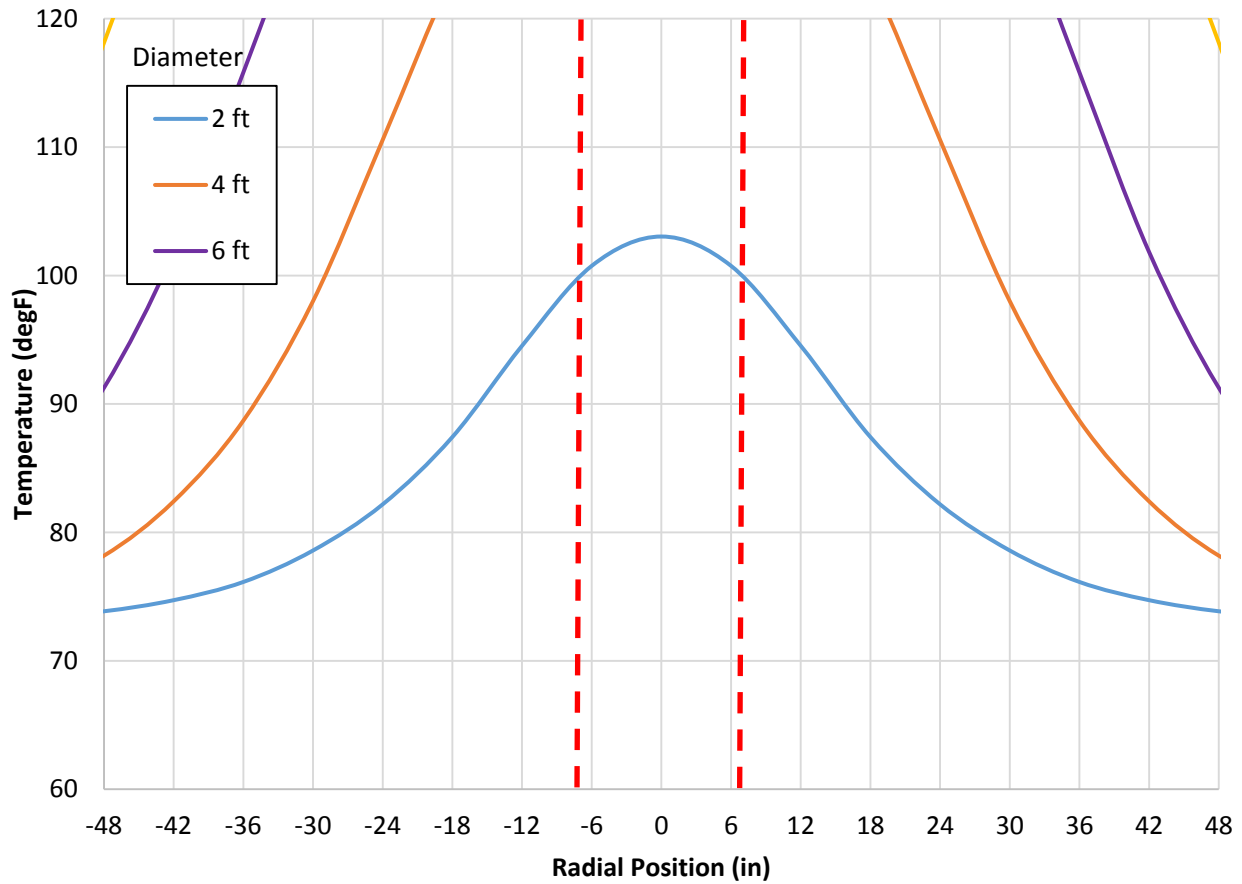


Figure 6.1. Rationale for determining smallest 4 tube (or wire) pile with full cage.

The average of opposing temperature measurements represents the shape of the shaft when the measurement locations are closer to the shaft edge than center and fall within the linear portion of the “bell curve.” More centrally located cages cannot directly apply that method. Further, measurements taken from more central regions of a shaft or auger-cast pile result in higher temperatures for a given radius and therefore are better suited to non-linear, hyperbolic tangent T to R relationships. However, an alternate methodology where the soil temperature is used to define zero radii may provide a closer estimate of the actual pile dimensions. Figure 6.2 shows the data presented in Figure 5.14 reevaluated using this method. This suggests that adapting the single point shaft method to a single point T-soil for augercast piles with center bar measurements is a reasonable approach.

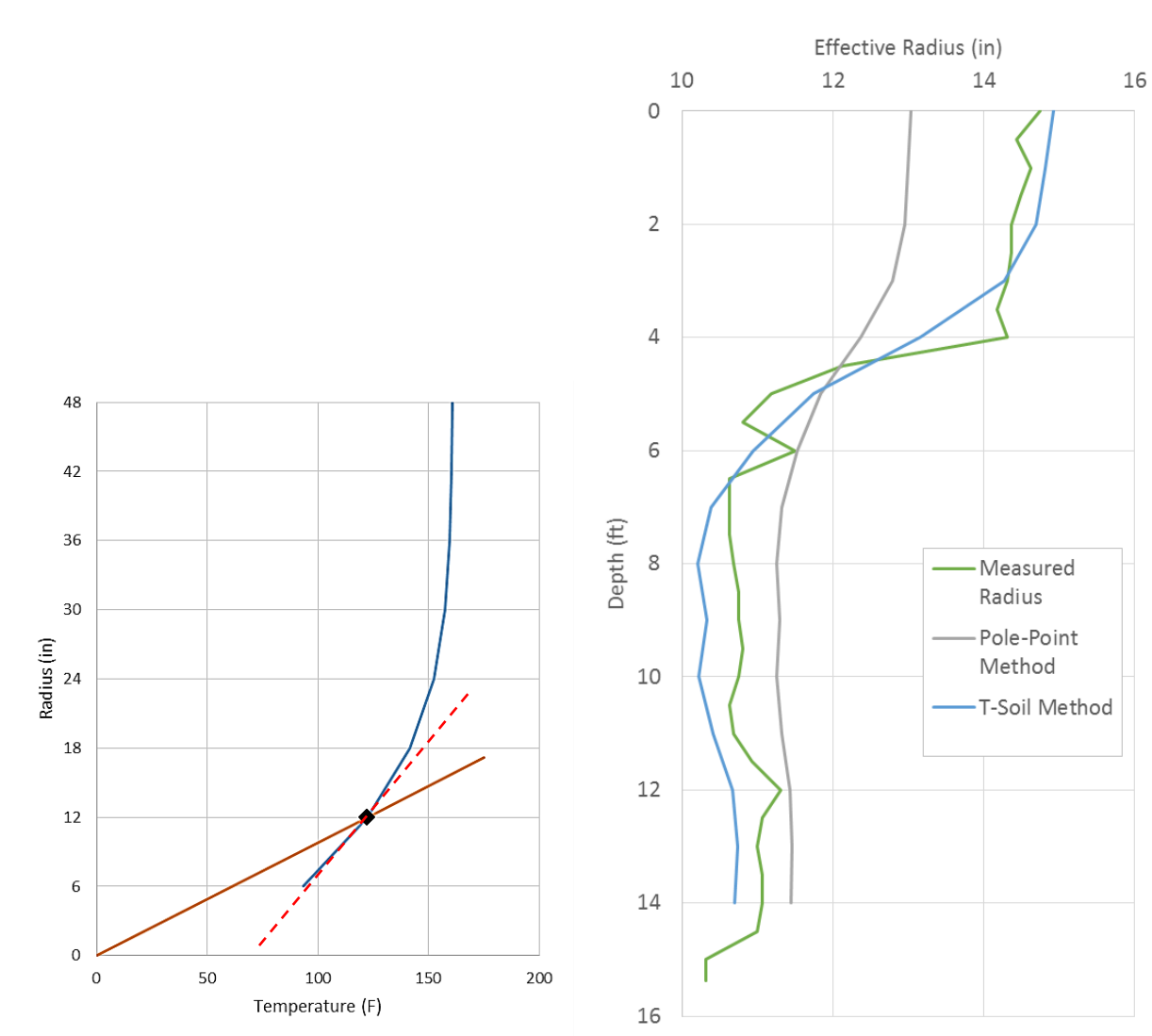


Figure 6.2. Alternate T-soil method for determining the T to R correlation.

## 6.5 Recommendations for Analyzing TIP Data

Six input parameters are required when analyzing field data whereby the temperature profile can be converted to a radius profile. Therein, the shape of the top and bottom of the shaft can be predicted by adjusting the temperature profile to account for energy dissipation both radially and longitudinally where the rest of the shaft dissipates only radially. Proper selection of the parameters is vital; these include: top of shaft inflection temperature, the top and bottom transition lengths, the top and bottom inflection depths/elevation, and the local at-depth soil temperature.

The top of shaft inflection temperature was found to be closely related to the average air temperature over the 12hr period prior to testing/time of evaluation (Figure 3.3). Further, in winter months, the inflection temperature closely aligned with the highest daily temperature; in

summer months aligned more closely with the lowest daily temperature; these values tended to be moderated by the local soil temperature (Figure 3.13). In general, the inflection temperature should not be outside the daily temperature extremes for the prior day.

The transition length for the bottom and top of shaft/pile follows a square root of time dependency where the most appropriate (average) value should be expressed as  $0.4\sqrt{\text{time}}$  (time in hours). Based on the frequency distribution of all observations, this value was shown vary within one standard deviation to be between  $0.3$  and  $0.5\sqrt{\text{time}}$  (Figure 3.12). Values that produce a good fit between the hyperbolic tangent function and the measured data that use transition lengths outside this range should be considered incorrect and indicate an abnormally shaped end (relative to a square ended cylindrical prism). In such cases, a value corresponding to  $0.4\sqrt{\text{time}}$  should be applied to show the most probable shape.

The top and bottom of the shaft elevations should align closely with the hyperbolic tangent inflection point location which indicates that the change from energy producer to energy dissipater. However, a single hyperbolic tangent function is used to represent the two material types. As a result, the best fit inflection point locations were shown to slightly move outside the shaft progressing farther away with time (Figure 3.14). If the inflection point location is ever found to be best fit inside the shaft or is disparate from the recommended/shown range, that value should not be used. Again, in such cases, an inflection point location corresponding to Figure 3.14 should be used in conjunction with the most appropriate transition length note above.

With exception to those cases where geothermal heat sources are present (not in Florida), the average annual air temperature for a given geographical location provides a direct indication of the at-depth constant temperature boundary condition used to fit the bottom of shaft hyperbolic tangent correction/adjustment. This value is perhaps the most trustworthy input parameter when analyzing field data and converting from temperature to radius profiles.

In cases where any cast-in-place element extends out of the ground (e.g., into water or air) or is known to have changed the external heat diffusing environment, the analysis should incorporate a mid-shaft (or pile) correction. Without a change in external environmental conditions over the length of a shaft or pile, intermediate corrections should not be used and are not warranted. Further, the analysis should take into consideration the strength/reliability of the concrete/grout volume values and when possible use known boundary conditions to adjust volume. Examples include known inspect-able dimension such as the top of shaft or permanent casing diameter. However, permanent casing in itself does not imply a perfect section.

## References

- Anderson, Byron Keith. (2011). *Thermal Integrity Profiling Instrumentation Development* (Master's Thesis). Tampa, FL; University of South Florida. <http://scholarcommons.usf.edu/etd/2987>
- Arya, S. Pal. (2001). *Introduction to Micrometeorology*. 2<sup>nd</sup> Edition. San Diego, CA. Academic Press. p.48.
- ASTM Standard D7949-14. "Standard Test Methods for Thermal Integrity Profiling of Concrete Deep Foundations," ASTM International, West Conshohocken, PA.
- Bogue, Robert H. (1947). *The Chemistry of Portland Cement*. New York. Reinhold Publishing Corporation.
- Brown, Dan A., Dapp, Steven D., Thompson, W. Robert, and Lazarte, Carlos A. (2007). *Design and Construction of Continuous Flight Auger (CFA) Piles*. Geotechnical Engineering Circular No. 8. FHWA-HIF-07-03.
- Brown, Dan A., Turner, John P., Castelli, Raymond J. (2010). *Drilled Shafts: Construction Procedures and LRFD Design Methods*. NHI Course No. 132014. Geotechnical Engineering Circular No. 10. FHWA NHI-10-016.
- Caltrans (2005). *Method of Ascertaining the Homogeneity of Concrete in Cast-in-Drilled-Hole (CIDH) Piles using the Gamma-Gamma Test Method*. California Test 233. State of California Business, Transportation, and Housing Agency. Sacramento, CA.
- COLOG. (2010). *4-Pi Gamma-Gamma Density Logging (GDL) Investigation of One Drilled Shaft Foundation* (Final Report). COLOG, a division of Layne Christensen Company. Lakewood, CO, March 22, 2010.
- Folliard, K.J., Juenger, M., Schindler, A., Riding, K., Poole, J., Kallivokas, L.F., Slatnick, S., Whigham, J., Meadows, J.L. (2008). *Prediction Model for Concrete Behavior* (Final Report). Austin, TX. Center for Transportation Research. The University of Austin at Texas. FHWA/TX-08/0-4563-1.
- Ge, Zhing. (2005). *Predicting temperature and strength development of the field concrete* (Doctoral Dissertation). Iowa State University. UMI No. 3200417.
- Hollema, D.A., and Olson, L.D. (2003). "Crosshole Sonic Logging and Velocity Tomography Imaging of Drilled Shaft Foundations." Proceedings from International Symposium

(NDT-CE 2003), *Non-Destructive Testing in Civil Engineering 2003* in Berlin, Germany.

Incropera, Frank P., and Dewitt, David P. (2007). *Fundamentals of Heat and Mass Transfer*. 6<sup>th</sup> Edition. New York, NY. John Wiley & Sons.

Johnson, K. (2014). "Temperature Prediction Modeling and Thermal Integrity Profiling of Drilled Shafts." Proceedings from ASCE Geo-Congress 2014. Pp. 1781-1794.

Kranc, S., and Mullins, G. (2007). "Inverse Method for the Detection of Voids in Drilled-Shaft Concrete Piles from Longitudinal Temperature Scans." Inverse Problems, Design and Optimization Symposium. Miami, FL, U.S.A., April 16-18, 2007.

Mindess, Sidney, Young, Francis J., and Darwin, David. (2003). *Concrete*. 2<sup>nd</sup> Edition. Upper Saddle River, NJ. Pearson Education, Inc.

Mullins, Gray. (2008). "Concrete Hydration Energy: Friend and Foe." Slideshow presented to ACI Florida Suncoast Chapter on March 13, 2008.

Mullins, Gray. (2010). "Thermal Integrity Profiling of Drilled Shafts." The Deep Foundations Institute Journal. Vol.4, No. 2. December 2010. Pp. 54-64.

Mullins, Gray. (2012). "Advancements in Drilled Shaft Construction, Design, and Quality Assurance: The Value of Research." Slideshow presented at the 17<sup>th</sup> Annual Great Lakes Geotechnical/Geoenvironmental Conference (GLGGC). Cleveland, OH. May 24.

Mullins, Gray. (2013). "Advancements in Drilled Shaft Construction, Design, and Quality Assurance: The Value of Research." International Journal of Pavement Research and Technology. Vol. 6 No. 2. March 2013. Pp. 93-99.

Mullins G., and Winters, D. (2011). *Infrared Thermal Integrity Testing Quality Assurance Test Method to Detect Drilled Shaft Defects (Final Report)*. Olympia, WS. Washington State Department of Transportation. Report No. WA-RD 770.1.

Mullins, G., and Winters, D. (2012). "Thermal Integrity Profiling of Concrete Deep Foundations." Slideshow presented at the Association of Drilled Shaft Contractors Expo 2012. San Antonio, TX. March 14-17.

Ozisik, M. Necati. (1993). *Heat Conduction*. 2<sup>nd</sup> Edition. New York, NY. John Wiley & Sons, Inc.

- Palm, Martin. (2012). *Single-hole sonic logging: A study of possibilities and limitations of detecting flaws in piles* (Master Thesis). Royal Institute of Technology, Department of Civil and Architectural Engineering. ISSN 1103-4297.
- Pauly, Nicole M. (2010). *Thermal Conductivity of Soils from the Analysis of Boring Logs* (Master's Thesis). Tampa, FL; University of South Florida, Department of Civil and Environmental Engineering.
- Pfeiffer, K. and Olson, J. (1981). *Basic Statistics for the Behavioral Sciences*. Holt, Rinehart, and Winston.
- Piscsalko, George. (2014). "Non-Destructive Testing of Drilled Shafts and CFA Piles – Current Practice and New Method." 2014 International Conference on Piling and Deep Foundations. Stockholm, Sweden. Pp. 533-546.
- Piscsalko, G., Alvarez, C., Belardo, D., and Galvan, M. (2014). "Using Thermal Integrity Profiling to Evaluate the Structural Integrity of Soil Nails." Deep Foundations Institute 39<sup>th</sup> Annual Conference on Deep Foundations: Atlanta, GA. Pp. 195-202.
- Poole, Jonathan L. (2007). *Modeling Temperature Sensitivity and Heat Evolution of Concrete* (Doctoral Dissertation). Austin, TX. University of Texas at Austin. UMI No. 3285913.
- Rausche, F., Likins, G., and Hussein, M. (1994). "Formalized Procedure for Quality Assessment of Cast-In-Place Shafts Using Sonic Echo Pulse Methods." Washington, D.C. Transportation Research Record No. 1447: *Design and Construction of Auger Cast Piles and Other Foundation Issues*. pp. 30-38.
- Schindler, A.K. and Folliard, K.J. (2002). *Temperature Control During Construction to Improve the Long Term Performance of Portland Cement Concrete Pavements*. Austin, TX. Center for Transportation Research. The University of Texas at Austin.
- Schindler, A.K. and Folliard, K.J. (2005). "Heat of Hydration Models for Cementitious Materials." Technical Paper. *ACI Materials Journal*, V. 102, No. 1. January-February 2005.
- Sellountou, A. and Alvarez, C. (2013). "Thermal Integrity Profiling: A Recent Technological Advancement in Integrity Evaluation of Concrete Piles." Proceedings from the First International Conference. Seminar on Deep Foundations: Santa Cruz, Bolivia.
- Silwinski, Z.J., and Fleming, W.G.K. (1983). "The Integrity and Performance of Bored Piles." Thomas Telford Publishing, London. *Piling and Ground Treatment for Foundations*. Pp. 153-165.

Taylor, H.F.W. (1997). *Cement Chemistry*. 2<sup>nd</sup> Edition. Thomas Telford Publishing, London.

USDOT, (2015). *Integrity Testing of Foundations*. Lakewood, CO. Central Federal Lands Highway Program, FHWA.

<http://www.cflhd.gov/resources/agm/engApplications/BridgeSystemSubstructure/221IntegrityTestingofFoundation.cfm>

*Appendix A*

# 3DM-GX4-25™ Attitude Heading Reference System (AHRS)

## Specifications

General			
<b>Integrated sensors</b>	Triaxial accelerometer, triaxial gyroscope, triaxial magnetometer, temperature sensors, and pressure altimeter		
<b>Data outputs</b>	<b>Inertial Measurement Unit (IMU) outputs:</b> acceleration, angular rate, magnetic field, ambient pressure, deltaTheta, deltaVelocity  <b>Computed outputs</b> <b>Adaptive Estimation Kalman Filter (AKF):</b> filter status, GPS timestamp, attitude estimates (in Euler angles, quaternion, orientation matrix), bias compensated angular rate, pressure altitude, gravity-free linear acceleration, attitude uncertainties, gyroscope and accelerometer bias, scale factors and uncertainties, gravity and magnetic models, and more. <b>Complementary Filter (CF):</b> attitude estimates (in Euler angles, quaternion, orientation matrix), stabilized north and gravity vectors, GPS correlation timestamp		
Inertial Measurement Unit (IMU) Sensor Outputs			
	Accelerometer	Gyroscope	Magnetometer
<b>Measurement range</b>	±5 g (standard) ±16 g (option)	300°/sec (standard) ±75, ±150, ±900 °/sec (options)	±2.5 Gauss
<b>Non-linearity</b>	±0.03 % fs	±0.03 % fs	±0.4 % fs
<b>Resolution</b>	<0.1 mg	<0.008°/sec	--
<b>Bias instability</b>	±0.04 mg	10°/hr	--
<b>Initial bias error</b>	±0.002 g	±0.05°/sec	±0.003 Gauss
<b>Scale factor stability</b>	±0.05 %	±0.05 %	±0.1 %
<b>Noise density</b>	100 µg/√Hz	0.005°/sec/√Hz	100 µGauss/√Hz
<b>Alignment error</b>	±0.05°	±0.05°	±0.05°
<b>Adjustable bandwidth</b>	225 Hz (max)	250 Hz (max)	-
<b>Offset error over temperature</b>	0.06% (typ)	0.05% (typ)	--
<b>Gain error over temperature</b>	0.05% (typ)	0.05% (typ)	--
<b>Scale factor non-linearity (@ 25° C)</b>	0.02% (typ) 0.06% (max)	0.02% (typ) 0.06% (max)	±0.0015 Gauss
<b>Vibration induced noise</b>	--	0.072°/s RMS/g RMS	--
<b>Vibration rectification error (VRE)</b>	--	0.001°/s/g <sup>2</sup> RMS	--
<b>IMU filtering</b>	4 stage filtering: analog bandwidth filter to digital sigma-delta wide band anti-aliasing filter to (user adjustable) digital averaging filter sampled at 4 kHz and scaled into physical units; coning and sculling integrals computed at 1 kHz		
<b>Sampling rate</b>	4 kHz	4 kHz	50 Hz
<b>IMU data output rate</b>	1 Hz to 1000 Hz		
Pressure Altimeter			
<b>Range</b>	-1800 m to 10,000 m		
<b>Resolution</b>	< 0.1 m		
<b>Noise density</b>	0.01 hPa RMS		
<b>Sampling rate</b>	10 Hz		

Computed Outputs	
<b>Attitude accuracy</b>	AKF outputs: ±0.25° RMS roll & pitch, ±0.8° RMS heading (typ) CF outputs: ±0.5° roll, pitch, and heading (static, typ), ±2.0° roll, pitch, and heading (dynamic, typ)
<b>Attitude heading range</b>	360° about all axes
<b>Attitude resolution</b>	< 0.01°
<b>Attitude repeatability</b>	0.3° (typ)
<b>Calculation update rate</b>	500 Hz
<b>Computed data output rate</b>	AKF outputs: 1 Hz to 500 Hz CF outputs: 1 Hz to 1000 Hz
Operating Parameters	
<b>Communication</b>	USB 2.0 (full speed) RS232 (9,600 bps to 921,600 bps, default 115,200)
<b>Power source</b>	+ 3.2 to +36 V dc
<b>Power consumption</b>	100 mA (typ), 120 mA (max) with Vpri = 3.2 V dc to 5.5 V dc 550 mW (typ), 800 mW (max) with Vaux = 5.2 V dc to 36 V dc
<b>Operating temperature</b>	-40 °C to +85 °C
<b>Mechanical shock limit</b>	500 g (calibration unaffected) 1000 g (bias may change) 5000 g (un-powered survivability)
<b>MTBF</b>	1.2 million hours (Telcordia method I, GL/35C) 0.45 million hours (Telcordia method I, GM/35C)
Physical Specifications	
<b>Dimensions</b>	36.0 mm x 24.4 mm x 11.1 mm (excluding mounting tabs), 36.6 mm (width across tabs)
<b>Weight</b>	16.5 grams
<b>Regulatory compliance</b>	ROHS, CE
Integration	
<b>Connectors</b>	Data/power output: micro-DB9
<b>Software</b>	MIP™ Monitor, MIP™ Hard and Soft Iron Calibration, Windows XP/Vista/7/8 compatible
<b>Compatibility</b>	Protocol compatibility with 3DM-GX3® and 3DM-RQ1™ sensor families.
<b>Software development kit (SDK)</b>	MIP™ data communications protocol with sample code available (OS and computing platform independent)

Copyright © 2014 LORD Corporation  
Document 8400-0090 Revision A. Subject to change without notice.

LORD Corporation  
MicroStrain® Sensing Systems  
459 Hurricane Lane, Suite 102  
Williston, VT 05495 USA  
www.microstrain.com  
ph: 802-962-6629  
fax: 802-963-4093  
sensing\_sales@LORD.com  
sensing\_support@LORD.com

Figure A.1. Lord Microstrain 3DM-GX4-25 datasheet



## 6 Electrical Characteristics

### 6.1 Gyroscope Specifications

VDD = 2.375V-3.46V, VLOGIC (MPU-6050 only) = 1.8V±5% or VDD, T<sub>A</sub> = 25°C

PARAMETER	CONDITIONS	MIN	TYP	MAX	UNITS	NOTES
<b>GYROSCOPE SENSITIVITY</b>						
Full-Scale Range	FS_SEL=0		±250		°/s	
	FS_SEL=1		±500		°/s	
	FS_SEL=2		±1000		°/s	
	FS_SEL=3		±2000		°/s	
Gyroscope ADC Word Length			16		bits	
Sensitivity Scale Factor	FS_SEL=0		131		LSB/(°/s)	
	FS_SEL=1		65.5		LSB/(°/s)	
	FS_SEL=2		32.8		LSB/(°/s)	
	FS_SEL=3		16.4		LSB/(°/s)	
Sensitivity Scale Factor Tolerance	25°C	-3		+3	%	
Sensitivity Scale Factor Variation Over Temperature			±2		%	
Nonlinearity	Best fit straight line; 25°C		0.2		%	
Cross-Axis Sensitivity			±2		%	
<b>GYROSCOPE ZERO-RATE OUTPUT (ZRO)</b>						
Initial ZRO Tolerance	25°C		±20		°/s	
ZRO Variation Over Temperature	-40°C to +85°C		±20		°/s	
Power-Supply Sensitivity (1-10Hz)	Sine wave, 100mVpp; VDD=2.5V		0.2		°/s	
Power-Supply Sensitivity (10 - 250Hz)	Sine wave, 100mVpp; VDD=2.5V		0.2		°/s	
Power-Supply Sensitivity (250Hz - 100kHz)	Sine wave, 100mVpp; VDD=2.5V		4		°/s	
Linear Acceleration Sensitivity	Static		0.1		°/s/g	
<b>SELF-TEST RESPONSE</b>						
Relative	Change from factory trim	-14		14	%	1
<b>GYROSCOPE NOISE PERFORMANCE</b>	<b>FS_SEL=0</b>					
Total RMS Noise	DLPFCFG=2 (100Hz)		0.05		°/s-rms	
Low-frequency RMS noise	Bandwidth 1Hz to10Hz		0.033		°/s-rms	
Rate Noise Spectral Density	At 10Hz		0.005		°/s/√Hz	
<b>GYROSCOPE MECHANICAL FREQUENCIES</b>						
X-Axis		30	33	36	kHz	
Y-Axis		27	30	33	kHz	
Z-Axis		24	27	30	kHz	
<b>LOW PASS FILTER RESPONSE</b>						
	Programmable Range	5		256	Hz	
<b>OUTPUT DATA RATE</b>						
	Programmable	4		8,000	Hz	
<b>GYROSCOPE START-UP TIME</b>						
ZRO Settling (from power-on)	DLPFCFG=0 to ±1°/s of Final		30		ms	

1. Please refer to the following document for further information on Self-Test: *MPU-6000/MPU-6050 Register Map and Descriptions*

Figure A.2. InvenSense MPU-6000 datasheet



**6.2 Accelerometer Specifications**

VDD = 2.375V-3.46V, VLOGIC (MPU-6050 only) = 1.8V±5% or VDD, T<sub>A</sub> = 25°C

PARAMETER	CONDITIONS	MIN	TYP	MAX	UNITS	NOTES
<b>ACCELEROMETER SENSITIVITY</b>						
Full-Scale Range	AFS_SEL=0 AFS_SEL=1 AFS_SEL=2 AFS_SEL=3		±2 ±4 ±8 ±16		g g g g	
ADC Word Length	Output in two's complement format		16		bits	
Sensitivity Scale Factor	AFS_SEL=0 AFS_SEL=1 AFS_SEL=2 AFS_SEL=3		16,384 8,192 4,096 2,048		LSB/g LSB/g LSB/g LSB/g	
Initial Calibration Tolerance			±3		%	
Sensitivity Change vs. Temperature	AFS_SEL=0, -40°C to +85°C		±0.02		%/°C	
Nonlinearity	Best Fit Straight Line		0.5		%	
Cross-Axis Sensitivity			±2		%	
<b>ZERO-G OUTPUT</b>						
Initial Calibration Tolerance	X and Y axes Z axis		±50 ±80		mg mg	1
Zero-G Level Change vs. Temperature	X and Y axes, 0°C to +70°C Z axis, 0°C to +70°C		±35 ±60		mg	
<b>SELF TEST RESPONSE</b>						
Relative	Change from factory trim	-14		14	%	2
<b>NOISE PERFORMANCE</b>						
Power Spectral Density	@10Hz, AFS_SEL=0 & ODR=1kHz		400		µg/√Hz	
<b>LOW PASS FILTER RESPONSE</b>						
	Programmable Range	5		260	Hz	
<b>OUTPUT DATA RATE</b>						
	Programmable Range	4		1,000	Hz	
<b>INTELLIGENCE FUNCTION INCREMENT</b>			32		mg/LSB	

1. Typical zero-g initial calibration tolerance value after MSL3 preconditioning
2. Please refer to the following document for further information on Self-Test: *MPU-6000/MPU-6050 Register Map and Descriptions*

Figure A.3. InvenSense MPU-6000 datasheet (cont'd)



**MPU-6000/MPU-6050 Product Specification**

Document Number: PS-MPU-6000A-00  
 Revision: 3.4  
 Release Date: 08/19/2013

**6.3 Electrical and Other Common Specifications**

VDD = 2.375V-3.46V, VLOGIC (MPU-6050 only) = 1.8V±5% or VDD, T<sub>A</sub> = 25°C

PARAMETER	CONDITIONS	MIN	TYP	MAX	Units	Notes
<b>TEMPERATURE SENSOR</b>						
Range			-40 to +85		°C	
Sensitivity	Untrimmed		340		LSB/°C	
Temperature Offset	35°C		-521		LSB	
Linearity	Best fit straight line (-40°C to +85°C)		±1		°C	
<b>VDD POWER SUPPLY</b>						
Operating Voltages		2.375		3.46	V	
Normal Operating Current	Gyroscope + Accelerometer + DMP		3.9		mA	
	Gyroscope + Accelerometer (DMP disabled)		3.8		mA	
	Gyroscope + DMP (Accelerometer disabled)		3.7		mA	
	Gyroscope only (DMP & Accelerometer disabled)		3.6		mA	
	Accelerometer only (DMP & Gyroscope disabled)		500		µA	
Accelerometer Low Power Mode Current	1.25 Hz update rate		10		µA	
	5 Hz update rate		20		µA	
	20 Hz update rate		70		µA	
	40 Hz update rate		140		µA	
Full-Chip Idle Mode Supply Current			5		µA	
Power Supply Ramp Rate	Monotonic ramp. Ramp rate is 10% to 90% of the final value			100	ms	
<b>VLOGIC REFERENCE VOLTAGE</b>						
Voltage Range	MPU-6050 only VLOGIC must be ≤VDD at all times	1.71		VDD	V	
Power Supply Ramp Rate	Monotonic ramp. Ramp rate is 10% to 90% of the final value			3	ms	
Normal Operating Current			100		µA	
<b>TEMPERATURE RANGE</b>						
Specified Temperature Range	Performance parameters are not applicable beyond Specified Temperature Range	-40		+85	°C	

Figure A.4. InvenSense MPU-6000 datasheet (cont'd)



**MPU-6000/MPU-6050 Product Specification**

Document Number: PS-MPU-6000A-00  
 Revision: 3.4  
 Release Date: 08/19/2013

**6.4 Electrical Specifications, Continued**

VDD = 2.375V-3.46V, VLOGIC (MPU-6050 only) = 1.8V±5% or VDD, TA = 25°C

PARAMETER	CONDITIONS	MIN	TYP	MAX	Units	Notes
<b>SERIAL INTERFACE</b>						
SPI Operating Frequency, All Registers Read/Write	MPU-6000 only, Low Speed Characterization		100 ±10%		kHz	
	MPU-6000 only, High Speed Characterization		1 ±10%		MHz	
SPI Operating Frequency, Sensor and Interrupt Registers Read Only	MPU-6000 only		20 ±10%		MHz	
I <sup>2</sup> C Operating Frequency	All registers, Fast-mode			400	kHz	
	All registers, Standard-mode			100	kHz	
<b>I<sup>2</sup>C ADDRESS</b>						
	AD0 = 0		1101000			
	AD0 = 1		1101001			
<b>DIGITAL INPUTS (SDI/SDA, AD0, SCLK/SCL, FSYNC, /CS, CLKIN)</b>						
V <sub>IH</sub> , High Level Input Voltage	MPU-6000	0.7*VDD			V	
	MPU-6050	0.7*VLOGIC			V	
V <sub>IL</sub> , Low Level Input Voltage	MPU-6000			0.3*VDD	V	
	MPU-6050			0.3*VLOGIC	V	
C <sub>I</sub> , Input Capacitance			< 5		pF	
<b>DIGITAL OUTPUT (SDO, INT)</b>						
V <sub>OH</sub> , High Level Output Voltage	R <sub>LOAD</sub> =1MΩ; MPU-6000	0.9*VDD			V	
	R <sub>LOAD</sub> =1MΩ; MPU-6050	0.9*VLOGIC			V	
V <sub>OL1</sub> , LOW-Level Output Voltage	R <sub>LOAD</sub> =1MΩ; MPU-6000			0.1*VDD	V	
	R <sub>LOAD</sub> =1MΩ; MPU-6050			0.1*VLOGIC	V	
V <sub>OLINT1</sub> , INT Low-Level Output Voltage	OPEN=1, 0.3mA sink Current			0.1	V	
Output Leakage Current	OPEN=1		100		nA	
t <sub>INT</sub> , INT Pulse Width	LATCH_INT_EN=0		50		μs	

Figure A.5. InvenSense MPU-6000 datasheet (cont'd)



**6.5 Electrical Specifications, Continued**

Typical Operating Circuit of Section 7.2, VDD = 2.375V-3.46V, VLOGIC (MPU-6050 only) = 1.8V±5% or VDD, T<sub>A</sub> = 25°C

Parameters	Conditions	Typical	Units	Notes	
<b>Primary I<sup>2</sup>C I/O (SCL, SDA)</b>					
V <sub>IL</sub> , LOW-Level Input Voltage	MPU-6000	-0.5 to 0.3*VDD	V		
V <sub>IH</sub> , HIGH-Level Input Voltage	MPU-6000	0.7*VDD to VDD + 0.5V	V		
V <sub>hys</sub> , Hysteresis	MPU-6000	0.1*VDD	V		
V <sub>IL</sub> , LOW Level Input Voltage	MPU-6050	-0.5V to 0.3*VLOGIC	V		
V <sub>IH</sub> , HIGH-Level Input Voltage	MPU-6050	0.7*VLOGIC to VLOGIC + 0.5V	V		
V <sub>hys</sub> , Hysteresis	MPU-6050	0.1*VLOGIC	V		
V <sub>OL1</sub> , LOW-Level Output Voltage	3mA sink current	0 to 0.4	V		
I <sub>OL</sub> , LOW-Level Output Current	V <sub>OL</sub> = 0.4V	3	mA		
	V <sub>OL</sub> = 0.6V	5	mA		
Output Leakage Current		100	nA		
t <sub>of</sub> , Output Fall Time from V <sub>IHmax</sub> to V <sub>ILmax</sub>	C <sub>b</sub> bus capacitance in pF	20+0.1C <sub>b</sub> to 250	ns		
C <sub>i</sub> , Capacitance for Each I/O pin		< 10	pF		
<b>Auxiliary I<sup>2</sup>C I/O (AUX_CL, AUX_DA)</b>					
V <sub>IL</sub> , LOW-Level Input Voltage	MPU-6050: AUX_VDDIO=0	-0.5V to 0.3*VLOGIC	V		
V <sub>IH</sub> , HIGH-Level Input Voltage		0.7*VLOGIC to VLOGIC + 0.5V	V		
V <sub>hys</sub> , Hysteresis		0.1*VLOGIC	V		
V <sub>OL1</sub> , LOW-Level Output Voltage		VLOGIC > 2V; 1mA sink current	0 to 0.4	V	
V <sub>OL3</sub> , LOW-Level Output Voltage		VLOGIC < 2V; 1mA sink current	0 to 0.2*VLOGIC	V	
I <sub>OL</sub> , LOW-Level Output Current		V <sub>OL</sub> = 0.4V	1	mA	
		V <sub>OL</sub> = 0.6V	1	mA	
Output Leakage Current			100	nA	
t <sub>of</sub> , Output Fall Time from V <sub>IHmax</sub> to V <sub>ILmax</sub>		C <sub>b</sub> bus capacitance in pF	20+0.1C <sub>b</sub> to 250	ns	
C <sub>i</sub> , Capacitance for Each I/O pin			< 10	pF	

Figure A.6. InvenSense MPU-6000 datasheet (cont'd)



**6.6 Electrical Specifications, Continued**

Typical Operating Circuit of Section 7.2, VDD = 2.375V-3.46V, VLOGIC (MPU-6050 only) = 1.8V±5% or VDD, T<sub>A</sub> = 25°C

Parameters	Conditions	Min	Typical	Max	Units	Notes
<b>INTERNAL CLOCK SOURCE</b>						
Gyroscope Sample Rate, Fast	CLK_SEL=0,1,2,3 DLPFCFG=0 SAMPLERATEDIV = 0		8		kHz	
Gyroscope Sample Rate, Slow	DLPFCFG=1,2,3,4,5, or 6 SAMPLERATEDIV = 0		1		kHz	
Accelerometer Sample Rate			1		kHz	
Clock Frequency Initial Tolerance	CLK_SEL=0, 25°C	-5		+5	%	
Frequency Variation over Temperature	CLK_SEL=1,2,3; 25°C	-1		+1	%	
	CLK_SEL=0		-15 to +10		%	
PLL Settling Time	CLK_SEL=1,2,3		±1		%	
	CLK_SEL=1,2,3		1	10	ms	
<b>EXTERNAL 32.768kHz CLOCK</b>						
External Clock Frequency	CLK_SEL=4		32.768		kHz	
External Clock Allowable Jitter	Cycle-to-cycle rms		1 to 2		µs	
Gyroscope Sample Rate, Fast	DLPFCFG=0 SAMPLERATEDIV = 0		8.192		kHz	
Gyroscope Sample Rate, Slow	DLPFCFG=1,2,3,4,5, or 6 SAMPLERATEDIV = 0		1.024		kHz	
Accelerometer Sample Rate			1.024		kHz	
PLL Settling Time			1	10	ms	
<b>EXTERNAL 19.2MHz CLOCK</b>						
External Clock Frequency	CLK_SEL=5		19.2		MHz	
Gyroscope Sample Rate	Full programmable range	3.9		8000	Hz	
Gyroscope Sample Rate, Fast Mode	DLPFCFG=0 SAMPLERATEDIV = 0		8		kHz	
Gyroscope Sample Rate, Slow Mode	DLPFCFG=1,2,3,4,5, or 6 SAMPLERATEDIV = 0		1		kHz	
Accelerometer Sample Rate			1		kHz	
PLL Settling Time			1	10	ms	

Figure A.7. InvenSense MPU-6000 datasheet (cont'd)

*Appendix B*

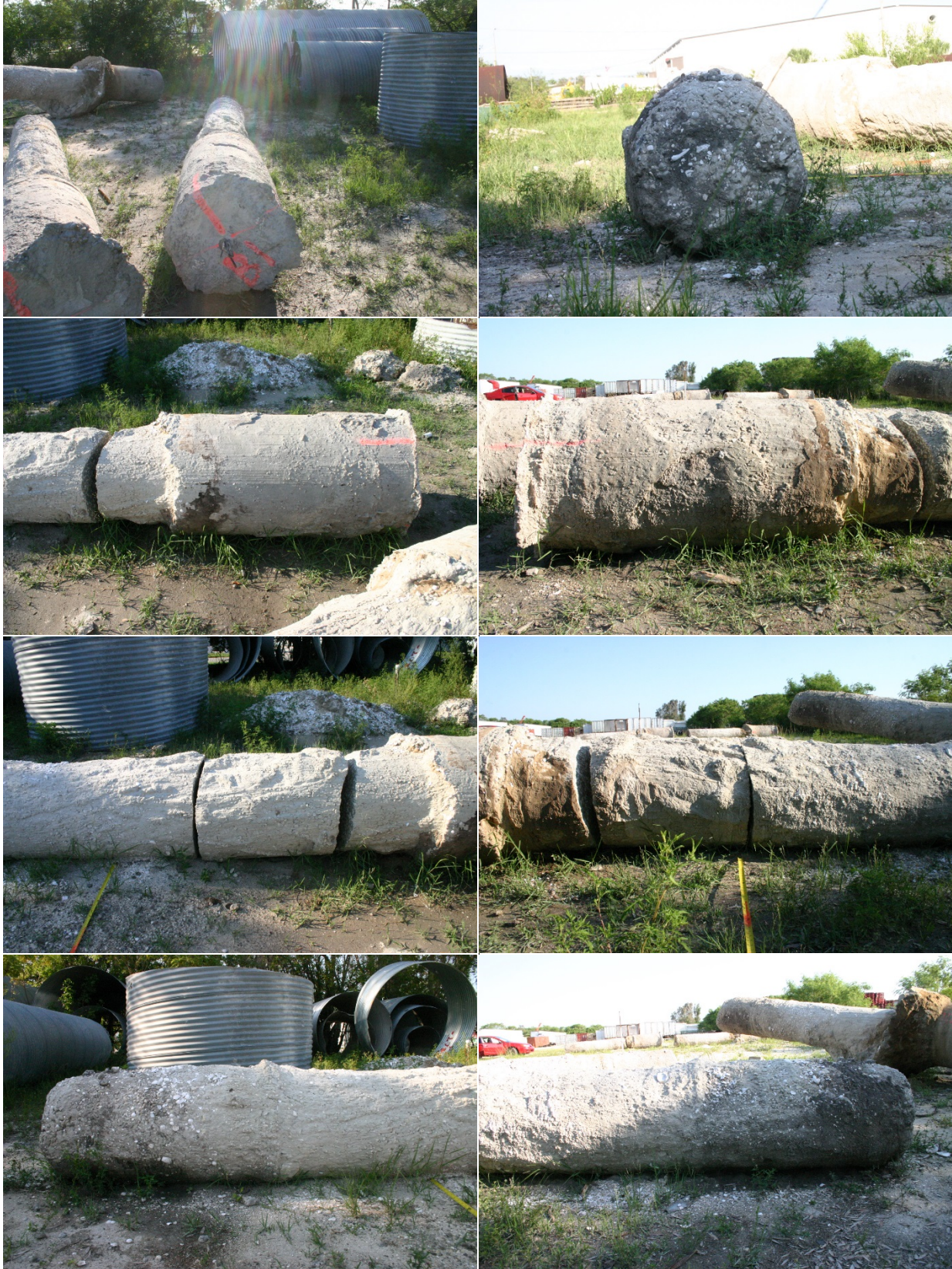


Figure B.1. Shaft B-1 (from top to bottom): shaft top (left) and toe (right); side views of shaft top section; side views of shaft middle section; side views of bottom section



Figure B.2. Shaft P-1 (from top to bottom): shaft top (left) and toe (right); side views of shaft top section; side views of shaft middle section; side views of bottom section



Figure B.3. Shaft P-3 (from top to bottom): shaft top (left) and toe (right); side views of shaft top section; side views of shaft middle section; side views of bottom section



Figure B.4. Shaft B-3 (from top to bottom): shaft top (left) and toe (right); side views of shaft top section; side views of shaft middle section; side views of bottom section



Figure B.5. Shaft P-2 (from top to bottom): shaft top (left) and toe (right); side views of shaft top section; side views of shaft middle section; side views of bottom section



Figure B.6. Shaft B-4 (from top to bottom): shaft top (left) and toe (right); side views of shaft top section; side views of shaft middle section; side views of bottom section



Figure B.7. Shaft B-5 (from top to bottom): shaft top (left) and toe (right); side views of shaft top section; side views of shaft middle section; side views of bottom section



Figure B.8. Shaft B-6 (from top to bottom): shaft top (left) and toe (right); side views of shaft top section; side views of shaft middle section; side views of bottom section



Figure B.9. Shaft P-5 (from top to bottom): shaft top (left) and toe (right); side views of shaft top section; side views of shaft middle section; side views of bottom section



Figure B.10. Shaft P-6 (from top to bottom): shaft top (left) and toe (right); side views of shaft top section; side views of shaft middle section; side views of bottom section